Transactions of the ASME

FLUIDS ENGINEERING DIVISION
Technical Editor
DEMETRI P. TELIONIS (1995)
Executive Secretary
PAT WHITE (1995)
Technical Editor's Office
SAAD A. RAGAB
Calendar Editor
M. F. ACKERSON

Associate Technical Editors
Fluid Machinery
WIDEN TABAKOFF (1991)
UPENDRA S. ROHATGI (1990)
Fluid Measurements
JOHN F. FOSS (1990)
Fluid Mechanics
J. CRAIG DUTTON (1990)
CHRISTOPHER J. FREITAS (1991)
DANIEL C. REDA (1990)
Fluid Tarnsients
FRANKLIN T. DODGE (1992)
Numerical Methods
DAVID G. LILLEY (1991)
Multiphase Flow
EFSATTHIOS E. MICHAELIDES (1991)
GEORGES L. CHAHINE (1990)
Review Articles
K. N. GHIA (1990)

BOARD ON COMMUNICATIONS
Chairman and Vice-President
M. E. FRANKE

Members-at-Large
W. BEGELL
T. F. CONRY
T. DEAR
R. L. KASTOR
R. MATES
E. M. PATTON
R. E. REDER
R. D. ROCKE
A. VAN DER SLUYS
A. J. WENNERSTROM
W. O. WINER
B. ZIELS

President, A. E. BERGLES
Exec. Dir.
D. L. BELDEN
Treasurer,
ROBERT A. BENNETT

PUBLISHING STAFF
Mng. Dir., Publ.,
CHARLES W. BEARDSLEY
Managing Editor,
CORNELIA MONAHAN
Production Asstistant, MARISOL ANDINO

Transactions of the ASME, Journal of Fluids Engineering (ISSN 0098-2202) is published quarterly (Mar., June, Sept., Dec.) for $110.00 per year by The American Society of Mechanical Engineers, 345 East 47th Street, New York, NY 10017. Second class postage paid at New York, NY and additional mailing offices. POSTMASTER: Send address changes to Transactions of the ASME, Journal of Fluids Engineering, c/o THE AMERICAN SOCIETY OF MECHANICAL ENGINEERS, 22 Law Drive, Box 2300, Fairfield, NJ 07007-2300.
CHANGES OF ADDRESS must be received at Society headquarters seven weeks before they are to be effective. Please send old label and new address.
PRICES: To members, $36.00, annually; to nonmembers, $110.00. Add $20.00 for postage to countries outside the United States and Canada.
STATEMENT from By-Laws. The Society shall not be responsible for statements or opinions advanced in papers or . . . printed in its publications (B7.1, Par. 3).

INDEXED by Applied Mechanics Reviews and Engineering Information, Inc.

Journal of Fluids Engineering

Published Quarterly by The American Society of Mechanical Engineers

VOLUME 112 • NUMBER 3 • SEPTEMBER 1990

Rotordynamic Coefficients and Leakage Flow of Circumferentially Grooved Liquid-Seals

J. J. Kilgore
Shell Development Company,
Houston, Texas

D. W. Childs
Turbomachinery Laboratory,
Texas A&M University,
College Station, Texas 77843-3123

Measured leakage flow and rotordynamic coefficients for six, circumferentially-grooved, liquid seals are compared to predictions based on Nordmann et al.'s (1986) grooved seal model. The grooved seal model uses a modification of Hirs' (1973) bulk-flow theory to account for the difference in friction factor in the circumferential and axial directions due to the grooves. Also, the model uses an average groove depth to account for the circumerential flow in the grooves. Comparison of the predicted and measured friction factors in grooved-seals with orbiting-rotors shows a poor correlation. In spite of the poor friction-factor correlation, the accuracy of predictions for rotordynamic coefficients are comparable to predictions of Childs et al. (1988) and Childs and Kim (1986) for smooth and hole pattern seals.

Introduction

The two seal types which have both the potential to develop significant rotor forces and influence the bending vibrations of the pump rotor are illustrated in Fig. 1. The neck or wear ring seals are provided to reduce the leakage flow back along the front surface of the impeller face, while the interstage seal reduces the leakage flow from an impeller inlet back along the shaft to the backside of the preceding impeller. Each of these seal types have geometries similar to plain journal bearings but typically have clearance-to-radius ratios on the order of 0.003 as compared to 0.001 for bearings. The seals in this study have smooth rotors and circumferentially grooved stators.

From a rotordynamics viewpoint, seal analysis has the objective of predicting the coefficients of the following motion/reaction-force model

$$-\begin{Bmatrix} F_X \\ F_Y \end{Bmatrix} = \begin{bmatrix} K & k \\ -k & K \end{bmatrix} \begin{Bmatrix} X \\ Y \end{Bmatrix} + \begin{bmatrix} C & c \\ -c & C \end{bmatrix} \begin{Bmatrix} \dot{X} \\ \dot{Y} \end{Bmatrix} + M \begin{Bmatrix} \ddot{X} \\ \ddot{Y} \end{Bmatrix}, \quad (1)$$

where X and Y are components of the seal-rotor displacement relative to its stator, and F_X and F_Y are components of the reaction force. The diagonal and off-diagonal stiffness and damping coefficients are referred to, respectively, as "direct" and "cross-coupled." The cross-coupled coefficients arise due to fluid rotation within the seal. The coefficient M models the seal's added fluid mass.

Recent analyses to predict the rotordynamic coefficients of liquid annular seals use an expansion in the eccentricity ratio to yield zeroth and first-order equations. The zeroth-order equations define the flow and pressure fields for a centered position. The first-order equations depend on the zeroth-order solution and are used to define the rotordynamic coefficients. As a consequence of these developments, the rotordynamic coefficients depend on essentially static data for the centered position, viz., friction factor and inlet-loss correlations.

Nordmann et al.'s (1986) grooved-seal analysis procedure is based on Childs (1983) finite length solution, which uses an extension of Hirs' (1973) bulk-flow theory to calculate the rotordynamic coefficients and leakage flow. The Hirs-based theory characterizes the shear stress at the rotor or stator as an empirical power-law function of the Reynolds number of the form

$$\tau_w = \frac{\rho}{2} V_w^2 n \mathrm{Re}^m, \quad (2)$$

where Re is the Reynolds number defined by

$$\mathrm{Re} = \frac{2\rho V_w H}{\mu}. \quad (3)$$

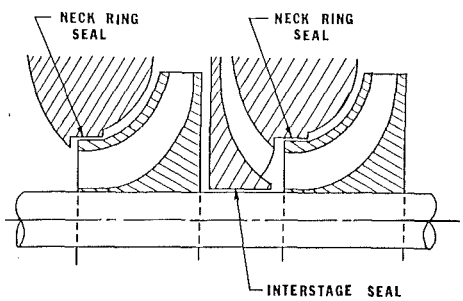

Fig. 1 Neck ring and interstage seals

Contributed by the Fluids Engineering Division for publication in the JOURNAL OF FLUIDS ENGINEERING. Manuscript received by the Fluids Engineering Division May 15, 1989.

and V_w is the magnitude of the velocity vector relative to the wall. The two empirical parameters change, depending on the relative roughness of the surface and the Reynolds number range. Nordmann et al. modify Hirs' turbulent lubricant equations to account for the difference in friction factor in the circumferential and axial directions due to the grooves. In addition, an average groove depth is introduced to consider the circumferential flow in the grooves. The grooved seal model can be applied to stator with smooth or grooved surfaces, and tapered or constant clearance geometries.

The grooved seal model of Nordmann et al. has been programmed for solution, and predictions for leakage flow and rotordynamic coefficients are compared to experimental results for six parallel-grooved liquid seals. This comparison provides an additional basis for evaluating the model for seals with different geometries and higher Reynolds numbers. Also, the Hirs' friction factor model is compared to results derived from experimental data to determine the applicability of Hirs' formulation to grooved seals.

Dynamic Measurements

Figure 2 illustrates the dynamic seal-test apparatus. Fluid enters the center and discharges axially across the two seals. For dynamic tests, the rotor elements of the seals are mounted eccentrically to the bearing-enforced axis of rotation. Because of the eccentricity, shaft rotation generates a rotating pressure field. This transient pressure field is measured via five, axially-spaced, strain-gauge, pressure transducers. Transient measurements are also made on the seal-rotor motion in the horizontal and vertical planes. The pressure signals are integrated to yield force coefficients which are parallel and transverse to the rotating, seal-eccentricity vector; i.e., radial and circumferential force coefficients are calculated from test data.

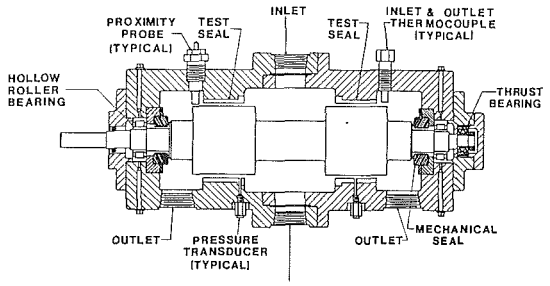

Fig. 2 High-Reynolds-number seal test section

The test section and flow loop achieve high-Reynolds number by pumping Halon ($CBrF_3$), a Dupont-manufactured fire extinguisher fluid and refrigerant. Additional details of the test section and flow loop are provided by Childs et al. (1982).

The dynamic test apparatus yields circular-orbital motion of the form

$$X = A \cos \omega t,\ Y = A \sin \omega t, \tag{4}$$

where the orbit-magnitude A is 89μm for the seals tested. When substituted into equation (1), this motion yields the following definition of force coefficients which are, respectively, parallel and perpendicular to the rotating displacement vector

$$F_r/A = -K - c\omega + M\omega^2$$
$$F_\theta/A = k - C\omega. \tag{5}$$

Observe that the cross-coupled-stiffness coefficient k yields a "driving" tangential contribution in the direction of rotation while the direct damping coefficient develops a drag force opposing the tangential velocity.

Nomenclature

A = rotor orbit magnitude, (L)
C,c = direct and cross-coupled damping coefficients, (FT/L)
$\bar{C}$ = minimum seal clearance, (L)
C_d = seal discharge coefficient defined by equation (8)
C_g = seal groove depth, (L)
C_g^* = average groove depth, (L)
F_X,F_Y = seal reaction-force components, introduced in equation (1), (F)
$F_r/A = f_r$, $F_\theta/A = f_\theta$ = experimental seal force components in the radial and circumferential directions, respectively, (F/L)
K,k = direct and cross-coupled stiffness coefficients, introduced in equation (1), (F/L)
K_{ef},C_{ef},M_{ef} = equivalent linear stiffness, damping, and added mass coefficients, introduced in equation (6)
L = seal length, (L)
L_G = seal groove width, (L)
L_L = seal groove land length, (L)
M = direct added fluid mass coefficient, introduced in equation (1), (M)
n_r,m_r = Hirs' coefficients for the rotor
n_{sz},m_{sz} = Hirs' coefficients for the stator in the axial direction
$n_{s\theta},m_{s\theta}$ = Hirs' coefficients for the stator in the circumferential direction
ΔP = nominal pressure-drop across seal, $(F/L)^2$
R = seal radius, (L)
$R_a = 2V\bar{C}\rho/\mu$ = axial Reynolds number
t = independent variable time, (T)
$u_\theta = U_\theta/Rw$ = dimensionless circumferential component of velocity
$\bar{V}$ = centered-position average axial fluid velocity, (L/T)
X,Y = seal rotor-to-stator relative displacement, (L)
$\epsilon = A/\bar{C}$ = seal dynamic eccentricity ratio
λ_c = dimensionless friction factor for the rotor and stator combined
λ_r = dimensionless rotor friction factor
$\lambda_{sx},\lambda_{s\theta}$ = dimensionless stator friction-factors in the axial and circumferential directions
ω = rotor angular velocity, T^{-1}
ρ = fluid density, M/L^3
ξ = inlet pressure-loss coefficient
μ = absolute viscosity FT/L^2

Table 1 Dimensions of grooved seals tested

$R = 50.42$ mm, $L = 50.8$ mm

Seal No.	$\bar{C}$ (mm)	C_g (mm)	L_L (mm)	L_G (mm)	No. of Grooves
1	0.470	0.445	2.00	2.00	12
2	0.472	0.275	1.50	2.50	12
3	0.381	1.143	1.60	1.60	15
4	0.508	1.016	1.60	1.60	15
5	0.635	0.889	1.60	1.60	15
6	0.762	0.762	1.60	1.60	15

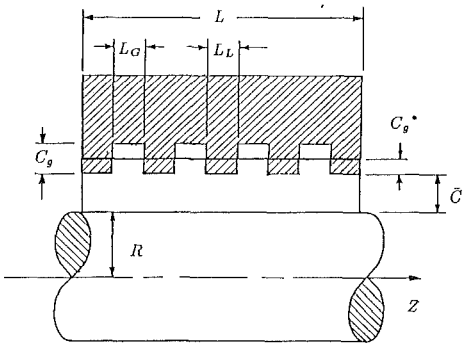

Rectangular groove cross-section

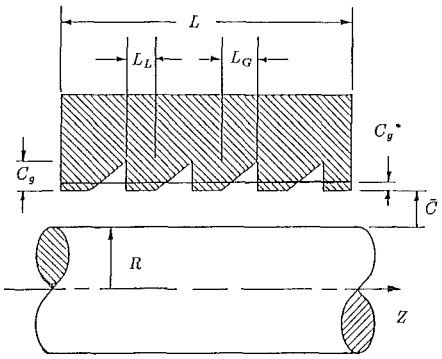

Saw-shaped groove cross-section

Fig. 3 Parallel-grooved seal geometry showing rectangular and saw-shaped groove cross-sections

The apparatus of Fig. 2 can be used to measure F_r/A and F_θ/A versus Reynolds number and running speed. However, it can not separately identify the coefficients of equation (5) because they depend on running speed. Equation (5) can be used as the basis for a quantitative comparison between theory and experiment. By assuming that k and c vary linearly with ω, the result is

$$f_\theta = F_\theta/A = C_{ef}\omega$$
$$f_r = F_r/A = K_{ef} + M_{ef}\omega^2. \quad (6)$$

The assumed forms of these equations are entirely consistent with the test data; i.e., f_θ is a linear function of ω and f_r is a function of ω^2.

Test results are obtained for a fixed, axial, Reynolds number over a range of running speeds and then curve-fitted to obtain K_{ef}, C_{ef}, and M_{ef}.

Static Measurements

Static measurements include upstream and downstream temperature and pressure measurements. Additionally, static pressure-gradient results are provided by the five axially spaced pressure transducers which are also used to measure the reaction force components. These transducers are located symmetrically about the midplane of the seal at .05, .23, and

Seal 1

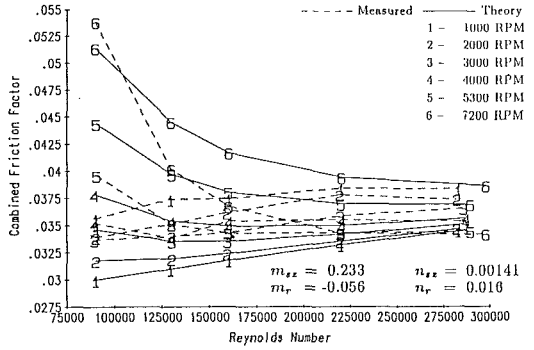

Seal 2

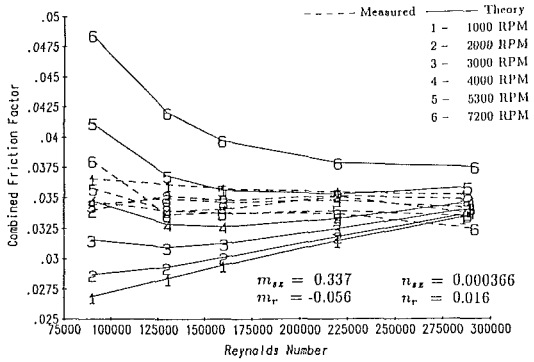

Fig. 4 Measured and theoretical values for λ_c versus R_a and ω for seals 1 and 2

Seal 3

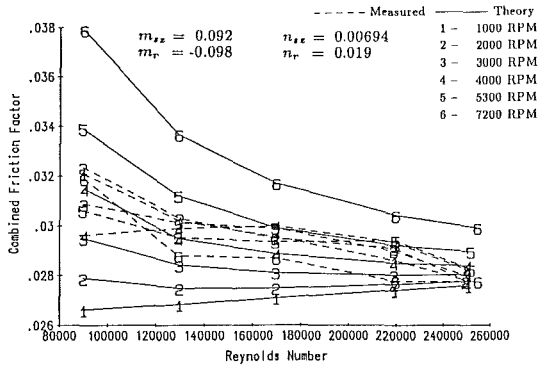

Seal 4

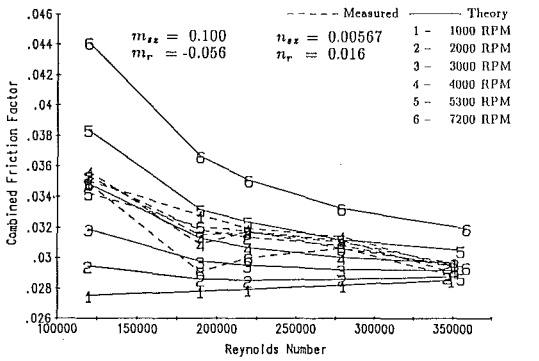

Fig. 5 Measured and theoretical values for λ_c versus R_a and ω for seals 3 and 4

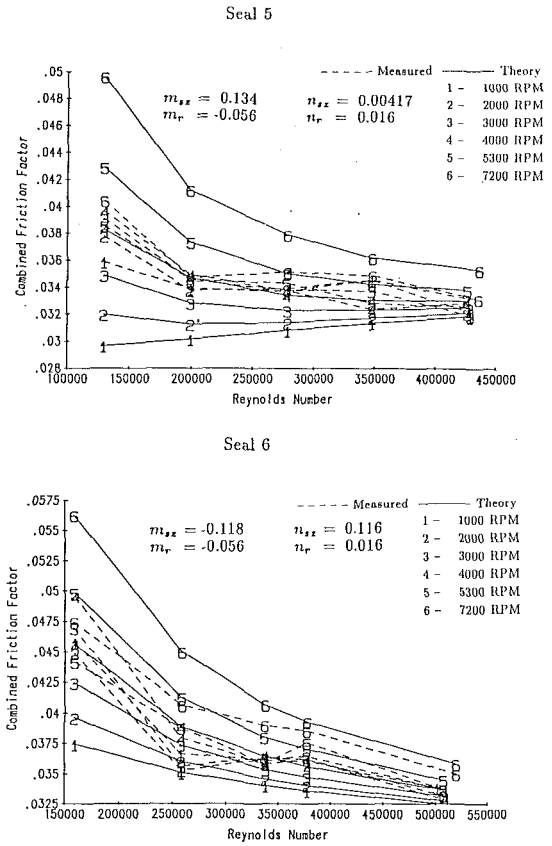

Fig. 6 Measured and theoretical values for λ_c versus R_a and ω seals 5 and 6

.5 of the seal length. The inlet-loss coefficient is defined by the pressure measurement upstream and immediately inside the seal. The axial pressure gradient is defined by the three centered pressure taps at .23L, 0.5L, and 0.77L.

Grooved Seal Geometry

The seals tested are not tapered and have the same length L and radius R. The groove geometry is described by the groove depth C_g and the groove length L_G and land length L_L. Nordmann et al.'s (1986) analysis assumes that the groove depth C_g has the same order of magnitude as the average seal clearance $\bar{C}$. The clearance-to-radius ratios used here are substantially larger than conventional practice to maximize the axial and circumferential Reynolds numbers. Table 1 shows the dimensions for each of the seals tested. Note that seals 3 through 6 simulate increasing clearances due to seal wear.

The average groove depth C_g^* is defined for a rectangular groove by

$$C_g^* = \frac{C_g}{1 + L_G/L_L} . \tag{7}$$

An exception for equation (7) occurs for seals 1 and 2, because these seals have a saw-shaped groove cross-section. To account for this difference, half of the actual groove depth was used in the average groove depth calculation. Figure 3 illustrates the geometry of seals with rectangular and saw-shaped groove cross-sections.

Empirical Turbulence Parameters

Nordmann et al.'s (1986) analysis characterizes the circumferential and axial surface roughness of the stator with the empirical parameters $n_{s\theta}$, $m_{s\theta}$, and n_{sx}, m_{sx}, respectively. Rotor surface roughness is characterized by the empirical

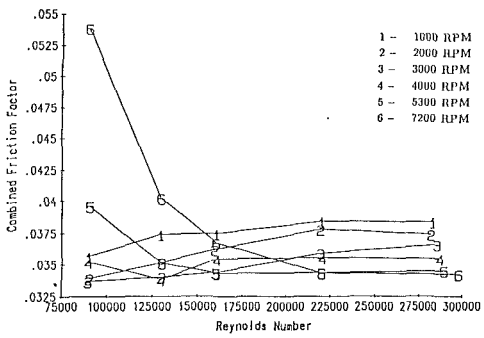

Fig. 7 Typical speed dependency for measured values of λ_c versus R_a and ω, shown for seal 1

parameters n_r and m_r. These empirical parameters must be determined before the predictions for the rotordynamic parameters and leakage flow can be made. The empirical parameters of the grooved stator in the circumferential direction $n_{s\theta}$, $m_{s\theta}$ and the smooth rotor n_r, m_r are assumed to be the same and are obtained from Childs et al. (1988), which shows the clearance effects on leakage and rotordynamic parameters of smooth seals. Parameters n_r, m_r, $n_{s\theta}$, and $m_{s\theta}$ are selected from Child's report by matching the grooved seal clearance, as closely as possible, to the smooth seals. Determination of empirical parameters n_{sx},m_{sx} for the friction factor of the grooved stator in the axial direction is done with Childs et al. (1989) method.

Friction Factor and Empirical-Parameter Results

For each of the six grooved seals tested, Figs. 4 through 6 presents the predicted and experimental results for the combined axial friction-factor of the rotor and stator, λ_c, which have been plotted versus axial Reynolds number $R_a = 2V\bar{C}\rho/\mu$ for each running speed case.

The curves in these figures show poor agreement between predicted and measured values of λ_c. The predicted curves for the combined friction factor λ_c show a much higher speed sensitivity than the measured curves over the entire Reynolds number range. Furthermore, the friction factor model characterizes combined friction factors as an exponential decaying function of Reynolds number, while the experimental results show friction factors that are either relatively constant or slightly decreasing functions of Reynolds number. Also, the predicted friction factors increase with increasing rotor speed, while, in general, the measured friction factors have mixed speed dependency at lower Reynolds numbers and have a definite decrease with increasing rotor speed at higher Reynolds numbers. Generally, this transition in speed dependency occurs at Reynolds numbers between 100,000 and 200,000. Figure 7 illustrates typical experimental friction factors λ_c versus Reynolds number and running speed to clearly show the speed dependency for the experimental curves, which is more difficult to see in Figs. 4 through 6.

Leakage Flow

Leakage flow results are presented in terms of the discharge coefficient. The predicted velocity $\bar{V}$ from the solution of the zeroth-order equation is used to calculate the predicted leakage coefficient $C_d^{-1/2}$ in the definition.

$$\bar{V} = C_d^{-1/2}\sqrt{\frac{2\Delta P}{\rho}} \tag{8}$$

Figures 8 through 10 illustrates the predicted and measured leadkage coefficient $C_d^{-1/2}$ versus average differential pressure ΔP and running speed for the each of the seals.

Seal 1

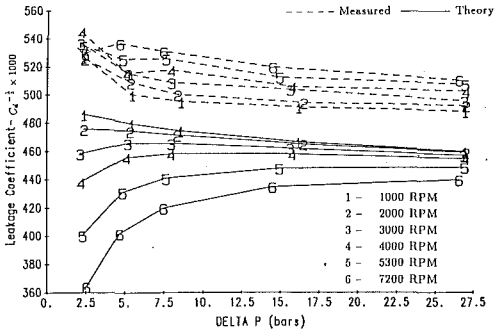

Seal 2

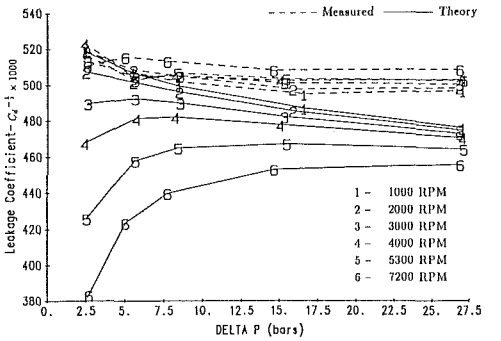

Fig. 8 Measured and predicted $C_d^{-1/2} \times 1000$ versus ΔP and ω for seals 1 and 2

Seal 3

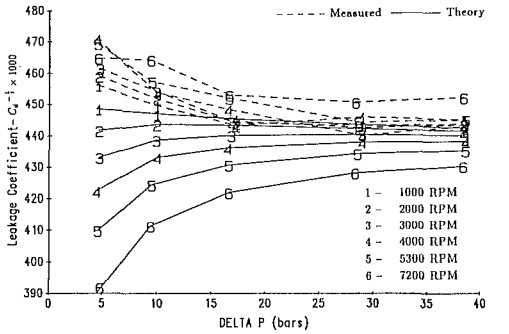

Seal 4

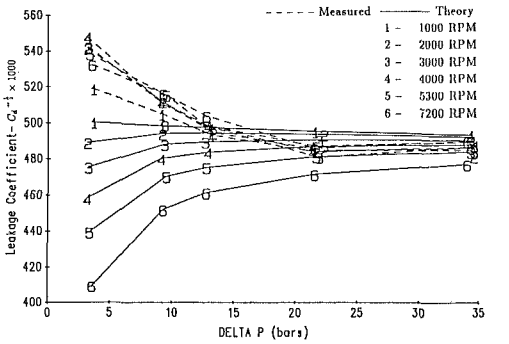

Fig. 9 Measured and predicted $C_d^{-1/2} \times 1000$ versus ΔP and ω for seals 3 and 4

Observe that in each of the plots the measured leakage coefficients are fairly constant over the ΔP range and are speed insensitive compared to the predicted leakage results. In general,

Seal 5

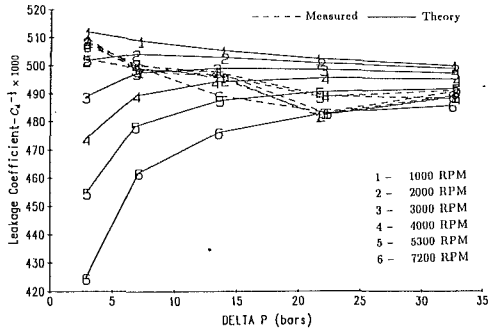

Seal 6

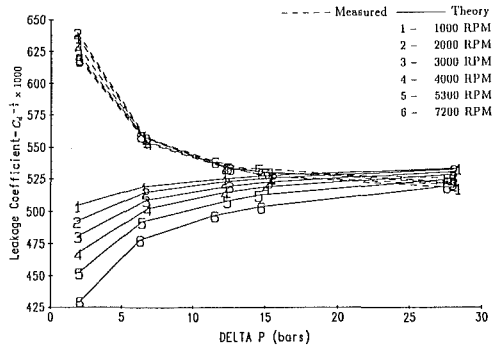

Fig. 10 Measured and predicted $C_d^{-1/2} \times 1000$ versus ΔP and ω for seals 5 and 6

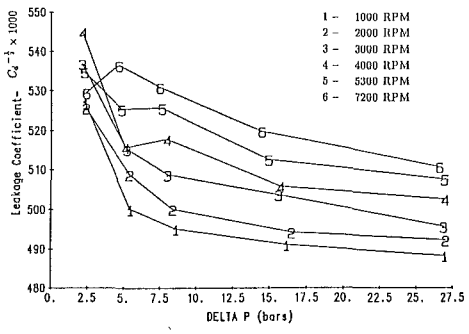

Fig. 11 Typical speed dependency for experimental values of $C_d^{-1/2} \times 1000$ versus ΔP and running speed, shown for seal 2

the speed sensitivity of the theoretical leakage coefficients are higher than the experimental leakage coefficients at lower ΔP and are the same or slightly higher at higher ΔP. Also, each of the plots shows the theoretical leakage coefficient decreases with increasing rotor speed, while the experimental leakage coefficients increases increases with increasing rotor speed over most of the higher ΔP range and have mixed rotor speed dependency at lower ΔP. The transition in speed dependency found in the measured friction factors is also found in the measured leakage coefficient results. Figure 11 illustrates typical experimental leakage coefficients $C_d^{-1/2}$ versus ΔP and running speed to clearly show the speed dependency which is more difficult to see in Figs. 8 through 10.

In general, there is poor agreement between the predicted and measured leakage coefficients at lower differential pressures, but improvement in the agreement is shown at high differential pressures. The theoretical leakage coefficient results show the same characteristics as the friction factor model; however, when the friction factor increases the leakage coefficient decreases. The measured leakage coefficient results

Table 2 Measured values for K_{ef}, C_{ef}, and M_{ef}; comparison of theory and experiment, SI units

$Ra_0 \times 10^{-5}$	$K_{ef} \times 10^{-6}$ (EXP)	C_{ef} (EXP)	M_{ef} (EXP)	K_{ef} (EXP/TH)	C_{ef} (EXP/TH)	M_{ef} (EXP/TH)
SEAL 1						
0.898	0.271	3160.	4.85	1.490	0.914	2.747
1.30	0.495	5210.	6.33	1.161	0.953	3.165
1.60	0.741	6450.	7.57	1.100	0.873	3.383
2.20	1.47	9300.	10.0	1.125	0.868	3.756
2.87	2.28	12700.	11.6	1.061	0.853	4.272
SEAL 2						
0.895	0.264	3590.	4.89	1.450	1.045	2.650
1.30	0.620	5530.	6.29	1.557	0.980	3.070
1.60	0.930	7040.	7.21	1.553	0.953	3.212
2.20	1.62	10100.	9.38	1.481	0.945	3.595
2.89	2.69	14000.	11.4	1.503	0.935	4.193
SEAL 3						
0.900	0.409	5540.	4.46	2.959	0.986	2.333
1.30	0.852	7800.	5.94	1.707	0.968	1.963
1.70	1.31	10200.	7.10	1.342	0.992	1.846
2.19	2.24	12100.	9.17	1.283	0.936	2.048
2.51	3.27	13400.	11.3	1.390	0.924	2.394
SEAL 4						
1.19	0.281	3840.	4.04	1.898	1.018	4.208
1.89	0.488	6880.	5.73	0.981	1.026	3.565
2.20	0.747	8000.	6.73	0.939	1.038	3.446
2.79	1.10	10600.	7.44	0.793	1.090	3.172
3.51	1.79	12500.	8.27	0.805	1.046	3.136
SEAL 5						
1.29	0.227	3060.	2.99	1.903	1.006	3.034
1.99	0.592	5020.	4.76	1.532	0.974	3.158
2.78	0.976	7700.	5.78	1.173	1.102	2.933
3.48	1.55	10300.	7.75	1.146	1.168	3.565
4.29	1.68	11500.	5.71	0.818	1.100	2.377
SEAL 6						
1.59	0.162	2300.	2.22	1.740	1.108	2.282
2.58	0.444	4260.	3.24	0.922	1.071	2.100
3.37	0.791	6190.	3.80	0.829	1.155	2.044
3.77	0.869	6640.	3.96	0.727	1.119	2.031
5.08	2.25	9260.	4.74	1.013	1.162	2.281

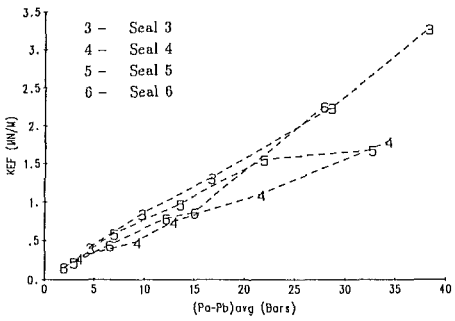

Fig. 12 Experimental K_{ef} versus average ΔP for seals 3, 4, 5, and 6

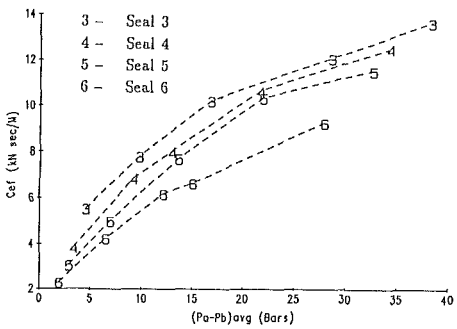

Fig. 13 Experimental C_{ef} versus average ΔP for seals, 3, 4, 5, and 6

are consistent with the measured friction factor curves, i.e., both show reduced speed sensitivity and relatively constant values as a function of Reynolds number or ΔP.

Rotordynamic Coefficients

After the empirical coefficients are determined for the friction-factor model, predictions can be made for rotordynamic coefficients. Integrating the pressure-field solution of the first-order equations yields f_r and f_θ which are curve-fitted to obtain the predicted effective rotordynamic coefficients.

Table 2 shows the experimental results and comparison between experiment and theory for K_{ef}, C_{ef}, and M_{ef}. Comparison between experiment and theory for K_{ef} shows an underprediction by theory for most seals, with most being within 40 percent and all showing improvement as Reynolds number increases. This improvement is expected since the friction factor correlation improves at higher Reynolds number. In addition, the present analysis uses a constant inlet-loss model where the inlet loss coefficient is found at the higher Reynolds numbers.

Comparison for M_{ef} shows the predicted values are much lower than the experimental values. The present model does not provide a useful prediction for M_{ef}, which is consistent with previous experience with Hirs-based, bulk-flow, predictions. The predicted values for C_{ef} are relatively close to the experimental values with most being underpredicted by theory and within 10 percent.

As a practical consideration, the geometry of seals 3 through 6 were designed to simulate increasing clearance due to wear. Comparing the experimental results in Fig. 12 at the same ΔP shows K_{ef} to decrease by about 40 percent between seals 3 and 6; however, K_{ef} for seal 6 shows an increase over seals 4 and 5 and is about the same as seal 3. In addition, Fig. 13 shows C_{ef} to decrease by about 30 percent as the seal clearance wears from 0.381 mm to 0.762 mm, which amounts to a doubling of the original clearance. In contrast to smooth seals, Childs et al. (1988) shows that both K_{ef} and C_{ef} decrease by about 40 percent when the clearance is doubled.

The principal uncertainty in the measurements arises from the pressure transducers and their associated filters and signal conditioners. The absolute uncertainty in the pressure measurements is approximately 6.9×10^3 Pa (1.5 psi). This yields a relative uncertainty in measured pressure gradients on the order of 10 percent at the lowest axial Reynolds numbers to 1 percent at the highest. Relative uncertainty of the radial force coefficient f_r is on the order of 10 percent across the operating speed range; while, f_θ has an uncertainty on the order of 5 percent.

Summary and Conclusions

The comparison of predicted friction factors to experimental results demonstrates that the Hirs' friction model does not adequately model the friction factor of grooved seals with orbiting-rotors. The friction factors of the model increase with increasing rotor speed, while the measured friction factors have mixed rotor speed dependency at lower Reynolds numbers and a definite decrease with increasing rotor speed at higher Reynolds numbers. Furthermore, while the model predicts the friction factor to be an exponential decaying function of Reynolds number, the data show it to be a fairly constant or slightly decreasing function of Reynolds number. Caution is recommended when using Nordmann et al.'s model for higher speed and Reynolds number applications, due to the divergence between the measured and predicted friction factors.

The effects of the nonconforming friction factor model can be seen in the predictions for leakage coefficients. The speed dependency of the friction factor model is particularly noticeable in the predictions for leakage coefficients. The predicted leakage coefficients decrease with increasing rotor speed, while the measured leakage coefficients increase with increasing rotor speed at higher ΔP. In addition, better leakage predictions are obtained at higher ΔP where, regardless of the difference in friction factor speed dependency, the predicted friction factors are closer to the measured results. At lower ΔP, leakage predictions and friction factor correlation are both poor.

In spite of the poor correlation of the Hirs' friction factor model, the predictions of rotordynamic coefficients for grooved seals are reasonable. In general, the present analysis tends to underpredict K_{ef} and slightly overpredict C_{ef}. Most of the predictions for K_{ef} are within 40 percent and most of the predictions for C_{ef} are within 10 percent. The grooved seal analysis does not provide a useful prediction for M_{ef}, which is consistent with past experience using Hirs-based models.

These resuls are encouraging, in that the grooved seal model predictions for rotordynamic coefficients are better than expected given the poor correlation of the friction-factor model. In fact, at this time Nordmann et al.'s grooved seal model is the best available method for predicting rotordynamic coefficients in liquid grooved seals without using a more expensive finite-element or finite-difference analysis. However, there is still motivation to find a new friction factor model to use in Nordmann's analysis, which would improve the prediction capability.

References

Childs, Dara, W., Nolan, Steven, A., and Nunez, Dean J., 1988, "Clearance Effects on Leakage and Rotordynamic Coefficients of Smooth, Liquid Annular Seals," *Proceedings IMechE 4th International Conference on Vibrations in Rotating Machinery*, Heriot-Watt University, Edinburg, U.K., Sept.

Childs, D. W., Nolan, S. A., and Kilgore, J. J., 1989, "Additional Test Results for Round-Hole-Pattern Damper Seals: Leakage, Friction Factors, and Rotordynamic Force Coefficients," submitted for the STLE/ASME Tribology Conference, 16–19 Oct.

Childs, Dara W., and Kim, Chang-Ho, 1986, "Test Results for Round-Hold-Pattern Damper Seals: Optimum Configurations and Dimensions for Maximum Net Damping," ASME *Journal of Tribology*, Vol. 108, Oct., pp. 605–611.

Childs, Dara W., 1983, "Finite Length Solutions for Rotordynamic Coefficients of Turbulent Annular Seals," ASME *Journal of Lubrication Technology*, Vol. 105, Oct., pp. 437–444.

Childs, D., Nelson, C., Noyes, T., and Dressman, J. B., 1982, "A High-Reynolds-Number Test Facility: Facility Description and Preliminary Data," NASA-Conference Publication 2250, *Proceeding of a Workshop on Rotordynamic Instability Problems in High-Performance Turbomachinery—1982*, held at Texas A&M University, College Station, Texas, 10–12 May 1982, pp. 157–171.

Hirs, G. G., 1973, "A Bulk-Flow Theory for Turbulence in Lubricant Film," ASME *Journal of Lubrication Technology*, Vol., Apr., pp. 137–146.

Nordmann, R., Dietzen, F. J., Janson, W., Frei, A., and Florjancic, S., 1986, "Rotordynamic Coefficients and Leakage Flow of Parallel Grooved Seals and Smooth Seals," *Proceedings of IFToMM International Conference on Rotordynamics*, Tokyo, Japan, Sept.

M. Agouzoul[1]

M. Reggio

R. Camarero

Applied Mathematics Department,
Ecole Polytechnique de Montréal,
Montréal, Canada, H3C 3A7

Calculation of Turbulent Flows in a Hydraulic Turbine Draft Tube

A numerical method to simulate three-dimensional incompressible turbulent flows has been developed and applied to the calculation of various flow situations in a draft tube. The conservative form of the primitive-variable formulation of the Reynolds averaged Navier-Stokes equations, written for a general curvilinear coordinate system, is employed. An overlapping grid combined with opposed differencing for mass and pressure gradients is used. All the properties are stored at the center of the same computational cell which is used for mass and transport balances. The k–ϵ model is used to describe the turbulent flow. The boundary conditions for the turbulent properties are treated with a particular attention.

1 Introduction

Internal flows are encountered in a wide variety of turbomachinery components. In most situations of practical relevance, these are three-dimensional and of a turbulent nature. In view of its importance in the design and analysis of such equipment, many attempts have been made to set up models to represent these complex phenomena accurately. These are usually based on the Reynolds averaged Navier-Stokes equations. A general aim is to make these Navier-Stokes solvers more reliable and cost effective to be incorporated in the design environment.

In this respect, a control-volume scheme previously applied to the solution of two-dimensional laminar [1] and turbulent flows [2, 3], and three-dimensional laminar flows [4] is extended to three-dimensional turbulent phenomenons, and applied to investigate the flow field in a draft tube. The flow behavior within this turbine component is complex, not only because its configuration changes dramatically from the inlet to the outlet, but also because the inlet flow is swirling and nonuniform. The use of this conduit of increasing cross-section which connects the runner exit to the tail race, results in a reduction of the velocity of the water exiting, and in a corresponding gain of pressure head. This has a direct impact in the efficiency of the turbine, thus a better understanding of the flow process within this component, is highly desirable.

The fluid flow is modelized by the time dependent Reynolds averaged Navier-Stokes equations closed with the two-equations model of turbulence k–ϵ. This set of equations is formulated in a strong conservative form for a general curvilinear coordinate system, which is numerically generated by using a body-conforming method [5].

The adopted k–ϵ turbulent model needs a special treatment near the solid wall to take into account the viscous-turbulent interaction. This problem is treated via the "wall function" technique. Instead of the standard "slip-velocity" approach currently applied to incorporate the boundary conditions, an alternative technique based on an "equivalent viscosity" and the actual zero-velocity condition is used. The main feature of this method is that it does not require the direction of the velocity at the first node near the wall. This not only implies an easy implementation for three-dimensional codes but a reduction on the computing time as well.

The approximation procedure is characterized by the use of the same element to compute the velocity components, the pressure, and the turbulent properties (k–ϵ). These variables are located at the center of the computational cell. In order to avoid unrealistic fields characteristic of such discretizations, an overlapping mesh structure, together with opposed differencing for pressure and mass flux in the main flow direction is applied.

The coupling between the pressure and velocity fields, associated with the computation of incompressible flows, is solved by following a fractional step methodology [6] modified and developed for a curvilinear mesh.

The present method has been first validated by computing

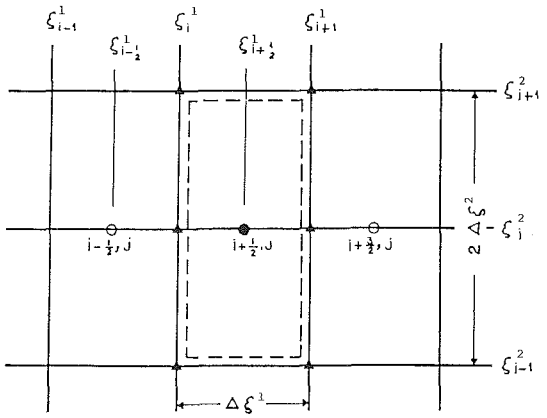

Fig. 1 Computational cell in the plane k = const

[1]Permanent address: Ecole Mohammadia d'Ingénieurs, B.P. 765, Rabat AGDAL, Morroco.

Contributed by the Fluids Engineering Division for publication in the JOURNAL OF FLUIDS ENGINEERING. Manuscript received by the Fluids Engineering Division December 19, 1988.

the flow within a curved duct of square section. Then, numerical simulations in a typical draft tube configuration, under different operating conditions, were carried out.

2 Governing Equations

The unsteady, Reynolds averaged Navier-Stokes equations for incompressible flows, along with the closure k-ϵ model, can be written in the following conservative form for a curvilinear system:

continuity:

$$\frac{\partial}{\partial \xi^m}(JU^m) = 0 \tag{1}$$

momentum:

$$\frac{\partial}{\partial t}(Ju_i) + \frac{\partial}{\partial \xi^m}\left(Ju_iU^m + Jp\frac{\partial \xi^m}{\partial x^i}\right) = \frac{\partial}{\partial \mu^m}\left(\nu_e J\left(g^{mj}\frac{\partial u_i}{\partial \xi^j} + \frac{\partial \xi^m}{\partial x^i}\frac{\partial u_j}{\partial x^j}\right)\right) \tag{2}$$

k-equation:

$$\frac{\partial}{\partial t}(Jk) + \frac{\partial}{\partial \xi^m}(JkU^m) = \frac{\partial}{\partial \xi^m}\left(\nu_e/\sigma_k J\left(g^{mj}\frac{\partial k}{\partial \xi^j}\right)\right) + \nu_e G_* - \epsilon \tag{3}$$

ϵ-equation:

$$\frac{\partial}{\partial t}(J\epsilon) + \frac{\partial}{\partial \xi^m}(J\epsilon U^m) = \frac{\partial}{\partial \xi^m}\left(\nu_e/\sigma_\epsilon J\left(g^{mj}\frac{\partial \epsilon}{\partial \xi^j}\right)\right) + \nu_e C_1 G_* \epsilon/k - C_2\frac{\epsilon^2}{k} \tag{4}$$

where ξ^m, with the superscript $m = 1, 2, 3$ indicates the "streamwise", "normal" and "binormal" directions respectively. The symbols J, and g^{mj} denote the Jacobian and the metric tensor components of the coordinate transformation respectively. The term ν_e appearing in the momentum equations, represents the effective viscosity given by:

$$\nu_e = \nu_t + \frac{1}{R_e} \tag{5}$$

in which $1/R_e$ stands for the dimensionless molecular viscosity, and ν_t the dimensionless turbulent viscosity. This is associated to k and ϵ by the relation:

$$\nu_t = C_d\frac{k^2}{\epsilon} \tag{6}$$

The source term G_* appearing in the k-ϵ equations is given by the following expression:

$$G_* = \left(\frac{\partial u^i}{\partial \xi^n}\frac{\partial \xi^n}{\partial x^j} + \frac{\partial u^i}{\partial \xi^n}\frac{\partial \xi^n}{\partial x^j}\right)\frac{\partial u^i}{\partial \xi^l}\frac{\partial \xi^l}{\partial x^j} \tag{7}$$

The value of the five empirical constants appearing in equations (3), (4), and (6) is given in [7] as:

$$C_1 = 1.44\ C_2 = 1.92\ \sigma_k = 1.\ \sigma_\epsilon = 1.3\ C_d = 0.09$$

Finally, the Cartesian velocity components u_i and the contravariant velocity components U^m are related by:

$$U^m = u_i\frac{\partial \xi^m}{\partial x^i} \tag{8}$$

where x^i, with the index $i = 1, 2, 3$, represents the Cartesian coordinates.

3 Numerical Procedure

3.1 Spatial Discretization. The control volume structure previously employed in the calculation of two-dimensional turbulent flows [2, 3], and three-dimensional laminar flows [4] is extended to the present three-dimensional turbulent simulations. Figure 1 shows the basic cell in the $\xi^1 - \xi^2$ plane (k = const). The treatment in the $\xi^1 - \xi^3$ plane is similar. This computing cell is used for the pressure and the transport equations, with the corresponding variables stored at the center $\left(i+\frac{1}{2}, j, k\right)$ of the element.

In order to perform the balance over a finite-volume, the fluxes at the cell faces are estimated as follows: in the "streamwise-ξ^1" direction, the mass flow U^1 and the pressure p are calculated via upwinding and downwinding respectively; in the two other directions ξ^2, ξ^3, and as a consequence of the overlapping mesh disposition, all the properties are known at the cell faces, with the exception of the pressure which is interpolated. On the other hand, the convected property fluxes and diffusion terms at all cell faces are calculated by following the weighted upstream difference scheme of Raithby and Torrance [8]. For more details see reference [4].

3.2 Temporal Differencing and Pressure Equation. The system to be solved includes the continuity equation, and five transport equations, three for the Cartesian velocity components and two for the k-ϵ turbulence properties. The time differencing used is semi-implicit, and in compact form can be written as:

Nomenclature

C_p = pressure coefficient
C_1, C_2, C_d, σ_ϵ, σ_k = constants in turbulent model
C_{pr} = pressure recovery factor
E_* = constant for the law of the wall
grad = stands for gradient
g^{ij} = meric tensor components
J = Jacobian of transformation matrix
k = turbulence kinetic energy
p = pressure
q = vector of conservation variables
Re = Reynolds number based on hydraulic diameter of the duct
t = time
u_i = time-averaged velocity components in x^i directions
u_* = friction velocity
u^i = time-averaged contravariant velocity components in ξ^i directions
x^i = Cartesian coordinates
y_p = conventional normal distance to the wall
ξ^i = curvilinear coordinates
δ_p = pressure correction
Δt = time step
ϵ = turbulence energy dissipation
κ = the von Karman constant
ν = kinematic viscosity
ν_e = effective viscosity
ν_t = turbulent viscosity

Subscripts

p = refers to the grid node next to the wall
i, j, k = variable location
0 = reference value

$$q^{n+1} = q^n + \Delta t(Tvq + Sq - Tcq)^n - \delta[\Delta t grad(p^{n+1})] \quad (9)$$

In this relation, the symbol q stands for all transported properties, n for the time level and Δt for the time step, while Tc, Tvq, and Sq denote the convective, viscous, and source terms, respectively. The parameter δ takes the value 1 for the momentum equations, and 0 for the other transport balances. It should be noted that only the pressure gradient in the momentum equations, is evaluated in an implicit manner. For the particular case of these equations, equation (9) leads to the following vector form:

$$V^{n+1} = V^n + \Delta t(TvV - TcV)^n - \Delta t grad(p^{n+1}) \quad (10)$$

This velocity must satisfy the continuity constraint:

$$\text{div}(v^{n+1}) = 0 \quad (11)$$

This last condition, is one of the major difficulties associated with the solution of incompressible flows, because it requires an adequate velocity-pressure coupling. Among the current techniques used for this purpose, a fractional step method similar to that presented by reference [6] has been developed.

Essentially one can describe the procedure as follows: first an intermediate velocity field $V^{n+1/2}$ is computed in a manner analogous to equation (10), but with a pressure at the level n instead of the level $n+1$. Then, taking the divergence of the difference $V^{n+1/2}$, which doesn't satisfy the continuity, and V^{n+1} given by equation (10), which does, yields:

$$\nabla^2(\delta p) = \text{div}(V^{n+1/2})/\Delta t \quad (12)$$

where δp represents the pressure correction $p^{n+1} - p^n$.

The numerical solution of this equation (12) needs some boundary conditions on the pressure correction which are not obvious. For internal incompressible flows, only the inlet velocity and the nonslip condition on the solid walls are known at any time. Consequently equation (12) cannot be used directly, unless some boundary conditions for the pressure, of derivative type for example, are incorporated.

When using this approach, the calculated pressure will not guarantee that the continuity equation is satisfied, unless the pressure field satisfies a compatibility condition, relating the source term of the pressure equation and its Neumann boundary conditions.

If a nonstaggered layout is applied as the basic discretization, this requirement it is not automatically satisfied. In order to achieve this in a discrete form, Abdallah [17-18] reported a formal procedure to determine appropriate boundary conditions in a Cartesian finite difference context.

On the other hand, if a staggered mesh is employed, a cure for compatibility condition is also found. In relation with this alternative, it is noted that the actual pressure cells do not overlap in the secondary directions (it is not the case of the momentum cells), and that the pressure on the element next to the wall is half a step from the boundary. In this sense, the present pressure computational cell agrees with the staggered mesh framework.

In particular, the pressure control volume has velocity components at all its six faces. The velocities on the faces related to the secondary directions, are obtained from the overlapping momentum cells, while those corresponding to the main flow direction, are defined from the upwinding procedure.

According to this computing cell structure, a technique which allows to consider only the boundary conditions on the velocity is employed. It can be described as follows:

The discrete form, in space, of $v^{n+1} - v^{n+1/2} = -\Delta t grad(\delta p)$ and equation (11) with the introduction of the velocity boundary condition yields:

$$I([v]^{n+1} - [v]^{n+1/2}) = \Delta t C[\delta p] \quad (13)$$

and

$$D[v]^{n+1} = 0 \quad (14)$$

where I stands for the identity matrix, while D and C denote the modified divergence and gradient matrices, respectively, which take into account the velocity boundary conditions. The brackets indicate global vector quantities.

After a simple combination of equations (13) and (14), the following relation can be obtained:

$$D[v]^{n+1/2} = \Delta t DC[\delta p] \quad (15)$$

This equation, which is a discrete approximation to equation (12), has now "built-in" velocity boundary conditions. By solving equation (15) the correction to the pressure is obtained, then the velocity field $v^{n+1/2}$ is corrected by:

$$v^{n+1} = v^{n+1/2} - \Delta t C[\delta p] \quad (16)$$

It is further noted that, due to the overlapping grid structure applied for the momentum equations in the secondary directions, the pressure is also required at the pressure volume faces. These values are obtained by the average of neighbouring values.

This technique allows the computation of the new cartesian velocity components without any averaging or coding, as it was previously reported in reference [4]. This not only implies a simpler code but more accurate calculations as well.

The global calculation procedure now can be summarized as follows: pressure, velocity, k, and ϵ fields are guessed, and a velocity $V^{n+1/2}$ is estimated according to equation (10). Then, a pressure correction δp is calculated from equation (13) and the predicted velocity field is subsequently corrected applying equation (14). The turbulence kinetic energy and dissipation rate transport equations are then solved, and the boundary conditions are calculated with the new mean velocity.

The time level is advanced and the above cycle is repeated until the steady state is reached.

4 Boundary Conditions

In order to connect the wall conditions to the variables just outside of the viscous region, the standard $k-\epsilon$ model is complemented with the wall function. Also an additional hypothesis is made to avoid errors on the computing of the shear stresses on the wall-adjacent elements. This is usually represented by using an imaginary wall slip-velocity, instead of actual zero velocity condition.

In the present work, a new approach has been implemented [9]. This treatment consists in applying an "equivalent" viscosity that replaces the laminar viscosity on the wall. This method offers two advantages over the classical wall slip-velocity. First, it only needs the value and not the direction of the velocity at the first node near the wall. This alleviates the geometric complexities associated with the calculations of the slip velocity, specially in three dimensional configurations. Second, the equivalent viscosity, which is applied jointly with the physical no-slip condition, provides an automatic procedure that only concerns the viscous terms, so no further precautions are required.

The calculation procedures for the $k-\epsilon$ properties is essentially the same as described in reference [3], so only a brief outline will be given. The boundary conditions for the turbulence properties are derived at the first node away from the wall as follows:

If the node next to the wall is outside the viscous sublayer, the following wall function [10, 11] is used:

$$\frac{u_p}{u_*} = \frac{1}{\kappa} \ln(E_* y_p/\nu) \quad (17)$$

On the other hand, if the node next to the wall is inside the laminar sublayer, the following relation is applied:

$$\frac{u_p}{u_*} = \frac{y_p u_*}{\nu} \quad (18)$$

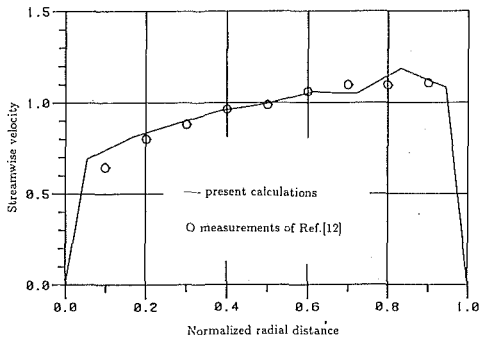

Fig. 2 Fully developed velocity profile

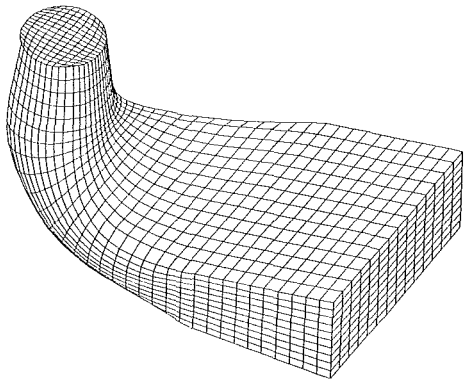

Fig. 3 Draft tube representation

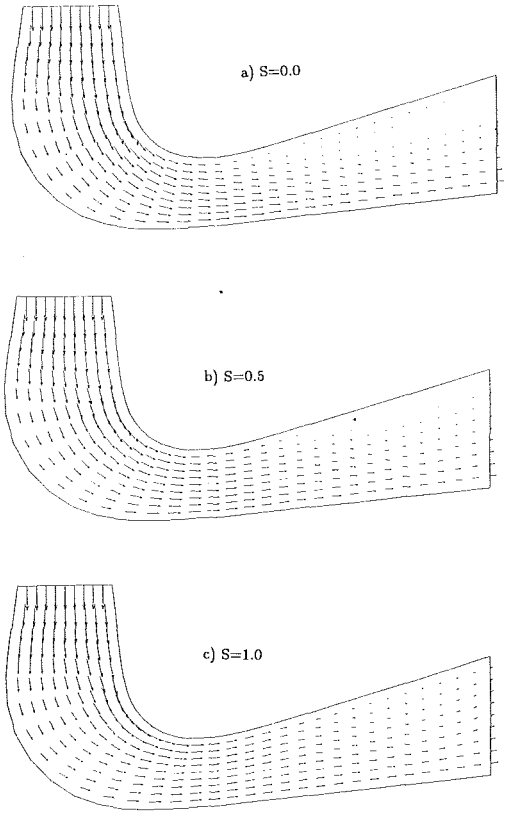

Fig. 4 Velocity field on the mid-plane

In both situations, the $k-\epsilon$ turbulence properties are obtained from:

$$k_p = \frac{u_*^2}{\sqrt{C_d}} \tag{19}$$

$$\epsilon_p = \frac{u_*^3}{\kappa y_p} \tag{20}$$

These values are used as the boundary conditions for the next time level $n+1$. When equation (17) is used, an updated "equivalent-viscosity" is calculated via:

$$\nu_{aw} = \frac{\kappa y_p u_*}{\ln(E_* y_p/\nu)} \tag{21}$$

while when using equation (18), the laminar viscosity instead of the "equivalent-viscosity" is employed.

At the inlet distribution of the turbulence kinetic energy and the dissipation of the turbulence energy are estimated heuristically or by setting a turbulence level. At the exit all the properties are extrapolated by assuming a fully developed flow.

5 Results

5.1 Basic Validation. A preliminary investigation was carried out in a circular arc channel of square cross section with a Reynolds number of 3980. For this case the Dean number defined as:

$$De = Re(Dh/R_m)^{0.5} \tag{22}$$

is 2517, where $Dh=1$ is the hydraulic diameter of the duct, and $R_m=2.5$ is the channel mean radius of curvature. The turning angle of the elbow is 90 degrees. In the streamwise direction 31 stations were used, while 19×15 points were used for the cross section. The fully developed streamwise velocity in the plane of symmetry is displayed in Fig. 2 and compared with the experimental results of reference [12]. A good agreement is observed, with only a small discrepancy of an inflexion of the predicted profile near the outside wall.

5.2 Draft Tube. The present scheme was then applied to a more complex geometry, chosen as a draft tube of a typical hydraulic turbine installation. The purpose of this type of component is to turn the water flow from the vertical to the horizontal direction with a minimum depth of excavation, and at the same time having a high efficiency. Similar to the study carried out by references [13, 14, 15], several calculations were made on the same draft tube.

Figure 3 displays a three-dimensional view of the draft tube geometry. This conduit is characterized by totally different cross-sections at the inlet and at the outlet, with an aspect ratio $A_{\text{outlet}}/A_{\text{inlet}}=4$. The transition from a circular section in the vertical leg to a rectangular section in the horizontal leg takes place in the bend, which has a varying elliptical cross-section.

For this element two kinds of calculations were carried out. The first type was conducted with the purpose of studying the flow configuration related to different inlet swirls. The second, to compare computed results with experimental data from D.E.W. of Montréal.

First Test. In this case, and in the same manner as reported in references [13, 14] the inlet velocity conditions were modelled by a plug flow combined with a solid body rotation. Following this, a factor S defined as the ratio of the maximum swirl velocity $w_{\max}$ to the bulk axial velocity u_{av} at the inlet is considered. In order to carry out the numerical simulations, this parameter was included, and a grid with $33\times15\times11$ nodes was employed.

As a preliminary calculation, the flow simulation was conducted without the presence of a swirl. In Fig. 4(*a*) the computed velocity field is illustrated at the mid-span. This shows that at the beginning of the bend, the maximum of the streamwise velocity appears near the inner wall. As the flow progresses into the duct, and as a consequence of the inertia forces, this

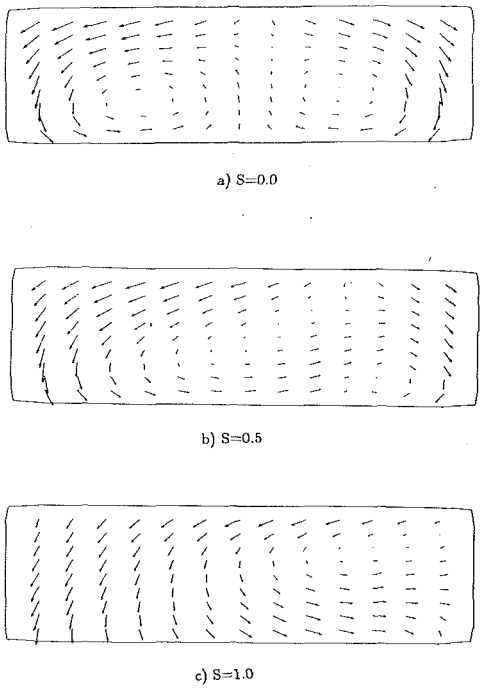

Fig. 5 Secondary flow on the cross section No. 22

maximum rapidly moves towards the outer wall, and finally a strong backflow region appears close to the exit of the passage.

In Figs. 4(*b*)–4(*c*) the effects of a progressive swirl of intensities of 0.5 and 1 are displayed at the mid-plane. The influence of this parameter on the flow behavior, can be better appreciated at the elbow and exiting regions. In the first zone at the 45 deg turning station, as the intensity of the swirl is increased, the velocity near the outlet wall increases, and for $S=1$ the velocity reaches maximum values around the inner and outer walls, and a core of a slightly lower velocity is detected. On the other hand, at the outlet the presence of a stronger swirl gradually implies a weaker streamwise backflow. This type of pattern, completely disappears for the maximum swirl intensity. This predicted flow behavior agrees with the results of reference [13], however in the current simulation a maximum velocity at the outlet is found near the lower wall, instead of the upper side, as reported in [13].

Certain aspects of the secondary flow can be appreciated by inspecting the velocity field in a plane at the end of the elbow, where a rectangular diffuser section completes the draft tube. In Figs. 5(*a–c*), this velocity vectors are illustrated for swirl intensities ranging from 0 to 1. The results in Fig. 5(*a*), for $S=0$, show the development of a pair of quasi-symmetric vortices (the draft tube is slightly asymmetric). This is the expected behavior of a flow through a bend. With the inclusion of the inlet swirl, the symmetry, the location and the intensity of these vortices are lost. For $S=0.5$ the secondary motion is represented by a big skew vortex and a very small one appearing near the upper left corner. As the swirl intensifies (Fig. 5(*b*)–5(*c*), the major vortex moves towards the left wall, at the same time the small vortex dies out.

Figure 6 shows the static pressure contours in the mid-plane for $S=0.5$. From a qualitative point of view, these results are comparable with those given by Shy and Braaten [13]. However the actual calculation does not predict the "cellular structure" in the expansion side obtained by these authors. It seems that this rather unexpected behavior of a changing direction of consecutive velocities near the inner wall could be attributed, at least in part, to the mesh size and to the type of scheme applied. These points have been discussed in reference [13]. For more details see reference [16].

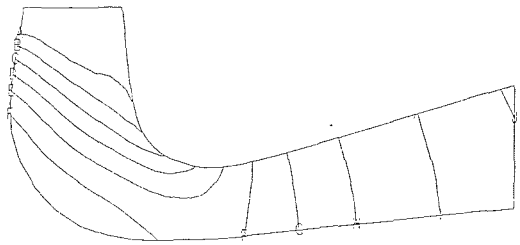

S=0.5

A=-0.30 B=-0.25 C=-0.20 D=-0.15 E=-0.10

F=-0.05 G= 0.00 H= 0.05 I= 0.1 J= 0.15

Fig. 6 Pressure distribution on the mid-plane

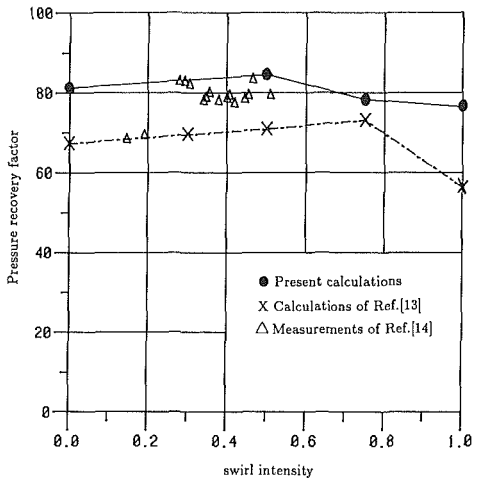

Fig. 7 Pressure recovery factor versus swirl intensity

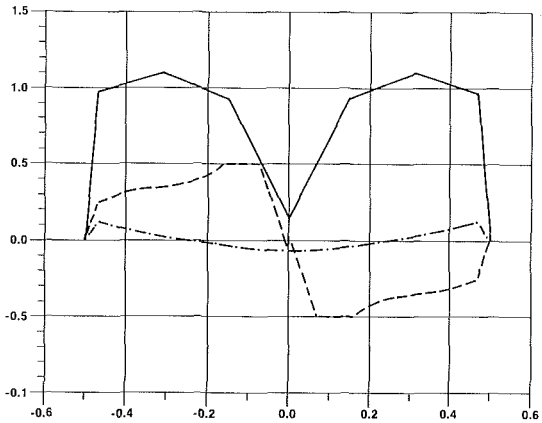

Fig. 8 Inlet velocity condition

—— axial velocity

--- tangential velocity

-·-· radial velocity

An important parameter that measures the performance of a diffuser, is the pressure recovery factor C_{pr}. This coefficient indicates the degree of conversion of kinetic energy into the static pressure. In this study, the following definition is employed:

$$C_{pr}=\frac{P_{\text{out}}-P_{\text{in}}}{\frac{1}{2}\rho(u^2+w^2)_{\text{in}}}$$

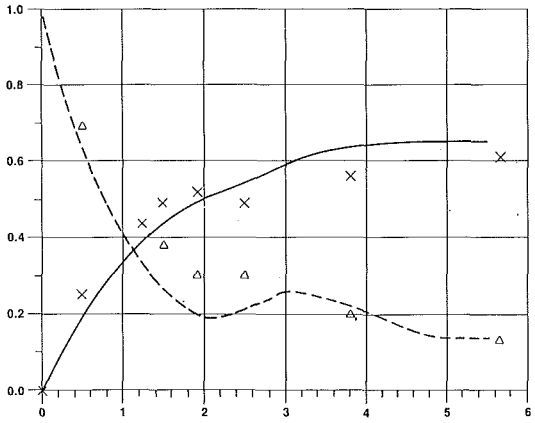

(*a*) coarse grid

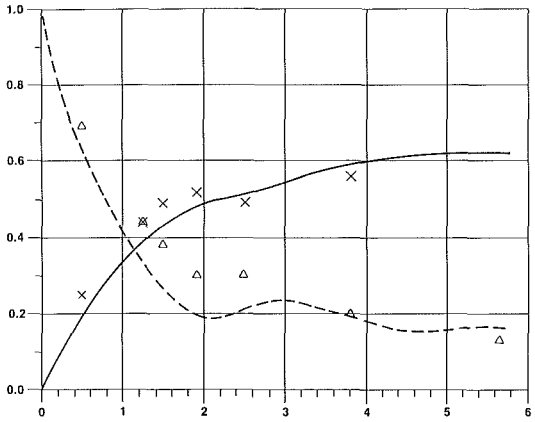

(*b*) fine grid

Fig. 9 Static and dynamic pressure versus streamwise direction

—— static pressure --- dynamic pressure

where P_{out} and P_{in} refer the outlet and inlet static averaged pressure, ρ for the fluid density, u_{in} for the mean inlet velocity, and w_{in} for the mean swirl velocity.

Figure 7 illustrates the computed pressure recovery factor together with experimental data and the numerical results of reference [13] as a function of swirl intensity. Although the range of the experimental values is very narrow, a comparison can be attempted.

The present numerical simulation predicts a maximum pressure recovery factor of 85 percent, while the numerical data given in reference [13] indicates a maximum around 75 percent. On the other hand, the experimental data obtained for different turbine runners, indicate optimal values ranging from 77 percent to 83 percent. In this regard, a better agreement in position as well as in intensity is obtained for the current numerical simulation. However, in the absence of more experimental measurements, it is not possible to assert a complete veracity of this concordance.

Second Test. The second investigation of the flow field was carried out using experimental values of an optimal inlet swirl flow after the hydraulic laboratory of D.E.W. The measured inlet conditions are displayed in Fig. 8, in terms of the axial, tangential, and radial velocities, represented by full, dashed and mixed lines respectively.

The main objective of this test was to compare the current numerical results, with experimental data concerning static and dynamic pressure.

In this case, and in order to study the scheme sensitivity related to the grid size, two different meshes were considered:

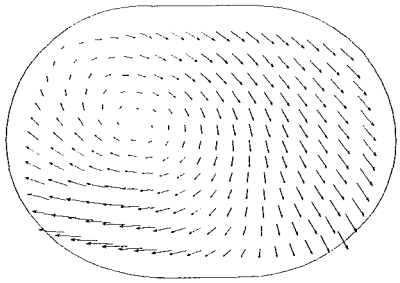

(*a*) beginning of the elbow ($i = 17$)

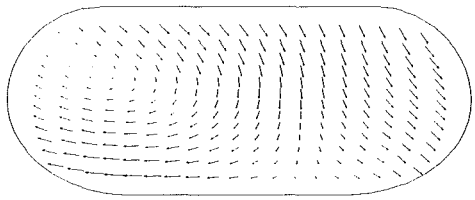

(*b*) end of the elbow ($i = 23$)

Fig. 10 Secondary flow (fine grid)

a coarse grid ($33 \times 15 \times 11$) and a fine one ($62 \times 21 \times 15$). The CPU time on a IBM 3090 was approximatively 6.10^{-4} s per point and per iteration. For the complete solution the total CPU time were 36 and 155 min. respectively.

In Figs. 9(*a*) and 9(*b*), the static and dynamic pressure along the main flow direction are compared with the experimental data for the coarse and fine grid respectively. As in reference [15] mass flow weighted average values are calculated for all properties at each section. The pressures are normalized by the inlet dynamic pressure.

From these figures a reasonable agreement of the calculated static pressure with the experimental values can be appreciated. However for the dynamic pressure some discrepancy is noted mainly at the end of the turning part of the draft tube.

Comparing the results for the two grids, we can observe that a better agreement is found for the static pressure for the fine grid as expected. For the dynamic pressure the solution is not as sensitive to a finer grid. For such a parameter the difference between numerical and experimental results decreases slowly.

The discrepancies can be attributed to the use of the logarithmic wall function that may not be very adequate to this type of flow, and also as noted in reference [15] to some possible uncertainty of the pitot measurements.

In a more qualitative way the results are now displayed as velocity fields representing the secondary flow at different sections from the inlet to the outlet, Figs. 10(*a–b*). At the beginning of the elbow, Fig. 10(*a*) shows a strong swirl shifted from the center of the section. This behavior is in accordance with the experimental data. Near the end of the elbow, in Fig. 10(*b*), the present numerical calculation predicts a single swirling flow, while the experimental information indicates two swirls. Along these lines, carrying out a similar numerical study reference [15] has found three swirls. In the previous figures, and for illustration purposes, the velocity vectors have been slightly amplified.

6 Conclusions

A numerical procedure which is suitable for application to three-dimensional turbulent, ducted flow problems of complex geometry, has been developed.

The calculation algorithm employs a fractional step approach, a nonstaggered mesh along with weighted upwind/central opposed spatial discretization. The method is based on the finite volume solution on a curvlinear mesh of the Reynolds

averaged Navier-Stokes equations. The discretization is carried out by the use of a body-fitted technique.

The method has been validated and applied to the simulation of the flow in an industrial hydraulic turbine draft tube. The computed results show an acceptable agreement with the measurements, indicating that the proposed flow simulation, can be used as a complement for the understanding and design of a satisfactory draft tube.

Acknowledgments

The financial support of the NSERC of Canada and of le Centre de Recherche Informatique de Montréal (CRIM) is acknowledged. The discussions with Mr. T. Vu of D. E. W. and Mr. W. Shy of G.E. are greatly appreciated.

References

1 Reggio, M., and Camarero, R., "A Numerical Solution Procedure for Viscous Incompressible Flows," *Numerical Heat Transfer*, Vol. 10, 1986, pp. 131–146.

2 Agouzoul, M., Reggio, M., and Camarero, R., "A Numerical Study of Turbulent Flows Using a Nonstaggered Mesh," CTAC-87/ISCFD-Sydney, Australia, 1987.

3 Reggio, M., Agouzoul, M., and Camarero, R., "Computation of Incompressible Turbulent Flows by an Opposed-Differencing Scheme," *Numerical Heat Transfer*, Vol. 12, 1987, pp. 307–320.

4 Reggio, M., and Camarero, R., "A Calculation Scheme for Three-Dimensional Incompressible Flows," ASME JOURNAL OF FLUIDS ENGINEERING, Vol. 109, 1987, pp. 345–352.

5 Camarero, R., Ozell, B., Reggio, M., and Garon, A., "Introduction to Grid Generation in Turbomachinery," VKI lecture Serie 2, *Numerical Techniques for Viscous Calculations in Turbomachinery*, Jan. 20–24, 1986.

6 Mizukami, A., and Tsuchiya, M., "A Finite Element Method for the Three-dimensional non-steady Navier-Stokes Equations," *Inter. Jour. for Num. Methods in Fluids*, Vol. 4, 1984, pp. 349–357.

7 Launder, D. E., and Spalding, D. B., *Lectures in Mathematical Models of Turbulence*, Academic Press, London, 1972.

8 Raithby, G. D., and Torrance, K. E., "Upstream Weighted Differencing Schemes and their Application to Elliptic Problems Involving Fluid Flows," *Computer Fluids*, Vol. 2, 1974, pp. 191–206.

9 Nakayama, A., "Three-Dimensional Flow Within Conduits of Arbitrary Geometrical Configurations," Ph.D. thesis, University of Illinois at Urbana-Champaign, 1981.

10 Launder; B. E., and Spalding, D. B., "The Numerical Calculation of Turbulent Flows," *Computer Methods in Applied Mechanics and Engineering*, Vol. 3, No. 2, 1974, pp. 269–289.

11 Rodi, W., "Turbulence Models and Their Application in Hydraulics," State of the Art Presented by the IAHR-Section on Fundamentals of Division II: Experimental and Mathematical Fluid Dynamics, 1980.

12 Mori, Y., Uchida, Y., and Ukon, T., "Forced Convective Heat Transfer in a Curved Channel with a Square Cross Section," *Int. J. Heat and Mass Transfer*, Vol. 14, 1971, p. 1781.

13 Shy, W., and Braaten, M., "Three-Dimensional Analysis of the Flow in a Curved Hydraulic Turbine Draft Tube," *International Journal for Numerical Methods in Fluids*, Vol. 6, 1986, pp. 861–882.

14 Thi, C., Vu, "Private Communication," Dominion Engineering Works, 1988.

15 Thi, C., Vu, and Shy, W., "Viscous Flow Analysis for Hydraulic Turbine Draft Tubes," IAHR Symposium, Trondheim, Norway, 1988.

16 Agouzoul, M., Reggio, M., and Camarero, R., "Simulation of Three-Dimensional Internal Turbulent Flows," ASME WAM, Chicago, Nov. 1988.

17 Abdallah, S., "Numerical Solutions for Pressure Poisson Equation with Newman Boundary Conditions Using a Non-Staggered Grid," *Journal of Computational Physics*, Vol. 70, 1987, pp. 189–192.

18 Abdallah, S., "Numerical Solutions for the Incompressible Navier-Stokes Equations in Primitive Variables Using Non-Staggered Grid, II," *Journal of Computational Physics*, Vol. 70, 1987, pp. 193–202.

The Rotordynamic Forces on a Centrifugal Pump Impeller in the Presence of Cavitation

R. Franz

A. J. Acosta

C. E. Brennen

T. K. Caughey

California Institute of Technology,
Pasadena, CA 91125

An experiment in forced vibration was conducted to study the fluid-induced rotordynamic force on an impeller whirling along a trajectory eccentric to its undeflected position in the presence of cavitation. The prescribed whirl trajectory of the rotor is a circular orbit of a fixed radius. The force measured is a combination of a steady radial force due to volute asymmetries and an unsteady force due to the eccentric motion of the rotor. These measurements have been conducted over a full range of whirl/impeller speed ratios at different flow coefficients without cavitation for various turbomachines. A destabilizing force was observed over a region of positive whirl ratio. The range of flow conditions examined for a centrifugal impeller in a spiral volute has been enlarged to include cavitation. Compared to the non-cavitating condition, cavitation corresponding to a head loss of three percent did not have a significant effect upon the unsteady force. However, a lesser degree of cavitation at the design point increased the destabilizing force for a particular set of whirl ratios.

Introduction

Fluid-induced forces acting on the impeller and therefore on the bearings of a turbomachine can cause self-excited whirl, where the rotor moves away from and whirls along a trajectory eccentric to its undeflected position. Knowledge of the unsteady force related to the lateral vibration of the rotor is crucial to understanding the rotordynamics of the turbomachine. This force has been measured on pump impelleres by various authors: Bolleter et al. (1987), Ohashi and Shoji (1987), Ohashi et al. (1988), Jery et al. (1985), and Jery (1987). Bolleter translated the impeller inside a vaned diffuser along a single axis using a "rocking arm" excited by a transient frequency sweep. The test section was typical of a single stage of a boiler feed pump. Ohashi, using a circular whirl motion, first tested two-dimensional impellers and then employed a rebuilt eccentric whirl mechanism to test a centrifugal impeller in a vaned diffuser. Also, a spacer was inserted to decrease the clearance around the impeller shroud.

This paper presents data taken using the same facility as Jery, who had measured the forces on a five bladed centrifugal impeller (designated Impeller X) in various vaneless and vaned diffusers, among them a spiral volute (Volute A). Adkins (1986) and Adkins and Brennen (1988) observed that the pressure distribution around the front shroud of Impeller X had a significant contribution to the hydrodynamic stiffness. He also reported measurements taken with the annular region surrounding the shroud exposed to the volute housing reservoir. This data was compared with measurements taken without the enlarged annular region surrounding the shroud and with a two dimensional version of the impeller, Franz et al. (1987), demonstrating that the large shroud clearances reduce the magnitude of the rotordynamic forces for reverse whirl and destabilizing forward whirl. Bolleter, who had a smaller gap between the impeller shroud and the casing, measured larger forces. The present investigation extends the range of operating conditions of the centrifugal impeller to include the effect of cavitation.

Experimental Facility

The references (Brennen et al. 1980, Jery 1987 and Franz 1989) provide a description of the Rotor Force Test Facility,

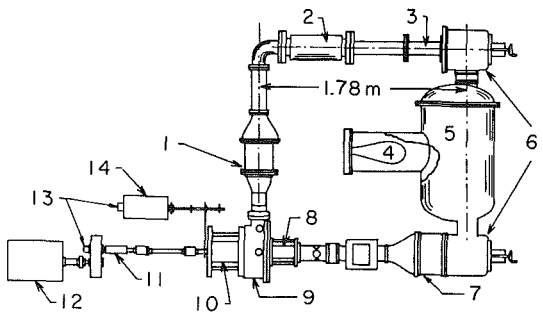

Fig. 1 Layout of the Rotor Force Test Facility. Downstream flow smoothing section (1), "silent" throttle valve (2), turbine flow meter (3), air bladder (4), reservoir, heat exchanger and air removal (5), flow fluctuators (dismantled) (6), upstream flow smoothing section (7), lucite viewing window (8), centrifugal pump test section (9), eccentric drive mechanism (10), slip ring assembly (11), main shaft motor (12), optical encoders (13), whirl motor (14).

Contributed by the Fluids Engineering Division for publication in the JOURNAL OF FLUIDS ENGINEERING. Manuscript received by the Fluids Engineering Division May 15, 1989.

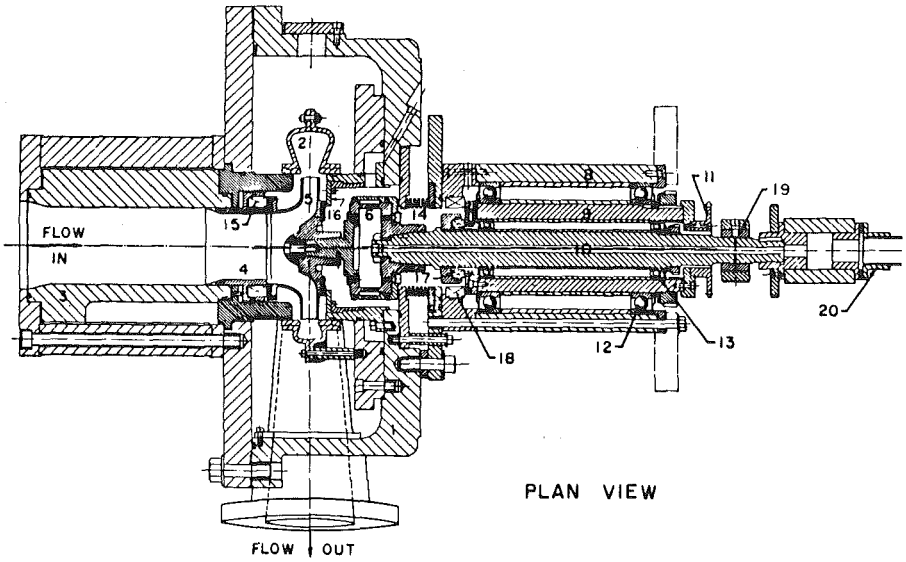

Fig. 2 Assembly drawing of the test section and the eccentric drive mechanism. Pump housing (1), volute (2), inlet connection (3), inlet bell (4), impeller (5), rotating dynamometer (6), eccentric drive mechanism: outer and inner bearing carriers (8 and 9), main shaft (10), orbiting motion sprocket (11), outer and inner bearing sets (12 and 13), bellows (14), impeller front face seal (15), back seal (16), eccentric drive inner and outer face seals (17 and 18), air bearing stator (19), flexible coupling (20).

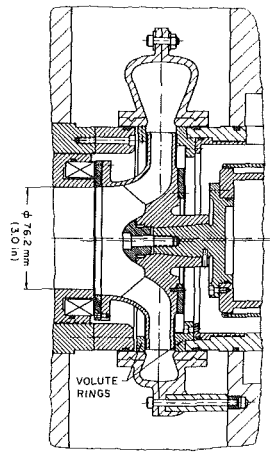

Fig. 3 Assembly drawing of Impeller X and Volute A installed in the test section

a water recirculating pump loop, closed to the atmosphere, Fig. 1. The flow was throttled by the "silent valve" which was comprised of a block of elastomer containing about 200 longitudinal holes that was squeezed axially by a hydraulic cylinder under feedback control to the turbine flow meter. Pressure transducers measured the static pressure after honeycomb screens at the end of the upstream and downstream flow smoothing sections. By altering the absolute pressure of air inside an air bladder in the reservoir, the datum pressure of the pump loop can be controlled, enabling tests in the presence of cavitation. The water had a dissolved air content of 4 ppm and a temperature of 120°F during the tests.

The force measuring device is a rotating dynamometer mounted between the impeller and the main drive shaft. The dynamometer consists of two parallel plates connected by four parallel bars which are strain gaged to measure the six components of force and moment. The strain gages are wired to form Wheatstone bridges. The impeller is made to whirl in a circular orbit eccentric to the volute center of radius $\epsilon = 1.26$ mm (.0495 in.), in addition to the normal shaft rotation, using a double bearing cartridge assembly. Figure 2 shows the test section and the eccentric drive mechanism. For the tests presented the main shaft speed was 2000 rpm. Using optical encoders to provide feedback, each motor was closed-loop controlled to be synchronized with data acquisition. The phase error of each motor was ±1 degree. Since the eccentric motion is in the lateral plane, perpendicular to the impeller centerline, only the force and moment in this lateral plane will be discussed.

The impeller used, designated Impeller X, was a five bladed, cast bronze impeller, donated by Byron-Jackson of Long Beach, CA. It has a specific speed of .57 and a discharge blade angle of 25 deg with respect to the axizmuthal tangent. The "well-matched" spiral volute of trapezoidal cross section, Volute A, was made of fiberglass. Drawings of the impeller and the volute are accessible in Adkins and Brennen (1988). Figure 3 is an assembly drawing of Impeller X and Volute A installed in the test section. The front face seal had a clearance of .13 mm (.005 in.). To reduce leakage flow from the impeller discharge, rings were installed inside the volute. The front and back volute rings had an axial clearance of .25 mm (.010 in.) and .13 mm (.005 in.), respectively.

Nomenclature

- $[\mathbf{A}]$ = hydrodynamic force matrix, nondimensionalized by $\frac{1}{2}\rho u_2^2 A_2/r_2$
- A_1, A_2 = impeller inlet area (πr_1^2), outlet area ($2\pi r_2 b_2$)
- $[\mathbf{B}]$ = hydrodynamic moment matrix, nondimensionalized by $\frac{1}{2}\rho u_2^2 A_2$
- b_2 = impeller discharge width, 15.7 mm (0.62 in.)
- $[\mathbf{C}]$ = hydrodynamic damping matrix, nondimensionalized by $\frac{1}{2}\rho u_2^2 A_2/(r_2\omega)$
- F_1, F_2 = components of the instantaneous lateral force on the impeller in the rotating dynamometer reference frame
- F_x, F_y = components of the instantaneous lateral force on the impeller in the stationary volute frame, nondimensionalized by $\frac{1}{2}\rho u_2^2 A_2$
- F_{ox}, F_{oy} = values of F_x and F_y if the impeller was located at the origin of the volute frame, non-dimensionalized by $\frac{1}{2}\rho u_2^2 A_2$
- F_n, F_t = components of the lateral force on the impeller which are normal to and tangential to the whirl orbit, averaged over the orbit, nondimensionalized by $\frac{1}{2}\rho u_2^2 A_2 \epsilon/r_2$
- $[\mathbf{K}]$ = hydrodynamic stiffness matrix, nondimensionalized by $\frac{1}{2}\rho u_2^2 A_2/r_2$
- $[\mathbf{M}]$ = hydrodynamic mass matrix, nondimensionalized by $\frac{1}{2}\rho u_2^2 A_2/(r_2\omega^2)$
- M_x, M_y = components of the instantaneous lateral moment on the impeller in the fixed volute frame, nondimensionlized by $\frac{1}{2}\rho u_2^2 A_2 r_2$
- M_{ox}, M_{oy} = values of M_x and M_y if the impeller was located at the origin of the volute frame, nondimensionalized by $\frac{1}{2}\rho u_2^2 A_2 r_2$
- M_n, M_t = components of the lateral moment on the impeller which are normal to and tangential to the whirl orbit, averaged over the orbit, nondimensionalized by $\frac{1}{2}\rho u_2^2 A_2 \epsilon$

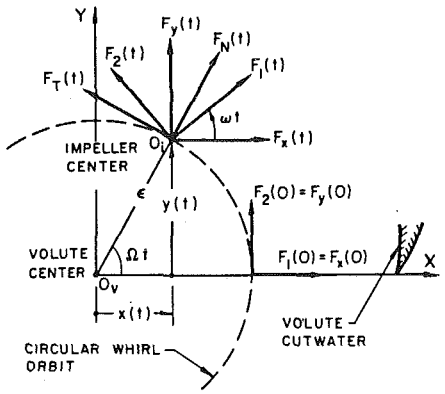

Fig. 4 Schematic representation of the lateral forces on an impeller whirling in a circular orbit. F_1 and F_2 are in the rotating dynamometer frame. F_x and F_y are in the stationary volute frame. F_n and F_t are in the local polar coordinate frame, normal to and tangential to the circular whirl orbit.

Data Processing

Referring to Fig. 4, the forces in the stationary volute frame of reference, assuming a small displacement, can be represented by

$$\mathbf{F}(t) = \mathbf{F}_0 + [\mathbf{A}]\mathbf{x}(t) \tag{1}$$

The lateral force, $\mathbf{F}(t)$, can be considered as the sum of two forces: a steady force, $\mathbf{F}_0$, which the impeller would experience if located at the volute center, and an unsteady force due to the eccentric motion of the impeller, represented by a force matrix $[\mathbf{A}]$; $\mathbf{x}(t)$ is the displacement vector of the impeller from the volute center.

For the forced vibration experiment conducted, the imposed whirl trajectory was a circular orbit of radius ϵ and frequency Ω. The lateral forces detected by the dynamometer in the rotating frame, F_1 and F_2, are related to the lateral forces in the volute frame, F_x and F_y, by a rotation through the angle $-\omega t$, where ω is the frequency of main shaft rotation.

$$\begin{aligned} F_1(t)\cos(\omega t) - F_2(t)\sin(\omega t) &= F_{ox} + \epsilon A_{xx}\cos(\Omega t) + \epsilon A_{xy}\sin(\Omega t) \\ F_1(t)\sin(\omega t) + F_2(t)\cos(\omega t) &= F_{oy} + \epsilon A_{yx}\cos(\Omega t) + \epsilon A_{yy}\sin(\Omega t) \end{aligned} \tag{2}$$

The components of the steady force are obtained by averaging each equation. The elements of the hydrodynamic force matrix: A_{xx}, A_{yx} and A_{xy}, A_{yy} are obtained by evaluating the cos and sin Fourier coefficients, respectively, of each equation.

The unsteady force, $[\mathbf{A}]\epsilon(t)$, due to the eccentric motion of the impeller can be resolved into its components, F_n and F_t, normal to and tangential to the whirl orbit, averaged over the orbit. The normal force is considered positive radially outward. The tangential force is positive when in the direction of the shaft rotation. For the imposed circular whirl orbit

$$\begin{aligned} F_n &= \frac{1}{2}(A_{xx} + A_{yy})\epsilon \\ F_t &= \frac{1}{2}(-A_{xy} + A_{yx})\epsilon \end{aligned} \tag{3}$$

Whenever the tangential force is in the same direction as the whirl motion it encourages the whirl motion and is thus destabilizing. A positive normal force tends to increase the radius of the whirl motion. F_n and F_t are nondimensionalized by the additional factor ϵ/r_2 so that they would be numerically equal to the average of the appropriate matrix elements. The Nomenclature gives the details.

The lateral moment experienced by the whirling impeller can be expressed in the stationary volute frame as

$$\mathbf{M}(t) = \mathbf{M}_0 + [\mathbf{B}]\epsilon(t) \tag{4}$$

The moment is measured in the plane bisecting the impeller discharge area. The expressions for $\mathbf{M}_0$ and $[\mathbf{B}]$ are similar to the force equations. A positive M_t would tend to tilt the impeller outward. M_n with the same sign as the whirl velocity would tend to tilt the impeller inlet away from the whirl direction.

To experimentally extract the fluid-induced forces at a given whirl ratio and operating condition, two identical tests are performed, one in air and the other in water. The forces from the former experiment are subtracted from the latter to yield the fluid-induced forces. The buoyancy force on the rotor is subtracted separately.

For data taken without whirl, the $\Omega/\omega = 0$ point, the impeller is placed at four locations on its eccentric orbit, each 90 degrees apart, corresponding to the location nearest the volute tongue, farthest, and the two intermediary locations. The steady force is computed from the average of the main shaft component. The matrix $[\mathbf{A}]$ at $\Omega/\omega = 0$, the stiffness matrix, is computed by subtracting the appropriate force components of diametrically opposite whirl orbit locations.

The dynamometer was calibrated statically in situ using an arrangement of cables, pulleys and weights. Its dynamic response was checked by rotating and whirling the impeller in air. The dynamometer measured as periodic forces gravity and the centrifugal force from whirling in a circular orbit. From rotating in air for various shaft speeds up to 3500 rpm, the weight of Impeller X was measured. The magnitude of the

Nomenclature (cont.)

p_1, p_{t1} = upstream static, total pressure
p_2, p_{t2} = downstream static, total pressure
p_I = static pressure at impeller inlet, $p_{t1} - \frac{1}{2}\rho\left(\frac{Q}{A_1}\right)^2$
p_v = vapor pressure of water
Q = flow rate
r_1, r_2 = impeller inlet, discharge radius; 40.5 mm (1.594 in.), 81.0 mm (3.188 in.)
t = time
u_1, u_2 = impeller tip speed at impeller inlet, ωr_1, at discharge, ωr_2
x, y = instantaneous coordinates of the impeller center in the stationary volute frame, nondimensionalized by r_2
z = coordinate of the machine axis, pointing upstream in the direction of impeller rotation from the plane bisecting the impeller outlet area, nondimensionalized by r_2
ϵ = radius of circular whirl orbit, 1.26 mm (.0495 in.)
θ = angular position of the impeller on the whirl orbit, measured from the volute tongue in the direction of impeller rotation
ρ = density of water
σ = cavitation number, $\frac{p_I - p_v}{\frac{1}{2}\rho u_1^2}$
σ^2 = variance
ϕ = flow coefficient, $\frac{Q}{u_2 A_2}$
ψ = total head coefficient, $\frac{p_{t2} - p_{t1}}{\rho u_2^2}$
ω = radian frequency of the impeller (shaft) rotation
Ω = radian frequency of the whirl motion

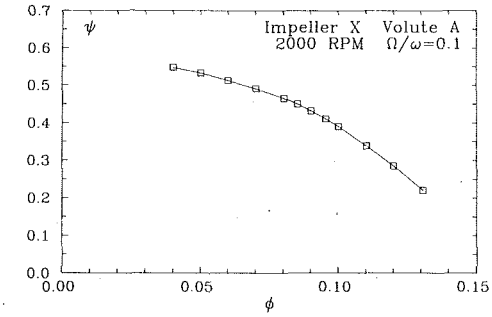

Fig. 5 Noncavitating performance curve of Impeller X in Volute A at 2000 rpm with $\Omega/\omega = .1$. Uncertainty expressed as a standard deviation: $\psi \pm .005$ and $\phi \pm .0005$.

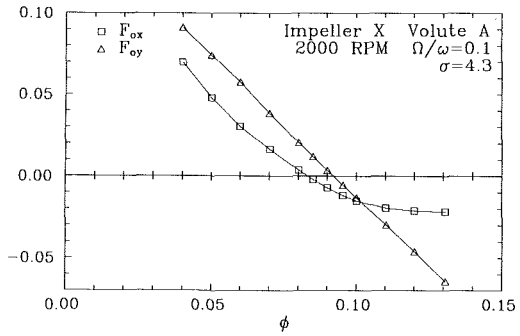

Fig. 6 The components of the steady force F_{ox} and F_{oy}, on Impeller X in Volute A at 2000 rpm as a function of flow coefficient. Uncertainty expressed as a standard devitation: F_{ox}, $F_{oy} \pm .00078$ and $\phi \pm .0005$.

components F_1 and F_2 were within 1 percent and the phase error was less than 1 degree. The phase angle of the forces measured while rotating and whirling in air was used to check the orientation of the optical encoders on the main and whirl shafts, for synchronization with data taking.

The unsymmetric lateral stiffness of the entire structure including the eccentric drive mechanism introduced a resonance into the measurements when observed in the rotating dynamometer frame, F_1 and F_2, due to the observed time dependent stiffness. When transformed into the stationary frame the resonance disappeared from the force components, Franz (1989), and did not affect the data presented.

Presentation of Data

For the present investigation of the rotor forces the phenomenon of cavitation could not be physically observed. Its presence was inferred from pump performance loss and from its influence upon the dynamometer measurements. The impeller force depends upon the location of the impeller within the volute. By whirling the impeller, a single measurement can be used to obtain the steady force. With $\Omega/\omega = .1$, the noncavitating performance and the components of the steady force, F_{ox} and F_{oy}, are plotted against flow coefficient in Figs. 5–6, respectively. In terms of the magnitude and angle of the force vector measured from the volute tongue in the direction of main shaft rotation, the minimum of the steady force and greatest angular change occur at design, $\phi = .092$.

The effect of cavitation upon the hydrodynamic forces was examined by testing three flow coefficients: $\phi = .120$, .092 (design) and .060. The cavitating performance curves are given in Fig. 7. The operating constraint of keeping the pressure of the back seal cavity above atmosphere permitted a breakdown in head rise across the pump of approximately 15, 20, and 25 percent for the flow coefficients $\phi = .120$, .092 (design) and .060, respectively.

The dependence of the magnitude and direction of the steady

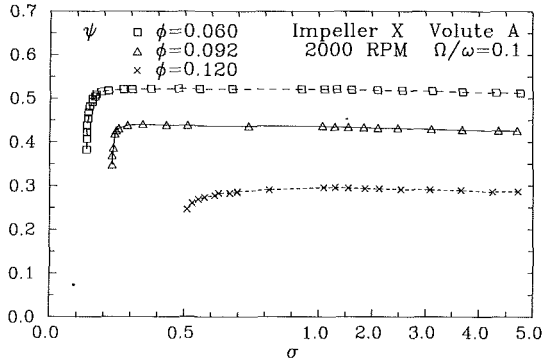

Fig. 7 Cavitation performance curve at 2000 rpm with $\Omega/\omega = .1$ for three flow coefficients: $\phi = .120$, .092 (design) and .060. Uncertainty expressed as a standard deviation: $\psi \pm .005$ and $\sigma \pm .008$.

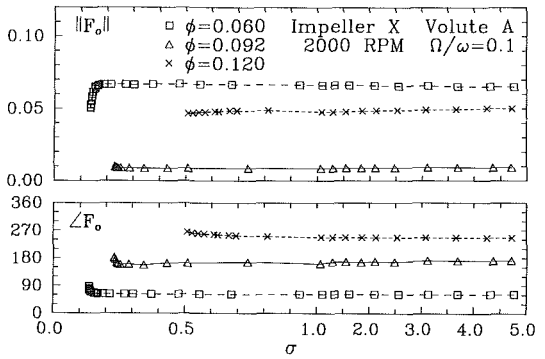

Fig. 8 The magnitude and direction of the steady force F_0 on Impeller X in Volute A at 2000 rpm with $\Omega/\omega = .1$ for the three coefficients: $\phi = .060$, .092 (design) and .120, as a function of the cavitation number. Uncertainty expressed as a standard deviation: $\|F_0\| \pm .00078$, $\angle F_0 \pm 1$ deg (5 deg for $\phi = .092$).

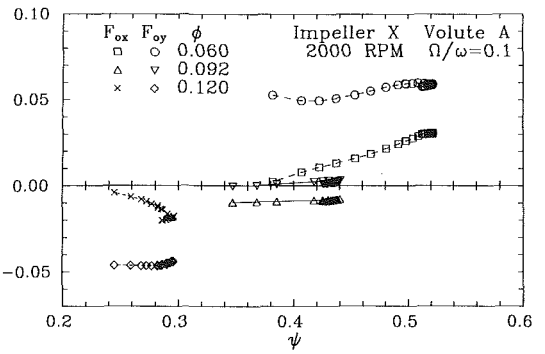

Fig. 9 The components of the steady force, F_{ox} and F_{oy}, on Impeller X in Volute A at 2000 rpm with $\Omega/\omega = .1$ for the three flow coefficients: $\phi = .060$, .092 (design) and .120, as a function of the head coefficient. Uncertainty expressed as a standard deviation: F_{ox}, $F_{ox} \pm .00078$ and $\psi \pm .005$.

force upon cavitation number is shown in Fig. 8. For off-design, $\phi = .120$ and $\phi = .060$, the magnitude of $\mathbf{F}_0$ decreases with breakdown. For design the magnitude of $\mathbf{F}_0$ decreases with decreasing cavitation number until the knee of the performance curve. It increases above the noncavitating value in breakdown. It varied less than 10 percent from the noncavitating value. The direction of $\mathbf{F}_0$ rotates away from the tongue in the direction of impeller shaft rotation for each flow coefficient through breakdown.

The components of $\mathbf{F}_0$ in the volute reference frame are plotted against head coefficient in Fig. 9. From preliminary data taken at 3000 rpm, Fig. 10 shows the steady force components for various flow coefficients at the operating points: noncavitating, 3 percent head loss and 10 percent head loss.

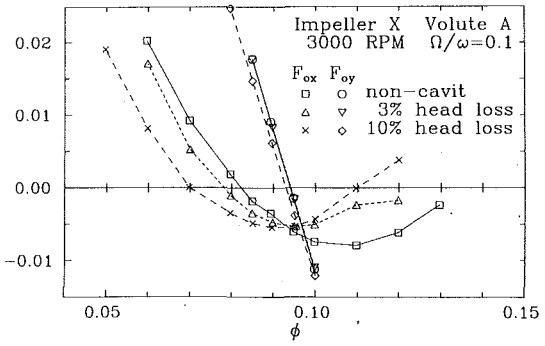

Fig. 10 The components of the steady force, F_{ox} and F_{oy}, on Impeller X in Volute A at 3000 rpm with $\Omega/\omega = .1$ for the three operating conditions: non-cavitating, 3 percent head loss and 10 percent head loss as a function of the flow coefficient focusing upon design. Uncertainty expressed as a standard deviation: F_{ox}, $F_{oy} \pm .00078$ and $\phi \pm .0005$.

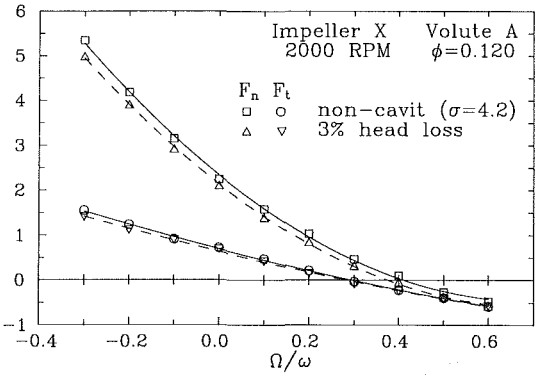

Fig. 11 The average normal and tangential force, F_n and F_t, on Impeller X in Volute A at 2000 rpm at a flow coefficient of $\phi = .120$ as a function of whirl ratio for flow without cavitation and with a head loss of 3 percent. Uncertainty expressed as a standard deviation: $F_n \pm .04$, $F_t \pm .047$ and $\Omega/\omega \pm .001$.

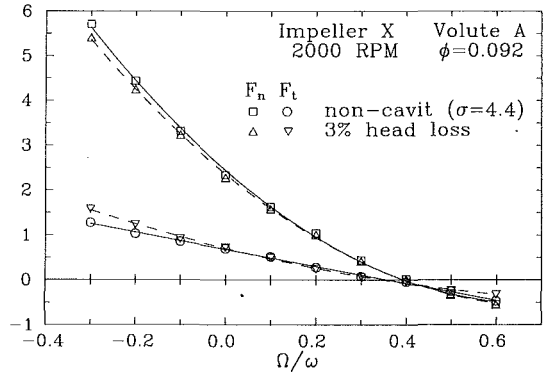

Fig. 12 The average normal and tangential force, F_n and F_t, on Impeller X in Volute A at 2000 rpm at design flow ($\phi = .092$) as a function of whirl ratio for flow without cavitation and with a head loss of 3 percent. Uncertainty expressed as a standard deviation: $F_n \pm .04$, $F_t \pm .047$ and $\Omega/\omega \pm .001$.

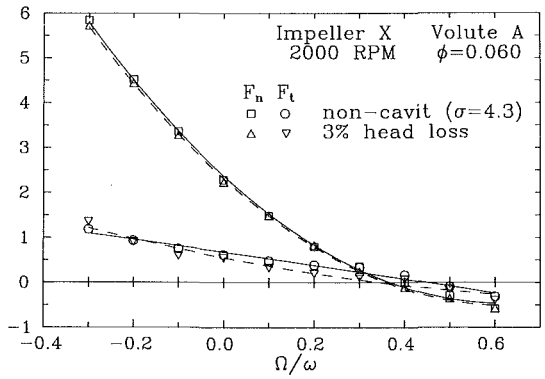

Fig. 13 The average normal and tangential force, F_n and F_t, on Impeller X in Volute A at 2000 rpm at a flow coefficient of $\phi = .060$ as a function of whirl ratio for flow without cavitation and with a head loss of 3 percent. Uncertainty expressed as a standard deviation: $F_n \pm .04$, $F_t \pm .047$ and $\Omega/\omega \pm .001$.

The setup was slightly different, so this figure should not be directly compared with the other data presented. The steady force component in the direction of the volute tongue, F_{ox}, was affected more by cavitation. With increasing head loss, the curve F_{ox} as a function of ϕ appears to rotate about design flow. For a centrifugal impeller in a volute pump tested at several flow coefficients above best efficiency, Uchida et al. (1971) had also observed that the steady force component in the tongue direction increases with developing cavitation.

For each flow coefficient measurements were taken over the whirl ratio range $-.3 \le \Omega/\omega \le .6$ in increments of .1 at two cavitation numbers: one non-cavitating and the other corresponding to a head loss of 3 percent. The normal and tangential forces as a function of whirl ratio are plotted in Figs. 11–13. For these figures the drawn curves are a quadratic fit to the data. Over a range of forward whirl F_t is in the same direction as the whirl motion, thus destabilizing. By $\Omega/\omega = .6$, the tangential force had become stabilizing again, consequently tests at higher whirl ratios were not necessary. At 3 percent head loss, F_n is slightly smaller and the magnitude of F_t is smaller for positive Ω/ω. At $\Omega/\omega = -.3$, $\phi = .120$, F_t is smaller; though for $\phi = .092$ (design) and $\phi = .060$, F_t is larger than for the non-cavitating case. The range of destabilizing forward whirl ratio was slightly reduced by cavitation at 3 percent head loss. For forward whirl there is a region over which $F_n < 0$, and tends to decrease the whirl radius. Based on past experiments, F_n will be positive again at higher whirl ratios, reflecting its parabolic character. At design, $\phi = .092$, the zero-crossing whirl ratios for F_n and F_t are nearly the same. F_t is destabilizing over the same range of whirl ratio as F_n tends to increase the whirl orbit radius. For $\phi = .060$, F_t is positive up to a higher Ω/ω, whereas for $\phi = .120$, the destabilizing region is smaller than the region over which F_n would increase the whirl radius. The region of destabilizing whirl ratio decreases with increasing flow coefficient.

For two whirl ratios in the region of destabilizing whirl, $\Omega/\omega = .1$ and .3, measurements were taken from non-cavitating conditions through breakdown of the head rise across the pump. Each set of the breakdown measurements was done in a single sitting. The steady force from $\Omega/\omega = .1$ has already been presented. The effect of cavitation upon the steady force components F_n and F_t is shown in Figs. 14–15. For the above design flow coefficient, $\phi = .120$, they decrease with head loss. For $\Omega/\omega = .3$, F_t becomes slightly more negative, increasing the stability margin.

At design flow, $\phi = .092$, for $\Omega/\omega = .1$, F_n and F_t decrease with head loss, however, for a head loss greater than 10 percent there is a slight rise in F_t. The data for $\Omega/\omega = .3$ exhibit similar behavior except in the region between the peak head rise and 1 percent head loss, where F_n goes through a trough and F_t a peak. Through this swing the unsteady force increases slightly in magnitude and rotates in a direction to increase the destabilizing tangential force, then rotates back. Evident from the later Fig. 21, both M_n and M_t increase in this region before decreasing with head loss. The unsteady moment vector swings only a few degrees in the direction to increase M_n. Figure 16 shows that this perturbation is reflected in the steady force calculated from the $\Omega/\omega = .3$ data, which swings in the direction of main shaft rotation. For this operating region the flow was sufficiently disturbed so that the linearization of $\mathbf{F}(t)$, equation (1), which represents the unsteady force by $[\mathbf{A}]\epsilon(t)$, is invalid; since for $\Omega/\omega = .3$, $\mathbf{F}_0$ was perturbed.

For below design flow, $\phi = .060$, F_n and F_t decrease with

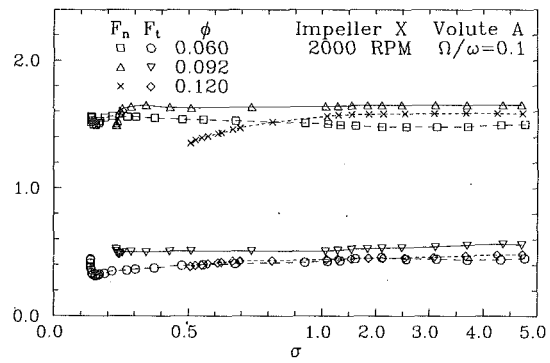

Fig. 14(*a*)

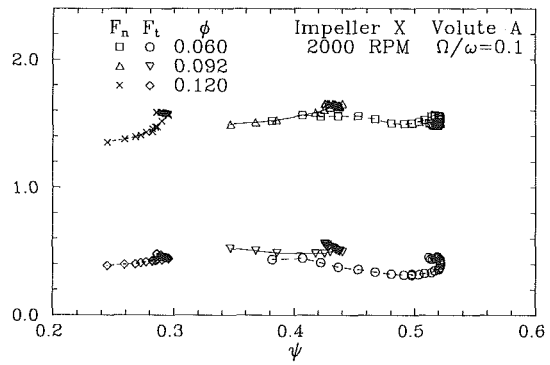

Fig. 14(*b*)

Fig. 14 The average normal and tangential force, F_n and F_t, on Impeller X in Volute A at 2000 rpm with $\Omega/\omega = .1$ for the three flow coefficients: $\phi = .060, .092$ (design) and .120, as a function of (*a*) the cavitation number and (*b*) the head coefficient. Uncertainty expressed as a standard deviation: $F_n \pm .04$, $F_t \pm .047$, $\sigma \pm .008$ and $\psi \pm .005$.

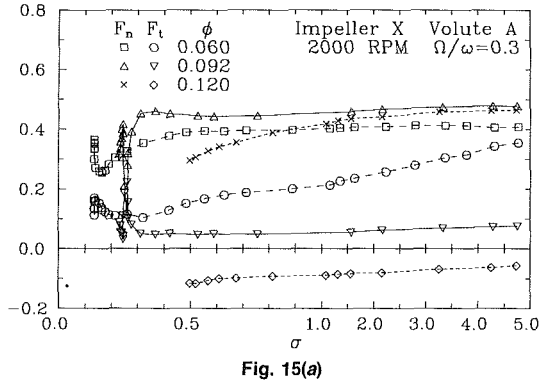

Fig. 15(*a*)

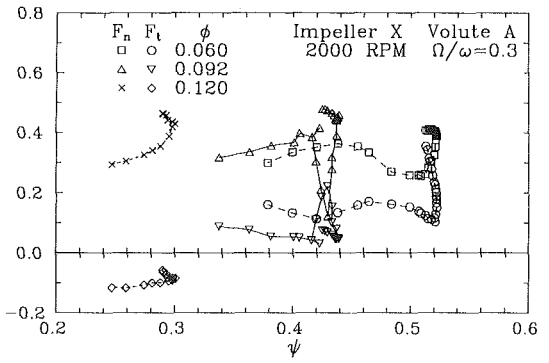

Fig. 15(*b*)

Fig. 15 The average normal and tangential force, F_n and F_t, on Impeller X in Volute A at 2000 rpm with $\Omega/\omega = .3$ for the three flow coefficients: $\phi = .060, .092$ (design) and .120, as a function of (*a*) the cavitation number and (*b*) the head coefficient. Uncertainty expressed as a standard deviation: $F_n \pm .04$, $F_t \pm .047$, $\sigma \pm .008$ and $\psi \pm .005$.

developing cavitation. For $\Omega/\omega = .1$, though, F_n increases approaching the knee before decreasing with breakdown, while F_t increases with loss. For $\Omega/\omega = .3$, F_n decreases with breakdown though momentarily increasing with head loss. F_t, doing the opposite, increases with breakdown.

Data were taken over 256 cycles of the reference frequency ω/J (where $\Omega/\omega = I/J$, I, J integers) at which the orientation of the dynamometer and its location on the whirl orbit geometrically repeat. For each cycle $\mathbf{F}_0$ and [**A**] were computed. The variances, over the 256 cycles, including the tests performed in air, were calculated for $\Omega/\omega = -.1, .1, .3$ and .5, from the whirl ratio sets and for selected runs of the breakdown sets. The standard deviations were typically less than .00078 for F_{ox} and F_{oy}, .04 for F_n and .047 for F_t. For $\Omega/\omega = .5$ the standard deviations were occasionally larger than the mentioned values. For the breakdown sets of $\Omega/\omega = .3$, frequently the small values of F_t were not significantly larger than the associated standard deviations.

Discussion of Moments

The lateral moments of the whirling impeller are measured in the calibration plane of the dynamometer which coincides with the plane bisecting the discharge area of the impeller. With primary interest in the unsteady rotor forces which can encourage self-excited whirl, attention will be focused on the unsteady moments.

For the three flow coefficients tested Figs. 17–19 present M_n and M_t as a function of whirl ratio for the two operating conditions: noncavitating and 3 percent head loss. M_t is positive, tending to tilt the impeller outward. The magnitude increases with increasing positive whirl ratio. The values are larger for lower flow coefficients. M_n is in the same direction as the whirl velocity, except in the region where the value is

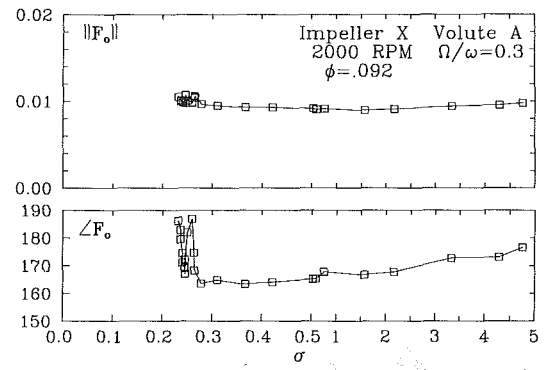

Fig. 16 The magnitude and direction of the steady force $\mathbf{F}_0$ on Impeller X in Volute A at 2000 rpm with $\Omega/\omega = .3$ at design flow ($\phi = .092$) as a function of the cavitation number. Uncertainty expressed as a standard deviation: $\|\mathbf{F}_0\| \pm .00078$, $\angle\, \mathbf{F}_0 \pm 5$ deg.

small for small whirl ratios. M_n resembles a cubic function of Ω/ω. From data taken in the past with non-cavitating flow, for higher reverse whirl ratios M_t increases and M_n decreases.

To obtain lever arms the relation $\mathbf{r} \times \mathbf{F} = \mathbf{M}$ is used with the assumption that the axial thrust acts along the impeller centerline. To simplify the discussion, the contribution of the unsteady lateral force to the moment from the external shroud and the impeller blades will be considered.

$$M_n = -z_{\text{shroud}} F_{t,\text{shroud}} - z_{\text{blade}} F_{t,\text{blade}} \qquad (5)$$
$$M_t = z_{\text{shroud}} F_{n,\text{shroud}} + z_{\text{blade}} F_{n,\text{blade}}$$

where the z axis points upstream. Unless the forces $\mathbf{F}_{\text{shroud}}$ and $\mathbf{F}_{\text{blade}}$ are parallel the introduced moment will not be perpendicular to $\mathbf{F}$, and $M_t/F_n \neq -M_n/F_t$.

The lever arms computed from $z = M_t/F_n$ and $-M_n/F_t$ depend significantly upon whirl ratio in the region of forward

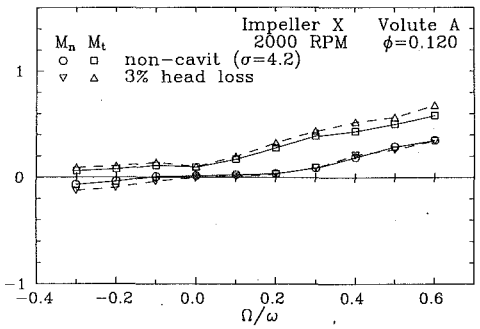

Fig. 17 The average normal and tangential moment, M_n and M_t, on Impeller X in Volute A at 2000 rpm at a flow coefficient of $\phi = .120$ as a function of whirl ratio for flow without cavitation and with a head loss of 3 percent. Uncertainty expressed as a standard deviation: M_n, $M_t \pm .11$ and $\Omega/\omega \pm .001$.

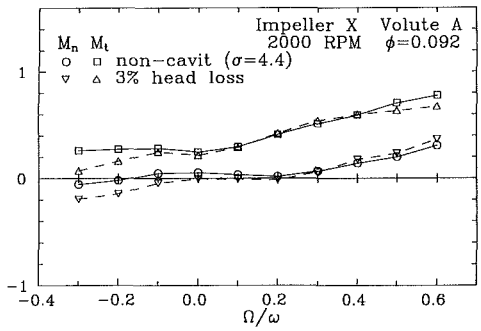

Fig. 18 The average normal and tangential moment, M_n and M_t, on Impeller X in Volute A at 2000 rpm at design flow ($\phi = .092$) as a function of whirl ratio for flow without cavitation and with a head loss of 3 percent. Uncertainty expressed as a standard deviation: M_n, $M_t \pm .11$ and $\Omega/\omega \pm .001$.

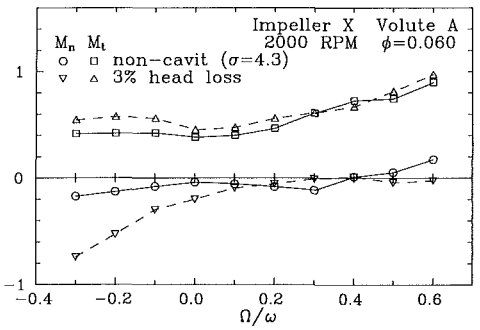

Fig. 19 The average normal and tangential moment, M_n and M_t, on Impeller X in Volute A at 2000 rpm at a flow coefficient of $\phi = .060$ as a function of whirl ratio for flow without cavitation and with a head loss of 3 percent. Uncertainty expressed as a standard deviation: M_n, $M_t \pm .11$ and $\Omega/\omega \pm .001$.

where F_n and F_t equal zero. For reverse whirl there is little change. For the breakdown tests taken with $\Omega/\omega = .1$ and .3, Figs. 20–21 present the lever arms as an alternative to the moments themselves. Since the measurements are integrated over the entire impeller, the contribution to the moment from each force element of the preceding paragraph is impossible to quantify.

During the course of the experiments, the rotordynamic forces were of primary interest. The moments were obtained during subsequent processing of the data. Fewer sets of instantaneous data were available to compute the variance of [B]. Evaluation of the data indicates that the standard deviations were typically less than .11 for M_n and M_t. For many of the whirl ratios presented, the mean of the unsteady moments is not large compared to the scatter over the 256 cycles of a single test. The error in the lever arms was computed using

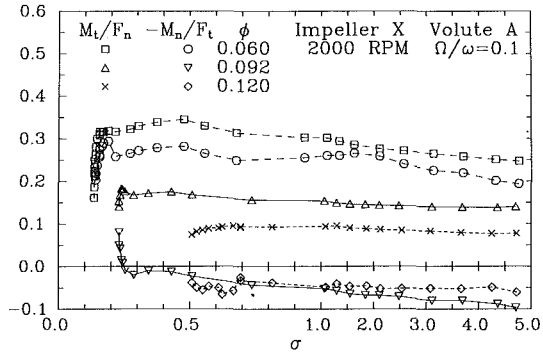

Fig. 20(*a*)

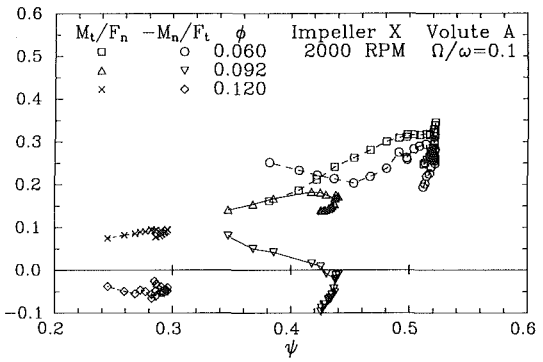

Fig. 20(*b*)

Fig. 20 The lever arms computed from the components of the unsteady moment and force on Impeller X in Volute A at 2000 rpm with $\Omega/\omega = .1$ for the three flow coefficients: $\phi = .060$, .092 (design) and .120, as a function of (*a*) the cavitation number and (*b*) the head coefficient. Uncertainty expressed as a standard deviation: M_t/F_n, M_n/F_t see text, $\sigma \pm .008$ and $\psi \pm .005$.

"root-sum-square" for the propagation of uncertainty. The variance of a function f of n independent variables x_i, $i = 1, n$, is $\sigma_f^2 = \sum_{i,j=1}^{n} \frac{\partial f}{\partial x_i} \frac{\partial f}{\partial x_j} \sigma_{x_i x_j}^2$. The error depends upon the magnitude of the denominator, F_n or F_t. For example, at noncavitating design flow the standard deviation of $-M_n/F_t$ for $\Omega/\omega = .1$ and .3 is approximately .09 and .5, respectively.

Rotordynamic Force Matrices

The mass-damping-stiffness model of the hydrodynamic force gives,

$$\mathbf{F}(t) = \mathbf{F}_0 - [\mathbf{K}]\mathbf{x}(t) - [\mathbf{C}]\dot{\mathbf{x}}(t) - [\mathbf{M}]\ddot{\mathbf{x}}(t) \tag{6}$$

For the imposed circular whirl orbit, the mass-damping-stiffness model implies that the matrix $[\mathbf{A}(\Omega/\omega)]$ is quadratic in Ω/ω. Since $[\mathbf{A}(\Omega/\omega)]$ does resemble a parabola for the impeller-volute combination presented, the coefficient matrices from a least squares fit are given in Table 1. For the set of Ω/ω tested, the curves A_{xy} and A_{yx} do not quite resemble a parabola for every flow condition. Figure 13 shows that F_t can flatten over the destabilizing whirl ratio range. The standard deviation in the coefficients is approximately .02, .08, and .2 for the stiffness, damping and mass matrices, respectively. For $\phi = .060$, they are larger, in particular .1 for the damping matrix. Over the whirl ratio range tested, the unsteady moments due to the imposed lateral displacement do not in general resemble a quadratic in Ω/ω. Consequently, the coefficients of a quadratic fit are not presented. A complete rotor dynamic analysis would require forces and moments for the deflection as well as the lateral rotation of the rotor about its undeflected position within the volute.

The coefficient matrices presented are for two operating

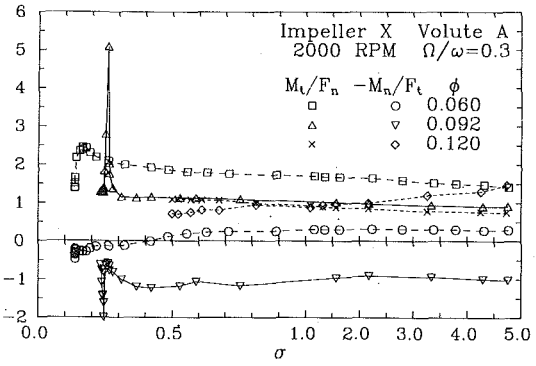

Fig. 21(*a*)

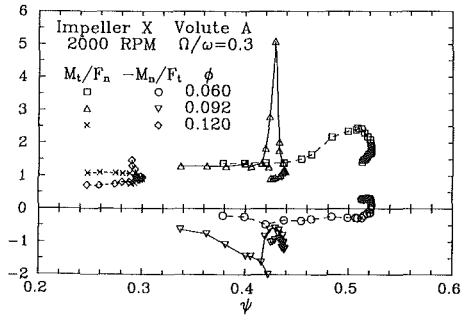

Fig. 21(*b*)

Fig. 21 The lever arms computed from the components of the unsteady moment and force on Impeller X in Volute A at 2000 rpm with $\Omega/\omega = .3$ for the three flow coefficients: $\phi = .060$, .092 (design) and .120, as a function of (*a*) the cavitation number and (*b*) the head coefficient. Uncertainty expressed as a standard deviation: M_t/F_n, M_n/F_t see text, $\sigma \pm .008$ and $\psi \pm .005$.

points: non-cavitating and cavitating with 3 percent head loss. Cavitation at 3 percent head loss did not make the rotor dynamic behavior of the impeller worse. The range of destabilizing whirl ratio was slightly reduced. A monotonic change in the coefficients between the two operating points cannot be assumed. At design flow [A] changes differently for $\Omega/\omega = .1$ and .3 with less cavitation.

Conclusion

Fluid-induced rotordynamic forces were measured in the presence of cavitation for a centrifugal impeller in a spiral volute. At 3 percent head loss there was little difference in the average normal and tangential force, F_n and F_t, for forward whirl, slightly more for the larger values of reverse whirl. The whirl ratio range of the destabilizing force had decreased slightly with cavitation. However a lesser degree of cavitation at the design point increased this destabilizing force for a particular set of whirl ratios. Through breakdown in head rise the destabilizing forces did not exceed their noncavitating values except for this one set of data.

Measurements of the rotordynamic forces on impellers made using the dynamometer of the Rotor Force Test Facility at Caltech are integrated measurements. The contribution to the total force from the varying clearance between the impeller front shroud and the casing wall during whirl is not distinguished from the contribution from the unsteady flow field between the whirling impeller and the volute. Further work is necessary to quantify the contribution of the shroud flow to the impeller force measurements. Childs (1989) has theoretically examined the forces on an impeller shroud. For the impeller-volute interaction Tsujimoto et al. (1988) includes a favorable comparison of his theory with measurements made on a two-dimensional version of Impeller X.

Table 1 Stiffness, damping, and mass matrices. Uncertainty expressed as a standard deviation: $K \pm .02$, $C \pm .08$ and $M \pm .2$. For $\phi = .060$, see text.

flow condition	K_{xx} K_{yx}	K_{xy} K_{yy}	C_{xx} C_{yx}	C_{xy} C_{yy}	M_{xx} M_{yx}	M_{xy} M_{yy}
ϕ=.120	-2.34	.68	2.46.	8.19	5.7	-1.2
non-cavit	-.70	-2.34	-7.96	2.70	.3	5.9
ϕ=.120	-2.15	.65	2.27	7.80	5.4	-.9
3% head loss	-.62	-2.12	-7.70	2.58	.4	5.6
ϕ=.092	-2.51	.58	1.88	8.76	6.1	-.4
non-cavit	-.78	-2.38	-8.66	1.92	-.3	6.6
ϕ=.092	-2.42	.60	2.47	8.39	5.6	-1.6
3% head loss	-.81	-2.30	-8.16	2.46	.9	6.0
ϕ=.060	-2.54	.50	1.6	9.2	7.1	-.3
non-cavit	-.84	-2.20	-9.2	1.3	-.6	7.8
ϕ=.060	-2.46	.43	2.0	8.9	6.7	-.9
3% head loss	-.67	-2.17	-9.2	1.8	1.0	7.9

Acknowledgments

The authors are indebted to the NASA George Marshall Space Flight Center, for continued sponsorship of this research under contract NAS8-33108. One of the authors (R. Franz) would like to thank the Shell Foundation for providing a fellowship that sponsored his graduate studies.

References

Adkins, D. R., 1986, "Analyses of Hydrodynamic Forces on Centrifugal Pump Impellers," Ph.D. thesis, Division of Engineering and Applied Science, California Institute of Technology, Pasadena, CA.

Adkins, D. R., Brennen, C. E., 1988, "Analyses of Hydrodynamic Radial Forces on Centrifugal Pump Impellers," ASME JOURNAL OF FLUIDS ENGINEERING, Vol. 110, No. 1, pp. 20–28.

Bolleter, U,. Wyss, A., Welte, I., and Stürchler, R., 1987, "Measurement of Hydrodynamic Interaction Matrices of Boiler Feed Pump Impellers," ASME *Journal of Vibration, Acoustics, Stress, and Reliability in Design*, Vol. 109, No. 2, pp. 144–151.

Brennen, C. E., Acosta, A. J., and Caughy, T. K., 1980, "A Test Program to Measure Fluid Mechanical Whirl-Excitation Forces in Centrifugal Pumps," *Proceedings of the First Workshop on Rotordynamic Instability Problems in High-Performance Turbomachinery*, Texas A&M University, College Station, Texas, NASA CP 2133, pp. 229–235.

Childs, D. W., 1989, "Fluid-Structure Interaction Forces at Pump-Impeller-Shroud Surfaces for Rotordynamic Calculations," ASME *Journal of Vibration, Acoustics, Stress and Reliability in Design*, Vol. 111, No. 3, pp. 216–225.

Franz, R., Arndt, N., Caughey, T. K., Brennen, C. E., and Acosta, A. J., 1987, "Rotordynamic Forces on Centrifugal Pump Impellers," *Proceedings of the Eighth Conference of Fluid Machinery*, Académiai Kiadó, Budapest, Hungary, Vol. 1, pp. 252–258.

Franz, R., 1989, "Experimental Investigation of the Effect of Cavitation on the Rotordynamic Forces on a Whirling Centrifugal Pump Impeller," Ph.D. thesis, Division of Engineering and Applied Science, California Institute of Technology, Pasadena, CA.

Jery, B., Brennen, C. E., Caughey, T. K., and Acosta, A. J., 1985, "Forces on Centrifugal Pump Impellers," *Second International Pump Symposium*, Houston, Texas, Apr. 29–May 2, 1985.

Jery, B., 1987, "Experimental Study of Unsteady Hydrodynamic Force Matrices on Whirling Centrifugal Pump Impellers," Ph.D. thesis, Division of Engineering and Applied Science, California Institute of Technology, Pasadena, CA.

Ohashi, H., Shoji, H., 1987, "Lateral Fluid Forces on a Whirling Centrifugal Impeller (2nd Report: Experiment in Vaneless Diffuser)," ASME JOURNAL OF FLUIDS ENGINEERING, Vol. 109, No. 2, pp. 100–106.

Ohashi, H., Sakurai, A., and Nishihama, J., 1988, "Influence of Impeller and Diffuser Geometries on the Lateral Forces of Whirling Centrifugal Impeller," *Proceedings of the Fifth Workshop on Rotordynamic Instability Problems in High-Performance Turbomachinery*, Texas A&M University, College Station, Texas, May 16–18, 1988.

Tsujimoto, Y., Acosta, A. J., and Brennen, C. E., 1988, "Theoretical Study of Fluid Forces on a Centrifugal Impeller Rotating and Whirling in a Volute," ASME *Journal of Vibration, Acoustics, Stress and Reliability in Design*, Vol. 110, No. 3, pp. 263–269.

Uchida, N., Imaichi, K., and Shirai, T., 1971, "Radial Force on the Impeller of a Centrifugal Pump," *Bulletin of the Japan Society of Mechanical Engineers*, Vol. 14, No. 76, pp. 1106–1117.

Using Viscous Calculations in Pump Design

F. Martelli
Professor.
Mem. ASME

V. Michelassi
Doctoral Candidate.

Dipartimento di Energetica,
50139 Firenze, Italy

A viscous computer code for designing the meridional channels of high-performance pumps is presented. An averaging technique is used to reduce the three-dimensional flow to a two-dimensional model. The code, based upon an implicit finite difference method for steady two-dimensional incompressible flows, was validated in complex flow geometries prior to application in the design analysis of an actual pump. Viscous effects are taken into account by two different turbulence models. The Navier-Stokes solver is used in conjunction with a standard blade-to-blade calculation by means of an automatic graphic procedure that exchanges geometric and flowfield data. Various meridional shape solutions are presented and discussed in relation to physical evidence.

Introduction

More and more sophisticated numerical codes are finding application in the fluid dynamic design of hydraulic machinery. This is because a growing number of applications involve extremely high/low specific speeds, tighter cavitation restrictions, and similar requirements, thereby necessitating far more accuracy in fluid dynamic design than attainable using classical approaches such as Stephanoff's (1967). These enhanced design requirements, calling for a notably high level of flow modeling, can be met by:

1. Using the classic method developed by Wu (1956) in which flow is studied by means of inviscid calculations. With combined viscous-inviscid methods no longer valid due to their inability to account for phenomena provoked by separation and strong turbulence, especially on the meridional plane, Wu's method constitutes the first step toward fully 3-D Navier-Stokes solvers.
2. Using a fully 3-D inviscid method capable of accounting for viscous effects inside the blade passages starting from their inception at blade inlet. This approach is best suited to machines with favorable pressure gradients.

The calculation models are constructed on the basis of Wu's theory in which two flowfield surfaces (designated S1 and S2) are examined. In previous approaches (Martelli and Manfrida, 1982; Martelli and Manfrida, 1983; Carnevale et al., 1983), interaction between inviscid blade-to-blade and meridional flows solved by finite elements (FE) was used in flow modeling. Thereafter, it was found that greater accuracy could be achieved by performing a viscous calculation on the meridional plane alone without impairing the results of the blade-to-blade inviscid calculation. Evidently, the system of data exchange between the two surface calculations must be totally revamped.

Hence, calculation of the mean meridional blade surface was abandoned in favor of a averaged approach allowing better evaluation and understanding of the approximations. The decision to use viscosity in the meridional plane prior to blade-to-blade originates from the awareness that the meridional form is of prime importance in centrifugal machines and that the wet surfaces are much more developed in the meridional section. Due to the difference in calculation methods (FE for blade-to-blade and finite differences for meridional flow), it was necessary to modify the code interface in order to ensure ease and rapidity of application.

In the proposed method, the Navier-Stokes solver is used in conjunction with the blade-to-blade calculation described in Martelli and Manfrida (1982), Martelli and Manfrida (1983), and Carnevale et al. (1983). It is implemented by means of an automatic graphic procedure that exchanges geometric and flowfield data.

Special assumptions are introduced to account for the effects of rotation and viscous terms. The viscous solver is based on an implicit finite difference procedure for steady two-dimensional incompressible flows. A nonorthogonal curvilinear mesh is provided for solving arbitrary geometries. Turbulence effects are accounted by combining two approaches, i.e., the Baldwin-Lomax model (1978) and Chien's k-ϵ model (1982) with the Reynolds averaged Navier-Stokes equations; the artificial compressibility equation described by Chorin (1967) is used to enforce mass conservation.

In order to get around the strict stability limitation, Michelassi and Benocci (1987), the implicit approximate factorization scheme developed by Beam and Warming (1982) and validated over a wide range of laminar flowfield geometries, was extended to the nonlinear k-ϵ source terms. An implicit, rather that explicit, scheme was selected to fit the stability limits and in view of the fact that implicit schemes—now extensively used to solve all kinds of flows from supersonic to incompressible—are often more convenient.

To ensure that all channel wall shapes could be solved, a nonorthogonal curvilinear coordinate system was developed using the method proposed by Thompson et al. (1977) to solve the transformed equations in the physical domain by the successive over-relaxation (SOR) point. The artificial compres-

Contributed by the Fluids Engineering Division for publication in the JOURNAL OF FLUIDS ENGINEERING. Manuscript received by the Fluids Engineering Division May 15, 1989.

sibility equation is especially useful when time-marching techniques are used to compute the incompressible flow steady states, since they make it possible to avoid cumbersome solutions to Laplace equations in which no time derivatives are present.

The Computational Model

The equations governing the steady viscous turbulent flow of an incompressible fluid can be written in general form as

$$\nabla \cdot \mathbf{W} = 0 \quad \text{(continuity)}$$
$$\nabla \cdot (\mathbf{W} \otimes \mathbf{W}) = \nabla \left(\frac{p}{\rho}\right) + \frac{F_d}{\rho} + \Omega^2 \cdot \mathbf{r} - 2\Omega \times \mathbf{W} \quad \text{(momentum)} \tag{1}$$

where $F_d = \nabla \cdot \tau$.

For the sake of generality, the reference frame is considered to be rotating at pump rotor speed Ω. The stress tensor is related to the deformation rate through the actual viscosity coefficient (laminar or, in the case of the Boussinesq assumption, laminar + turbulent, according to flow conditions).

Accurate modeling is required to close the set of turbulent flow equations when solving—as in our case—the Reynolds-averaged Navier-Stokes equations. In this work, two models are considered: the Baldwin-Lomax algebraic formula (1978) commonly adopted for turbomachinery calculations and a low Reynolds number form of the $k-\epsilon$ model. This procedure may be considered a first attempt at increasing calculation accuracy—especially in the recirculating regions—which, however, also involves a considerable increase in computational effort.

The procedure proposed by Hirsch (1978) was used to derive a two-dimensional meridional model, since it provides an averaged picture of the flowfield in the meridional plane and allows semiempirical modeling of blade surface effects. The Hirsch averaging technique is based on the following formula for a generic variable.

$$\bar{f} = [\theta_s - \theta_p]^{-1} \cdot \int_p^s f \cdot d\theta \tag{2}$$

where the averaging range is given by

$$[\theta_s - \theta_p] = 2 \cdot \pi / N \cdot b$$

in which b is computed as

$$b = 1 - s/g$$

The ensuing expression for averaging the derivative is also given in Hirsch.

Applying this technique to system (1), the equations become (note that overbar for averaged values has been omitted for simplicity.):

$$\left[\frac{\partial}{\partial r}(b \cdot r \cdot W_r)\right] + \left[\frac{\partial}{\partial z}(b \cdot r \cdot W_t a)\right] = 0 \tag{3}$$

$$\frac{1}{(b \cdot r)} \cdot \left[\frac{\partial}{\partial r}(b \cdot r \cdot W_r \cdot W_r)\right] + \frac{1}{(b \cdot r)}\left[\frac{\partial}{\partial z}(b \cdot r \cdot W_r \cdot W_a)\right] = \text{RHS} \tag{4}$$

where $\text{RHS} = \left(-\frac{\partial p}{\partial r} + F_{br} + F_{dr}\right) \cdot \frac{1}{\rho} + F_A$

$$\frac{1}{(b \cdot r)} \cdot \left[\frac{\partial}{\partial r}(b \cdot r \cdot W_a \cdot W_r)\right] + \frac{1}{(b \cdot r)} \cdot \left[\frac{\partial}{\partial z}(b \cdot r \cdot W_a \cdot W_a)\right] = \text{ZHS} \tag{5}$$

$$\text{where ZHS} = \left(-\frac{\partial p}{\partial z} + F_{bz} + F_{dz}\right)\frac{1}{\rho}$$

$$\left[\frac{\partial}{\partial r}(r \cdot V_t) \cdot \left(\frac{W_r}{r}\right) + \frac{\partial}{\partial z}(r \cdot V_t) \cdot \left(\frac{W_a}{r}\right)\right] = \left(\frac{W}{r}\right) \cdot \frac{\partial}{\partial m}(r \cdot V_t) = \text{THS} \tag{6}$$

where $\text{THS} = (F_b + F_{dt})/\rho$ and, due to the reference frame's rotating speed, F_A is

$$F_A = [W_t \cdot W_t / r + \Omega^2 \cdot r + 2 \cdot \Omega \cdot W_t] \tag{4'}$$

Using the definition of fluctuating as part of an arbitrary flow function (f') with respect to its circumferential average value (f):

$$f = \bar{f} + f'$$

the terms can be rewritten, for example, as

$$\overline{W_a \cdot W_r} = \overline{W_a} \cdot \overline{W_r} + \overline{W_a' \cdot W_r'}$$

In the system comprising (3) - (6), the mean value of the fluctuating part is ignored. This means that, although quasi-axisymmetric, the equations must be considered as having been written for their values averaged in θ direction.

Certain terms which might be expected from the averaging process fail to appear in the system. This is due to the condition (viscous or inviscid) on the blade linking the velocity components. Actually, what is ignored is the contribution of the fluctuating part of the type $\overline{W_a' W_r'}$ which is assumed small and not able to be computed.

The F_b terms (Blade Forces) resulting from the presence of the blade represent the effect of different blade-side pressures and allow for flow turning. They come from the upper and lower integration limits and can be written

Nomenclature

b = blockage factor
g = pitch
k = turbulent kinetic energy
m = meridional coordinate
N = blade number
C_p = pressure coefficient
C_μ = k-ϵ model constant
p = pressure
r = radial coordinate
$\mathbf{r}$ = radial vector
Re = Reynolds
s = blade tangential thickness
t = time
V = absolute velocity component or modulus
W = relative velocity component or modulus
$\mathbf{W}$ = relative velocity vector
z = axial coordinate
τ = stress tensor
δt = time step
α, β = curvilinear coordinates system
α' = angle in the meridional plane (Fig. 10)
η, ϕ = blade angles
Φ = stream function
ϵ = turbulent energy dissipation
θ = tangential coordinate
μ = viscosity
ρ = density
Ω = rotational speed
$\boldsymbol{\Omega}$ = rotation speed vector

Subscripts

a = axial
b = blade
d = diffusive
p = pressure side
r = radial
s = suction side
t = tangential
x = vector product
$\otimes$ = tensor product
$\cdot$ = scalar product
∇ = nabla operator
T = transposed matrix

$$F_{br} = \begin{cases} 0 & \text{outside blade} \\ F_b \cdot tg\ \eta & \text{inside blade} \end{cases} \quad (7)$$

$$F_{bz} = \begin{cases} 0 & \text{outside blade} \\ F_b \cdot tg\ \phi & \text{inside blade} \end{cases} \quad (8)$$

where $F_b = [(p_s - p_p)/(b \cdot g)]$ and η and ϕ and geometric blade angles which can be set on the camberline in the case of small and quasi-constant thicknesses.

Their meaning is

$$tg\ \eta = -r \cdot \left(\frac{\partial \theta}{\partial r}\right) \quad tg\ \phi = r \cdot \left(\frac{\partial \theta}{\partial z}\right)$$

It is possible to neglect other terms related to blockage change which are not really significant and, in many cases, are actually null:

$$[\bar{p} - (p_s + p_p)/2] \cdot \left(\frac{\partial b}{\partial r}\right) \cdot \frac{1}{b}$$

$$[\bar{p} - (p_s + p_p)/2] \cdot \left(\frac{\partial b}{\partial z}\right) \cdot \frac{1}{b}$$

Generally speaking, all of the derivatives of b will be assumed as zero so that the term can disappear from equations (3) to (6).

Handling of the viscous terms F_d is theoretically a very complicated matter, since $F_d = \nabla \cdot \tau$. The stress tensor can be expressed by assuming eddy viscosity, which can be evaluated in the turbulence model as

$$\tau = \mu \cdot [(\nabla \otimes \mathbf{W}) + \nabla \otimes \mathbf{W})^T] \quad (9)$$

Because of certain assumptions made in averaging, the viscous flow terms are expressed axisymmetrically. These assumptions are made for the area inside the blade passage, since the axisymmetric expression may be readily obtained if the prior-assessed fluctuating part is neglected on the outside. Therefore, it is assumed that the difference in stress tensor on the blade side and the velocity derivatives may be ignored. This is consistent with the use of an inviscid calculation on the blade-to-blade surface. On the other hand, the principal effect of the terms would otherwise be in the viscous component of the tangential momentum used in the blade. In view of these considerations, the F_d terms can be written in cylindrical coordinates as

$$F_{dr} = \frac{\partial}{\partial z}\left[\mu\left(\frac{\partial W_r}{\partial z} + \frac{\partial W_a}{\partial r}\right)\right] + 2 \cdot \frac{\mu}{r} \cdot \left[\frac{\partial W_r}{\partial r} - \frac{W_r}{r}\right] + 2\frac{\partial}{\partial r}\left[\mu\left(\frac{\partial W_r}{\partial r}\right)\right] \quad (10)$$

$$F_{dz} = \frac{\partial}{\partial r}\left[\mu\left(\frac{\partial W_r}{\partial z} + \frac{\partial W_a}{\partial r}\right)\right] + 2\frac{\partial}{\partial z}\left[\mu\left(\frac{\partial W_a}{\partial z}\right)\right] \quad (11)$$

The system comprising (3), (4), (5), (7), (8), (10), (11) represents the model to be used in calculating meridional channel flow. Note that (7) and (8) contain terms, such as F_A in (4′), that cannot be derived from other equations. These terms represent the link with the blade-to-blade calculation in the earlier hypothesis of inviscid flow solved by FE method (Martelli and Manfrida, 1983).

The blade-to-blade calculation is performed on an axisymmetric stream surface and is based on the solution, by a Finite Element discretization, of the momentum equation projected in the direction locally orthogonal to the streamwise direction. The introduction of the stream function Φ, satisfying the continuity condition, allows the equation to be written as follows:

$$\frac{\partial}{\partial \theta}\left(\frac{1}{r^2}\frac{\partial \Phi}{\partial \theta}\right) + \frac{\partial^2 \Phi}{\partial m^2} = \text{RHS} + \sin(\alpha')\left(\frac{W_\theta}{r} + 2\Omega\right)$$

Where RHS takes into account the gradient of rotalpy and entropy. The equation is then expressed in a quasi-variational form suitable for Finite Element discretization.

This formulation in θ-m coordinates system can easily treat any geometry from axial to radial and by the variation of the streamtube thickness can take into account the effect of the meridional flow configuration. On the basis of the results of the inviscid calculation performed at the hub and shroud, an interface model prepares the F_b and F_A required for the viscous calculation.

Equation (6) is used to ensure the physical correctness of the calculation outside the blade. In this way, it is possible to avoid calculating F_{vt}—which would require a viscous blade-to-blade calculation. With equation (6), the moment of the angular momentum is imposed as a constant along the streamline outside the blade (with no swirl at the inlet, F_A will be zero up to the blade origin section), whereas (V_t r) is imposed as a constant along the streamline starting from blade outlet. This allows restricting the use of the blade-to-blade code only inside the blading and rigorously evaluating the extra-blade F_A terms. In the current version, a swirl-less inlet is assumed: This avoids iteration in the estimation of the F_A values on the meridional lines (coordinate m).

Another important part of computational modeling is the choice of the turbulence model to be used in closing the equation systems and evaluating the actual viscosity. Our approach (Boussinesq approximation) precludes the use of models based upon Reynolds stress that would appear valid for recirculating flows, but which are actually somewhat burdensome to use at the design stage. Our choice fell upon the algebraic model developed by Baldwin and Lomax (1978) which is widely used in turbomachinery design, and, in the cases where the Baldwin-Lomax model proved inadequate, we used a low Reynolds number (LR) k-ϵ formulation.

The classic Baldwin-Lomax model was implemented to handle duct flows, since selection of the reference section to be used in calculating the distance in the outer region is not automatic. Since the simple geometric division of the channel into two equal parts could give rise to marked discontinuities in the eddy viscosity, especially in zones where recirculation occurs, the model evaluates the function of the outer region for each surface and weights the two parts' contribution to each point. The result is perfect continuity in the viscosity between the two walls. Special evaluation of friction velocity is performed at the initial separation zone; the value of the velocity tends to zero making the mixing length meaningless.

An attempt to increase calculation accuracy, especially in the recirculating region, was made by using LR forms of the k-ϵ two equation model applicable to solving parabolic flows. One of the main advantages of the LR forms is that the viscous layer does not require bridging by means of wall functions; down-to-the-wall solutions may be achieved by introducing damping functions in the high Reynolds number form of the k-ϵ model to account for viscous effects that become dominant in the region close to the wall.

It should be pointed out, however that the gains in accuracy afforded by the LR form are accompanied by a consistent increase in computational effort, since a high degree of mesh refinement is required in the buffer layer flow region. The LR form selected for our investigation (Chien, 1982) solves for the isotropic part of the turbulence dissipation ϵ while introducing a new term to account for the nonisotropic effect dominating the viscous layer.

The original set of functions and related constants Chien (1982) was left unchanged. Due to the introduction of these additional terms, the solid wall value of the turbulent kinetic energy and the isotropic part of the turbulent dissipation were set at zero. The model also provides diagonal dominance, at least under the fully developed flow conditions investigated (Chien, 1982). For an implicit coupled method, this charac-

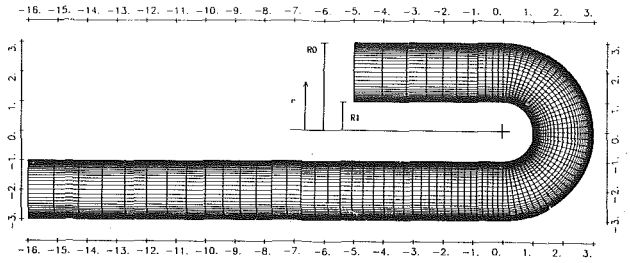

Fig. 1 Planar turnaround duct; 90×65 mesh

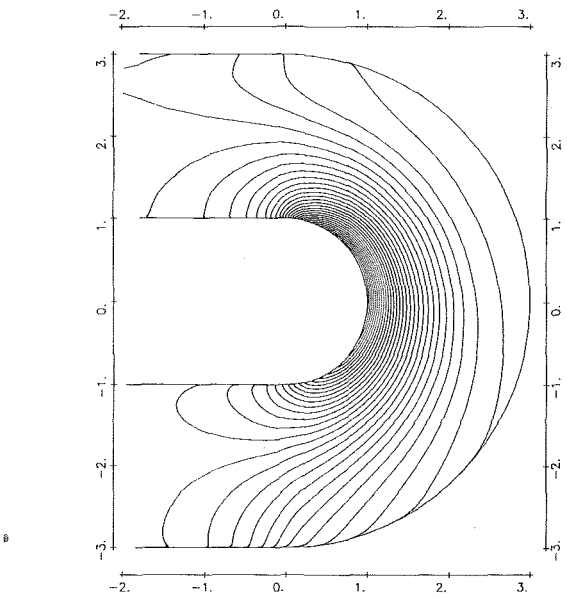

Fig. 2 Planar turnaround duct; close-up view of pressure isolines

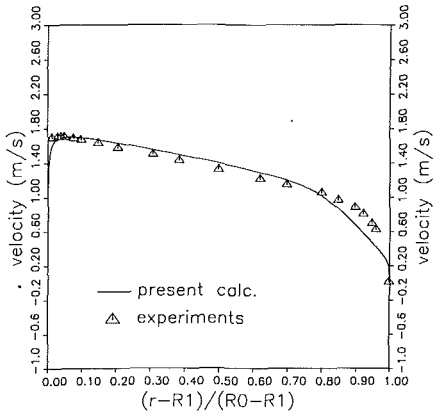

Fig. 3 Planar turnaround duct; bend inlet streamwise velocity profile

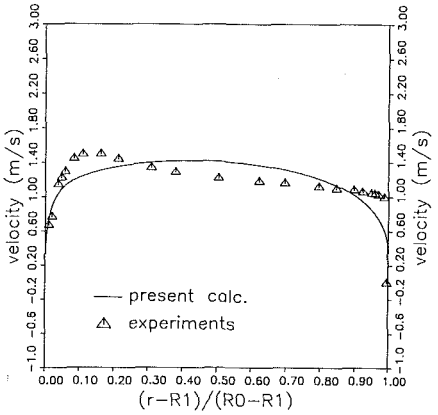

Fig. 4 Planar turnaround duct; bend outlet streamwise velocity profile

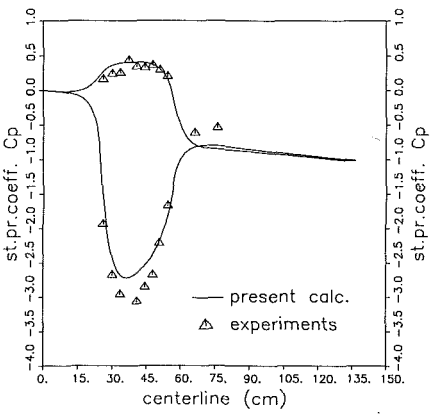

Fig. 5 Planar turnaround duct; wall pressure distribution

teristic ensures good convergence rates, even in elliptic flowfields.

Numerical Procedure

The main drawback of a steady incompressible flow formulation is the absence of time derivatives in the continuity equation. This imposes direct solution of the continuity equation or a Poisson-like equation obtained by cross differencing the momentum equations, and, in most cases, prevents the use of time-marching techniques.

In order to have a pseudounsteady form of the continuity equation, Chorin's artificial compressibility method (1967) was adopted by Michelassi and Benocci (1987) for the solution of the incompressible Navier-Stokes equations. In this formulation, a fictitious state equation is defined and the pressure is placed in the time-dependent form of the continuity equation that reduces to:

$$\frac{\partial p}{\partial t}+E\cdot\left[\frac{\partial W_a}{\partial z}+\frac{\partial W_r}{\partial r}+\frac{W_r}{r}\right]=0 \tag{12}$$

where $E > 0$ is an artificial compressibility parameter. Evidently, equation (12) will enforce mass conservation only at the steady state so that it is impossible to follow a physical time transient. The unsteady form of the N-S equations are then coupled to (12):

$$\frac{\partial W_r}{\partial t}+\frac{\partial W_r W_r}{\partial r}+\frac{\partial W_r W_a}{\partial z}=\left(-\frac{\partial p}{\partial r}-\frac{W_r W_r}{r}+F_{dr}+F_{br}\right)\frac{1}{\rho}+F_A \tag{13}$$

$$\frac{\partial W_\theta}{\partial t}+\frac{\partial W_r W_\theta}{\partial r}+\frac{\partial W_\theta W_\theta}{\partial z}=\left(-\frac{\partial p}{\partial z}-\frac{W_\theta W_r}{r}+F_{dz}+F_{bz}\right)\frac{1}{\rho} \tag{14}$$

The solution of viscous turbulent flows necessitates exceedingly stretched out grids. Also, if the physical domain is irregular—as is usually the case in turbomachine channels—then nonorthogonal coordinate systems must be used. The curvilinear coordinate system (α, β) is generated by a preprocessor that operates according to either a simple algebraic procedure or a more sophisticated method proposed by Thompson et al. (1977) that was found particularly convenient for channel application (Martelli and Michelassi, 1988). The discretization of the partial differential equations was carried out using the centered finite differences of the strong conservative form developed by Pulliam and Steger (1980). With this form, it is possible to minimize the errors caused by undifferentiated metrics in the curvilinear coordinate systems. If these are not

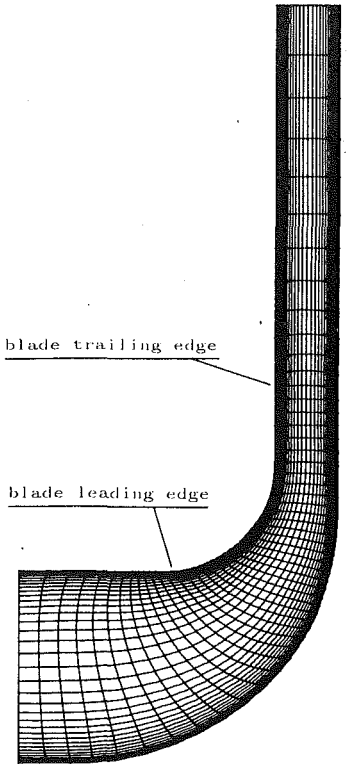

Fig. 6 S.H.F. pump; meridional plane 35 × 52 mesh

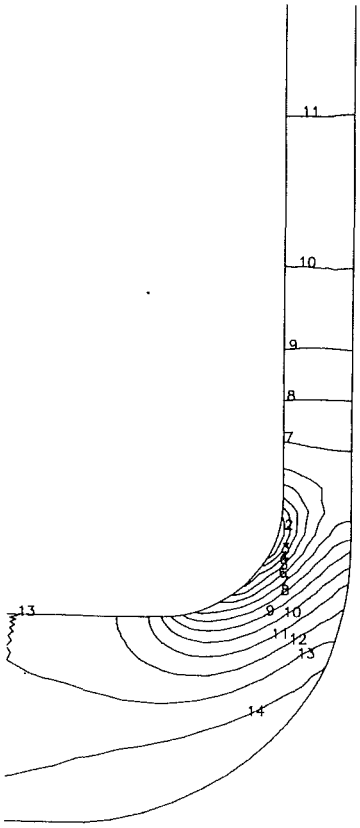

Fig. 7 S.H.F. pump; pressure isolines without source terms. ($P(1) = -1.15$ / $p(14) = 0.39$).

properly differentiated, the ensuring errors can act as source terms that may affect the solution. Introducing the artificial compressibility equation, it is possible to write the time-dependent system of the five coupled equations (three in the case of the Baldwin-Lomax model) in vector form:

$$\frac{\partial \mathbf{q}}{\partial t}+\frac{\partial \mathbf{F}}{\partial \alpha}+\frac{\partial \mathbf{G}}{\partial \beta}=\frac{\partial \mathbf{F}_d}{\partial \alpha}+\frac{\partial \mathbf{G}_d}{\partial \beta}+\mathbf{H} \tag{15}$$

in which the unknown vector is:

$$\mathbf{q}=\mathrm{J}^{-1}\,(p,\ W_a,\ W_r,\ \epsilon,\ k)^T$$

where J is the Jacobian of the transformation from r, z to α, β, $\mathbf{F}$ and $\mathbf{G}$ are the convective terms flux vectors, $\mathbf{F}_d$, $\mathbf{G}_d$ are the diffusive terms flux vectors, $\mathbf{H}$ is source vector. The system is solved with respect to the cartesian velocities; details of the flux vectors and the solution procedure may be found in Martelli and Michelassi (1988). Evidently, when a laminar flow is solved or the Baldwin-Lomax model is used, the last two equations are dropped and the differential system reduces to three equations. In practice, the Jacobians of the flux vectors are simplified, but the procedure remains unchanged.

The approximate factorization method proposed by Beam and Warming (1982) is probably so well known that no further explanation is necessary. The linear system resulting from (15) can be written as it follows:

$$\begin{aligned}&[\mathbf{I}+\theta\delta t(\mathbf{H}j/2+\delta_\alpha(\mathbf{A}+\delta_\alpha(\mathbf{R},\alpha))-\delta_{\alpha\alpha}\mathbf{R}]\delta\mathbf{q}=\mathrm{RHS}\\&[\mathbf{I}+\theta\delta t(\mathbf{H}j/2+\delta_\beta(\mathbf{B}+\delta_\beta(\mathbf{S},\beta))-\delta_{\beta\beta}\ \mathbf{S}]\delta\mathbf{q}^*=\delta\mathbf{q}^*\end{aligned} \tag{16}$$

where δ is a central finite difference operator,

$$\mathrm{RHS}=-\delta t\left(-\frac{\partial \mathbf{F}}{\partial \alpha}-\frac{\partial \mathbf{G}}{\partial \beta}+\frac{\partial \mathbf{F}_d}{\partial \alpha}+\frac{\partial \mathbf{G}_d}{\partial \beta}+\mathbf{H}\right),$$

$\mathbf{A}$ and $\mathbf{B}$ are the Jacobians of the convective terms, $\mathbf{R}$ and $\mathbf{S}$ are the Jacobians of the diffusive terms, $\mathbf{H}_j$ are the Jacobians of the source terms introduced in both the sweeps, δt is the timestep, $\mathbf{q}^n$ is the solution at time $t = n\,\delta t$, and $\delta\mathbf{q}^{n+1} - \mathbf{q}^n$.

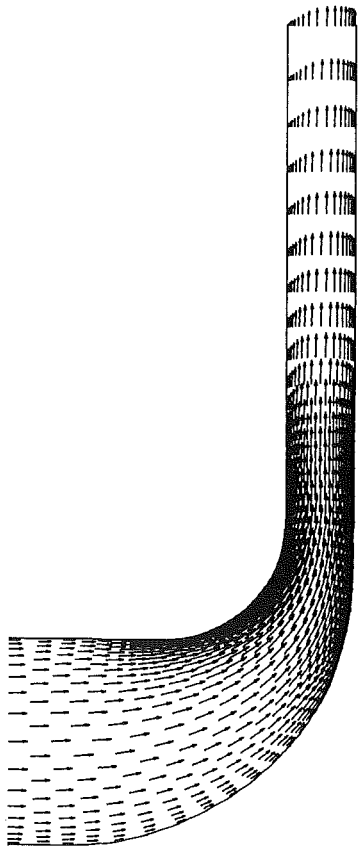

Fig. 8 S.H.F. pump; velocity field without source terms

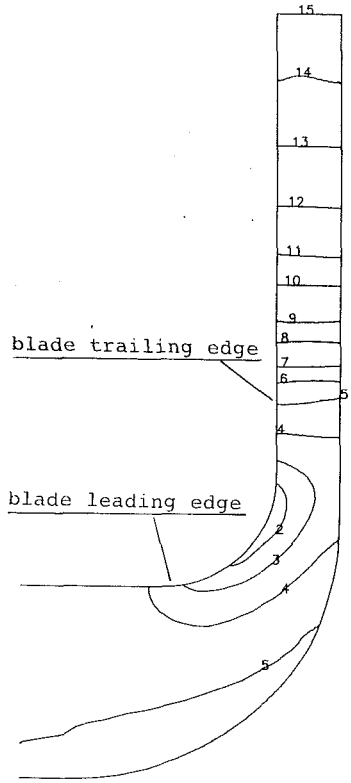

Fig. 9 S.H.F. pump; pressure isolines. ($P(1) = -4.35$ / $p(15) = 0.$)

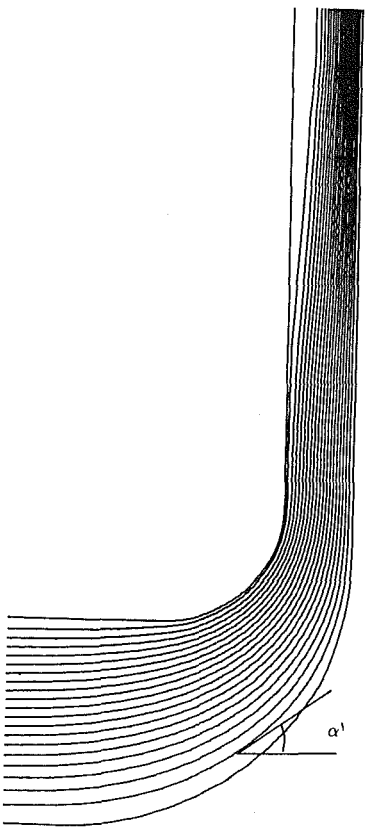

Fig. 10 S.H.F. pump; streamlines pattern

The resulting linear system is solved by block tridiagonal matrix inversion. Moreover, with respect to the classical decoupled technique, the coupling of the five equations implicitly accounts for the k and ϵ convection terms, thereby giving rise to a welcome gain in computational stability especially in complex domains.

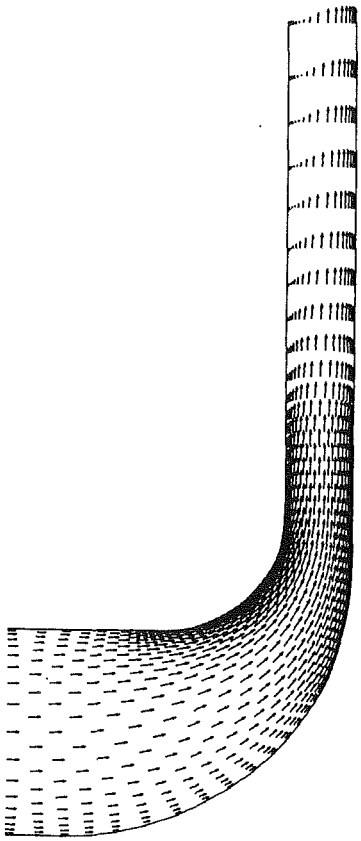

Fig. 11 S.H.F. pump; velocity field

The θ parameter weights the implicit and explicit contribution to the space operators; all the calculations described were carried out using $\theta = 1$. The use of the artificial compressibility formulation does not allow following a physical time transient so that, in order to take full advantage of the implicit solver, a local time step formula is implemented. Fourth-order explicit and second-order implicit numerical dissipation terms are then added in order to damp the numerical modes with the highest wave numbers (Pulliam, 1986). The use of artificial damping was necessary only in the artificial compressibility equation which does not contain any physical damping term, in order to avoid significant decreases in convergence speed.

Results

After prior validation had been attained from two-dimensional geometries (Martelli and Michelassi, 1988; Michelassi, 1988), the first assessment of the proposed method was carried out on an especially complex geometry much resembling pump meridional channels. The method was then applied to the meridional channel of the S.H.F. pump analyzed by Philibert (1985); the S.H.F. is a typical configuration of a high performance centrifugal pump with backward curved blades.

Planar Turnaround Duct

After a successful validation of the code in a straight channel flow at various Reynolds number numbers, Re (Michelassi, 1988), the Chien LR formulation was implemented to study the flow in a planar turnaround duct. The test Reynolds number, based on the inlet section width and the inlet average velocity was 80,000. In the test geometry proposed by Sandborn and Shin (1987), the flow exhibits a 180-deg inversion in a

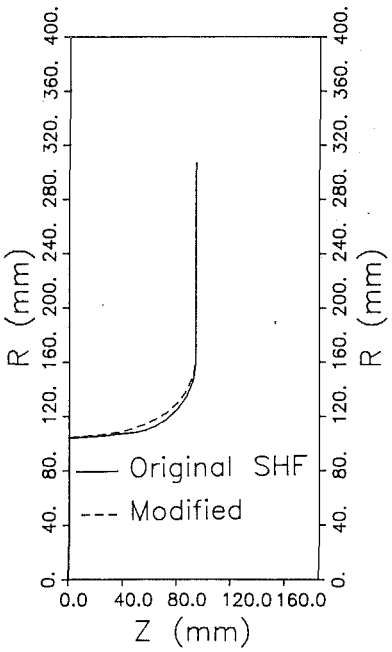

Fig. 12 S.H.F. pump; modification to the shroud profile

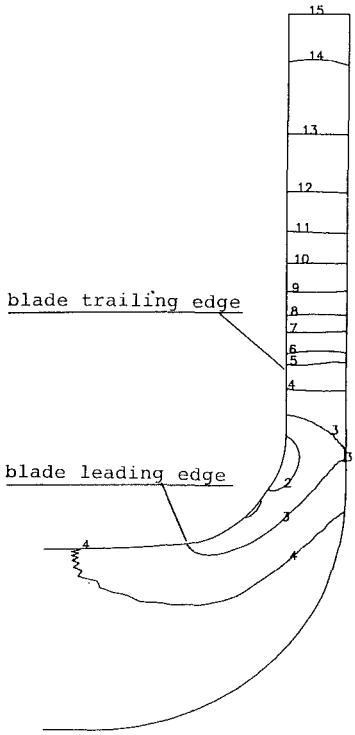

Fig.14 S.H.F. modified pump; pressure isolines. (P (1) = −4.12 / p(15) = 0.)

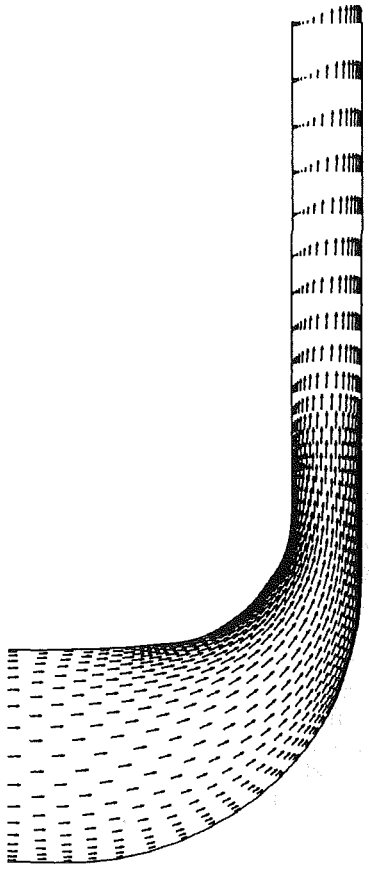

Fig. 13 S.H.F. modified pump; velocity field

constant cross section channel with smooth walls. The experimental uncertainty is weakly influenced by small flow rate variations that caused the data to be scaled with the inlet flow velocity; the Reynolds number variation was ≤ 10 percent. The computational mesh was obtained by a simple algebraic method that produced the strictly orthogonal grid shown in Fig. 1; 90 points in the streamwise direction and 65 points in the cross-stream direction were used. A brief preliminary mesh independence test was carried out for a fully developed channel flow at Re = 80,000 in order to evaluate the minimum number of points that allowed capturing the peak in turbulent kinetic energy located in the boundary layer. A reasonable prediction of this peak could be obtained with 65 points in the cross-stream direction; the mesh expansion ratio in the cross-stream direction is 1.15.

Converged pressure isolines (dimensionalized with respect to ρV_{inlet}^2), are given in Fig. 2 for the 180-deg bend region. It is evident that while wiggles are absent in the core region, weak pressure oscillations are present at the bend exit close to the outer wall. This is probably caused by insufficient mesh refinement in the main flow direction. The use of large artificial damping would definitely smooth the pressure wiggles, but would also seriously affect the quality of the results by increasing the overall mass error which was approximately 10^{-4}. Figure 3 shows the bend inlet streamwise velocity profile compared with experiments; agreement with measurements is good. Nevertheless, the velocities are weakly underestimated close to the outer wall, suggesting that the experimental boundary layer is probably thicker than the computed one. Conversely, it seems that the computed boundary layer is slightly thicker than the experimental one close to the inner wall. In Fig. 4 which shows the velocity profile at the bend exit section, agreement deteriorates. It is clear that the model predicts a stronger momentum transfer in the cross-flow direction than the measurements.

This results in a smoother velocity profile in the entire duct section. Moreover, the velocity module in the outer wall proximity is underestimated; this proves the presence of a strong cross-stream diffusion. While this problem is common whenever a flow with strong streamlines curvature is solved by a k-ϵ model it is worthwhile observing that there is no flow separation, as the experimental velocity profile indicates, even though a certain flow unsteadiness caused uncertainties in the measurements. This result conflicts with an investigation by

Brankovic and Stowers (1988) where, using Chien's low-Reynolds number form of the k-ϵ model, a strong separation was detected.

This discrepancy in the models' behavior may be attributed to the friction velocity u_* definition. Chien's model used exponential damping functions based on u_* defined as:

$$u_* = \sqrt{\tau_{\text{wall}}/\rho}$$

In separated regions, or whenever τ_{wall} approaches zero, the use of this parameter may cause the prediction of a nonphysical growth of the boundary layer. Following the wall function approach, we decided to correlate u_* to the cross-sectional peak in turbulent kinetic energy as follows:

$$u^* \approx \sqrt{k\sqrt{C_\mu}}$$

This choice ensures no separation at the bend outlet section.

The computed inner and outer wall distributions of the static pressure coefficient C_p (Fig. 5), are defined as:

$$C_p = p/(1/2\ \rho\ V_{\text{inlet}}{}^2)$$

Comparison with measurements shows that, while the pressure in the outer wall is well predicted, the model underestimates the minimum pressure at the inner wall. This discrepancy must not be entirely attributed to the relatively coarse grid; the higher pressure computed at the inner wall is strongly related to the predicted velocity at the bend exit section. Due to the smoother velocity profile, losses are redistributed in the cross-stream direction yielding to different static pressure at the walls.

Although, it would have been interesting to compare the total pressure distribution in the flow centerline, this quantity was not available from the experiments.

An attempt to solve the same flow using the Baldwin-Lomax turbulence model failed to obtain a steady converged result. Using the present solver we were unable to control the growth of a nonphysically large recirculating region located immediately downstream of the bend exit.

S.H.F. (Société Hydrotechnique de France) Radial Impeller

The algebraic model was used for convenience and cost; a k-ϵ would have required a very high number of transversal points (over 65) to capture K and ϵ peaks near the wall. At the same time, the algebraic model appeared to give physical results without convergence problems, since the geometry was not as curved (90-deg turning) as in the previous case (180-deg turning). The 35 $\times$ 52 mesh shown in Fig. 6 was extended considerably beyond the blade edge in order to improve downstream pressure conditions which do not influence the blade exit area. In the same figure the grid lines in the cross-flow direction corresponding the to the blade leading and trailing edges are clearly marked.

The first test shown in Figs. 7 and 8 refers to the flow in the meridional channel of the S.H.F. pump with no source terms from blade-to-blade calculations. The Reynolds number based on the inlet maximum axial velocity and inlet section width is approximately 180,000. It can be seen that the boundary layer grows slightly on the shroud and pressure remains virtually constant along the end of the duct. In Figs. 9–11 showing the results of the calculations for the S.H.F. blades, the source terms F_b and F_A (from the presence of the blades and previously evaluated through a blade-to-blade calculation) are introduced. Pressure distribution (Fig. 9) shows a marked displacement of the maximum and a greater uniformity at the end in comparison with the just mentioned calculation. Analysis of the streamlines (Fig. 10) and velocity clearly shows early separation on the shroud wall and a higher energy level for the flow close to the hub. The separation going beyond the blade appears reasonable; as the code did not reveal any convergence problems. The computer results most likely represent a true physical description of the flow.

Another test was conducted on a slightly different geometry, obtained by smoothing the shroud boundary (Fig. 12) to assess the model's sensitivity to channel shape. Even if only slight modifications are made, the code shows appreciable gain (approximately 5 percent) in the static pressure rise when compared with the original S.H.F. geometry (Fig. 13) and a partial displacement of the separation point (Fig. 14). The low-energy fluid zone is not significantly affected, despite the overall rise in total pressure.

Comments

Calculations have validated the method's capability to accurately represent flow in the design of radial machinery. The codes' interaction structure notably facilitates management and, in addition, the grid-generation method has been proven of producing meshes of adequate size for achieving accurate flow evaluation. The code also offers the possibility of using the k-ϵ turbulence model in place of the algebraic model in the case of problems encountering strong separations.

The method proved to be able to model the main features of the flow, within the meridional passages of pumps. The capacity of the method to feel slight modifications of the boundary shape qualifies it for design purposes at a good level of accuracy. Some limitations arise because of the averaging concept, which neglects fully three-dimensional effects. A more sophisticated approach requires a full 3D solver, which is not always easy to handle for design purposes.

The method requires further straightforward development in order to deal with flows with non-radial exit and inlet swirl. A promising development is the elimination of the blade-to-blade calculation that allows computing the extra forces F, thereby avoiding the iterative part. This might be possible using the equation averaged in θ (6) simplified on the basis of assumptions suggested by experimental correlations for blade-to-blade flows regarding the distribution of the angular components of the velocity. This would allow to maintain the two-dimensional nature of the numerical model in which the extra forces could be computed by much simpler approaches than the inviscid blade-to-blade calculation. We are currently attempting to achieve a simpler, more flexible system which could be used by the designer prior to passing on to more sophisticated three-dimensional methods.

Acknowledgments

This work was supported by the Italian Ministero della Pubblica Istruzione (MPI) under Grant MPI 40%.

References

Baldwin, B. S., and Lomax, H., 1978, "Thin Layer Approximation and Algebraic Model for Separated Turbulent Flows," *Proceedings, 16th AIAA Aerospace Science Meeting*, Alabama, GA, AIAA Paper 78-257.

Beam, R. M., and Warming, R. F., 1982, "Implicit Numerical Methods for the Compressible Navier-Stokes and Euler Equations," *Computational Fluid Dynamics*, Von Karman Institute LS 1982-04.

Brankovic, A., and Stowers, S. T., 1988, "Review of Low Reynolds Number Turbulence Models for Complex Internal Separated Flows," *Proceedings, AIAA/ASME/SAE/ASEE 24th Joint Propulsion Conference*, Boston, MA.

Carnevale, E., Giusti, S., Manfrida, G., and Martelli, F., 1983, "Quasi Three-Dimensional Finite Element Flow Calculation in Pumps," *Proceedings, 7th Conference on Fluid Machinery*, Akadèmiai Kiadò, Budapest, Hungary.

Chien, K. Y., 1982, "Predictions of Channel and Boundary Layer Flows with a Low-Reynolds Number Turbulence Model," *AIAA Journal*, Vol. 20, No. 1, pp. 33–38.

Chorin, A. J., 1967, "A Numerical Method for Solving Incompressible Viscous Flow Problems," *Journal of Computational Physics*, Vol. 2, No. 1, pp. 12–26.

Hirsch, C., 1979, "Application of Numerical Methods to Flow Calculations in Turbomachines," *Finite Element Calculations of Turbomachine Flows*, Von Karman Institute LS 1979-7.

Martelli, F., and Manfrida, G., 1982, "Studio del Flusso Interpalare in Pompe Assoradiali Con Il Metodo Degli Elementi Finiti," *Proceedings, 37th ATI Conference*, Padua, Italy.

Martelli, F., and Manfrida, G., 1983, "Flow Calculation in Pump Impellers by Finite Elements," *Proceedings, 7th Conference on Fluid Machinery*, Akadèmiai Kiadò, Budapest, Hungary.

Martelli, F., and Michelassi, V., 1988, "An Implicit Factored Solver for Inner Turbulent Flows," *Proceedings, AIAA/ASME/SAE/ASEE 24th Joint Propulsion Conference*, Boston, Mass., AIAA Paper 88-3099.

Michelassi, V., 1988, "Testing of Turbulence Models with an Artificial Compressibility Solution Method" Report SFB 210/T/49, University of Karlsruhe, Karlsruhe, West Germany.

Michelassi, V., and Benocci, C., 1987, "Prediction of Incompressible Flow Separation with the Approximate Factorization Technique," *International Journal for Numerical Methods in Fluids*, Vol. 7, pp. 1383–1403.

Philibert, R., and Verry, A., 1985, "Synthèse des calculs d'écoulement effectés sur la Pompe S.H.F. au debit nominal et à 80% du débit nominal," La Houille Blanche No. 7-8.

Pulliam, T. H., and Steger, J. L., 1980, "Implicit Finite-Difference Simulations of Three-Dimensional Compressible Flow," *AIAA Journal*, Vol. 18, No. 2, pp. 159–167.

Pulliam, T. H., 1986, "Efficient Solution Methods for the Navier-Stokes Equations," Van Karman Institute Lecture Series in Numerical Techniques for Viscous Flow Computation in Turbomachinery Blading, LS 5-86.

Sandborn, V. A., and Shin, J. C., 1987, "Evaluation of Turbulent Flow in a 180-Degree Bend for Bulk Reynolds Numbers from 70000 to 160000," NASA CR NAS8-36354.

Stepanoff, A. J., 1967, *Centrifugal and Axial Flow Pumps*, Wiley, New York, NY.

Thompson, J. F., Thames, F. C., and Mastin, C. W., 1977, "Boundary Fitted Curvilinear Coordinate Systems for Solution of Partial Differential Equations on Fields Containing Any Number of Arbitrary Two-Dimensional Bodies," NASA CR 2729.

Wu, C. H., 1956, "A General Theory of the Two-Dimensional Flow in Subsonic and Supersonic Turbomachines of Axial, Radial, and Mixed-Flow Types," NACA TN-2604.

Pressure and Three-Component Velocity Measurements on a Diffuser That Generates Longitudinal Vortices

L. N. Goenka[1]

R. L. Panton

D. G. Bogard

The University of Texas,
Department of Mechanical Engineering,
Austin, TX 78712

This paper presents flowfield measurements on a wide-angle, three-dimensional diffuser that has a vastly improved static-pressure recovery over the corresponding plane-wall diffuser when discharging into a plenum. The diffuser geometry consists of a pyramid-shaped insert attached to the diffuser expansion wall. The upsweep on the upper surface of the pyramid generates a transverse pressure gradient that causes the incoming flow to roll up into two symmetric, longitudinal vortices. Earlier flow-visualization studies have shown that these vortices replace the closed separated regions along the diffuser expansion wall, eliminating flow oscillations and hysteresis. This paper presents quantitative information, in the form of static pressure, total pressure, and three-component Laser Doppler Velocimeter (LDV) measurements, on the diffuser flowfield for two variations in the pyramid geometry. Information from these studies is useful in developing configurations with enhanced pressure recoveries. The greatly improved static-pressure recovery of this diffuser, combined with its superior flowfield features, make it particularly suitable for exhaust diffuser applications.

1 Introduction

The adverse pressure gradient in diffusers often results in flow separation, sometimes creating unsteady effects within the diffuser as well as in the rest of the flow system (Reneau, Johnston, and Kline, 1967). In addition, diffusers tend to amplify the nonuniformities present in the inlet velocity profile. These factors often limit the design to diffusion angles less than seven degs. This has the effect of dramatically increasing the diffusion length required and thus seriously limiting their application.

Well-known techniques exist to improve the performance of nonoptimal diffusers. These include boundary-layer suction, boundary-layer blowing, and the use of vortex generators that energize the boundary-layer fluid. However, these techniques do not work for extremely wide-angle diffusers. This paper presents flowfield measurements on a wide-angle, three-dimensional diffuser design that generates two longitudinal vortices. The diffuser geometry is shown in Fig. 1. The basic configuration is a plane-wall diffuser having an expansion half-angle of 20 deg so that the flow would normally separate, producing a large recirculation region. To prevent such separation, a pyramid-shaped insert is attached to the basic diffuser's expansion wall. The upsweep on the pyramid upper surface creates a transverse pressure gradient that causes the incoming flow to form two symmetric longitudinal vortices along the pyramid side surfaces.

Previous flow-visualization studies (Goenka, Panton, and Bogard, 1989) showed that the flow past the pyramid is somewhat analogous to that past a delta wing. The upsweep on the insert upper surface has the same effect on the flow as the delta wing's sweepback angle. Those studies also showed that at Reynolds number greater than 6000 (based on the diffuser-inlet height), the separated regions along the basic diffuser's expansion wall were eliminated by the pyramid and replaced by two longitudinal turbulent vortices. Further, the flow exhibited little or no hysteresis, which can occur with separation, with respect to changes in Reynolds number.

This article complements the previous study with quantitative information about the diffuser flowfield. It presents static-pressure, total pressure, and three-component mean and

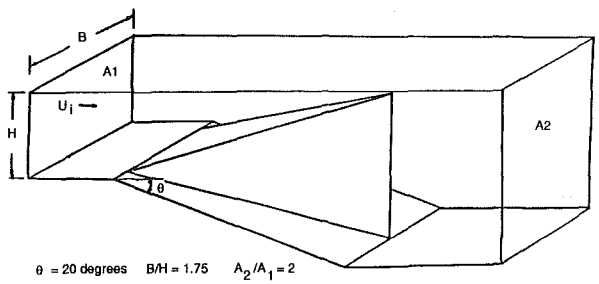

Fig. 1 Test diffuser geometry

[1]Presently, at Sverdrup Technology, Inc., Tullahoma, TN 37388.

Contributed by the Fluids Engineering Division and presented at the Fluids Engineering Conference, Toronto, Canada, June 4–7, 1990 of THE AMERICAN SOCIETY OF MECHANICAL ENGINEERS. Manuscript received by the Fluids Engineering Division March 9, 1989. Paper No. 90-FE-2.

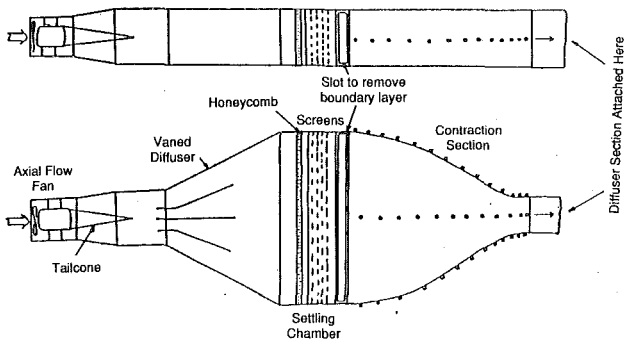

Fig. 2(a) Schematic of air channel facility (upstream portion)

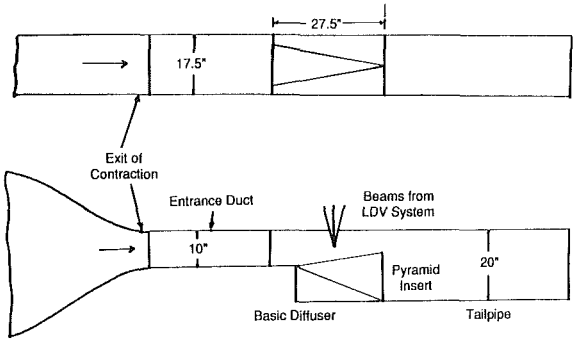

Fig. 2(b) Schematic of air channel facility (downstream portion)

rms velocity measurements made on the diffuser flowfield. The effect of variations in the pyramid geometry on the flow are also presented, and can serve as a guide to designers of similar devices.

The diffuser configurations tested demonstrated much better static-pressure recoveries than a plane-wall diffuser when discharging into a plenum. In addition, the absence of closed separated regions along the expansion wall of this diffuser eliminates low-frequency oscillations that are characteristic of such regions. These features make this design particularly suitable for exhaust diffuser applications, such as exhaust diffusers for turbomachinery. The understanding gained from this study is also useful in developing configurations with superior pressure recoveries.

2 Experimental Apparatus and Procedures

The measurements described in this paper were made in an air channel facility, a sketch of which is shown in Fig. 2. A 5 hp axial-flow fan forced air through a vaned diffuser into a 1221 mm-by-445 mm cross-section settling chamber containing a 30 mm-thick honeycomb and four 18-mesh aluminum screens. The air then entered a 4.8:1 contraction section made from 16-gage sheet metal before flowing into a 254 mm-by-445 mm cross-section entrance duct made from 18 mm-thick plywood. The test diffuser had an expansion half-angle of 20 deg, an area ratio of 2.0, and an aspect ratio of 1.75. The top wall of the diffuser was made from 12 mm-thick clear acrylic to allow optical access for LDV measurements. The diffuser section was followed by a tailpipe which exhausted to the atmosphere.

Several air channel configurations were used during the measurements. Tests on the diffusers were conducted with two different tailpipe lengths. The shorter tailpipe was two exit widths long, while the longer tailpipe was four and a half exit widths in length. An entrance duct of two different lengths was used between the contraction exit and the diffuser inlet during the tests. This was done to vary the boundary-layer thickness at the diffuser inlet, and thus vary the inlet blockage factor, B (defined as (1-2d/H), where d is the inlet boundary-layer displacement thickness, and H the inlet height of the duct).

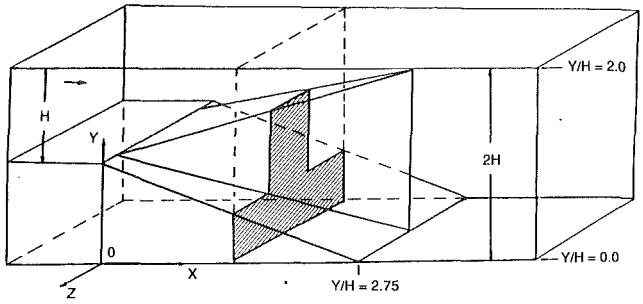

Fig. 3 Coordinate system used for presenting LDV measurements

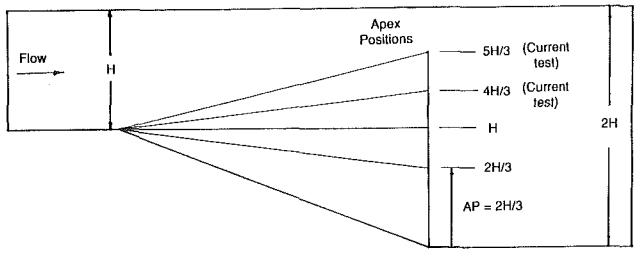

Fig. 4 Side view of diffuser showing the four different apex positions for the pyramid inserts

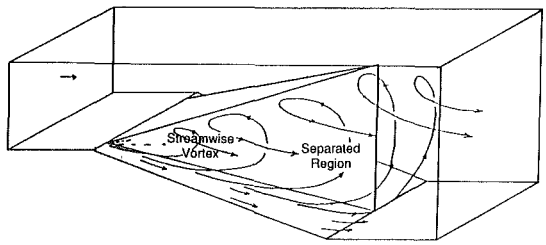

Fig. 5 Diffuser flow field characteristics

Tests were conducted at a nominal diffuser inlet speed of 20 m/s. This corresponds to a Reynolds number of 2.75×10^5 based on the diffuser inlet height.

Wall static-pressure measurements were made at several locations along the streamwise direction. Because the flowfield is three-dimensional, static-pressure measurements at a given cross-section were made at an average of five different locations. These measurements are presented as a pressure coefficient based on the static and dynamic pressures at the diffuser entrance; $Cp = (p - p_1)/q_1$. Uncertainty in these measurements is assessed to be ± 0.003.

Diffuser exit total-pressure surveys were made with a Keil probe. This information is presented as a loss coefficient based on the total and dynamic pressures at the diffuser inlet; $L_c = (p_{t1} - p_t)/q_1$.

Velocity measurements were made using a TSI 9100-10 LDV system. The radiation from a two-watt Argon-Ion laser was split up into five beams of two wavelengths so as to measure three velocity components simultaneously. Frequency shifting was used on all three components so that flow reversals could be detected. The angles between the beams were measured to determine the fringe spacing in the probe volume. This was accomplished by directing the beams onto a vertical surface, and measuring the change in distance between the beams on that surface when the LDV was moved forward a known distance.

A six-jet atomizer was used with sugar to produce the seed, which was introduced at the blower inlet. A check on the seed uniformity was made by measuring the data rate across the contraction exit. The data rate was found to be a constant, indicating a uniform seed density in the flow.

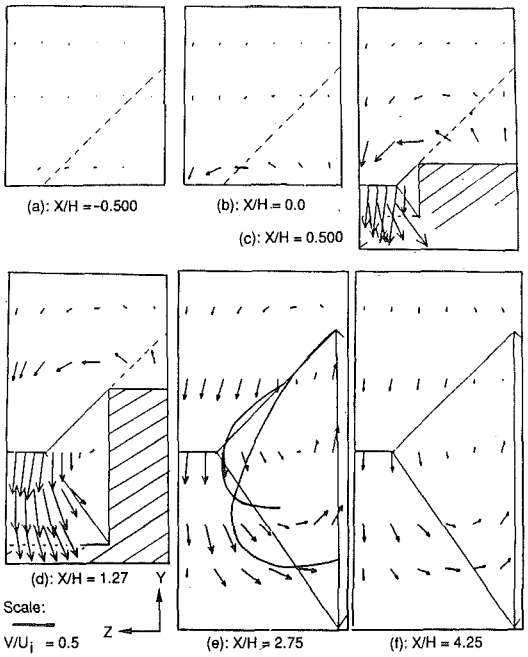

Fig. 6 Mean-velocity measurements in *y-z* planes. High-upsweep configuration. Coordinates and cross-sections are defined in Fig. 3. Dashed line is shadow of pyramid projected forward.

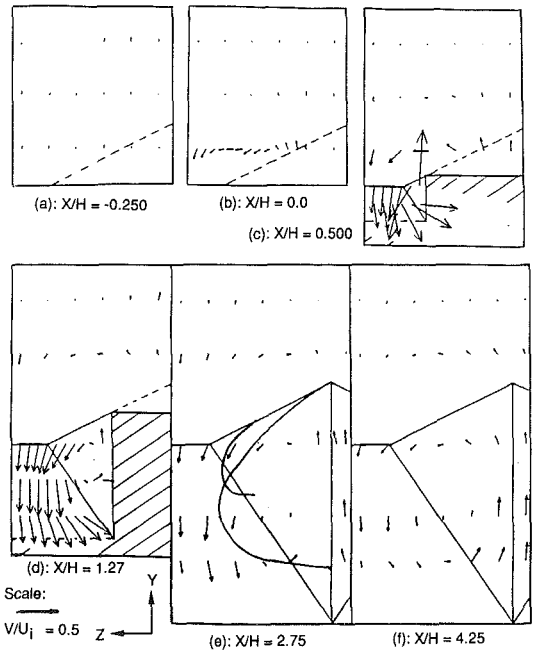

Fig. 7 Mean velocity measurements in *y-z* planes. Low-upsweep configuration.

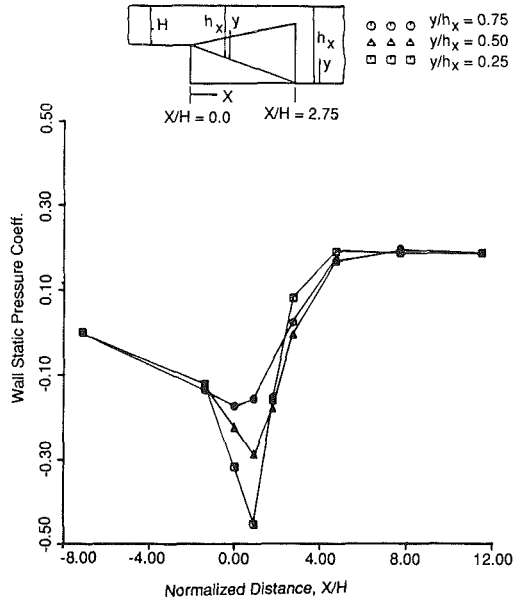

Fig. 8*(a)* Side wall pressure measurements for high-upsweep configuration

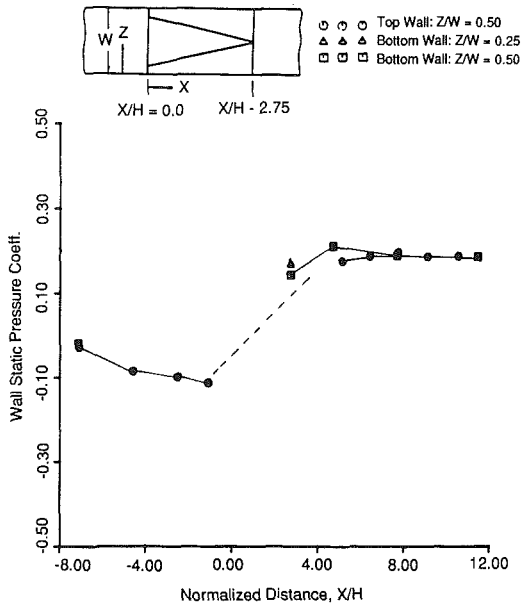

Fig. 8*(b)* Wall static pressure measurements for high-upsweep configuration—top and bottom walls

Between 400 and 600 data samples were used for each measurement and a typical measurement period was from 15 to 30 seconds. Velocity biasing corrections were made using Doppler residence time weighting as recommended by Edwards (1987).

LDV velocity measurements were taken at several cross-sections of the flowfield. The coordinate system used to define these cross-sectional planes is shown in Fig. 3. The origin of this coordinate system is located such that $X=0$ corresponds to the diffuser inlet, while $Y=0$ corresponds to the bottom wall of the tailpipe. Rms velocity fluctuations are represented by three mutually orthogonal vectors which represent the magnitude of u_{rms}, v_{rms}, and w_{rms}, respectively. Both mean and rms velocities are normalized with the mean velocity at the diffuser inlet.

The precision uncertainty in the mean velocity measurements is assessed to be ± 0.6 percent of the streamwise velocity at the diffuser inlet in regions of low turbulence, while it increases to ± 1.3 percent in regions of high turbulence. The uncertainty in the rms measurements is about 0.5 percent of the diffuser inlet velocity.

3 Characteristics of the Flowfield

Two pyramid configurations having different amounts of upsweep on their top faces were selected for detailed flowfield investigation. This choice provides two cases so that the physical flow effects of geometry can be assessed; neither is necessarily the optimum configuration. The low-upsweep configuration had an upper surface which swept up one third of the way to the top wall of the diffuser, while the high-

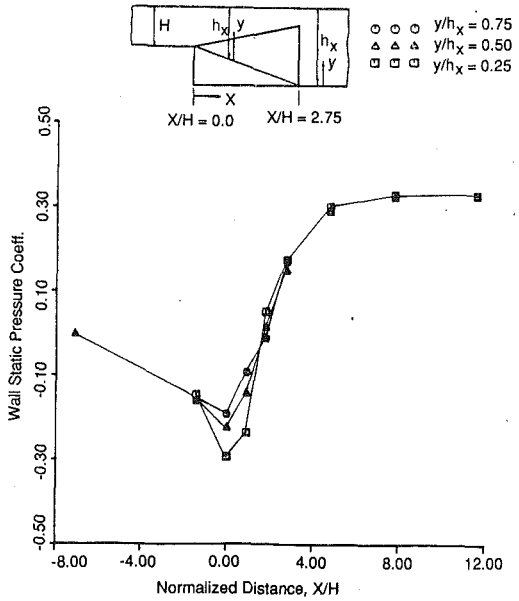

Fig. 9(*a*) Side wall pressure measurements for low-upsweep configuration

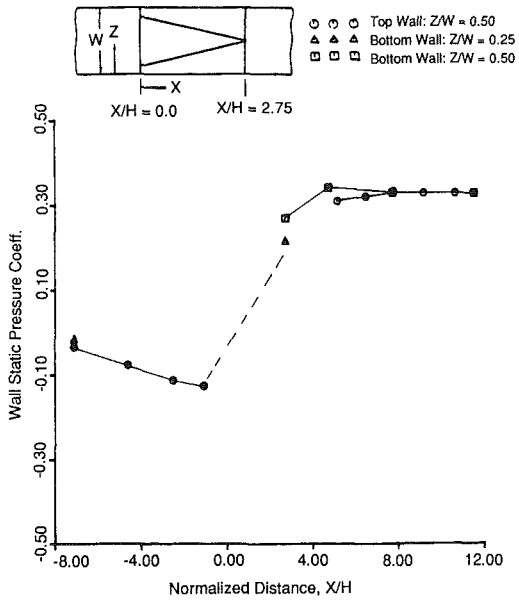

Fig. 9(*b*) Wall static pressure measurements for low-upsweep configuration—top and bottom walls

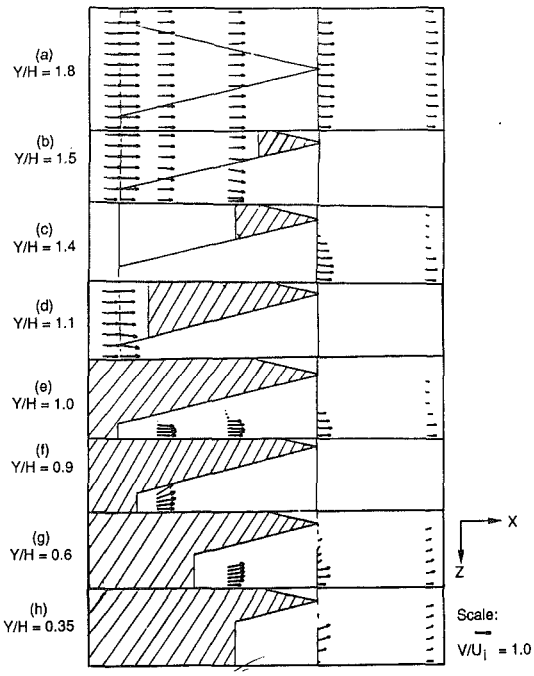

Fig. 10 Mean velocity measurements in *x-z* planes. High-upsweep configuration.

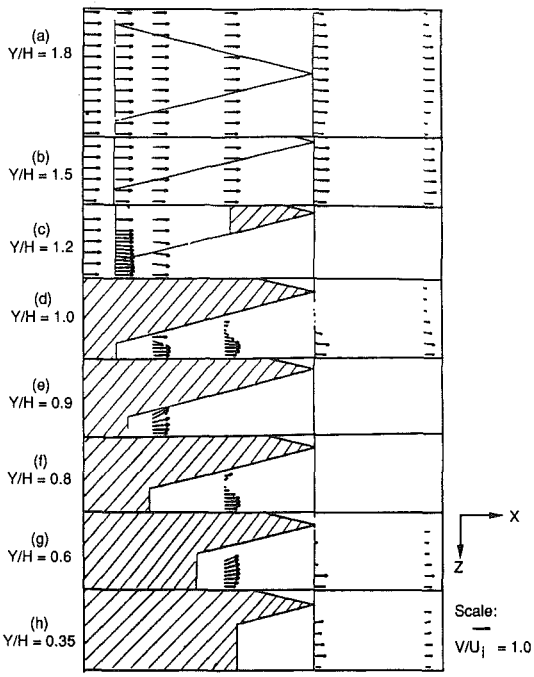

Fig. 11 Mean velocity measurements in *x-z* planes. Low-upsweep configuration.

upsweep configuration had an upper face which swept up two thirds of the way to the top wall. These configurations are shown in Fig. 4, and correspond, respectively, to the cases AP = 4H/3 and 5H/3 in the flow visualization studies in Goenka et al. (1989).

Various features of the diffuser flowfield were analyzed with the help of the pressure and velocity measurements. A schematic representation of the flowfield, shown in Fig. 5, is based on the previous flow-visualization studies and the present measurements. Important features include the streamwise vortex, its breakdown, and the presence of "open" separated regions in the flow. Comparisons between studies on the present diffuser and those conducted on the plane-wall diffuser are made when appropriate.

Streamwise Vortex. The amount of upsweep on the insert upper surface markedly affected the strength of the streamwise vortices. Without any upsweep, that is H or 2H/3 in Fig. 4, the pyramid is submerged in a separated flow. The upswept face projecting into the flow creates a transverse pressure gradient that imparts a lateral motion to the approaching flow and generates streamwise vorticity (see Fig. 6(*b*)). As the flow crosses the swept ledge it then dives down and the angular momentum is wrapped into the longitudinal vortex (Fig. 6(*c*),(*d*),(*e*),(*f*)). Comparing the velocity vectors in Figs. 6 and 7 shows evidence of much greater vortex strength for the high-upsweep case. In particular, the cross-flow velocities in the diffuser exit plane, shown in Figs. 6(*e*) and 7(*e*), were higher for the high-upsweep case. Higher swirl velocities at the tailpipe exit resulted in increased exit kinetic energy losses. Figures 8 and 9 are static-pressure measurements for the high- and low-upsweep cases. They show that the static-pressure

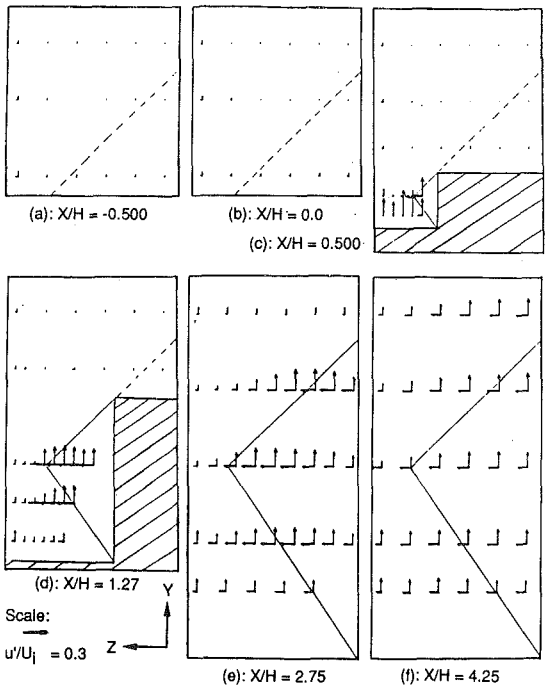

Fig. 12 Rms measurements in *y-z* planes. High-upsweep configuration.

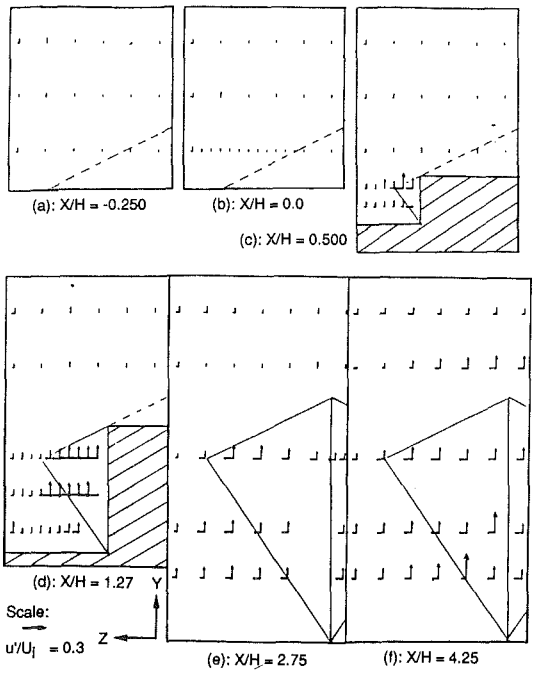

Fig. 14 Rms measurements in *y-z* planes. Low-upsweep configuration.

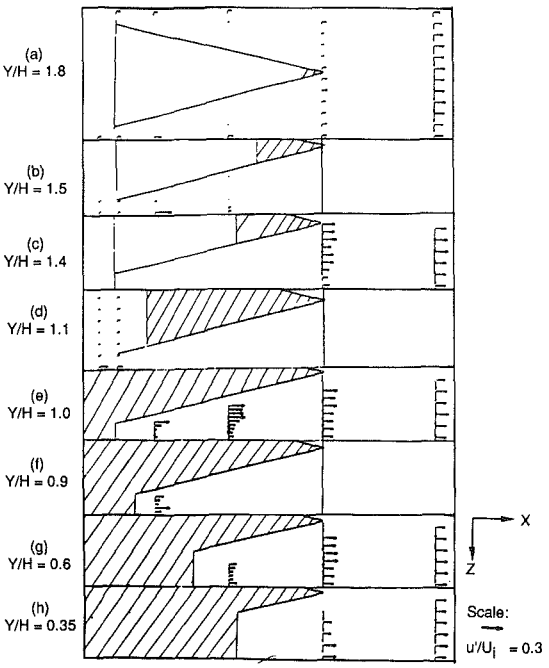

Fig. 13 Rms measurements in *x-z* planes. High-upsweep configuration.

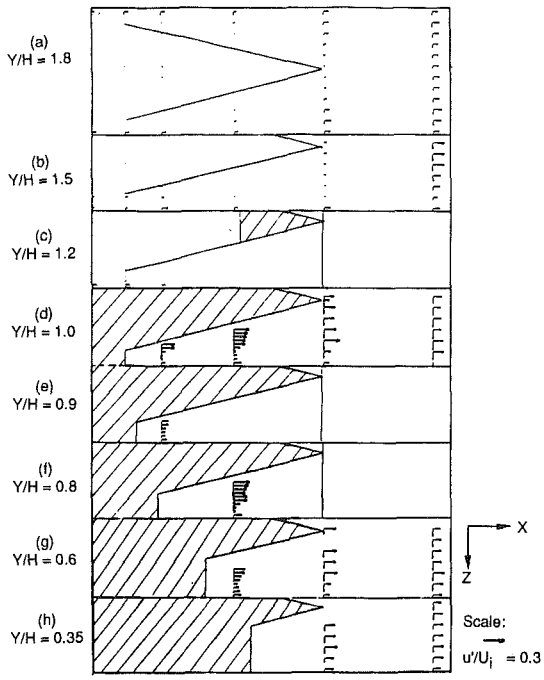

Fig. 15 Rms measurements in *x-z* planes. Low-upsweep configuration.

experienced a greater drop for the high-upsweep case; this is a direct result of higher velocity magnitudes due to a stronger vortex. These measurements will be analyzed further in the following sections.

Vortex Breakdown. Vortex breakdown was promoted by the adverse pressure gradient in the diffuser, and occurred close to the diffuser inlet. The velocity measurements in Figs. 6, 7, 10, and 11 indicate that the vortex breakdown occurred earlier for the high-upsweep case. Figures 10 and 11 show velocity measurements at different *X-Z* planes for the high and low-upsweep cases respectively. Figure 6(*c*) shows the cross-flow velocity measurements made on the vortex at $X/H=0.5$ for the high-upsweep case, while Fig. 10(*e*) shows that the corresponding axial velocity along the vortex axis was very low. This might suggest that the vortex had experienced a breakdown by $X/H=0.5$. Figure 7(*c*) shows transverse velocity measurements made on the vortex at $X/H=0.5$ for the low-upsweep case. The corresponding velocities in the *X-Z* plane are shown in Fig. 11(*d*) and (*e*). As can be seen in Fig. 11(*d*), velocity magnitudes along the vortex axis were still high, implying perhaps that the vortex had not as yet suffered a breakdown.

Rms velocity fluctuations in the flow are presented in Figs. 12 and 13 for the high-upsweep case and in Figs. 14 and 15 for the low-upsweep case. Although rms values were only about 10 percent higher following breakdown, accompanying lower local mean velocities increased the turbulence intensity significantly.

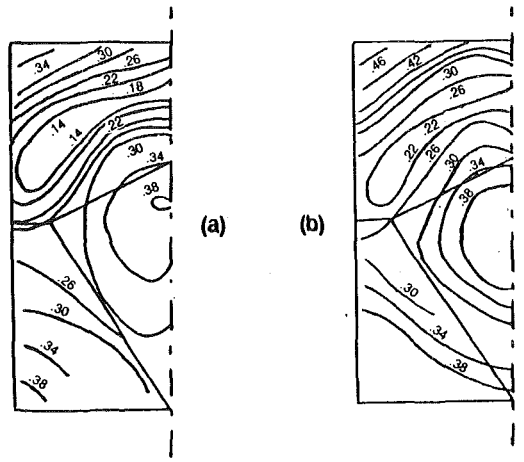

Fig. 16 Total pressure loss for low-upsweep case. *(a)* $B = 0.025$; *(b)* $B = 0.033$. Short tailpipe, exit plane.

Total-pressure losses in the flow were due primarily to vortex breakdown losses. This is evident from exit total-pressure surveys conducted on the low-upsweep configuration with the shorter tailpipe attached. These surveys are presented in Fig. 16 as contour plots for inlet blockage factors of 0.025 and 0.033, and show that the total-pressure losses were highest downstream of the breakdown location.

Open Separated Regions. The vortex and its subsequent breakdown gave rise to open separated regions in the flow and LDV measurements showed that the flow in these regions suffered streamwise velocity defects. This is evident from Fig. 10(*c*), (*e*), and (*g*) for the high-upsweep, and from Fig. 11(*d*) and (*g*), for the low-upsweep case.

The extent of the open separated regions for the high and low-upsweep cases is indicated in Figs. 6 and 7. The lines indicating the boundaries of these regions were based on locations where high streamwise velocity gradients occurred in the flow. The separated region was smaller in extent for the low-upsweep case and bulged out further towards the diffuser side walls as compared to the high-upsweep case. These separated regions, which extended into the tailpipe, reduced the effective diffusion area of the flow. The shear layers surrounding these regions generated frictional losses in the flow, and the contour plots in Fig. 16 show that the total-pressure loss in these regions was high. Interestingly, the lines showing the boundaries of these regions in Figs. 6 and 7, and the total-pressure contours in Fig. 16 show the same extent for these separated flow regions.

Turbulence. As is evident from Figs. 13 and 15, rms values of velocity were low in regions where the flow did not interact with the insert. This was true especially for the flow along the top wall of the diffuser.

Rms values were in general higher for the high-upsweep case. Typically, rms values for the flow in the tailpipe were 50 percent higher for the high-upsweep case than for the low-upsweep case. All three rms components had about the same magnitude at a given point in the flow, indicating that the turbulence was roughly isotropic.

Streamwise Velocity. The diffusion of the streamwise velocity component was curtailed by the presence of open separated regions. They reduced the effective flow area and created streamwise velocity defects at the diffuser exit plane. This can be seen in Figs. 10 and 11.

The streamwise flow uniformity in the tailpipe improved rapidly due to the swirl in the flow. Significant additional static-pressure recovery occurred in the tailpipe section due to an improvement in the uniformity of the velocity profile. This is

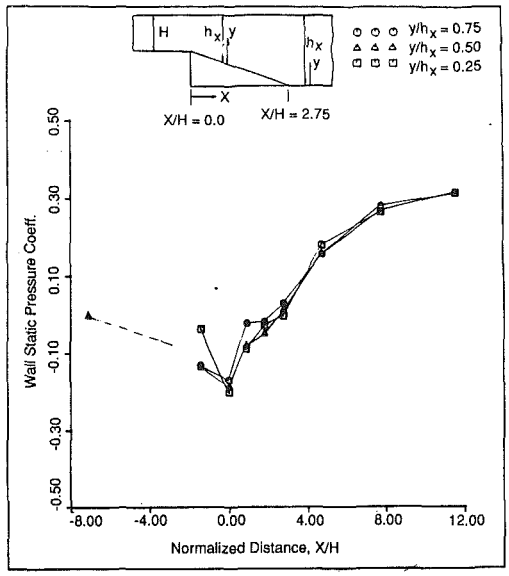

Fig. 17*(a)* Side wall pressure measurements for plane-wall diffuser

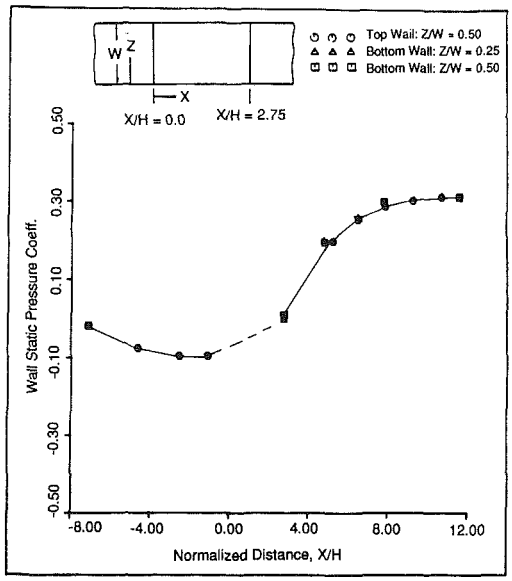

Fig. 17*(b)* Wall static pressure measurements for plane-wall diffuser—top and bottom walls

Table 1 Mass-averaged total-pressure loss—results from exit total-pressure surveys

Diffuser	P_t Loss of inlet blockage factor B: $B = 0.025$	$B = 0.033$	Change In P_t Loss
Plane-wall	.253	.326	+29%
Low-upsweep	.294	.341	+16%
High-upsweep	.391	.452	+16%

of course true for any diffuser connected to a tailpipe. The flow will eventually become uniform and recover some energy (in contrast to a plenum). When the flow becomes fully developed, there is no further increase in the static-pressure within the tailpipe. Figure 8 shows that the velocity profile was fully developed at four exit hydraulic diameters (7.5 inlet heights) for the high-upsweep case, while Fig. 9 shows that the velocity profile was fully developed at six exit hydraulic diameters (11.2 inlet heights) for the low-upsweep case. The greater swirl and high turbulence intensities in the high-upsweep case introduced a greater amount of mixing in the tailpipe, and this resulted

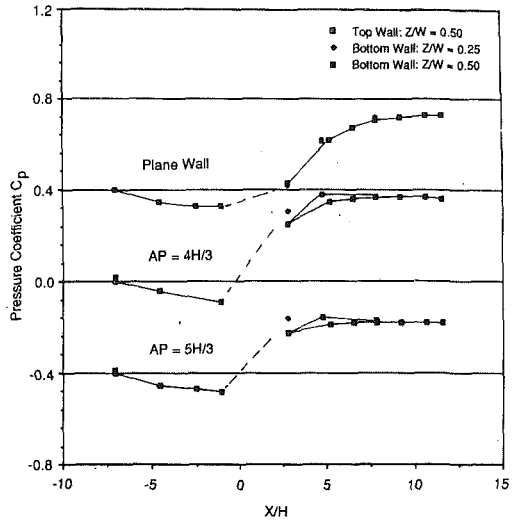

Fig. 18 Comparison of wall static pressure measurements for the plane-wall diffuser, the low-upsweep configuration, and the high-upsweep configuration

in the flow becoming fully developed earlier. Figure 17 shows static-pressure measurements for the plane-wall diffuser. These show that the flow was not fully developed even at the tailpipe exit. This is due to the smaller amount of mixing in the tailpipe for the plane-wall diffuser compared to the configurations with the insert.

Total-Pressure Recovery. Exit total-pressure surveys for the low-upsweep case with the short tailpipe are shown in Fig. 16. These measurements were conducted for two different values of the inlet blockage factor. As expected, the measurements indicate high losses in the separated regions, especially downstream of vortex breakdown. Also, losses in the corners were higher, since boundary layers were thicker in the corners due to the presence of the swirl in the diffuser. In principle, a thick inlet boundary layer would thicken the vortex core and reduce the total-pressure there. However, the value of the loss-coefficient in the flow downstream of breakdown is relatively insensitive to changes in the inlet boundary-layer thickness. This implies that the total-pressure loss experienced by the fluid in a stream filament within the vortex core after vortex breakdown was reduced due to a thickening of the diffuser-inlet boundary-layer. This suggests that the breakdown was less "intense," but was spread over a larger cross-sectional area, with a thicker boundary layer.

Exit total-pressure surveys for the high-upsweep case with the short tailpipe attached showed no specific trends. This was due to the higher turbulence intensities that are present in the flow for the high-upsweep case.

Exit total-pressure surveys on the plane-wall, the high-upsweep case, and the low-upsweep case, with the longer tailpipe attached, were conducted for the inlet blockage factor, B, equal to 0.025 and 0.033. The results are presented in Table 1, and show that the total-pressure loss increased by 29 percent for the plane-wall diffuser, but by only about 16 percent for the high- and low-upsweep cases, when the value of B increases from 0.025 to 0.033.

Static-Pressure Recovery. Static-pressure measurements along the diffuser top, bottom and side walls were presented in Figs. 8, 9, and 17 for the high-upsweep, low-upsweep and plane-wall cases, respectively. The top and bottom wall distributions are presented together in Fig. 18 for comparison. The presence of the vortex, as well as streamline curvature effects, made the static-pressure distribution highly three-dimensional within the diffuser expansion section. Additional

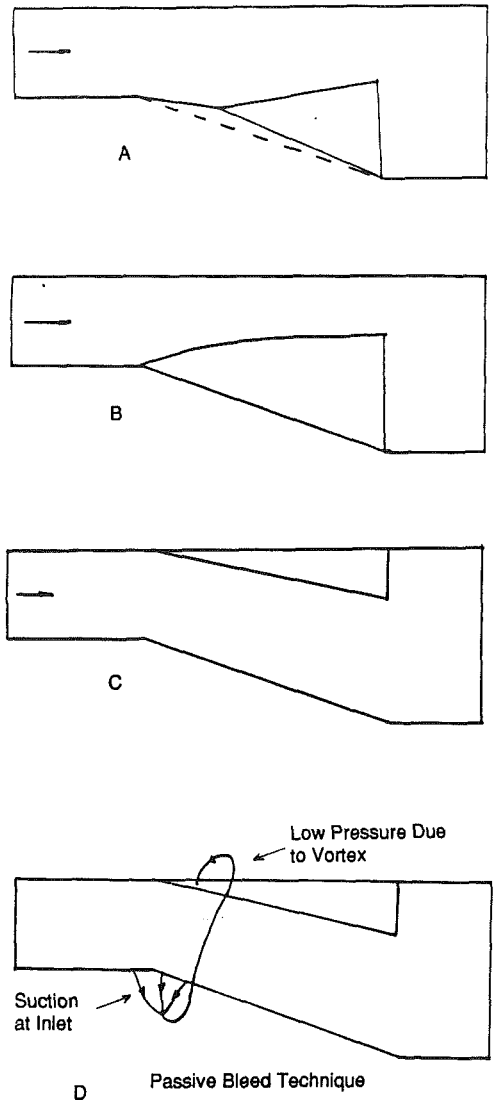

Fig. 19 Suggested geometric modifications to improve diffuser pressure recovery

static-pressure recovery occurred in the tailpipe due to an improvement in the uniformity of the streamwise flow and decay of the swirl. Pressure measurements along the upper wall are actually a better indication of the diffuser static-pressure recovery, since flow streamline curvature effects are smaller near the upper, flat wall. As can be seen from Fig. 18, a significant amount of the static-pressure recovery occurs within the diffuser expansion section for the low and high upsweep cases, whereas most of the pressure recovery of the plane-wall diffuser occurs in the tailpipe.

The diffuser static-pressure recovery was also measured while it was discharging into a plenum rather than a tail pipe. The pressure recovery was 0.11 for the plane-wall diffuser and 0.32 for the low-upsweep case, for an inlet blockage factor, B, of 0.033. No pressure recovery measurements were made for the high-upsweep case. Thus, in the absence of a tailpipe, the low upsweep configuration shows a significantly superior static-pressure recovery compared to a plane-wall diffuser. This means that a system dumping into a reservoir at a given pressure would have a higher flow with the diffuser insert. In addition, the three-dimensional diffuser exhibits superior flowfield characteristics. Low frequency effects in the flow are eliminated due to the absence of closed separated regions along the diffuser expansion wall, and the flow is free of hysteresis with respect to changes in Reynolds number. These features make

this design particularly suitable for exhaust diffuser applications, such as exhaust diffusers for power plant cooling water.

4 Conclusions

(*a*) The three-dimensional diffuser design has several features that make it desirable for exhaust diffuser applications. Its static-pressure recovery is much superior to that of a plane-wall diffuser when both are discharging into a plenum. The static-pressure recovery coefficients are 0.32 for the low-upsweep configuration as compared to 0.11 for the plane-wall diffuser. In addition, the pyramid diffuser exhibits superior flowfield characteristics. The absence of separated regions along the diffuser expansion wall implies that the flow is free of low-frequency oscillations that are characteristic of such regions. Further, the flow exhibits little or no hysteresis with respect to changes in Reynolds number.

(*b*) Too intense a vortex is detrimental to pressure recovery. Losses are higher primarily due to an increase in the vortex breakdown losses, as well as the ensuing turbulence and mixing. In addition, the swirl developed in the flow represents wasted exit kinetic energy. An optimum configuration would be one in which the vortex strength was just sufficient to eliminate separation along the diffuser expansion wall.

(*c*) Velocity measurements indicated that the strength of the streamwise vortex increased with the upsweep on the top face of the insert. By analogy with a delta wing, it may also be increased by increasing the inlet width of the top surface of the insert. Increasing the upsweep increased the extent of open separated regions in the flow, which further increased flowfield losses.

5 Recommendations

Speculations for alternate configurations can be based on the conclusions. Figure 19 shows some design modifications which might improve diffuser pressure recovery:

(i) Fig. 19(*a*): In this design, an initial diffusion could be achieved by having a gently sloping expansion wall. This is followed by an abrupt increase in the slope of the expansion wall. A pyramid insert located on this portion of the expansion wall may keep the flow attached. Pressure recovery might improve due to an increase in the diffusion area and a reduction in the extent of the open separated regions in the flow.

(ii) Fig. 19(*b*): The top face of the insert is curved, and has an initially high upsweep followed by a gradual decrease in slope of the top surface. The initial high upsweep may create the pressure rise necessary to generate the longitudinal vortices, while the subsequent reduction in the insert height would reduce the extent of the separated regions in the flow, thus enhancing diffuser pressure recovery.

(iii) Fig. 19(*c*): Pressure recovery could be enhanced by using an insert that is mounted on the upper, flat wall of the diffuser. The top face of the insert would help deflect the flow down along the diffuser expansion wall and keep the flow attached. It is hoped that the overall effect of this configuration would be to reduce the extent of the open separated regions in the flow while eliminating any closed separated regions.

(iv) Fig. 19(*d*): The low pressure created along the insert surface due to the presence of the vortex could be used to apply suction at the diffuser inlet. This passive-bleed technique could prove particularly effective with the insert mounted on the upper flat wall of the diffuser, since it could be used to keep the flow attached along the expansion wall by applying suction near the diffuser inlet.

References

Reneau, L. R., Johnston, J. P., and Kline, S. J., 1967, "Performance and Design of Straight, Two-Dimensional Diffusers," ASME *Journal of Basic Engineering*, Mar.

Goenka, L. N., Panton, R. L., and Bogard, D. G., 1989, "Studies of Flow Patterns in a Diffuser Designed to Generate Longitudinal Vortices," ASME JOURNAL OF FLUIDS ENGINEERING, Vol. 111, June.

Edwards, R. V., 1987, "Report of the Special Panel on Statistical Bias Problems in Laser Anemometry," ASME JOURNAL OF FLUIDS ENGINEERING, Vol. 109, pp. 89-93.

ERRATUM

"The Outflow of Buoyant Releases Including Fire Gases From a Long Corridor Closed at One End," JOURNAL OF FLUID ENGINEERING, Vol. 112, No. 1, 1990, pp. 28–32, Michael A. Delichatsios, Factory Mutual Research Corporation.

Equation (2) that appears on p. 29 is incorrect; it should read as follows:

$$m_0 = \frac{\rho_f u_f^2 BW}{\rho_\infty W} = \frac{\rho_f}{\rho_\infty} u_f^2 B.$$

Macroscopic Wetting Behavior and a Method for Measuring Contact Angles

K. Katoh
Research Associate.

H. Fujita
Professor.

Department of Mechanical Engineering,
Nagoya University,
Nagoya 464, Japan

H. Sasaki
Engineer,
Toshiba Corp.,
Fuchu 183, Japan

Macroscopic wetting behavior is investigated theoretically from a thermodynamic viewpoint. The axisymmetric liquid meniscus formed under a conical solid surface is chosen as the subject of the theoretical analysis. Using the meniscus configuration obtained by the Laplace equation, the total free energy of the system is calculated. In the case of the half vertical angle of the cone $\phi = 90$ deg (horizontal plate), the system shows thermodynamic instability when the meniscus attaches to the solid surface at the contact angle. This result, unlike the conventional view, agrees well with the practical wetting behavior observed in this study. On the other hand, when 0 deg $< \phi <$ 90 deg, the system shows thermodynamic stability at the contact angle. However, when the solid cone is held at a position higher than the critical height from a stationary liquid surface, the system becomes unstable. It is possible to measure the contact angle easily using this unstable phenomenon.

1 Introduction

A wetting phenomenon on a solid-liquid interface is frequently observed in daily life and is an important problem in industry. In the field of thermal engineering, the wetting characteristics between solid and liquid influences the performance of the apparatus dealing with boiling or condensing heat transfer (Mori et al., 1984; Liaw and Dhir, 1986), and since it is closely related to the dryout phenomenon observed on boiler tubes or on fuel rods of nuclear reactors, the safety of the apparatus is significantly dependent on it (Mori et al., 1984).

The solid-liquid contact angle is generally used as a significant property representing the wetting characteristics. Therefore, it is important to understand the mechanism of how the magnitude of the contact angle is determined. There are many reports concerning the practical wetting behavior. In particular, the contact angle hysteresis observed on the solid surface with infinitesimal roughness or impurities has attracted the interest of many researchers. Johnson and Dettre (1964), Neumann and Good (1972), and Eick et al. (1975) considered the hysteresis problem analytically for a liquid droplet or a meniscus on a solid surface. They calculated the system energy for the solid surface with infinitesimal roughness or impurities, and they explained the contact angle hysteresis by showing that there were some stable contact angles at which the system took a minimum energy. Recently, Joanny and de Gennes (1984) also tried to describe the hysteresis phenomenon by considering a force balance at the solid-liquid-gas contact line on the solid surface with impurities. Although the mechanism of the contact angle hysteresis has been clarified to some degree from the above microscopic considerations, there are many unsolved problems related to practical wetting behavior and the macroscopic consideration is needed to understand the apparent wetting phenomenon observed practically.

As is well known, the liquid wets a solid momentarily when the solid plate comes in contact with the liquid surface. Lifting the plate gradually, the liquid meniscus is formed under the solid surface. When the plate reaches a certain height, the meniscus detaches from the solid surface and falls spontaneously because the energy equilibrium of the system has broken down. This problem has close connection with that of flotation (Lucassen-Reynders and Lucassen, 1984). The detailed discussion regarding the thermodynamic stability of the problem, however, has not been carried out so far. It is difficult to explain these macroscopic unstable phenomena from a microscopic viewpoint as mentioned above.

The purpose of this study is to clarify macroscopic wetting phenomenon. In order to consider the macroscopic wetting behavior, an assumption was made for the well-known Young's equation in this study. For the axisymmetric liquid meniscus formed under the solid surface, the unstable wetting phenomenon mentioned above is investigated theoretically by

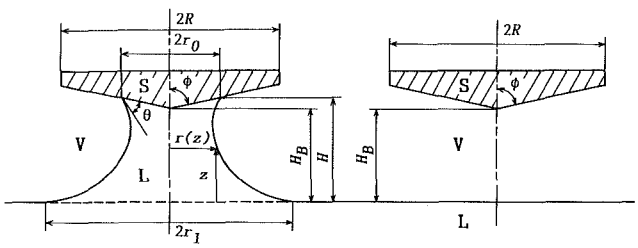

Fig. 1 Coordinate system

Contributed by the Fluids Engineering Division and presented at the Fluids Engineering Conference, Toronto, Canada, June 4–7, 1990 of THE AMERICAN SOCIETY OF MECHANICAL ENGINEERS. Manuscript received by the Fluids Engineering Division April 4, 1989. Paper No. 90-FE-3.

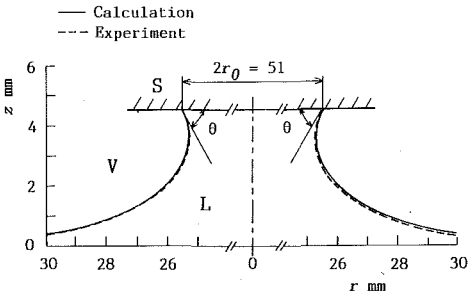

Fig. 2 Axisymmetric meniscus profile

considering the macroscopic energy change of the system. Based on the theoretical results for the condition that the liquid meniscus detaches and falls spontaneously, a novel method for measuring the contact angle is proposed.

2 Profile of Axisymmetric Meniscus

In this paper, the energy change with the solid-liquid-gas contact line moving on the solid surface is considered for the axisymmetric meniscus under a cone surface as shown in Fig. 1(*a*). The axisymmetric meniscus is chosen as the present subject because it is considered that the meniscus detaches from the solid surface axisymmetrically, although the analysis of an axisymmetric meniscus profile is more complicated than that of a two-dimensional one.

The system considered in the present study is shown in Fig. 1. The symbols S, L, V in the figure indicate the solid, liquid, and gas phases, respectively. First, the meniscus profile will be obtained because it is necessary to calculate the system energy shown in Fig. 1(*a*). The force balance on the meniscus surface is described, as is well known, by the Laplace equation

$$\Delta P = \sigma_{LV}\left(\frac{1}{R_1} + \frac{1}{R_2}\right) \tag{1}$$

where ΔP is the pressure difference between the gas and liquid phases, σ_{LV} is the surface tension of the liquid-gas interface, and R_1 and R_2 are the principal radii of curvature of the meniscus surface. As shown in Fig. 1(*a*), r and z indicate the radial distance from the cone vertex and the vertical height from the still liquid surface, respectively. If the meniscus profile is described by $r(z)$, R_1 and R_2 are obtained by differential calculation. Then, the Laplace equation (1) may be rewritten as follows, using the relation $\Delta P = \Delta\rho g z$, where $\Delta\rho$ is the density difference between the liquid and gas and g is the gravitational acceleration:

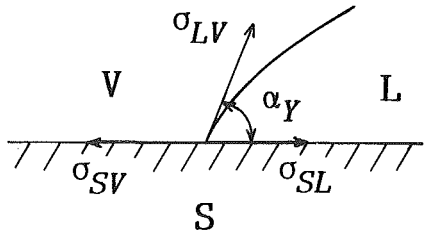

Fig. 3 Force balance at solid-liquid-gas interface

$$r\frac{d^2r}{dz^2} - \left(\frac{dr}{dz}\right)^2 - 1 - \frac{1}{\sigma_{LV}}\Delta\rho g r z\left\{1+\left(\frac{dr}{dz}\right)^2\right\}^{3/2} = 0 \tag{2}$$

Non-dimensionalizing equation (2) by the capillary constant

$$a = \sqrt{\sigma_{LV}/\Delta\rho g},$$

a parameter-free equation is obtained as

$$\bar{r}\frac{d^2\bar{r}}{d\bar{z}^2} - \left(\frac{d\bar{r}}{d\bar{z}}\right)^2 - 1 - \bar{r}\bar{z}\left\{1+\left(\frac{d\bar{r}}{d\bar{z}}\right)^2\right\}^{3/2} = 0 \tag{3}$$

where $\bar{r} = r/a$ and $\bar{z} = z/a$. The boundary conditions are

$$\bar{z} = 0: \quad \frac{d\bar{r}}{d\bar{z}} = -\infty \tag{4}$$

$$\bar{z} = \bar{H}: \quad \bar{r} = \bar{r}_0 \tag{5}$$

where $\bar{H} = H/a$ and $\bar{r}_0 = r_0/a$. H is the meniscus height and r_0 is the meniscus radius at $z = H$. The solution of axi-symmetric meniscus profile was obtained previously by other investigators (Huh and Scriven, 1969; Rapacchietta and Neumann, 1977). In this paper, the solution of equations (3), (4), and (5) is obtained numerically by using the Adams and shooting method. The calculated results agree well with the photographed meniscus profiles, as shown in Fig. 2.

3 System Energy

3.1 Consideration of Young's Equation. When the liquid wets the solid surface as shown in Fig. 3, the well-known Young's equation holds for the horizontal force balance at the contact line (de Gennes, 1985).

$$\sigma_{SV} - \sigma_{SL} = \sigma_{LV}\cos\alpha_Y \tag{6}$$

where σ_{SV} and σ_{SL} are the solid surface tension and the solid-liquid interfacial tension, respectively. α_Y in equation (6) is the

Nomenclature

a = capillary constant ($=\sqrt{\sigma_{LV}/\Delta\rho g}$)
ΔP = pressure difference between liquid and gas phases
E = free energy of system
E_{SV-SL} = free energy change by conversion of solid-gas interface into solid-liquid one
E_{LV} = free energy change by liquid surface increase
E_p = potential energy of meniscus
g = gravitational acceleration
H = height from stationary liquid surface
H_B = height of cone vertex from stationary liquid surface
R = radius of cylinder
R_1 and R_2 = principal radii of meniscus surface
$r(z)$ = radius of meniscus at z
r_0 = radius of meniscus at solid surface
r_1 = radius of meniscus at stationary liquid surface
z = vertical distance from stationary liquid surface
α_Y = Young's contact angle
θ = angle at which meniscus curve contacts with solid surface
θ_Y = apparent contact angle
θ_{YA} = advancing contact angle
θ_{YR} = receding contact angle
$\Delta\rho$ = density difference between liquid and gas
σ_{LV} = liquid-gas surface tension
σ_{SL} = solid-liquid interfacial tension
σ_{SV} = solid-gas surface tension
ϕ = half vertical angle of cone surface
$-$ = nondimensional quantity

so-called Young's contact angle. Each surface tension in equation (6) may be regarded as the surface free energy per unit area. Hence, the energy difference $(\sigma_{SV}-\sigma_{SL})$ generated when the liquid wets the solid surface by unit area can be calculated by using σ_{LV} and α_Y instead of σ_{SV} and σ_{SL}, which involve great difficulties in measurement.

It is generally considered that α_Y in equation (6) is uniquely determined only when the solid surface is ideally smooth and homogeneous. In general, the advancing contact angle observed while the liquid is wetting the solid is different from the receding contact angle while the solid is drying. These macroscopic contact angles differ from the Young's one and are considered to be the macroscopic apparent angles observed when roughness or nonhomogeneous parts exist on the solid surface. However, the details are not clear. Since the rough and nonhomogeneous surface can be regarded to be an aggregation of infinitesimal smooth and homogeneous parts, it is generally considered that the contact angle observed microscopically is equal to the Young's one. Based on these facts, Johnson and Dettre (1964); Neumann and Good (1972); and Eick et al. (1975), as stated in Section 1, calculated the system energy change while the solid-liquid-gas contact line moves along the solid surface with infinitesimal roughness or nonhomogeneous parts such as impurities. They attempted to explain the contact angle hysteresis by showing that there were some quasi-stable contact angles at which the system had a minimum energy.

Since the purpose of this study is to investigate the apparent macroscopic wetting behavior, we do not treat the effect of the microscopic structure of the solid surface such as infinitesimal roughness or nonhomogeneous parts. We assume that equation (6) also can be applied to the apparent macroscopic case. Thus, we assume that if $(\sigma_{SV}-\sigma_{SL})$ on the left-hand side of equation (6) is regarded as the necessary work to convert the macroscopic apparent solid-liquid interface into solid-gas interface by unit area, the work may be calculated by using the apparent contact angle observed macroscopically such as the advancing or receding contact angle instead of α_Y on the right-hand side of equation (6). This hypothesis says that the surface energy change is different, whether the liquid advances or recedes on the solid surface by unit area. This may be caused by the residual liquid effects on the rough surface and so on. The well-known Cassie's and Wenzel's contact angles may be considered as examples of equation (6) application to the macroscopic apparent system (Chappius, 1982). Since the contact angles found in the following discussion indicate the apparent ones, the symbol θ_Y will be used to discriminate from Young's contact angle α_Y and equation (6) is rewritten as

$$\sigma_{SV}-\sigma_{SL}=\sigma_{LV}\cos\theta_Y \tag{7}$$

3.2 Calculation of System Energy. The system energy E of Fig. 1 (a) is calculated based on the reference state shown in Fig. 1 (b), which consists of a staionary liquid surface and a dry solid. The components are (i) the energy increase E_{SV-SL} by the conversion of a solid-gas interface into a solid-liquid one, (ii) the surface energy gain E_{LV} by increase of the liquid surface, and (iii) the potential energy of the meniscus E_p. Each energy can be calculated as follows:

(i) Based on the hypothesis stated in Section 3.1, E_{SV-SL} can be obtained by

$$\bar{E}_{SV-SL}=-\frac{\pi\bar{r}_0^2}{\sin\phi}\cos\theta_Y, \tag{8}$$

where ϕ is the half vertical angle of the cone. Equation (8) is nondimensionalized by the parameter $\sigma_{LV}^2/\Delta\rho g$. In the following discussion, the energies are nondimensionalized in the same manner as equation (8).

(ii) The energy change $\bar{E}_{LV}$ by the liquid surface increase can be calculated using the meniscus profile $\bar{r}(\bar{z})$ obtained in Section 2.

$$\bar{E}_{LV}=2\pi\int_0^{\bar{H}}\bar{r}\left\{1+\left(\frac{d\bar{r}}{d\bar{z}}\right)^2\right\}^{1/2}d\bar{z}-\pi\bar{r}_1^2 \tag{9}$$

(iii) The potential energy of the meniscus $\bar{E}_P$ can be obtained by the following expression.

$$\bar{E}_P=\int_0^{\bar{H}}\pi\bar{r}^2\bar{z}d\bar{z}-\int_{\bar{H}_B}^{\bar{H}}\pi(\bar{z}-\bar{H}_B)^2\tan^2\phi\cdot\bar{z}d\bar{z} \tag{10}$$

where $\bar{r}_1=r_1/a$ and $\bar{H}_B=H_B/a$ are the nondimensional values of the meniscus radius at the stationary liquid surface and the cone vertex height, respectively.

The total energy increase $\bar{E}$ by the meniscus formation can be obtained by the sum of equations (8), (9) and (10).

$$\bar{E}=\bar{E}_{SV-SL}+\bar{E}_{LV}+\bar{E}_p \tag{11}$$

The integrations in equations (9) and (10) were numerically calculated.

4 Calculated Results and Discussion

The calculated results of the energy $\bar{E}$ are shown in Figs. 4, 5, 6, 7, and 9. The abscissa θ in each figure indicates the angle between the meniscus curve obtained by the Laplace equation and the solid surface at the contact point of the meniscus with the solid. The angle θ is different from θ_Y determined by equation (7) and is independent of it. In Figs. 4, 5, and 6, the calculated results for the contact angles $\theta_Y=40$ deg and $\theta_Y=60$ deg are shown. The curves in Figs. 5, 6, 7, and 9 are obtained in the region in which the meniscus profile satisfies the Laplace equation (3). In the following, we will discuss the wetting behavior of the liquid meniscus on the vertical cylindrical, on the horizontal plate, and on the cone in that order.

4.1 Vertical Cylinder ($\phi=0$ deg). Figure 4 shows the results of $\phi=0$ deg for which the meniscus is attached to a vertical cylinder. $\bar{R}$ is the nondimensional cylinder radius and $\bar{R}=14.7$ corresponds to the cylinder of $R=40$ mm for water at 25°C. The abscissa $\bar{H}$ of Fig. 4 (a) indicates the meniscus height at which the liquid contacts the cylinder. A one-to-one correspondence is found between $\bar{H}$ and θ in Fig. 4 (b). It is noted that the system energy $\bar{E}$ in Fig. 4(b) takes a minimum at $\theta=40$ deg for $\theta_Y=40$ deg and $\theta=60$ deg for $\theta_Y=60$ deg. Therefore, it can be said that the system becomes stable when the meniscus is in contact with the solid surface at a contact angle. These results coincide with the settled view (Johnson and Dettre, 1964).

Assuming that the receding contact angle is $\theta_{YR}=40$ deg and the advancing contact angle $\theta_{YA}=60$ deg, we consider the wetting behavior of the meniscus with a vertical motion of the cylinder referring to Fig. 4.

First, when the cylinder is rising vertically, the system energy varies along the $\theta_Y=40$ deg line in Fig. 4 because the solid surface is being dried and the liquid is receding. Since the system energy takes the minimum at point A of $\theta_{YR}=40$ deg, the meniscus in contact with the cylinder at θ_{YR} is formed.

Next, we consider the case in which the cylinder penetrates the liquid after the liquid meniscus of $\theta=40$ deg has been formed. Then the energy change should be described by the line of $\theta_Y=60$ deg instead of that of $\theta_Y=40$ deg for the rising of the cylinder. The system state changes from the point A to B on the $\theta_Y=60$ deg line. Since the $\theta_Y=60$ deg line takes its minimum at a smaller $\bar{H}$ than for the $\theta_Y=40$ deg line, the system approaches the stable state as the meniscus height $\bar{H}$ decreases by the penetration of the cylinder. Therefore, the meniscus height decreases with the cylinder penetration and the contact line of meniscus with the solid surface does not move relative to the cylinder surface. As shown in Fig. 4 (a) and (b), when the system state changes from point B to C, θ increases as $\bar{H}$ decreases and the system becomes stable at a

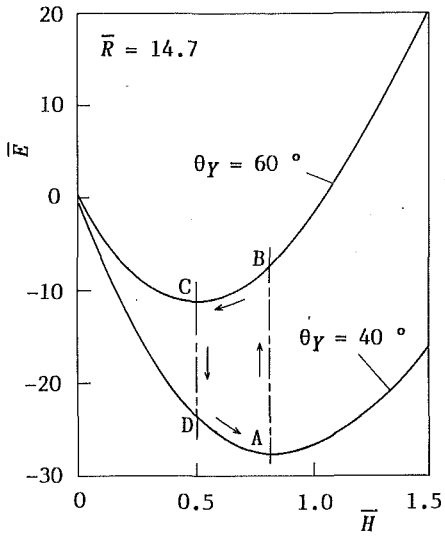

Fig. 4(*a*) Energy change with $\bar{H}$

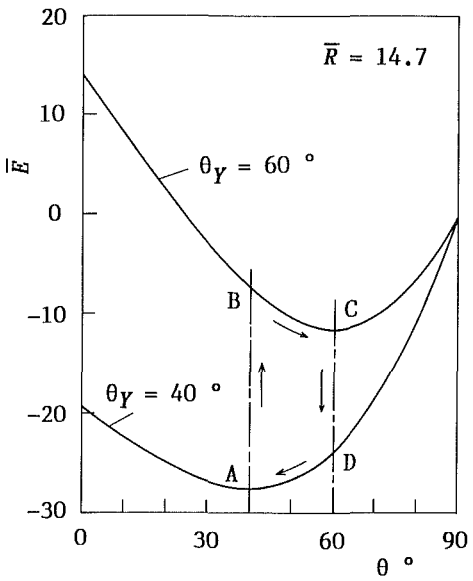

Fig. 4(*b*) Energy change with θ

Fig. 4 Energy of meniscus attaching to vertical cylinder

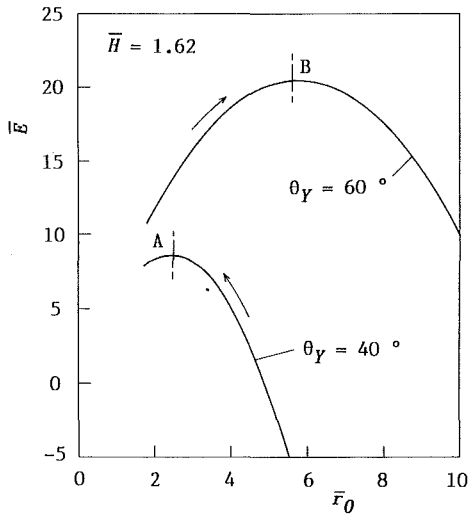

Fig. 5(*a*) Energy change with $\bar{r}_0$

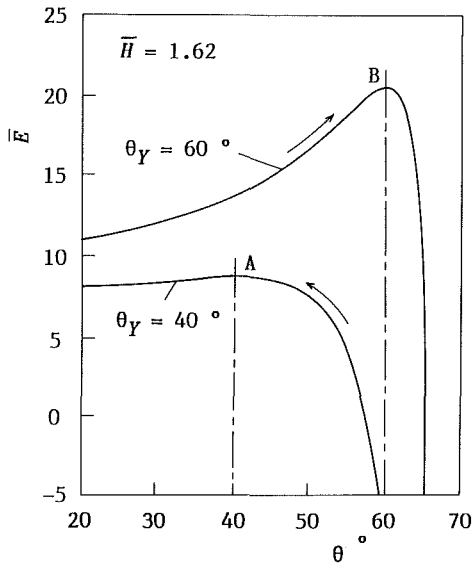

Fig. 5(*b*) Energy change with θ

Fig. 5 Energy of meniscus formed under horizontal plate

point C of $\theta = 60$ deg. After the system reaches C, the meniscus height $\bar{H}$ does not change, maintaining the stable condition C. Hence, as soon as the system reaches $\theta = 60$ deg, the liquid starts to advance on the solid surface. In the above discussion, when the cylinder penetrates the liquid just after rising, it is impossible for the meniscus to decrease the height $\bar{H}$ and to move to the stable point C momentarily, because the liquid must recede on the solid if the meniscus height descends faster than the cylinder. Also, when the cylinder is rising after its penetration, the system energy changes through the path C to A through D in the same manner as mentioned above. These considerations describe well the wetting behavior observed practically.

In the above discussion, the energy changes discontinuously from the value at A on the line of $\theta_Y = 40$ deg to that at B on the line of $\theta_Y = 60$ deg when the cylinder penetrates the liquid just after rising. This is due to the fact that the energy needed to change the solid-gas interface into the solid-liquid one for each curve in Fig. 4 is calculated using each contact angle for the sake of convenience. When we consider the case in which the cylinder penetrates the liquid after the cylinder is forced to rise, correctly speaking, the energy of the solid-liquid interface at the beginning of the cylinder penetration should be calculated using the receding contact angle $\theta_Y = 40$ deg. In that case, the curve $\theta_Y = 60$ deg for the cylinder penetration shifts vertically and point B coincides with point A. However, the wetting behavior discussed above is not changed at all. In this paper, only the behavior of energy $\bar{E}$ on the curve is significant and the vertical shift of the curve is not so important.

4.2 Horizontal Plate ($\phi = 90$ deg). The results for the meniscus formed under a horizontal plate $\phi = 90$ deg are shown in Fig. 5. The abscissa $\bar{r}_0$ in Fig. 5(*a*) indicates the radius at which the meniscus is attached to the plate. As shown in Fig. 5(*b*), the energy $\bar{E}$ of two curves takes a maximum at each contact angle, contrary to the case of the vertical cylinder in Fig. 4(*b*). This interesting result is different from the popular view. It seems that since there is no energy minimum in Fig. 5, the meniscus under the horizontal plate is unstable and detaches from the plate spontaneously. A stable meniscus, however, can be formed practically. In the following, we will discuss this problem assuming $\theta_{YA} = 60$ deg and $\theta_{YR} = 40$ deg in the same manner as for the vertical cylinder.

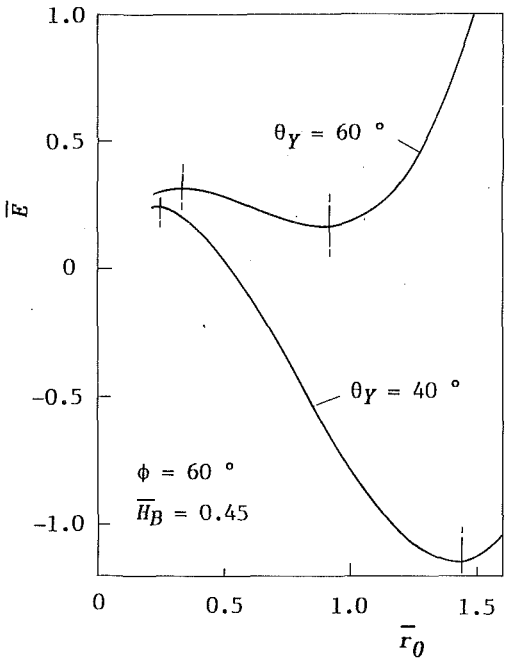

Fig. 6(*a*) Energy change with $\bar{r}_0$

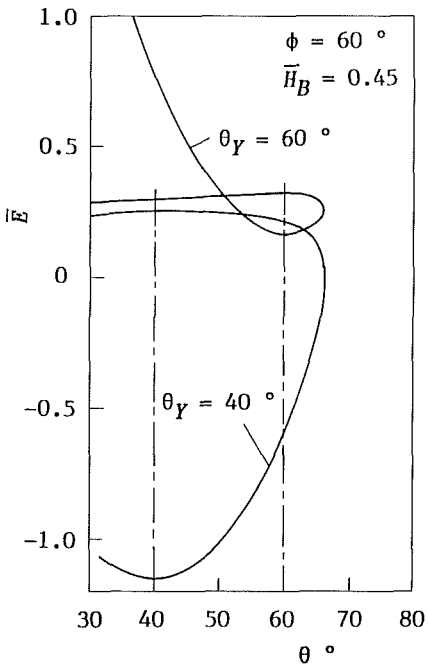

Fig. 6(*b*) Energy change with θ

Fig. 6 Energy of meniscus formed under downward cone

When the contact angle hysteresis is observed, the system is considered stable between the maxima A and B in Fig. 5(*b*). Thus, the meniscus is stable when the angle θ at which the meniscus curve attaches to the solid surface is between the advancing conatct angle θ_{YA} and the receding one θ_{YR}. This is explained as follows: When the meniscus is wetting the solid surface and the radius $\bar{r}_0$ is increasing, the behavior of $\bar{E}$ is described by the θ_{YA} curve. Since the slope of the curve is positive between the maxima A and B, the meniscus does not advance spontaneously and is stable. On the other hand, when $\bar{r}_0$ is decreasing, $\bar{E}$ varies on the θ_{YR} curve. Since the energy $\bar{E}$ also increases as $\bar{r}_0$ decreases, the system is stable when receding. Outside of the region between the maxima A and B, however, the system becomes unstable since the energy decreases in the direction of meniscus advance or retreat.

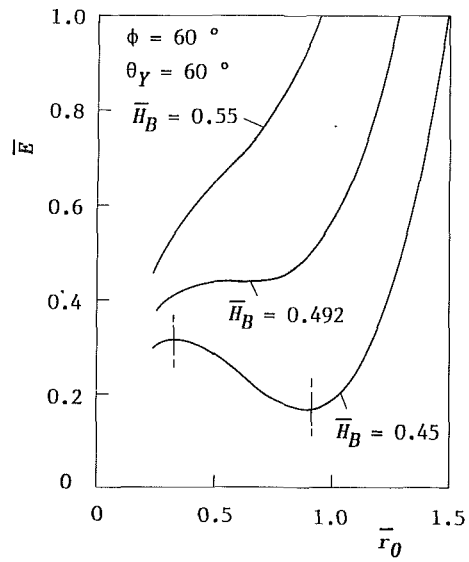

Fig. 7(*a*) Energy change with $\bar{r}_0$

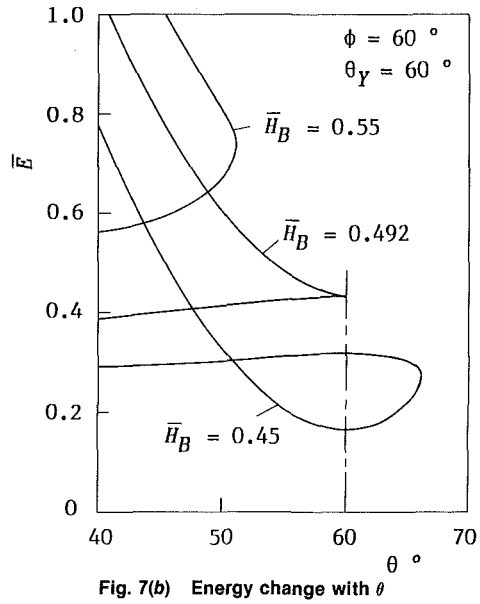

Fig. 7(*b*) Energy change with θ

Fig. 7 System energy for various $\bar{H}_B$ (downward cone)

From the calculated results of Laplace's equation, θ decreases with the increase of the plate height $\bar{H}$. In accordance with the above discussion, when the plate is going up and θ is decreasing, the system becomes unstable at the receding contact angle θ_{YR}. On the other hand, when the plate is going down and θ is increasing, the system becomes unstable at the advancing contact angle θ_{YA}. Therefore, we can conclude that the contact angle θ_Y indicates the boundary between the stable and the unstable condition for the meniscus formed under the horizontal plate. The system is stable between θ_{YA} and θ_{YR}. There is no stable region when θ_Y is uniquely determined; namely, when the contact angle hysteresis is not observed. The above description agrees well with the system behavior observed in this study. The hypothesis stated in Section 3.1 is verified by the above results.

4.3 Downward Cone (0 deg < ϕ < 90 deg). Now we discuss the meniscus under a downward cone shown in Fig. 1. Figure 6 shows the calculated results of $\bar{E}$. In Fig. 6(*b*), it is remarked that $\bar{E}$ takes both the minimum and the maximum at $\theta = 40$ deg for $\theta_Y = 40$ deg and $\theta = 60$ deg for $\theta_Y = 60$ deg. It is considered

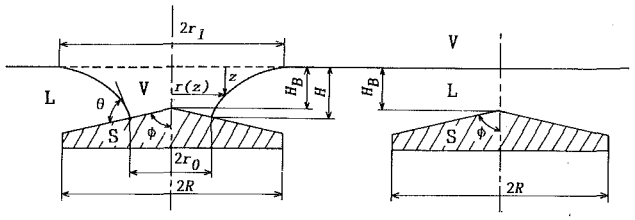

Fig. 8 Coordinate system for upward cone

that the meniscus formed under a downward cone has intermediate characteristics between the vertical cylinder and the horizontal plate.

The change of $\bar{E}$ with respect to $\bar{r}_0$ and θ for various $\bar{H}_B$'s, the height of cone vertex from the stationary liquid surface, is shown in Fig. 7. The figure shows an example of a cone half vertical angle $\phi = 60$ deg with the contact angle $\theta_Y = 60$ deg. There is a minimum energy and the meniscus is stable at $\bar{H}_B = 0.45$. However, as $\bar{H}_B$ increases, there is no minimum for $\bar{H}_B$ higher than $\bar{H}_B = 0.492$. As shown in Fig. 7(*a*), since the system energy $\bar{E}$ decreases monotonically as $\bar{r}_0$ decreases for $\bar{H}_B \geqq 0.492$, the meniscus recedes spontaneously and detaches from the cone surfacce. Therefore, $\bar{H}_B = 0.492$ for $\theta_Y = 60$ deg in Fig. 7 indicates the critical height at which the energy equilibrium is destroyed. The occurrence of instability depends on phenomena relating to the receding contact angle, because the direction of energy decrease corresponds to the receding of the liquid.

Similar results are obtained for the meniscus on the upward cone as shown in Fig. 8(*a*). The coordinate system is the same as Fig. 1 for the downward cone except that the z axis is oriented downward from the stationary liquid surface. As shown in Fig. 8(*b*), the system energy when the solid surface is submerged in the liquid is chosen as a reference. The energy $\bar{E}$ for a meniscus formed on the upward cone is also calculated in the same manner as stated in Section 3 except for the sign of the energy increase $\bar{E}_{SV-SL}$. For the upward cone, $\bar{E}_{SV-SL}$ can be written as

$$\bar{E}_{SV-SL} = \frac{\pi \bar{r}_0^2}{\sin \phi} \cos \theta_Y \tag{12}$$

Figure 9 shows the results for $\phi = 75$ deg and $\theta_Y = 90$ deg. For the immersion of the cone into the liquid, when the cone vertex moves downward from the stationary liquid surface by $\bar{H}_B = 0.590$, the system becomes unstable and the liquid wets the solid surface spontaneously. This phenomenon depends on the advancing contact angle.

As shown in Fig. 7 and Fig. 9, a one-to-one correspondence is found between the $\bar{H}_B$ at which instability occurs and the contact angle θ_Y. It is possible to apply this principle to the measurement of contact angles. Thus, the advancing and receding contact angles may be obtained by simple measurement of $\bar{H}_B$ instead of the direct measurement of contact angles. Good reproducibility is also expected because the occurrence of unstable phenomena is used for the measurement.

The above results for the wetting behavior in this section agree well with those observed in our laboratory. It is expected that the same results as above may be obtained by the microscopic viewpoint, such as Eick et al. (1975); Johnson and Dettre (1964); and Neumann and Good (1972); namely, in the case of the downward cone, for example, there may be many meta-stable points on the cone surface when the cone is lower than the critical height. When the cone is higher than the critical height, there may not exist the meta-stable points and hence the liquid may fall down spontaneously. However, the analysis may be much more complicated than that of this paper. The method used in this paper can explain easily the wetting behavior observed macroscopically because the complicated effect of the microscopic structure of the solid surface

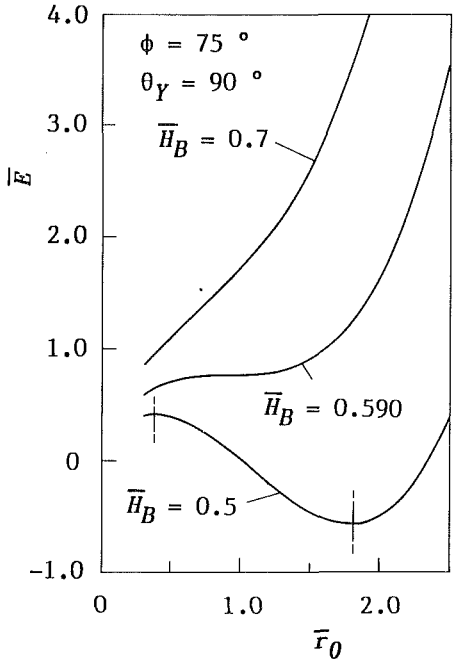

Fig. 9(*a*) Energy change with $\bar{r}_0$

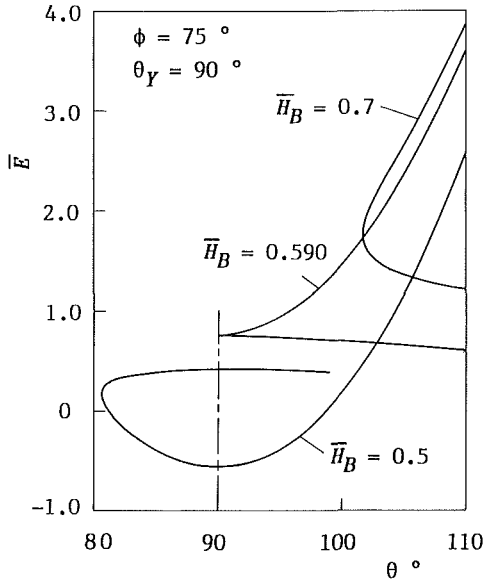

Fig. 9(*b*) Energy change with θ

Fig. 9 System energy for various $\bar{H}_B$ (upward cone)

such as the roughness or impurities on the wetting behavior can be included entirely in the value of the contact angles, and the energy difference between the solid-gas and the solid-liquid interfaces can be easily calculated by equation (7).

5 Conclusions

(1) The energy of the macroscopic system in which the axisymmetric meniscus is formed under the solid cone is calculated with the hypothesis that Young's equation can be applied to a macroscopic system in which the contact angle hysteresis is observed. Based on the calculated results, the physical mechanism of macroscopic wetting behavior was discussed.

(2) For the meniscus attached to a vertical cylinder ($\phi=0$ deg), the system energy takes a minimum when the meniscus surface is in contact with the solid at a contact angle θ_Y. This result agrees with the conventional view.

(3) For the axisymmetric meniscus formed under a horizontal plate ($\phi=90$ deg) the system energy takes a maximum at a contact angle contrary to the above result (2). The system is stable when the angle θ at which the meniscus curve attaches to the solid is between the advancing contact angle θ_{YA} and the receding one θ_{YR}. These results agreed well with the wetting behavior observed in the experiments.

(4) From results (2) and (3) above, the validity of the hypothesis with regard to Young's equation stated in (1) was adequately demonstrated. Therefore, the macroscopic wetting behavior may be described by using the modified Young's equation without considering the details of the microscopic wetting behavior.

(5) For the meniscus formed under a downward cone (0 deg $<\phi<$ 90 deg), the calculated system energy takes both the maximum annd minimum when θ is a contact angle θ_Y. When the cone vertex is rising from the stationary liquid surface by a certain height, the system becomes unstable and the meniscus detaches from the solid surface spontaneously.

(6) Applying the results of (5) above, a new method for measuring the contact angle is proposed.

References

Chappius, J. (Edited by Hewitt, G. F., Delhaye, J. M., and Zuber, N.), 1982, "Contact Angles," *Multiphase Science and Technology*, Vol. 1, pp. 459–460.

de Gennes, P. G., 1985, "Wetting: Statics and Dynamics," *Reviews of Modern Physics*, Vol. 57, pp. 828–829.

Eick, J. D., Good, R. J., and Neumann, A. W., 1975, "Thermodynamics of Contact Angles II, Rough Solid Surfaces," *Journal of Colloid and Interface Science*, Vol. 53, pp. 235–248.

Huh, C., and Scriven, L. E., 1969, "Shapes of Axisymmetric Fluid Interfaces of Unbounded Extent," *Journal of Colloid and Interface Science*, Vol. 30, pp. 323–337.

Joanny, J. F., and de Gennes, P. G., 1984, "A Model for Contact Angle Hysteresis," *Journal of Chemical Physics*, Vol. 81, pp. 552–562.

Johnson, R. E., and Dettre, R. H., 1964, "Contact Angle Hysteresis 1, Study of an Idealized Rough Surface," *Advances in Chemistry Series*, No. 43, pp. 112–135.

Liaw, Shin-Pin and Dhir, V. K., 1986, "Effect of Surface Wettability on Transition Boiling Heat Transfer from a Vertical Surface," *Proceedings of the 8th International Heat Transfer Conference*, pp. 2031–2036.

Lucassen-Reynders, E. H., and Lucassen, J., 1984, "Thin Films, Contact Angles, Wetting," *NATO Advanced Study Institute Series, Series E*, No. 75, pp. 79–109.

Mori, Y., Hijikata, K., and Mizuta, K., 1984, "Fundamental Study on High Performance Evaporating Surface," *Transactions of Japan Society of Mechanical Engineering, Series B* (in Japanese), Vol. 50, pp. 888–895.

Neumann, A. W., and Good, R. J., 1972, "Thermodynamics of Contact Angles I, Heterogeneous Solid Surfaces," *Journal of Colloid and Interface Science*, Vol. 38, pp. 341–358.

Rapacchietta, A. V., and Neumann, A. W., 1977, "Force and Free-Energy Analyses of Small Particles at Fluid Interfaces II, Spheres," *Journal of Colloid and Interface Science*, Vol. 59, pp. 555–567.

Control of Surface Tension Flows: Instability of a Liquid Jet

N. M. Nahas
Graduate Student.

Ronald L. Panton
Professor.

Mechanical Engineering Department,
University of Texas,
Austin, Texas 78712

A technique of controlling surface tension flows using thermal radiation is proposed. This method takes advantage of the dependence on temperature of the surface tension forces to produce the desired controlling effects. In this research, a capillary water jet is taken as an example of a surface tension dominated flow. The ability to cancel a preexisting unstable perturbation is demonstrated. First an acoustical disturbance that dominates the naturally occurring perturbations is applied to the jet. This causes jet breakup at a shorter and constant distance from the orifice. Next, a CO_2 laser beam, modulated at the same frequency as the primary disturbance, is focused on the surface of the jet. By proper adjustment of intensity and phase the two perturbations cancel each other and the natural breakup of the jet is recovered. The influences of phase and intensity mismatches were tested and are reported. In addition to its application to delaying breakup of capillary jets, this technique is a promising method of controlling both suface tension driven flows and instabilities in different industrial applications.

Introduction

Recently more and more attention has been given to flow situations where surface tension effects are significant. Such flows occur in several modern industrial applications. Examples related to manufacturing processes are: fiber spinning, wave soldering, an abundance of film coating processes, paper making, welding, and crystal growing processes. Some of these situations also occur in space manufacturing and space construction where surface tension effects are not dominated by gravity forces. Moreover, the physics of surface tension flows is important for the successful operation of industrial equipment such as sprays and ink jet printers. In practically all of these examples a positive benefit could be attained by exerting control over the surface tension forces.

Surface tension flows are driven by tangential and/or normal forces. Tangential forces arise from a tension gradient (caused by a temperature gradient and/or an uneven concentration of impurities) along the surface. This force is balanced by a viscous force in the bulk fluid and generates a Marangoni (thermocapillary) type flow. On the other hand, normal pressure forces are active when interfacial surfaces are highly curved. The pressure jump across a curved surface is governed by the equation

$$\Delta P = \sigma(1/R_1 + 1/R_2) \tag{1}$$

Here ΔP is the pressure jump and R_1 and R_2 are the principal radii of curvature of the surface. The surface tension σ is a function of the types of fluids, the temperature, and the concentration of other dissolved species. In this paper we promote the general idea that surface tension flows are susceptible to control with reasonable effort. The approach is to alter the surface tension by using its strong dependence on temperature. This can be done through convection from surfaces, say at a contact line, or by direct thermal radiation, which is easily manipulated.

For this research project, a capillary liquid jet into air was selected as an example of a surface tension dominated flow. It is well known that infinitesimal disturbances of the jet diameter are unstable and will grow to eventually cause the jet to breakup into droplets. Rayleigh [1] showed that varicose (axisymmetric) disturbances are unstable if their wavelength is larger than the circumference of the jet. In a typical natural situation, random disturbances with a spectrum of wavelengths will cause the breakup distance from the orifice to constantly change. In experiments to measure the amplification rate it is typical to introduce a single frequency disturbance by a loudspeaker. The interaction of the sound wave with the orifice produces an infinitesimal variation in the diameter of the jet that easily overpowers the natural random disturbances. In fact, the distance to jet breakup can be varried by changing the intensity of the sound. Note that the jet receptivity to acoustic forcing occurs at the orifice; acoustic pressures along the length of the jet are not important for growth of the radius variations.

The present research goal is to demonstrate the physical feasibility of controlling surface tension flows by altering the surface tension. To be specific, the surface tension will be modified by local heating to change the surface temperature. In previous work, Faidley and Panton [2] (based on the analysis of Panton [3]), controlled the breakup of a liquid jet by inducing an oscillation in the surface temperature as the jet was formed. They used a thin-film electric heating element in the orifice wall. In the current research, the surface will be heated by radiation from a CO_2 laser. This method is much more flexible in that both the location and timing of the radiation can be controlled. Modulating the surface tension by laser radiation can obviously be used for control of jet breakup as

Contributed by the Fluids Engineering Division for publication in the JOURNAL OF FLUIDS ENGINEERING. Manuscript received by the Fluids Engineering Division June 27, 1989.

demonstrated in reference [2]. In the present work, however, the more difficult task of cancelling an existing radius perturbation is addressed. This can be viewed as the first step in developing an active control for stabilizing a jet from random natural disturbances. The concept would be readily adapted to stabilizing the ribbing disturbances that occur in coating flows. It should be mentioned that the concept is not limited to cancelling instabilities, but can also be applied to control flow patterns in steady state flows.

Thermal means have been used in the manufacture of target pellets for fusion research. The authors appreciate that a referee pointed out to them the papers of Kim and coworkers [4, 5, 6]. These authors produced small spherical pellets that had a uniform coating of material. The thickness of liquid material was made uniform by imposing a thermal gradient in the surface so that surface tension would counteract the slumping caused by the gravity force.

In the present experiments, a periodic input disturbance of fixed amplitude and constant wavelength was acoustically applied to the jet. This caused breakup at a specific distance from the orifice. The higher the input amplitude, the closer to the orifice the jet breakup occurred. This diameter perturbation was to be cancelled by selectively heating portions of the surface of the jet. Heating was accomplished by focusing a CO_2 laser at the jet. The laser was switched on and off at the same frequency as the input disturbance. When the laser energy was absorbed, the surface temperature was altered (and σ) and thus by equation (1) the pressure jump across the interface changed. In principle, for any distribution of radius perturbations there is a variation of surface tension that will exactly cancel and leave Δp constant. Without the axial pressure gradient induced flow, breakup into droplets is delayed. The object was to heat the neck region of the perturbation and decrease the local pressure jump to correspond to the pressure jump at the bulges.

The scope of the present work includes the study of cancellation of single disturbances over a range of wavelengths with two different jet velocities. In other experiments, at a single wavelength, the effects of mismatches in laser intensity and phase were measured.

Experimental Set-Up

The experimental set-up had four parts: the fluid system to produce a long liquid jet, the acoustic system to produce an input disturbance, the laser-optical system to cancel the perturbation, and the measurement system to take relevant data.

The experiments were conducted using the fluid system shown in Fig. 1. A cylindrical reservoir tank, held at a constant regulated pressure of 28 psig, contained untreated tap water. Just downstream of the tank a globe valve was used to throttle the flow to achieve different flowrates. Next, the water was filtered and then passed to the settling chamber where a honeycomb and a series of screens dampen out any undesirable turbulence. The jet was finally formed using a 2.4 mm diameter 1.8 mm length square edge orifice. Due to the sharp edges of the orifice, the initial diameter of the jet was smaller than the orifice itself and was estimated to be 2.0 mm. In addition, gravity had a stretching effect on the jet, however, analysis revealed that the radius did not change by more than 10 percent. During the blow-down cycle, the flowrate decreases by less than 1 percent because the maximum hydrostatic head lost in the tank represents only 1 percent of the pressure supplied by the regulator. Similar flowrates for different experiments were obtained by setting the same static pressures at the pressure gauge.

Figure 2 shows the laser-optical and acoustical systems. The most important part of this set-up was the CO_2 laser. The laser emits far infrared radiation of 10.6 μm wavelength with a maximum power of 10–12 watts. Water is opaque at this

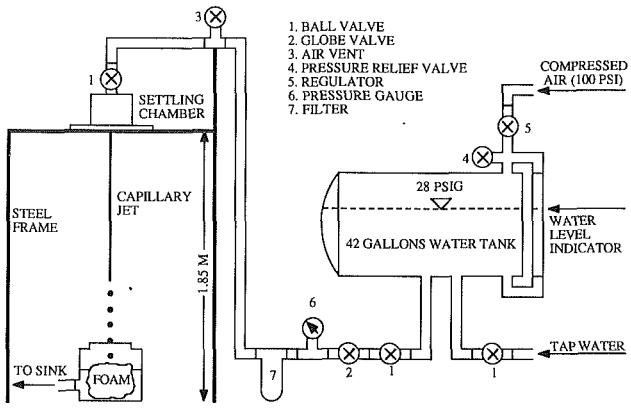

Fig. 1 Fluid system

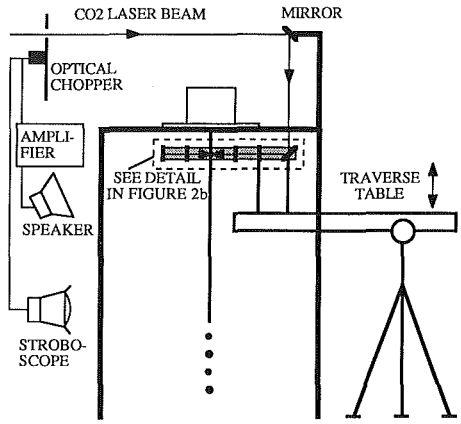

Fig. 2(*a*) Optical and acoustical system

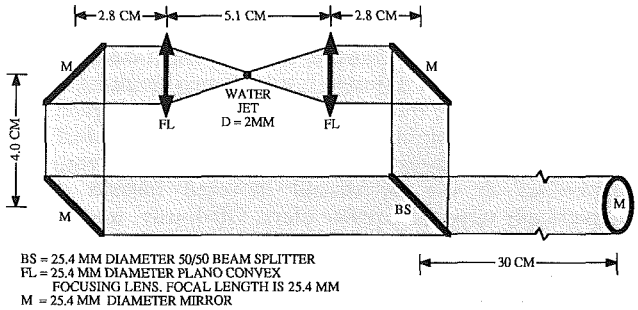

Fig. 2(*b*) Detailed top view of traverse table optics (drawn to scale)

wavelength and absorbs all of the radiated energy in a very thin surface layer. At the laser tube exit the emitted beam had a 2.3 mm radius and a full divergence angle of 2.9 mrad (both values are measured at the $1/e^2$ intensity points). At this position, the beam was chopped at a variable frequency from 0-3000 Hz. In order to achieve this frequency interval, two chopper disks (10 blades, 30 blades) were used. If the laser beam had an infinitesimally small diameter, the resulting modulation would be a 50 percent duty cycle square wave. However, due to the diameter of the beam and its Gaussian intensity distribution, the resulting modulation was smoothed as shown in Fig. 3 for both the 10 blade chopper and the 30 blade chopper. After passing through the chopper, the laser beam was deflected and directed vertically to a traverse table where it was split in two and focused on each side of the water jet. This is shown in detail on Fig. 2(b). It is important to note that by the time the beams reach the water jet, they had traveled a distance of approximately 5 meters, thus diverging to a radius of 9.5 mm. The optics on the traverse table have a

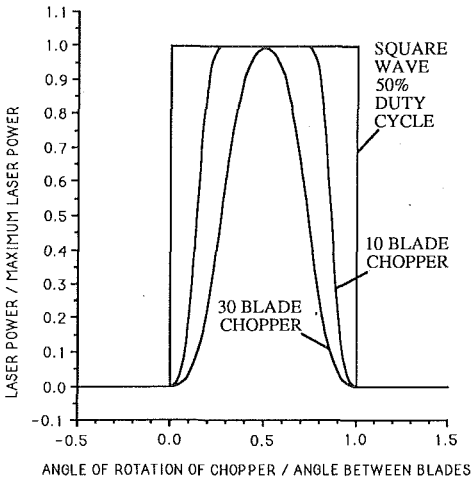

Fig. 3 Estimated laser waveform

radius of 12.7 mm and some of them are tilted at an angle of 45 deg resulting in a projected radius of 9 mm. Therefore, a portion of the beams misses the optics and was absorbed by the mounts. Due to this effect, approximately 17 percent of the laser power was lost. Moreover, each mirror or lens absorbs some energy contributing to an additional 25 percent power loss. It was estimated from optical specifications that of the original 10–12 watts, 6–7 watts were available at the water jet.

After being split in two, the beams were focused on the jet using two plano-convex lenses. Since the laser beam diameter was relatively large, spherical aberration effects were important and resulted in an estimated focused blur having a minimum diameter (circle of least confusion) of 0.3 mm and a length (longitudinal spherical aberration) of 1.5 mm. Clearly the alignment of the optics was very important. It was achieved by mounting a piece of acrylic with a thickness similar to the water jet diameter between the focusing lenses. The optics were then adjusted until the two resulting burned spots on the acrylic due to laser radiation were aligned. It is appropriate to mention that in order to achieve ideal symmetry a very thin sheet of light focused around the entire circumference of the jet should be used instead of the diametrically opposed circular blurs. Obviously, many of the problems mentioned above could have been avoided if the CO_2 laser was mounted directly on the traverse table. Unfortunately the laser was shared by different people for different research purposes and its position could not be changed.

The focusing lenses and optics of Fig. 2 were arranged in a plane perpendicular to the water jet. Since the beam from the laser source comes to the traverse table vertically, the focused beams can be moved up and down without altering the alignment of the optics. In effect, the acoustic perturbations originate at the jet orifice. Therefore, traversing the focused laser beams along the axis of the jet was equivalent to changing the phase angle of the laser perturbation with respect to the acoustic perturbation. The displacement of the laser beam (traverse table) was measured using a ruler secured on the traverse table and a needle fixed on the frame of the experimental set-up. A change in phase angle between the acoustic and laser perturbation was therefore measured as the displacement of the ruler with respect to the pointer. The uncertainty of this measurement was ± 0.5 mm.

The acoustical system was comprised of a speaker that was either secured to the steel frame, in order to induce disturbances in the form of mechanical vibration, or on a separate tripod to create acoustical perturbations. To drive the speaker at the same frequency as the laser, an infrared LED was directed across the optical chopper. A photodiode detected this signal in the form of a TTL output voltage that was attenuated or amplified and then fed to the speaker. The intensity of the acoustical disturbance could therefore be varied using the amplifier. In addition, the same TTL signal triggered a stroboscope that froze the water jet for flow visualization purposes.

The effectiveness of modulating the surface tension can easily be estimated. Let the surface tension be approximated locally by

$$\sigma = \sigma_0 - M(T - T_0) \tag{2}$$

Assume that at the laser location the input acoustic perturbation is dr/r_0. Using equations (1) and (2) one may derive the temperature change that would be required to cancel this perturbation.

$$dr/r_0 = d\sigma/\sigma_0 = -(MT_0/\sigma_0)(dT/T_0) \tag{3}$$

For water at room temperature (MT_0/σ_0) is 0.59 (from reference [7]). In our experiments a typical acoustic perturbation at the laser location can be estimated using methods of reference [2]. It was $dr/r_0 = -0.0009$ which requires $dT = 0.5°C$ for canccellation. This gives an indication of the modest energy required using theral control. Note that a lower dT is required for cancellation if the laser location is the closer to the jet orifice. In our experiment, due to physical constraints in the experimental set-up, the closest position of the laser was 5 cm from the orifice.

The intensity of the acoustic and/or the laser perturbation was found indirectly by measuring the breakup distance of the jet. Higher amplitudes cause shorter breakup distances. The distance to the first break in the liquid was measured on a photograph of the jet that included a ruler aligned next to the jet. For the same experimental situation several pictures were taken. These values were then averaged and plotted with an error bar representing the 90 percent confidence interval on the mean. Finally, the volumetric flowrate and thus the jet velocity was measured using the classical "calibrated tank and stopwatch" method.

Experimental Procedure

The experimental procedure used to induce an input perturbation and then cancel it using the CO_2 laser will be described. Jet breakup photographs from different situations are pictured in Fig. 4. Note that the ruler in Fig. 4 does not directly represent the breakup distance of the jet as it was placed in this particular position for experimental convenience. However, knowing the position of the ruler with respect to the orifice of the jet, an accurate breakup distance can be measured.

In the first step, the natural breakup distance of the jet was measured (Fig. 4(a)). In this case, the distance between the bulges and necks was not constant as they are caused by random disturbances, each having a different wavelength. In addition, this random nature produces a breakup distance (distance to the first break in the liquid filament) that constantly varies, therefore from twelve to twenty-five pictures must be taken to obtain an acceptable value of the mean breakup distance.

The next step was to apply an input disturbance. A constant frequency, and thus a constant wavelength, disturbance was induced using the acoustic speaker. This caused breakup of the jet at a shorter and almost constant distance from the orifice (Fig. 4(b)). The breakup distance was very stable, therefore only three pictures were necessary to compute an accurate breakup distance. In various tests the frequency and amplitude of the disturbance were changed.

For the third step, the speaker was turned off and the laser turned on at the same frequency as the previous acoustical disturbance. The resulting hot and cold spots on the surface of the jet induce a flow that caused breakup at a constant

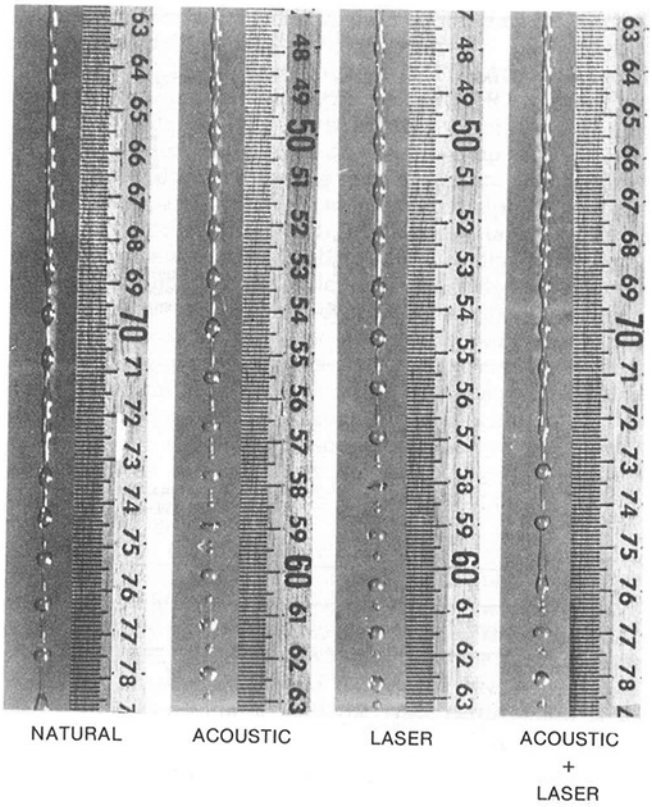

Fig. 4 The four types of experimental conditions. (Flow is from top to bottom.)

distance from the orifice (Fig. 4(*c*)). As in the previous experiment, the distances between the bulges and necks was constant and only three pictures were necessary to estimate the breakup distance.

Finally, both the speaker and the laser were turned on at the same time. The effect of the input (acoustic) radius disturbance and the surface tension control (laser heater) on the breakup of the jet was observed. Figure 4(*d*) shows the situation where the control "exactly" cancels the input. Indeed, by proper adjustment of the relative intensity and phase, the input and control disturbances would cancel each other and the total recovery of the natural breakup distance was obtained. In matching the breakup distances we are implicitly assuming that the breakup processes from the two different types of perturbation are the same.

The power of the laser was limited to 12 watts and the traverse table was positioned such that the laser beams were focused at the closest possible location to the jet orifice (5 cm from orifice). Since the equivalent acoustic disturbance could range far beyond this power, it was decided to set the laser to its maximum power and vary the amplitude of the acoustic input disturbance. The 12 watts setting for the laser beam power was maintained for all the experiments in this paper.

In the next section, the effects of relative intensity and phase angle in addition to the effects of disturbance wavelength and jet velocity will be discussed.

Discussion and Results

In his research, Rayleigh showed that only disturbances with wavelengths larger than the circumference of the jet are unstable and will cause jet breakup. In addition, he demonstrated that the perturbation with the fastest growing rate (or highest amplification rate, or causing the shortest breakup distance) has a wavelength equal to 1.43 times the circumference of the jet. This corresponds to a nondimensional

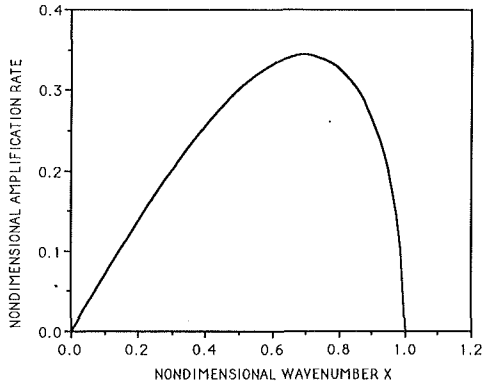

Fig. 5 Rayleigh's stability analysis

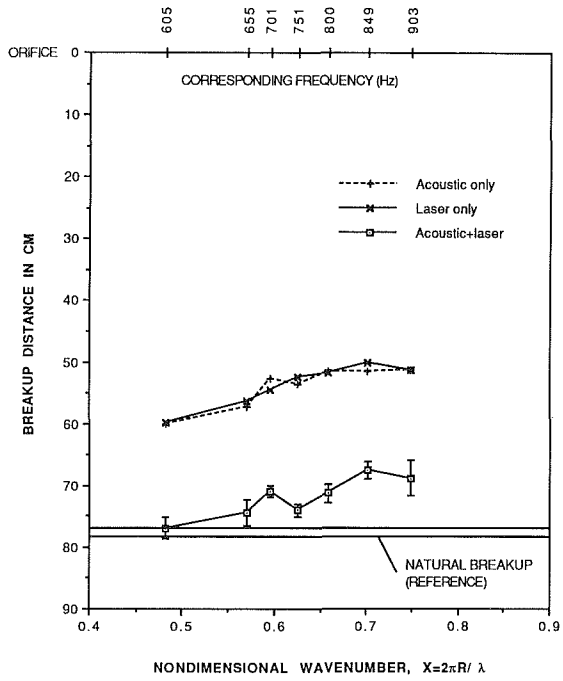

Fig. 6 Cancellation of input perturbation. Velocity at orifice is 6 m/s.

wavenumber $x = 2\pi R/\lambda = 0.697$. Figure 5 shows the growth rate curve from the theory. The maximum is rather broad and the entire range $0.4 < x < 0.9$ has significant amplification.

In the experiments shown in Fig. 6, the exact cancellation of the input perturbation was attempted. The individual breakup lengths for each perturbation are nominally equal as is shown by the curves labeled "acoustic only" and "laser only." Breakup distance is plotted downward to be consistent with the physical orientation of the equipment and photographs of Figure 4. The error bars represent the 90 percent confidence interval on the mean of the measured data. Notice that as the wavenumber increases, the breakup distance of the two individual perturbations decreases. This is consistent with Rayleigh's stability theory where the maximum amplification rates occur around a wavenumber of 0.7.

When turning on the input and control perturbations at the same time, breakup delay occurs as represented by the solid line labeled "acoustic + laser." The laser and acoustical perturbations were adjusted to be in antiphase by slightly moving the laser location until a maximum delay of breakup was attained. At small wavenumbers, total recovery of the natural breakup was obtained. This demonstrates a major goal of the experiments. However, as the wavenumber was increased, the cancellation of the acoustic disturbance by the laser was not

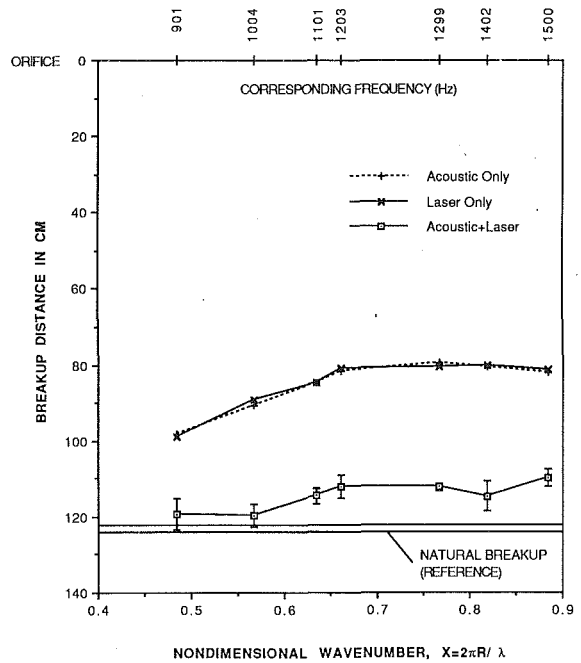

Fig. 7 Cancellation of input perturbation. Velocity at orifice is 10 m/s.

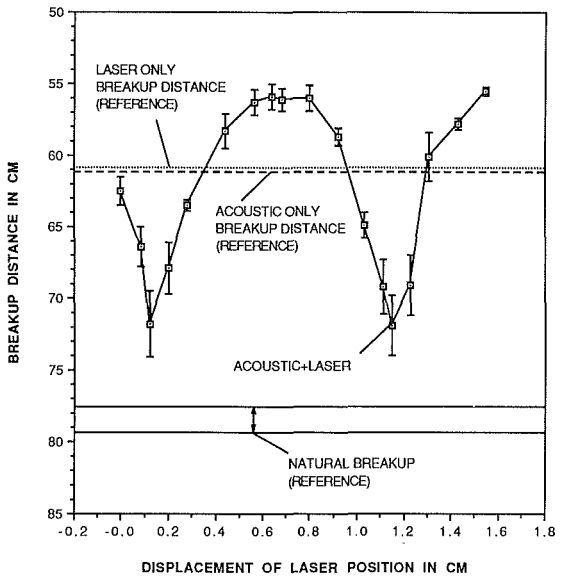

Fig. 8 Effect of relative phase angle. Velocity at orifice is 6 m/s, wavenumber is 0.49, frequency is 605 Hz.

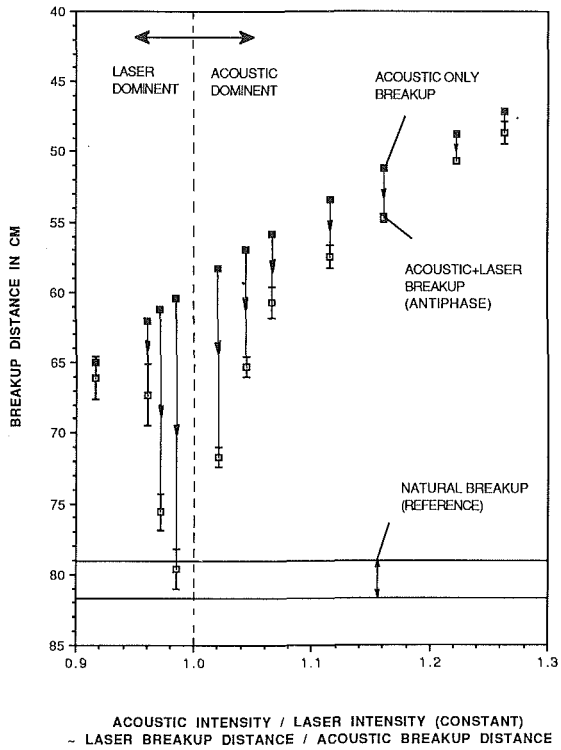

Fig. 9 Effect of relative perturbation intensity. Velocity at orifice is 6 m/s, wavenumber is 0.49, frequency is 605 Hz.

quite complete. The reason for this discrepancy is thought to be associated with laser focusing and phase alignment. As the wavenumber is increased the distance between the bulges and necks decreases. This means that the phasing of the focused beam is more difficult to accomplish properly.

The physics of the growth of a geometric perturbation (change in jet diameter) and the growth of a thermal perturbation have subtle differences. The acoustic perturbation is an isothermal flow with a constant surface tension. In the laser heating experiments, the variation in surface tension not only alters the pressure jump through equation (1) but also produces a tangential shear stress on the liquid ($\tau = \nabla\sigma$) that should, if given sufficient time, create a thermocapillary flow that redistributes the surface material. In addition, the transient thermal perturbation is conducted into the interior. Apparently, from the success of the cancellation experiments, these effects are secondary. Once the surface is perturbed by the laser heating, the growth process is dominated by the usual isothermal fluid mechanics.

The jet velocity affects the length of the natural breakup; the faster the jet, the longer the breakup length. With a faster jet wavenumbers similar to those obtained in Fig. 6 now correspond to higher perturbation frequencies. In the experiments for Fig. 7 the jet velocity was 10 m/s compared to 6 m/s for the previous case. In addition, to obtain the high frequencies in Fig. 7, the 30 blade chopper was used as opposed to the 10 blade chopper used in the previous experiments. This causes a slight change in waveshape (Fig. 3). Figures 6 and 7 are very similar and follow the same trends. This indicates that only the phase angle and the relative intensity of the two perturbations are important, whereas the jet velocity and the minor change in waveshape have no significant effect. As expected, the breakup distances on Fig. 7 are approximately 10/6 times the distances on Fig. 6. The lack of importance of waveshape can be rationalized by noting that any left-over higher-order harmonics would be in the stable region of the linear theory.

A study of phase angle dependency is summarized in Fig. 8. First, the breakup distances of the two individual perturbations were matched as shown by the "acoustic only" and the "laser only" breakup distance reference lines in Fig. 8. The two perturbations were then turned on at the same time and the phase angle was varied by moving the traverse table along the axis of the jet as discussed in the experimental set-up section. The results are shown by the data points labeled "acoustic + laser." As the traverse table is moved, two (inverse) peaks appear 10.3 ± 0.5 mm apart. These peaks represent maximum cancellation of the input disturbance by the laser and correspond to the laser heating two neighboring neck regions on the jet. Indeed, using a photograph similar to the one in Fig. 4, the distance between two adjacent necks at the breakup point was measured to be 11.5 ± 0.5 mm. These two measurements are in agreement if they are corrected for the 10 percent stretching effect, due to gravity, that occurs between the laser location and the picture location. Major points to be observed in Fig. 8 are that phase matching is very impor-

tant for cancellation of a disturbance, but it is relatively unimportant for addition of disturbances.

As opposed to the case pictured in Fig. 4(*d*), the total recovery of the natural breakup distance was not achieved for Fig. 8. Indeed, the confidence interval of the "acoustic + laser" experiment does not overlap with the confidence interval for the natural breakup distance. The reason for this discrepancy is thought to be a focusing problem in our relatively crude equipment. If the traverse table is moved along an axis not exactly parallel to the incoming laser beam, the initial alignment of the optics is altered. This results in out-of-focus beams and/or a non-diametrically opposed beam on the other side of the jet. Thus, the effective intensity of the laser heating was changed as the table was traversed. Also note that the natural breakup in Figure 8 does not exactly correspond to the one in Fig. 6, although the velocities in the two cases were the same. The reason is that the two experiments were taken on different days and the background random disturbances had changed. This remark also applies to the experiment in Fig. 9.

The effect of the relative intensity of the input and the control perturbations was also investigated and results are displayed on Fig. 9. As before, the intensity of a disturbance is represented by the jet breakup distance. The smaller the breakup length, the larger the intensity of the perturbation. Therefore, a useful measure of the relative intensity between the acoustic perturbation and the laser perturbation is to divide the "laser only" breakup length by the "acoustic only" breakup length. This ratio is a function of the ratio of the acoustical perturbation intensity to the laser perturbation intensity. Ratios larger than unity represent breakup dominated by the acoustical disturbance whereas ratios smaller than one represent breakup dominated by the laser disturbance. The solid squares in Fig. 9 show the breakup distance due to the acoustical signal only. When the laser perturbation (constant intensity) was added and the phase adjusted (peak position in Fig. 8), the breakup distance is delayed; the arrows on the graph show the shift for each intensity ratio. In the extreme cases when the laser or the acoustic intensity is dominant, the delay of the breakup is minimal. However, there is a range of perhaps 5 percent in "intensity ratio" where it is clear that the natural breakup distance is recovered.

Finally, some remarks are in order on how the principles demonstrated here might be extended to cancel natural disturbances in a jet. First one would have to measure the waveform of the disturbance at a specific location. This can be done optically with a low power slit laser. A photomultiplier tube records the intensity of the jet shadow described in references [3], [8], and [9]. An active control system would then be used to drive the control laser at the proper intensity and phase. Either an external optical-beam intensity modulator or an internally RF excited laser control are possibilities. Using this type of equipment, it would be possible to electronically adjust the phase of the control laser perturbation. If the waveform measurement position and control laser are not close together, then the different growth rates of different frequency components must be accounted for. Fortunately, and this is a very important physical fact, wavelengths shorter than the circumference of the jet are stable and can be completely ignored.

Summary

An external method of controlling surface tension flows has been proposed and evaluated in this research work. The method consists of altering the surface temperature and thus the surface tension by selectively heating the surface of the fluid using a laser. This method has been successfully applied to a liquid capillary jet. Its application to critical regions of other surface tension flows, regions such as a moving contact line or a pinned interface, are interesting possibilities.

In experiments on a liquid jet the task of cancelling a preexisting unstable radius perturbation of a single frequency was accomplished. This might be considered as a first step that shows the viability of stabilizing natural disturbances of arbitrary waveform. As a side issue the current experiments have also shown the feasibility of controlling the breakup of a liquid jet by periodically heating the surface with laser radiation.

Important parameters in the stabilizing experiments were varied. Cancellation was demonstrated for wavenumbers from 0.5 to 0.75 for a 2 mm diameter water jet having a velocity of 6 m/s. For the same jet at 10 m/s the wavenumber range was 0.5 to 0.9. The anticpated effects of jet velocity were observed. It was also noticed that the waveshape of the laser modulation does not have an effect on the cancellation process. However, it was shown that the cancellation effect is very sensitive to the phase of the laser beam. With regard to beam intensity, matching the input and control perturbations to about ±2–3 percent (in terms of breakup distance) is necessary for complete cancellation.

Acknowledgment

This research project could not have been accomplished without the financial support of the National Science Foundation. The help of Dr. Stephen Traugott in obtaining this funding from the "Accelerated Grants for Innovative Research" program is greatly appreciated.

References

1 Rayleigh, Lord, "On the Instability of Jets," *Proceedings of the London Mathematical Society*, Vol. 10, 1879, p. 4.

2 Faidley, R., and Panton, R. L., "Liquid Jet Instability Induced by Surface Tension Variations," *Experimental Thermal and Fluid Science*, 1989.

3 Panton, R. L., "Thermally Driven Instability of Liquid Jets," *Bulletin of the American Physical Society*, Vol. 30, 1985, p. 1733.

4 Kim, K., Mok, L., Erlenborn, M. J., and Bernat, T. P., "Noncontact Thermal Gradient Method for Fabrication of Uniform Cryogenic Inertial Fusion Target," *Journal of Vacuum Science and Technology*, Vol. A3, 1985, p. 1196.

5 Kim, K., and Krahn, D. L., "Fabrication of High-Grain Inertial Fusion Targets Using Gas Jet Cooling and Intensity-Graded Laser Illumination," *Journal of Applied Physics*, Vol. 61, 1987, p. 2729.

6 Varadarajan, V., Kim, K., and Bernat, T. P., "Thermally-Induced Behavior of Liquid Mixtures of Hydrogen Isotopes Inside a Spherical IFC Target," *Journal of Vacuum Science and Technology*, Vol. A5, 1987, p. 2750.

7 Jasper, J. J., "The Surface Tension of Pure Liquid Compounds," *Journal of Physical and Chemical Reference Data*, Vol. 1, 1972, p. 841.

8 Stalla, L., "An Optical Technique for Dye Laser Jet Stream Thickness Measurement in Real Time," *IEEE Journal of Quantum Electronics*, Vol. QE-14, 1978, p. 565.

9 Bulloni, M., et al., "High Resolution Measurement of Jet Stream Thickness by Optical Ranging," *Optics Communications*, Vol. 66, 1988, p. 280.

T.-M. Liou
Professor,
Power Mechanical Engineering Department.

Y. Chang

D.-W. Hwang
Graduate Students,
Power Mechanical Engineering Department.

National Tsing Hua University,
Hsin-Chu, Taiwan

Experimental and Computational Study of Turbulent Flows in a Channel With Two Pairs of Turbulence Promoters in Tandem

Measurements and computations are presented of mean velocity and turbulence intensity for an arrangement of two pairs of turbulence promoters mounted in tandem in developing channel flow. The Reynolds number (Re_D) and the pitch ratio (PR) were varied in the range of 1.2×10^4 to 1.2×10^5 and 1 to 100, respectively. The three pitch ratios 5, 10, 15 were found to provide three characteristic flows which are a useful test of the computational models. The effects of PR on the reattachment lengths and the pressure loss as well as the influence of Re_D on the reattachment length were documented in detail. It was found that $PR=10$ was preferable to $PR=5$ and $PR=15$ from the standpoint of heat transfer enhancement.

Introduction

Channels or pipes containing ribs are often used for heat transfer augmentation (Webb et al., 1971; Arvizu and Moffat, 1981; Metzger et al., 1983; Han et al., 1985). In gas turbine blade cooling design, repeated rib elements are cast onto two opposite walls of the internal cooling passages in order to enhance the removal of heat from the blade external surfaces which are directly exposed to the flow of hot gases. The cooling passages can be approximately modeled as a rectangular channel with two opposite rib-roughened walls. There have been very few publications in the literature on the heat transfer and fluid flow characteristics, especially the local temperature and velocity, of channels of this kind. In fact, even studies in cooling channels containing only a pair of ribs are very limited.

Bunditkful and Yang (1979) conducted a numerical analysis to investigate transport phenomena in parallel channels with a short flow obstruction under both isothermal and isoflux thermal boundary conditions. However, only laminar flow was considered in their analysis. Rastogi et al. (1980) theoretically and experimentally studied the turbulent flow in a circular pipe containing a ring obstruction of rectangular cross section due to interest in internal corrosion of pipelines. The results were mainly concerned with the mass transfer rates. Deshpande and Giddens (1980) performed turbulence measurements in a constricted tube for a range of low Reynolds numbers 5000 to 15000. The contoured occlusion had a cosine shape to simulate arterial stenosis. To compare with above turbulence measurements, Rastogi (1984) further employed the k-ϵ turbulence model to study the hydrodynamics in tubes perturbed by curvilinear obstructions, but the information reported was confined in flow field and mass transfer. Hung et al. (1987) presented theoretical results of turbulent flow in pipes with an internal ring obstruction. Moreover, they proposed curve-fitting correlations for the heat transfer coefficients. Unfortunately, there is no experimental data of flow-field patterns for comparison with their numerical prediction. Recently, Liou and Kao (1988) performed an extensive investigation on symmetric and asymmetric turbulent flows in a rectangular duct with a pair of ribs. However, the relative influence between successive ribs was not studied by them. Durst et al. (1988) performed measurements and computations of the mean streamwise velocity and its fluctuations for two similar fences mounted in tandem in fully developed channel flow. The fences were mounted on one wall of the channel and the spacing (pitch) between the two fences was fixed.

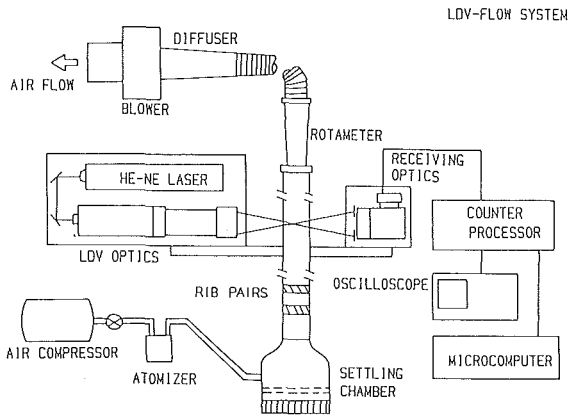

Fig. 1 Schematic drawing of overall experimental system

Contributed by the Fluids Engineering Division for publication in the JOURNAL OF FLUIDS ENGINEERING. Manuscript received by the Fluids Engineering Division April 10, 1989.

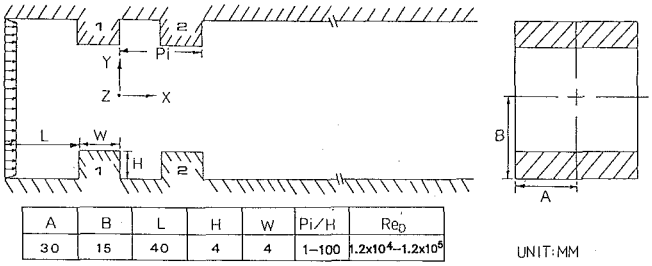

A	B	L	H	W	Pi/H	Re_D
30	15	40	4	4	1–100	1.2×10^4–1.2×10^5

UNIT: MM

Fig. 2 Sketch of coordinate system and dimensions of rectangular duct with two pairs of ribs in tandem. (Uncertainty in *H*: ± 0.5mm, in *W*: ± 0.5mm, in *A* and *B*: ± 0.5mm to 1mm, in axial position: ± 0.3mm, in transverse position: ± 0.3mm, in spanwise position: ± 0.5mm.)

The foregoing literature survey indicates the lack of both experimental and computational studies on turbulent flows past multi-pair of ribs on two sides of a duct. Even the most basic information such as profiles of mean velocity and turbulence kinetic energy are lacking. The influence of the spacing between two ribs on the flow characteristics is also needed to be understood. Therefore, the present paper attempts to both experimentally and computationally characterize the turbulent flows past two pairs of ribs arranged on opposite sides of a rectangular duct under various Reynolds numbers and pitches.

The experimental technique chosen was laser-Doppler velocimetry (LDV) since the flow reversals and large turbulence fluctuations in the separation zones make the use of hot wire technique unpractical. The computations were performed by numerically solving the fully elliptic two dimensional (2-D) Navier-Stokes equations with the k–ϵ turbulence model. To reduce numerical diffusion as large cross-flow gradients exist and the flow cuts across the grid lines at a large angle, and to avoid numerical oscillation during iteration as the Peclet number equals two, a smoothed hybrid central/skew upstream difference scheme (SCSUDS) was developed for the treatment of the convection and diffusion terms. The gathered data and insight as well as the comparison between the measured and predicted results will provide researchers with a useful reference to develop both turbulence and numerical models for predicting the flow field in such ducts.

Experimental Apparatus and Conditions

Experimental System. The flow system and LDV experimental setup are shown in schematic form in Fig. 1. Air was drawn into the test section through a flow straightener and six screens in the settling chamber and a 10:1 contraction by a blower (3500 rpm, three-phase, 10 hp) at the downstream end. The air then flowed through the two pairs of ribs in tandem, a flow straightener, a rotameter, and a bellows and was exhausted by the blower.

The LDV optics was set up in a dual-beam forward scattering configuration. A linearly polarized 15 mW helium-neon laser (632.8nm wavelength) provided the coherent light source. This beam was split into two parallel beams of equal intensity by a beam splitter. A Bragg cell was used to cause a 40 MHz frequency shift in one of the beams to eliminate directional ambiguity. This is essential when there is flow reversal as is expected in a rectangular duct with ribs. The resulting pair of beams were then passed through a 120 or 250 mm focal length lens. The focused beams entered the test section through a transparent Plexiglas wall and intersected inside the duct, giving a probe volume with dimensions of 0.52 mm × 0.10 mm (120 mm focal length lens, forward scattering) or 1.96 mm × 0.19 mm (250 mm focal lengths lens, forward scattering) at e^{-2} extent of light intensity and then passed through another side wall into the beam traps. The entire LDV system was mounted on a milling machine with four vibration-isolation mounts. The light scattered from the seeding particles was collected by a receiving optical package which reflects the collected light into a photomultiplier. The detected signal was electrically downmixed to the appropriate frequency shift (0.1–10 MHz in this experiment).

A TSI (Thermo-Systems, Inc.) counter processor with 2 ns resolution was then used to process the Doppler signal. The Doppler signal was monitored on an oscilloscope, and the digital output of the counter processor was fed directly to a microcomputer for storage and analysis. The seeding particles were introduced into the airstream by four atomizers symmetrically located on the walls of the settling chamber. The atomizers were operated by filtered compressed air and salt water and produced particles in the size range 0.5–5 μm. The salt solution was mixed to give a nominal 0.8 μm particle after the droplet dried.

Test Section and Experimental Conditions. The configuration of the duct, the coordinate system, and the dimensions of the present work are sketched in Fig. 2. The duct was made of 5 mm Plexiglas and had a cross section of 60mm × 30mm. The leading edges of the first pair of ribs were placed 100mm downstream of the bell-mouth 10:1 contraction.

The velocity measurements were carried out along the cen-

Nomenclature

A = half width of duct
B = half height of duct
C_p = pressure coefficient $\left(= \dfrac{P-P_{in}}{1/2 \cdot \rho U_b^2}\right)$
D = duct hydraulic diameter
H = rib height
k = turbulent kinetic energy
P = static pressure
Pi = pitch length
PR = pitch ratio ($=Pi/H$)
P_{in} = inlet static pressure
Re_D = Reynolds number $\left(= \dfrac{U_b D}{\nu}\right)$
U = streamwise mean velocity
U_b = duct bulk mean velocity
U_c = centerline streamwise mean velocity
U_i, U_j = mean velocity in tensor notation
U_{max} = maximum streamwise mean velocity at inlet
U_{REF} = reference mean velocity ($=U_b$)
u = streamwise velocity fluctuation
u' = streamwise turbulence intensity ($=(\overline{u^2})^{1/2}$)
u_i, u_j = velocity fluctuation in tensor notation
V = transverse mean velocity
W = rib width
X = streamwise coordinate
X_i, X_j = coordinate in tensor notation
X_{R1}, X_{R2} = reattachment lengths downstream of the first and second rib pair, respectively
Y = transverse coordinate
Z = spanwise coordinate
ϵ = dissipation rate of turbulent kinetic energy
μ_l = laminar viscosity
μ_t = turbulent viscosity
ν = laminar kinematic viscosity ($=\mu/\rho$)
ψ = dimensionless stream function ($=\int_0^y U dy/(U_b \cdot B)$)
ρ = air density

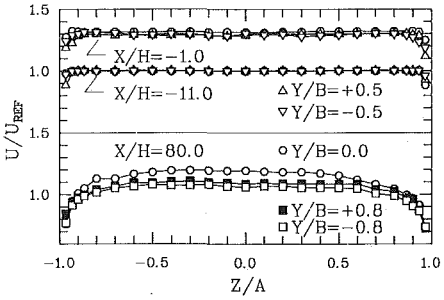

Fig. 3 Spanwise mean axial velocity profiles at selected axial stations along various *Y/B* for *PR* = 15 (Uncertainty in U/U_{REF}: less than ± 3.2 percent.)

tral plane ($Z/A = 0$) of the duct and were made at various stations for rib pitch-to-height ratios of 5, 10, and 15. In each station the measurements were made at 11 to 27 locations. The bulk mean velocity $U_b = 16.40$ m/s measured at the upstream plane $X/W = -11.0$, where the velocity distribution is rather uniform, was used as a reference to non-dimensionalize the experimental results. This velocity corresponds to a Reynolds number of 4.2×10^4 ($\mathrm{Re}_D = D \cdot U_b/\nu$), where $F = 40$mm is the hydraulic diameter of the duct. In this study the Reynolds number was also varied between 1.2×10^4 and 1.2×10^5. In addition, the ratio of rib pitch to height was varied from 1 to 100 to study its effect on the reattachment length.

The present experimental investigation was undertaken in a duct with an aspect ratio of 2. The same aspect ratio was also previously used by both Abbot and Kline (1962) and Cherdron et al. (1978) to study the flow downstream of a plane symmetric sudden expansion. In this study, the two-dimensionality check of the spanwise mean axial velocity profiles has been conducted and the results for the inlet reference station ($X/W = -11$), the sudden contraction station ($X/W = -1$), and the far downstream station ($X/W = 80$) are plotted in Fig. 3. All the profiles are rather symmetric. The two-dimensionality is over the center 54mm, 52mm, and 42mm of its spanwise width to within +/− 0.5, 1, and 4 percent of U_{REF} for $X/W = -11$, $X/H = -1$, and $X/H = 80$, respectively. Additionally, the two-dimensionality of the reattachment lengths and the three-dimensionality inside the separation zones are similar to those shown in Liou and Kao (1988).

Theoretical Treatment

The computations were performed by numerically solving the fully elliptic 2-D Navier-Stokes equations. To simplify the problem, the flow was considered to be isothermal, incompressible, and steady-state in the mean.

The Mean Flow Equations. The time averaged equations for conservation of mass and momentum can be expressed in the tensor notation as

$$\frac{\partial U_i}{\partial X_i} = 0 \tag{1}$$

$$\frac{\partial}{\partial X_j}(\rho U_i U_j) = -\frac{\partial P}{\partial X_i} + \frac{\partial}{\partial X_j}\left(\mu_1\left(\frac{\partial U_i}{\partial X_j} + \frac{\partial U_j}{\partial X_i}\right) - \rho\overline{u_i u_j}\right) \tag{2}$$

Note that the body force term has been neglected in the momentum equation and the turbulence correlation $\overline{u_i u_j}$ is the time averaged $u_i u_j$ and stands for the Reynolds stresses which must be modeled to close the above set of equations.

The Turbulence Model. In the present calculation, the k-ϵ turbulence model (Launder and Spalding, 1974) which adopts the generalized Boussinesq eddy viscosity concept, in analogy with the laminar flow, is expressed as

$$-\rho\overline{u_i u_j} = \mu_t\left(\frac{\partial U_i}{\partial X_j} + \frac{\partial U_j}{\partial X_i}\right) - \frac{2}{3}\delta_{ij} \cdot \rho k \tag{3}$$

where δ_{ij} is the Kronecker-Delta function and μ_t is the turbulence viscosity that may be related to the kinetic energy of turbulence, k, and its dissipation rate, ϵ, by dimensional analysis

$$\mu_t = C_\mu \cdot \rho \frac{k^2}{\epsilon} \tag{4}$$

where $C_\mu = 0.09$ is a constant of the model. The differential equations for k and ϵ are

$$\frac{\partial}{\partial X_j}(\rho U_j k) = \frac{\partial}{\partial X_j}\left(\left(\mu_1 + \frac{\mu_t}{\sigma_k}\right)\frac{\partial k}{\partial X_j}\right) - \rho\overline{u_i u_j}\frac{\partial U_i}{\partial X_j} - \rho\epsilon \tag{5}$$

$$\frac{\partial}{\partial X_j}(\rho U_j \epsilon) = \frac{\partial}{\partial X_j}\left(\left(\mu_1 + \frac{\mu_t}{\sigma_\epsilon}\right)\frac{\partial \epsilon}{\partial X_j}\right) - C_1\frac{\epsilon}{k}\rho\overline{u_i u_j}\frac{\partial U_i}{\partial X_j} - C_2\rho\frac{\epsilon^2}{k} \tag{6}$$

where $C_1 = 1.44$ and $C_2 = 1.92$ are further constants of this model. Furthermore, $\sigma_k = 1.0$ and $\sigma_\epsilon = 1.3$ are turbulent Prandtl numbers for k and ϵ, respectively. Equations (3) and (4) can be substituted into equations (2), (5), and (6) to form a set of equations which have the same number of equations and unknowns. The system of 5 equations for 5 unknowns U_i, P, k, and ϵ with prescribed laminar viscosity and density complete the closure problem for the turbulent flow investigated.

Boundary Conditions. The above set of elliptic partial differential equations has to be solved with the following boundary conditions (see Fig. 2)

(i). Symmetric plane ($Y = 0$)

$$\frac{\partial U}{\partial Y} = \frac{\partial k}{\partial Y} = \frac{\partial \epsilon}{\partial Y} = 0 \; ; \; V = 0 \tag{7}$$

(ii). Exit

$$\frac{\partial U}{\partial X} = \frac{\partial k}{\partial X} = \frac{\partial \epsilon}{\partial X} = 0 \; ; \; V = 0 \tag{8}$$

In this study, the location of the computational downstream boundary was determined from the measured results or from the computational tests. In fact, the computational tests showed that there is no noticeable change in the flow field as long as the location of the exit was far enough to allow the flow to become unidirectional.

(iii). Inlet

U = measured U_{in} ; $V = 0$

$k = k_{in} = 1.5 \cdot (u'_{in})^2 = \alpha_k \cdot U^2_{REF}$

$\epsilon = \epsilon_{in} = k_{in}^{3/2}/(B \cdot \lambda)$

where

u'_{in} = measured inlet axial turbulence intensity

$= 0.01 \cdot U_{REF}$

$\alpha_k = 1.5 \times 10^{-4}$ and $\lambda = 2 \times 10^{-2}$

(iv). Walls

$U = 0$; $V = 0$

Since the k-ϵ model is valid only in those regions that are strongly turbulent, that is, in regions where the eddy diffus-

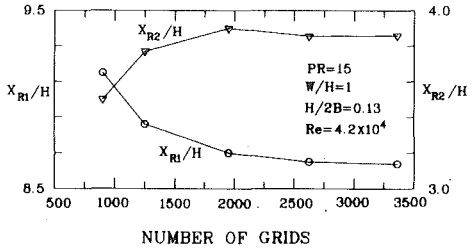

Fig. 4 Computed reattachment lengths as a function of grid points

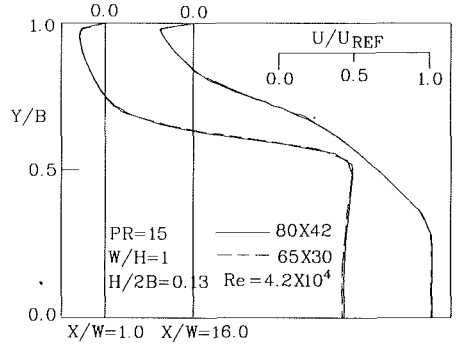

Fig. 5 Grid dependence of calculated mean velocity profiles

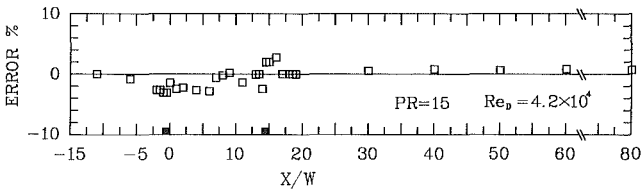

Fig. 6 Percent error in mass flow rate computed from measured mean axial velocity distribution

ivity overwhelms the molecular diffusivity, it is not applicable in the viscous sublayer. In the other way, the steep change of flow properties in the wall region needs an extremely fine grid arrangment and makes the computational efforts unpractical. Therefore, in this study, the near-wall region was simulated by a semi-empirical two-zone model, i.e., viscous sublayer and fully turbulent zone, and wall function (Launder and Spalding, 1974) was used to bridge the viscous sublayer.

Numerical Scheme. To reduce numerical diffusion associated with one-dimensional discretization schemes (e.g., hybrid difference scheme and power law difference scheme) as large cross-flow gradients exist and the flow cuts across the grid lines at a large angle (Raithby, 1976), as expected for the flow field in the present work, a finite difference scheme SCSUDS (Smoothed hybrid Central/Skew Upstream Difference Scheme) is proposed in the present study and described in detail in Hwang (1988). The SCSUDS is basically an improvement of Leschziner's CSUDS (hybrid Central/Skew Upstream Difference Scheme) (1980) which leads to a discontinuity occurring as the Peclet number (Pe) equals two and, in turn, leads to numerical oscillation during iteration. In SCSUDS, both convection and diffusion terms are discretized using the central difference scheme as $|\mathrm{Pe}|<2$; however, as $|\mathrm{Pe}|>2$, the diffusion term and convection term are discretized by employing the upwind difference scheme and Raithby's SUDS (Skew Upstream Difference Scheme) (Raithby, 1976), respectively. Note that this is different from CSUDS which employs the central difference scheme for the diffusion term as $|\mathrm{Pe}|>2$. For $|\mathrm{Pe}|>2$, the convection dominates over the diffusion and the prediction by the upwind difference scheme is generally better than by the central difference scheme (Patankar, 1980). This is the reason for the aforementioned treatment adopted by the present SCSUDS scheme, the discretization results thus show no discontinuity occurring as $|\mathrm{Pe}|=2$ and the iteration running quite smoothly.

As for handling the pressure-velocity coupling arising in the implicitly discretized fluid flow equations, the method PISO (Pressure Implicit with Splitting of Operators) (Issa, 1986) is utilized in this paper for the reason of stable and faster convergence (Jang et al. 1986). The solution procedure starts by supplying initial guesses of the velocity and pressure fields and then proceeds the line by line solution. After each sweep over the solution domain, two steps of adjustments for the pressure field are made to satisfy the continuity along each line of cells. These adjustments in turn destroy the compliance of the velocity and pressure fields with the momentum equations. Further iterations are thus needed until the continuity and momentum equations are simultaneously satisfied to the requisite degree of accuracy. The tolerance of the nondimensionalized residual is typically 0.005. The k and ϵ are also solved line by line simultaneously with the mean velocity distribution.

The grid distribution in the calculation domain was nonuniform in both X and Y coordinate directions. A large number of grid points were placed in the areas where steep variations in velocities were revealed from experimental measurements. To ensure grid independence, the solutions were calculated by using different grid sizes. The tested grid sizes were 45×20, 50×25, 65×30, 75×35, and 80×42. Since the reattachment length is a sensitive parameter that has historically been used to assess the overall predictive capability of turbulence models (Driver and Seegmiller, 1985), it has often been used to check the grid independence of the computational results (Amano and Goel, 1985; Benodekar et al., 1985). Figure 4 shows the computed reattachment lengths, X_{R1} and X_{R2}, downstream of the first and second rib pair, respectively, as a function of grid points. It is seen that 6 and 9 percent differences in X_{R1} and X_{R2}, respectively, were found between grid sizes of 45×20 and 80×42, while less than 1 percent difference both in X_{R1} and X_{R2} was found between grid sizes of 65×30 and 80×42. Furthermore, a comparison of the calculated mean velocity profiles between using 65×30 and 80×42 grids were made in Fig. 5 where the two axial stations, $X/W=1.0$ and $X/W=16.0$, happened to be two of the overlap nodes between 65×30 and 80×42 grids and were selected because they crossed separation bubbles downstream of the first and second rib pair, respectively. Less than 2 percent difference in U/U_{REF} was found between these two grids. Consequently the grid size 65×30 was chosen in the present work. The corresponding CPU time on a CDC-CYBER 180-840 computer is about 3.4 seconds for each iteration, and it typically needs 300 to 350 iterations to reach convergence.

There is one more aspect concerning the near-wall grid worth addressing here. The constraints on the choice of the first grid node y_p are that it must lie outside of the linear sublayer ($y_P^+ = y_P \times$ shear velocity$/\nu < 11.63$) and yet, close enough to the wall to accurately resolve the flow in the near-wall region. For the present calculations, y_P^+ is approximately 18 in the recirculation zone for most cases. It was found that very limited improvement in the accuracy of the calculated reattachment lengths can be obtained for $18<y_p^+<38$.

Uncertainty Estimates. Representative values of uncertainty estimates are noted in figure captions. More detailed uncertainty estimates such as velocity gradient broadening, day to day variations, and statistical error associated with finite number of measurements (typically 4096) at each measuring location are included in Liou and Wu (1988).

In this study, the LDV velocity bias error was first corrected by using the well known weighting method of McLaughlin and

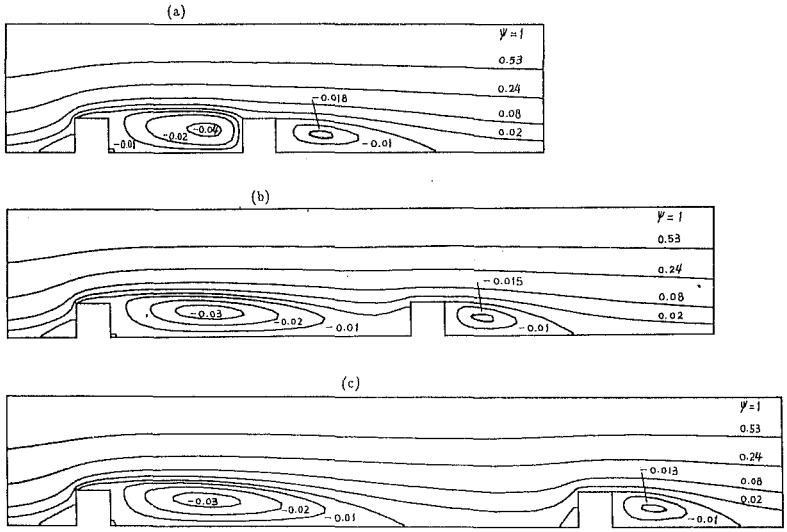

Fig. 7 Calculated streamlines for (*a*) $PR = 5$, (*b*) $PR = 10$, (*c*) $PR = 15$

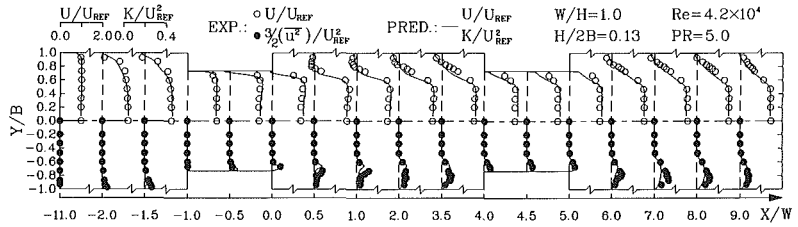

Fig. 8 Streamwise mean-velocity and turbulent kinetic energy profiles at various stations along plane $Z/A = 0$ for $PR = 5$. (Uncertainty in U/U_{REF}: less than ± 3.2 percent, in $k^{1/2}/U_{REF}$: less than ± 10 percent, in Y/B: less than ± 1.4 percent, in X/W: less than ± 1.4 percent.)

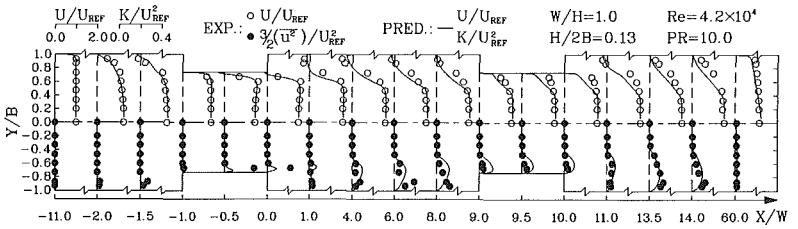

Fig. 9 Streamwise mean-velocity and turbulent kinetic energy profiles at various stations along plane $Z/A = 0$ for $PR = 10$. (Uncertainty: see Fig. 8 caption.)

Tiederman (1973) for regions where local turbulence intensity was below about 25 percent (Drain, 1980). The difference between weighted and unweighted data sets was found to be below 2 percent. The advantage of this widely used method is its simplicity, the weighting factor being simply the inverse of the velocity or the particle residence time. However, for regions around the reattachment and within the separation bubbles the turbulence level was typically very high and near-zero velocities frequently appear due to flow reversal resulting in very large weighting factors and, in turn, in an overcorrection. For these regions, therefore, measurements were repeated using the equal time interval sampling to correct the velocity bias error and the mass-balance error from direct integration of the biased and unbiased mean axial velocity profiles at axial stations investigated was found to be within 12.4 percent.

The check of mass continuities for the measured mean axial velocity profiles is necessary before comparing with the predicted results since the computed mean axial velocity profiles are mass conserving. Figure 6 depicts the streamwise variation of the mass-balance error relative to the inlet flow rate for all the measured axial mean velocity profiles which have been corrected for velocity bias error. It is observed that the continuity error is within 3.1 percent and is larger for separated flow regions located immediately in front of, on the top of, and downstream of the rib pairs. These separated flow regions will be shown shortly. The sources of the continuity error may be reduced by developing the ability of taking measurements closer to the wall to improve the numerical integration, by using a rotameter (Fig. 1) with a finer scale to monitor the blower output more accurately, and especially by adopting a better scheme to correct the velocity bias error more appropriately. It should be mentioned that without adequate velocity-bias correction the continuity error would worsen; for example, the discrepancy in flow rate at the plane of sudden contraction, $X/W = -1$, would increase from 3 percent of Fig. 4 to 9 percent.

Results and Discussion

General Flow Pattern. The calculated mean flow patterns for pitch ratios of 5, 10, and 15 are presented in Fig. 7.

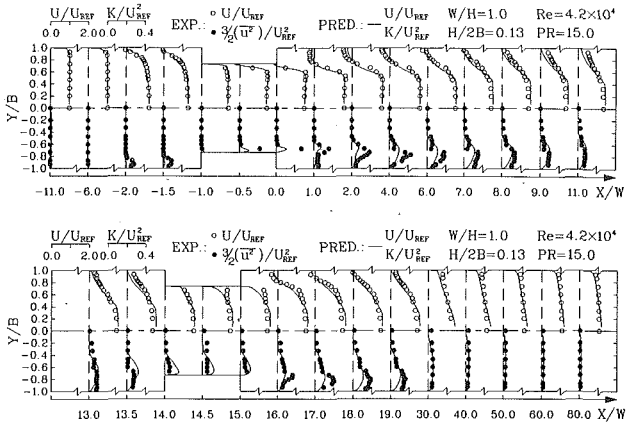

Fig. 10 Streamwise mean-velocity and turbulence kinetic energy profiles at various stations along plane $Z/A = 0$ for $PR = 15$. (Uncertainty: see Fig. 8 caption.)

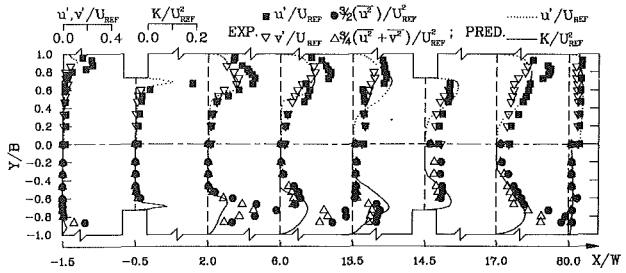

Fig. 11 Profiles of measured u'/U_{REF}, v'/U_{REF}, $3/2\ \overline{u^2}/U^2_{REF}$ and $3/4\ (\overline{u^2}+\overline{v^2})/U^2_{REF}$, and profiles of predicted u'/U_{REF} and k/U^2_{REF} for $PR = 15$. (Uncertainty in u'/U_{REF} and v'/U_{REF}: less than ±4.4 percent.)

Upstream of the first pair of ribs, the streamlines show similar flow distributions for all three cases because of the same inlet conditions and the same rib height. In this region the flow is adjusting itself with the streamwise mean velocity increasing centrally and decreasing near the walls. The near-wall fluids are partly retarded by the ribs with the formation of two small separation zones in the concave corners of the abrupt contraction and partly forced to turn into the rib gap with separation occurring at the salient points of the rib leading edges due to the large curvature of the flow.

For the region between the two pairs of ribs, however, a driven cavity flow is found for $PR = 5$, a wake interference flow, where the reattachment process behind the ribs first becomes evident, is found for $PR = 10$, and a reattaching followed by redeveloping flow is found for $PR = 15$. It is obvious that different heat transfer characteristics will associate with the aforementioned three types of flows occurring between the rib pairs. Downstream of the second rib pair, similar flow distributions are found for all three cases again since flow separation occurs at the same trailing salient points of the second rib pair. In this region, the flow is characterized by the larger separation bubbles resulted from the sudden expansion. Further downstream, the flow profile will eventually approach that of the fully developed duct flow.

Comparison With LDV Measurements. The streamwise mean velocity and the turbulent kinetic energy along $Z/A = 0$ plane are plotted versus dimensionless Y/B coordinate at various axial stations in Figs. 8 to 10 or pitch ratios 5, 10, and 15, respectively. In general, it is seen that the agreement between the computed and measured results is reasonably good. It is also observed that the streamwise mean-velocity profiles at inlet reference plane, $X/W = -11.0$, are rather uniform, except near the walls, due to the acceleration of the bell-mouth-like contraction. The corresponding turbulence level and boundary layer thickness (defined at 0.95 of U_{max} locally) are 1 percent and 0.03D, respectively. The corresponding momentum thickness is 1.48×10^{-4}m. The negative velocity near the walls at $X/W = -1.5$ and $X/W = -2.0$ indicates the existence of the foregoing two small separation regions in the concave corners of the abrupt contraction formed by ribs. The distance between the separation point and the rib is 1.05H and 1.10H according to the computation and the experiment, respectively.

The calculated negative velocity adjacent to the walls for the region between the first pair of ribs indicates the flow separated at the convex corners of the abrupt contraction. Although the LDV measurements did not cover this near-wall layer, less than 1mm from the wall, due to the finite size probe spatial resolution and due to the noise associated with the walls, the measured velocity profiles at $X/W = 0.5$ and $X/W = 1.0$, where the flow reversal extends from the wall to a vertical distance of 0.85H to 1.0H, also suggest the separation occurring at the convex corners of the abrupt contraction. In addition, both calculated and measured results show that the velocity maximum at $X/W = -0.5$ is no longer occurring along the centerline. This phenomena is often referred to as velocity overshoot which is a turbulence generating source. Its formation is due to the curvature of the flow around and downstream of the salient separation point. The phenomena of velocity overshoot is gradually diminishing from $X/W = -0.5$ to $X/W = 3.5$ due to the viscous effect.

Downstream of the first rib pair, Figs. 7 to 9 show that the reattachment of the aforementioned separation flow occurs at the convex corners and at a position slightly below the convex corners of the abrupt contraction formed by the second rib pair for $PR = 5$ and $PR = 10$, respectively. Consequently, the flow almost does not feel the presence of the abrupt contraction formed by the second rib pair. This fact illustrates the absence of the velocity overshoot and flow separation for the flow region between the second pair of ribs for both $PR = 5$ and $PR = 10$, as shown in Figs. 7 and 8. For the case of $PR = 15$, Fig. 10 shows that the separated flow reattaches to the duct walls at a position between the two pairs of ribs. The computed reattachment length is $8.7H$ downstream of the first pair of ribs and the measured one $8.1H$. The discrepancy is 7 percent. Note that the determination of the measured reattachment length has been documented in Liou and Kao (1988). After reattachment the flow starts to redevelop and the new developing shear layer is gradually spreading into the old shear layer which is originated from the first pair of ribs. The interaction of the above two shear layers provides additional turbulent kinetic energy to the flow. Hence, there is no flow separation occurring at the leading convex corners of the second pair of ribs for the case of $PR = 15$. However, a tendency toward the velocity overshoot can be seen at $X/W = 14.5$ (Fig. 10) since the curvature of the flow around the aforementioned convex corners still has effect on the fluid motion between the second pair of ribs, although not so large as that occurring between the first pair of ribs.

Downstream of the second pair of ribs the flow pattern is similar to that sudden expansion duct flow. The calculated and measured reattachment lengths are $4.2H$, $3.9H$, $3.9H$, and $3.8H$, $3.7H$, $3.7H$, respectively, for $PR = 5$, 10, and 15. The corresponding discrepancies between the calculated and measured values are 11, 3, and 5 percent, respectively. It may be interesting to point out that the reattachment length behind the first rib pair is about twice that behind the second rib pair for $PR = 15$. This comparison is similar to that found by Durst et al. (1988) for flow over two fences in tandem on the single wall of a 2-D channel with $PR = 20.8$.

It is to be noticed that the comparison made above reveals that almost all the calculations underpredict the velocity recovery behind the ribs. This is particularly evident for the $PR = 10$ case shown in Fig. 8 where discrepancies of the order

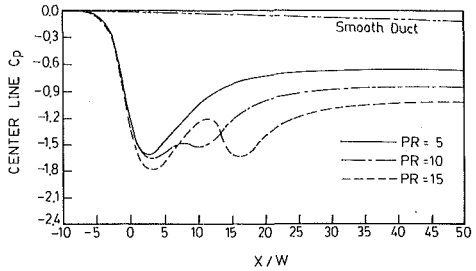

Fig. 12 Calculated streamwise distribution of dimensionless static pressure along the centerline

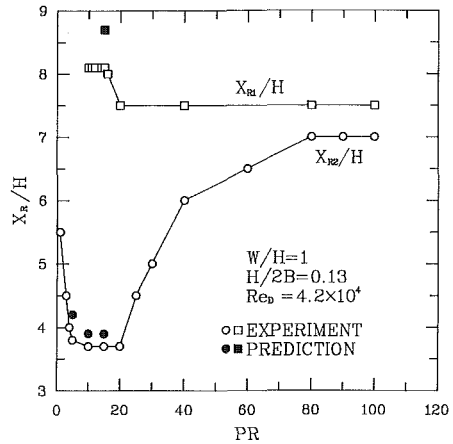

Fig. 13 Measured and computed reattachment lengths as a function of pitch ratio. (Uncertainty in X_{R1}/H and X_{R2}/H: less than ± 5 percent, in PR: less than ± 1.5 percent.)

of $0.5U_{REF}$ have been observed. A survey of related calculations using k–ϵ and higher-order turbulence models in separated and reattaching flows (Leschziner, 1989; Amano et al., 1988; Benodekar et al., 1985) also indicates similar underpredictions from the order of 0.5 to 1.0 U_{REF}. Since all the underpredictions are in the separation bubble and near the wall and since the near-wall treatment of all the aforementioned calculations using different turbulence models is based on the law of the wall which is valid for the normal boundary layers, these observations may suggest that a more appropriate wall-law for separated flows should be developed in the future work in order to achieve a better prediction.

As for the turbulent kinetic energy, the isotropic assumption has been employed to obtain the measured k ($=1.5 \cdot \overline{u^2}$) since detailed measurements of turbulence intensity were only made for the axial component. It is seen from Figs. 8 to 10 that the value of k is nearly zero in the potential-flow regions, as expected. On the other hand, large value of k is found in the shear layers and in the flow-separation regions where high velocity gradient exists. The discrepancy between the calculated and measured k is mainly in the flow-separation regions and near-wall regions, and is partly due to the isotropic assumption and partly due to the law of the wall mentioned above.

The above isotropic assumption only implies qualitative behavior of k. Therefore, experiment was repeated by measuring both u' and v' at several selected axial stations for the case of $PR=15$, using a four-beam two-component LDV system borrowed from other laboratory, to check isotropy and provide more quantitative data. First, the comparison of measured u' and v' in Fig. 11 ($Y/B>0$) indicates that anisotropy is within 20 percent of U_{REF} and is more significant along the shear layers, inside the separation bubbles, and near the walls. Second, using the widely used assumption that values of the spanwise normal stress lie midway between $\overline{u^2}$ and $\overline{v^2}$, the total turbulent kinetic energy can be approximated by 3/4 ($\overline{u^2}+\overline{v^2}$). Comparing measured 3/4 ($\overline{u^2}+\overline{v^2}$) and isotropic total turbulent kinetic energy 3/2 $\overline{u^2}$ with the predicted k in Fig. 11 ($Y/B<0$), one sees that profile of 3/4 ($\overline{u^2}+\overline{v^2}$) is closer to that of predicted k for most stations. Third, the comparison between the measured and predicted profiles suggests that to achieve a better prediction a modification to the isotropic eddy viscosity assumption used in the standard k–ϵ turbulence model will be necessary in the future work.

Pressure Distribution. Figure 12 shows the computed streamwise distribution of dimensionless static pressures along the centerline for the three pitches investigated. Basically, the variation of the centerline pressure parallels that of main stream tube. For $PR=5$, because of the presence of the cavity flow, the stream tube $\psi=0.02$ (Fig. 7(a)) first converges and then diverges with a throat located between the two pairs of ribs. Hence, the corresponding centerline pressure shown in Fig. 12 first decreases due to the acceleration and then increases due to the deceleration. As the flow proceeds further downstream, the effect of ribs on the flow field gradually diminishes and the pressure distribution is similar to that in the smooth duct flow. Similarly, for $PR=10$ the stream tube $\psi=0.02$ (Fig. 7(b)) is slightly concave in a region at a short distance upstream of the second pair of ribs and the centerline pressure curve is accordingly slightly convex at the corresponding region, as shown in Fig. 12. For $PR=15$, the stream tube $\psi=0.02$ behaves like two convergent-divergent nozzles in tandem due to the flow reattachment between the two pairs of ribs and the corresponding centerline pressure accordingly decreases and increases twice, as shown in Fig. 12.

It is worthwhile to note that a comparison of C_p values at $X/W=50$ (Fig. 12) between the smooth duct flow and the ribbed duct flow investigated by the present work clearly reveals the large pressure loss caused by the existence of the rib pairs. Figure 12 further shows that the pressure loss increases with increasing pitch ratio since the retardation by the second pair of ribs increases with increasing pitch ratio.

Effect of Pitch. The nondimensionalized reattachment lengths downstream of the first and the second rib pair (X_{R1} and X_{R2}) measured from this study are plotted versus nondimensionalized pitch (PR) in Fig. 13, where the computed results are also included for reference, although the comparison has already been made in previous section. The results show a decrease in X_{R2} with increasing PR for $PR<5$, an almost constant X_{R2} for $5\le PR\le 20$, an increase in X_{R2} with increasing PR for $20<PR<80$, and a constant X_{R2} for $PR\ge 80$. The above behavior is attributed to the significant influence of the pitch variation on the flow field between the rib pairs. The results also show that X_{R1} is a weak function of PR since the flow field upstream of the first rib pair is not affected by the variation in PR.

Physically, for $PR<5$ the decrease of the wall pressures on the top surfaces of the ribs with increasing pitch ratio (Liou and Kao, 1988) implies the suction of the detached shear layers from the leading corners of the first pair of ribs towards the top surfaces of the ribs (i.e. the angle of the separation line is decreased) resulting therefore in a quicker reattachment downstream of the second rib pair, and thus a decrease in the reattachment length (X_{R2}). Eventually ($PR\ge 5$) the aforementioned detached shear layers will reattach on the top surfaces of the second pair of ribs (Fig. 7(a)). Once the above reattachment occurs the flow downstream will always separate at the trailing corners of the second pair of ribs, and thus a nearly constant reattachment length ($5\le PR\le 20$). For $20<PR<80$ the influence of the second rib pair on the wake flow behind the first rib pair is gradually diminishing with increasing pitch ratio and the redeveloping flow started from

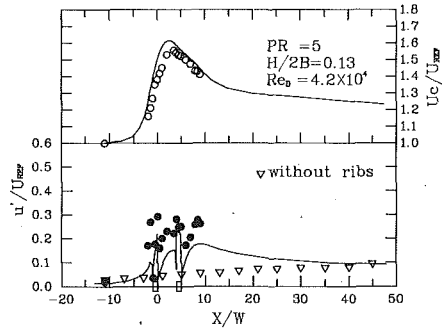

Fig. 14(a)

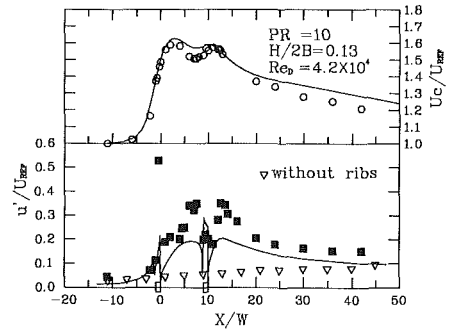

Fig. 14(b)

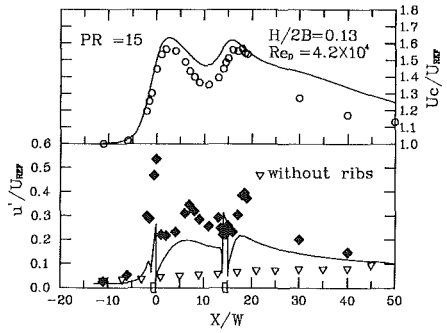

Fig. 14(c)

Fig. 14 Streamwise distributions of measured (symbols) and computed (solid line) centerline mean velocity and turbulence intensity at 1mm from the wall for (a) $PR = 5$, (b) $PR = 10$, (c) $PR = 15$. (Uncertainty in U/U_{REF}: less than ± 3.2 percent, in u'/U_{REF}: less than ± 4.4 percent, in X/W: less than ± 1.4 percent.)

$X = X_{R1}$ has increasing distance to develop. In other words, the two rib pairs become more and more independent and X_{R2} will tend to increase and approach, X_{R1}. However, Fig. 13 shows that X_{R2} will eventually become constant ($PR \geq 80$) and has a value smaller than X_{R1} since the two rib pairs have different initial-flow profiles. The initial flow for the first rib pair has an uniform profile at $X/W = -11.0$, whereas the initial flow for the second rib pair has a more complicated profile at the redeveloping point (i.e., reattachment point behind the first rib pair).

It is also of interest to observe the effect of pitch on the centerline mean velocity and the turbulence intensity at a vertical distance 1mm from the walls. First, Figs. 14(*a*) through 14(*c*) clearly reveal the presence of rib pairs enhances the local turbulence intensity near the walls. Second, for all three pitch ratios tested, a peak turbulence intensity is always found to occur at the trailing corners of the first rib pair where the flow is characterized by recirculation and steep mean velocity gradient (Figs. 7 to 10). Third, Figs. 14(*a*) and 14(*b*) depict an increase of both the flow acceleration and the local turbulence intensity from $PR = 5$ to $PR = 10$. Thus an enhancement of the local heat transfer rate is expected as PR increases from 5 to 10. Comparing Figs. 14(*b*) and 14(*c*), one finds that the combined effect of the acceleration and the turbulence enhancement provided by $PR = 10$ is slightly larger than that provided by $PR = 15$. Moreover, the previous section indicates that $PR = 15$ results in a higher pressure loss than $PR = 10$. Thus $PR = 10$ is preferable to $PR = 15$. The above observation parallels the heat transfer result of Han et al. (1985) who found that $PR = 10$ has a higher average Nusselt number than $PR = 20$ for the flow in channels with repeated turbulence promoters.

As for the comparison between the computed and measured U_C/U_{REF} and u'/U_{REF} in Fig. 14, the qualitative trends are in reasonable agreement. For u'/U_{REF}, however, it is important to point out that using the present LDV system the axial component of the velocity can only be measured to about 4mm from the leading or trailing surface of the rib. Within less than 4mm of the leading or trailing surface of the rib, one of the laser beams will be blocked by the rib. It is for this reason that the measured $u'U_{REF}$ does not reveal the rapid decrease or increase around the ribs, as shown by the computed u'/U_{REF}. Moreover, the quantitative discrepancies displayed in Fig. 14 for the distribution of u'/U_{REF} at a distance 1mm from the wall again reflect the necessity of improving the wall function and turbulence model adopted in the present computation.

Effect of Reynolds Number. The data presented above are for $Re_D = 4.2 \times 10^4$. Similar results were found for Re_D from 1.2×10^4 to 1.2×10^5 in this experiment. In fact, the reattachment length X_{R2} was found to be a weak function of the Reynolds number tested. This trend is in agreement with the results reported in Liou and Kao (1988) for a rectangular duct with a single pair of ribs. It also parallels the well-known result that for all Reynolds numbers sufficient to give turbulent boundary layer at the inlet, the reattachment length of the flow field in a suddenly enlarged duct (Moon and Rudinger, 1977) is a rather weak function of the Reynolds number.

Summary and Conclusions

The flow field in a channel with two pairs of turbulence promoters in tandem has been investigated both experimentally and computationally. The computer code incorporating the SCSUDS scheme proposed in the present study smoothly and reasonably reproduced the flow details measured by using the LDV. The three types of flow associated with the three pitch ratios examined in detail in the present study provided a good test of computational models. The reattachment length after the first rib pair was found to be a weak function of the pitch ratio, whereas the reattachment length behind the second rib pair was found to strongly depend on the pitch ratio. This contrast would also be a useful test of computational models. Large turbulent kinetic energy and significant anisotopy occurred in the shear layers and in the flow-separation regions where the current turbulence model and wall function should be improved in the future study.

Within the range of Reynolds number tested (1.2×10^4 to 1.2×10^5), the reattachment lengths behind the rib pairs appeared to vary slightly with Reynolds number. The pressure loss increased with increasing pitch ratio. It was found that $PR = 10$ was preferable to $PR = 5$ and $PR = 15$ for the reason of larger flow acceleration and turbulence enhancement and, hence, larger heat transfer enhancement expected. This finding parallels the previously reported results that $PR = 10$ provided larger average Nusselt number for channels with repeated rib pairs.

References

Abbot, D. E., and Kline, S. J., 1962, "Experimental Investigations of Subsonic Turbulent Flow over Single and Double Backward-Facing Steps," ASME *Journal of Basic Engineering*, Vol. 84, pp. 317–352.

Amano, R. S., and Goel, P., 1985, "Computations of Turbulent Flow Beyond Backward-Facing Steps Using Reynolds-Stress Closure," *AIAA Journal*, Vol. 23, pp. 1356–1361.

Amano, R. S., Geol, P., and Chai, J. C., 1988, "Turbulence Energy and Diffusion Transport of Third-Moments in a Separating and Reattaching Flow," *AIAA Journal*, Vol. 26, pp. 273–282.

Arvizu, D. E., and Moffat, R. J., 1981, "Experimental Heat Transfer from an Array of Heated Cubical Elements on a Adiabatic Channel Wall," Report HMT-33, Department of Mechanical Engineering, Stanford University, Stanford, Calif., pp. 82–83.

Benodekar, R. W., Goddard, A. J. H., Gosman, A. D., and Issa, R. I., 1985, "Numerical Prediction of Turbulent Flow Over Surface-Mounted Ribs," *AIAA Journal*, Vol. 23, pp. 359–366.

Bunditkful, S., and Yang, W.-J., 1981, "Laminar Transport Phenomena in Parallel Channels with a Short Flow Obstruction," ASME *Journal of Heat Transfer*, Vol. 101, pp. 217–221.

Cherdron, W., Durst, F., and Whitelaw, J. H., 1978, "Asymmetric Flows and Instabilities in Symmetric Ducts with Sudden Expansions," *Journal of Fluid Mechanics*, Vol. 84, Part 1. pp. 13–31.

Deshpande, M. D., and Giddens, D. P., 1980, "Turbulence Measurements in a Constricted Tube," *Journal of Fluid Mechanics*, Vol. 97, pp. 65–89.

Drain, L. E., 1980, *The Laser Doppler Technique*, Wiley, pp. 136–141.

Driver, D. M., and Seegmiller, H. L., 1985, "Features of a Reattaching Turbulent Shear Layer in Divergent Channel Flow," *AIAA Journal*, Vol. 23, pp. 163–171.

Durst, F., Founti, M., and Obi, S., 1988, "Experimental and Computational Investigation of the Two-Dimensional Channel Flow over Two Fences in Tandem," ASME JOURNAL OF FLUIDS ENGINEERING, Vol. 110, pp. 48–54.

Durst, F., and Rastogi, A. K., 1977, "Theoretical and Experimental Investigations of Turbulent Flows with Separation," *Turbulent Shear Flow, I*, edited by Durst, F., Launder, B. E., Schmidt, F. W., and Whitelaw, J. H., Springer-Verlag, Berlin, pp. 208–216.

Han, J. C., Park, J. S., and Lei, C. K., 1985, "Heat Transfer Enhancement in Channels with Turbulence Promoters," ASME *Journal of Engineering for Gas Turbine and Power*, Vol. 107, pp. 628–635.

Hung, Y.-H., Liou, T.-M., and Syang, Y.-C., 1987, "Heat Transfer Enhancement of Turbulent Flow in Pipes with Various Internal Ribs," *Advances in Enhanced Heat Transfer*, edited by Jensen, M. K. and Carey, V. P., ASME HTD, Vol. 68, pp. 55–63.

Hwang, D.-W., 1988, "Numerical Computation of Turbulent Flow and Heat Transfer in a Two-Dimensional Channel with Rectangular Ribs Applied to Walls," Master thesis, National Tsing Hua University, Hsinchu, Taiwan.

Issa, R. I., 1986, "Solution of Implicitly Discretized Fluid Flow Equations by Operator-Splitting," *Journal of Computational Physics*, Vol. 62, pp. 40–85.

Jang, D. S., Jelti, R., and Acharya, S., 1986, "Comparison of PISO, SIMPLER, and SIMPLE-C Algorithms for the Treatment of the Pressure Velocity Coupling in Steady Flow Problems," *Numerical Heat Transfer*, Vol. 10, pp. 209–228.

Launder, B. E., and Spalding, D. B., 1974, "The Numerical Computation of Turbulent Flows," *Computer Methods in Applied Mechanics and Engineering*, Vol. 3, pp. 269–289.

Leschziner, M. A., 1980, "Practical Evaluation of Three Finite Difference Schemes for the Computation of Steady-State Recirculation Flows," *Computer Methods in Applied Mechanics and Engineering*, Vol. 23, pp. 293–312.

Leschziner, M. A., 1989, "Modeling Jet Injection in Three Dimensional Swirling Flow with Reynolds-Stress Turbulence Models," Report, Dept. of Mechanical Engineering, University of Manchester, Manchester, United Kingdom, pp. 14–15.

Liou, T. M., and Kao, C. F., 1988, "Symmetric and Asymmetric Turbulent Flows in a Rectangular Duct with a Pair of Ribs," ASME JOURNAL OF FLUIDS ENGINEERING, Vol. 110, pp. 373–379.

McLaughlin, D. K., and Tiederman, W. G., 1973, "Biasing Correlation for Individual Realization of Laser Anemometer Measurements in Turbulent Flows," *Phys. of Fluids*, Vol. 16, No. 12, pp. 371–385.

Metzger, D. E., Fan, C. S., and Pennington, J. W., 1983, "Heat Transfer and Flow Friction Characteristics of Very Rough Transfer Ribbed Surfaces with and without Pin Fins," *Proceeding ASME-JSME Thermal Engineering Conference*, Vol. 1, pp. 429–436.

Moon, L. F., and Rudinger, G., 1977, "Velocity Distribution in an Abruptly Expanding Circular Duct," ASME JOURNAL OF FLUIDS ENGINEERING, Vol. 99, pp. 226–230.

Patankar, S. V., 1980, *Numerical Heat Transfer and Fluid Flow*, Hemisphere Publishing Co., New York, pp. 95–96.

Raithby, G. D., 1976, "Skew Upstream Difference Schemes for Problems Involving Fluid Flow," *Computer Methods in Applied Mechanics and Engineering*, Vol. 9, pp. 153–164.

Rastogi, A. K., Kvernvold, O., and Sontvedt, T., 1980, "Flow and Mass Transfer in a Perturbed Turbulent Pipe Flow," *Momentum and Heat Transfer Processes in Recirculating Flows*, edited by Launder, B. E. and Humphrey, J. A. C., ASME HTD, Vol. 13, pp. 91–96.

Rastogi, A. K., 1984, "Hydrodynamics in Tubes Perturbed by Curvilinear Obstructions," ASME JOURNAL OF FLUIDS ENGINEERING, Vol. 106, pp. 262–269.

Webb, R. L., Eckert, E. R. G., and Goldstein, R. J., 1971, "Heat Transfer and Friction in Tubes with Repeated-rib Roughness," *International Journal for Heat and Mass Transfer*, Vol. 14, pp. 601–617.

M. W. Lesmez
Hydraulic Research Laboratory,
City of Los Angeles, CA

D. C. Wiggert
Mem. ASME

F. J. Hatfield
Mem. ASME

Department of Civil and
Environmental Engineering,
Michigan State University,
East Lansing, Mich. 48824

Modal Analysis of Vibrations in Liquid-Filled Piping Systems

The motions of liquid-filled pipe reaches in which long wavelength assumptions are valid can be described by Poisson-coupled axial stress waves in the pipe and in the liquid column, and in the piping structure, by torsional and flexural waves. Based on linearized assumptions, a simultaneous solution of the wave equations is presented. Eigenvalues and mode shapes are derived for the variables fluid pressure and displacements, and pipe forces and displacements. The results are assembled into a transfer matrix, which represents the motion of a single pipe section. Combined with point matrices that describe specified boundary conditions, an overall transfer matrix for a piping system can be assembled. Corresponding state vectors can then be evaluated to predict the piping and liquid motion, and the accompanying forces. The results from two experimental piping systems are compared with the ones obtained by the modal analysis method.

Introduction

Free vibrations and resonance of liquid columns contained in piping systems have been topics of interest for some time, and analytical developments are presented in books by Chaudhry [1] and Wylie and Streeter [2]. The theory is based in part on the assumption that the piping system—consisting of pipe reaches, supports, valves, tees, bends, and the like—is sufficiently rigid to remain immobile, and interacts dynamically neither with the fluid oscillations nor with external loads such as machine vibrations or seismic excitation. On the other hand, well-known modal analysis techniques, e.g., Clough and Penzien [3], can be used to analyze vibrations of piping structures if the motion of the contained liquid is neglected.

It has been shown by Hatfield et al. [4] and Wilkinson [5] that under certain conditions, vibrations of liquid columns and piping structural elements can interact and respond dynamically in a manner different than if the two components were treated independently. These earlier studies, however, did not include a possibly significant coupling mechanism, namely, Poisson coupling. The effect of Poisson coupling between the pipe wall and the fluid column has been recognized by Skalak [6], Williams [7], and Walker and Phillips [8]; however, these studies dealt with transient flows in a single straight reach of pipe. Wiggert et al. [9] considered Poisson coupling in a pipe with two bends; the type of excitation was transient, and piping modes other than in the axial direction were either neglected or, in the case of a single bending mode, treated in a simplified ad hoc manner by assuming an equivalent lumped stiffness at the pipe elbows.

The motions of liquid-filled pipe reaches in which long wavelength assumptions are valid can be described by Poisson-coupled axial stress waves in the pipe and in the fluid column, and in the piping structure by torsional and flexural waves. Additional coupling takes place at piping discontinuities. Attempts have been made to solve these wave equations for transient excitation conditions using the method of characteristics [10]; unfortunately, numerical limitations have thwarted the evolution of a generalized solution methodology.

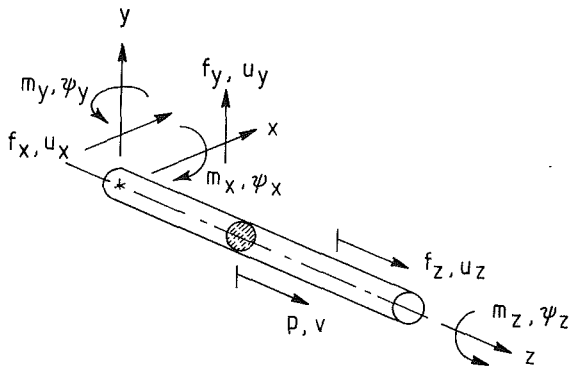

Fig. 1 Elementary liquid-filled pipe section

Based on linearized assumptions and periodic motion, a simultaneous solution of the coupled fluid-structure system equations in wave form is possible, and is presented herein. The resulting eigenvalues and mode shapes can be derived for relevant fluid and structural variables with no need to utilize finite element approximations. Wilkinson [5] has presented a similar model, but did not include the Poisson coupling, and used the Bernoulli beam equation to describe the piping flexure.

Analytical Model

Consider a piping system to consist of pipe sections (i.e., the reaches) and pipe discontinuities (i.e., bends, valves, junctions, etc.). Structural constraints are situated at the discontinuities. The differential equations describing the coupled structural and fluid motion of a single pipe section are pre-

Contributed by the Fluids Engineering Division for publication in the JOURNAL OF FLUIDS ENGINEERING. Manuscript received by the Fluids Engineering Division March 1, 1988.

Table 1 Solution of linearized equations: field transfer matrices

$$[T_{fp}] = \begin{bmatrix} \sigma C_2 - C_0 & \frac{\nu b}{h}[C_1 - (\sigma+\tau+\gamma)C_3] & \frac{\nu b}{h}\tau C_2 & -C_1 + (\sigma+\gamma)C_3 \\ 2\nu\sigma\tau C_3 & (\tau+\gamma)C_2 - C_0 & \tau[(\tau+\gamma)C_3 - C_1 & -2\nu\tau C_2 \\ 2\nu\sigma C_2 & \frac{1}{\tau}\left((\tau+\gamma)C_1 - [(\tau+\gamma)^2+\sigma\gamma]C_3\right) & (\tau+\gamma)C_2 - C_0 & 2\nu[(\sigma+\tau+\gamma)C_3 - C_1] \\ \sigma(C_2 - \sigma C_3) & -\frac{\nu b}{h}\sigma C_2 & -\frac{\nu b}{g}\sigma\tau C_3 & \sigma C_2 - C_0 \end{bmatrix} \quad (1)$$

$$\tau = \frac{\omega^2 l^2}{a_f^2} \quad (a)$$

$$\sigma = \frac{\omega^2 l^2}{a_p^2} \quad (b)$$

$$\gamma = 2\nu^2 \frac{b\sigma}{d} \quad (c)$$

$$b = \frac{r}{e} \quad (d)$$

$$d = \frac{\rho_p}{\rho_f} \quad (e)$$

$$h = \frac{E}{K^*} \quad (f) \quad (2)$$

$$C_0 = \Delta\left[\lambda_2^2\cos(\lambda_1) - \lambda_1^2\cos(\lambda_2)\right] \quad (g)$$

$$C_0 = \Delta\left[\frac{\lambda^2}{\lambda_1}\sin(\lambda_1) - \frac{\lambda_1^2}{\lambda_2}\sin(\lambda_2)\right] \quad (h)$$

$$C_2 = \Delta\left[\cos(\lambda_1) - \cos(\lambda_2)\right] \quad (i)$$

$$C_3 = \Delta\left[\frac{1}{\lambda_1}\sin(\lambda_1) - \frac{1}{\lambda_2}\sin(\lambda_2)\right] \quad (j)$$

$$\Delta = \left(\lambda_1^2 - \lambda_2^2\right)^{-1} \quad (k)$$

$$\lambda_1^2 = \frac{1}{2}\left\{(\tau+\sigma+\gamma) - \left[(\tau+\sigma+\gamma)^2 - 4\sigma\tau\right]^{1/2}\right\} \quad (l)$$

$$\lambda_2^2 = \frac{1}{2}\left\{(\tau+\sigma+\gamma) + \left[(\tau+\sigma+\gamma)^2 - 4\sigma\tau\right]^{1/2}\right\} \quad (m)$$

$$[T_{xz}] = \begin{bmatrix} C_0 - \sigma C_2 & C_1 - (\sigma+\tau)C_3 & C_2 & -\frac{1}{\gamma}[-\sigma C_1 + (\gamma+\sigma^2)C_3] \\ \gamma C_3 & C_0 - \tau C_2 & C_2 - \tau C_3 & -C_2 \\ \gamma C_2 & (\gamma+\tau^2)C_3 - \tau C_1 & C_0 - \tau C_2 & -[C_1 - (\sigma+\tau)C_3] \\ -\gamma(C_1 - \sigma C_3) & -\gamma C_2 & -\gamma C_3 & C_0 - \sigma C_2 \end{bmatrix} \quad (3)$$

(continued)

Nomenclature

A = cross-sectional area
C = transfer matrix coefficient
E = modulus of elasticity
e = thickness of pipe wall
F = force amplitude
f = force
G = shear modulus of rigidity
I = moment of inertia
J = polar moment of inertia
K = bulk modulus
K^* = modified bulk modulus
l = length of pipe section
M = moment amplitude
m = moment
P = pressure amplitude
p = pressure
r = radius of pipe cross-section
S = state vector
T = field transfer matrix
t = time
U = pipe displacement amplitude
u = pipe displacement
V = liquid displacement amplitude
v = liquid displacement
ρ = mass density
ν = Poisson's ratio
Ψ = rotation amplitude
ψ = rotation
λ = eigenvalues
σ, τ, β = transfer matrix coefficients
ω = circular frequency

Superscripts

L = left of discontinuity
R = right of discontinuity
T = matrix transposition

Subscripts

f = liquid
i = pipe end
p = pipe
x, y, z = local coordinate direction

Table 1 (*continued*)

$$\sigma = \frac{(\rho_p A_p + \rho_f A_f)}{GA_p}\omega^2 l^2 \qquad (a)$$

$$\tau = \frac{(\rho_p I_p + \rho_f I_f)}{EI_p}\omega^2 l^2 \qquad (b)$$

$$\gamma = \frac{(\rho_p A_p + \rho_f A_f)}{EI_p}\omega^2 l^4 \qquad (c)$$

$$C_0 = \Delta\left[\lambda_2^2\cosh(\lambda_1) + \lambda_1^2\cos(\lambda_2)\right] \qquad (d)$$

$$C_1 = \Delta\left[\frac{\lambda_2^2}{\lambda_1}\sinh(\lambda_1) + \frac{\lambda_1^2}{\lambda_2}\sin(\lambda_2)\right] \qquad (e) \quad (4)$$

$$C_2 = \Delta\left[\cosh(\lambda_1) - \cos(\lambda_2)\right] \qquad (f)$$

$$C_3 = \Delta\left[\frac{1}{\lambda_1}\sinh(\lambda_1) - \frac{1}{\lambda_2}\sin(\lambda_2)\right] \qquad (g)$$

$$\Delta = \left(\lambda_1^2 + \lambda_2^2\right)^{-1} \qquad (h)$$

$$\lambda_1^2 = \left(\gamma + \frac{1}{4}(\sigma-\tau)^2\right)^{1/2} - \frac{1}{2}(\sigma+\tau) \qquad (i)$$

$$\lambda_2^2 = \left(\gamma + \frac{1}{4}(\sigma-\tau)^2\right)^{1/2} + \frac{1}{2}(\sigma+\tau) \qquad (j)$$

$$[T_{yz}] = \begin{bmatrix} C_0 - \sigma C_2 & -[C_1 - (\sigma+\tau)C_3 & -C_2 & -\frac{1}{\gamma}[-\sigma C_1 + (\gamma+\sigma^2)C_3] \\ -\gamma C_3 & C_0 - \tau C_2 & C_1 - \tau C_3 & C_2 \\ -\gamma C_2 & (\gamma+\tau^2)C_3 - \tau C_1 & C_0 - \tau C_2 & [C_1 - (\sigma+\tau)C_3] \\ -\gamma(C_1 - \sigma C_3) & \gamma C_2 & \gamma C_3 & C_0 - \sigma C_2 \end{bmatrix} \qquad (5)$$

$$[T_{tz}] = \begin{bmatrix} -\cos(\lambda) & -\frac{1}{\lambda}\sin(\lambda) \\ \lambda\sin(\lambda) & -\cos(\lambda) \end{bmatrix} \qquad (6)$$

$$\lambda^2 = \omega^2 l^2 \frac{\rho_p}{G} \qquad (7)$$

sented in the Appendix. Assumptions include: long waves; negligible fluid friction; low Mach numbers; absence of liquid column separation; linear elastic behavior of piping material; no buckling; negligible damping; and negligible inertia in the radial direction. Figure 1 shows a representative pipe reach, the local *x-y-z* coordinate system, and the fourteen unknown variables.

Solution of Linearized Equations; Field Transfer Matrices. Solutions are sought for periodic motion in the form of exp ($i\omega t$). Following a separation of variables technique they are given in the field transfer matrix forms shown as equations (1)–(7) in Table 1.

The solutions can be assembled in an overall field transfer matrix for the given pipe section:

$$\{S\}_i = [T]\{S\}_{i-1} \qquad (8)$$

in which

$$[T] = \begin{bmatrix} [T_{fp}] & & & \\ & [T_{xz}] & & \\ & & [T_{yz}] & \\ & & & [T_{tz}] \end{bmatrix} \qquad (9)$$

and the state vector is

$$\{S\} = \left[\frac{U_z}{l}, \frac{P}{K^*}, \frac{V}{l}, \frac{F_z}{A_p E}, \frac{U_x}{l}, \Psi_y, \frac{M_y l}{EI_p}, \frac{F_x l^2}{EI_p}, \frac{U_y}{l}, \Psi_x, \frac{M_x l}{EI_p}, \frac{F_y l^2}{EI_p}, \Psi_z, \frac{M_z l}{GJ_p}\right]^T \qquad (10)$$

Point Matrices and Boundary Conditions. A transfer field matrix for each pipe section in a network system is assembled. Connectivity of the section equations to the network is accomplished by formulating point matrices at the piping discontinuities. These point matrices account for the transfer of forces and displacements from one pipe section to another, as well as dynamic coupling between the fluid and structure at that location. In addition, the point matrices include boundary conditions which are given at specified locations in the network.

As an example, consider the pipe bend discontinuity shown in Fig. 2. It is connected to a pipe section at each end and makes an angle α with the vertical direction. Force and moment equilibria in the respective coordinate directions are maintained, and in addition, conservation of mass of liquid and continuity of the structural components are satisfied assuming constant material properties. The resulting point transfer matrix equation is

$$\begin{Bmatrix} P \\ \Psi_x \\ U_y \\ U_z \\ V \\ M_x \\ F_y \\ F_z \end{Bmatrix}_R = \begin{bmatrix} 1 & 0 & 0 & 0 & 0 & 0 & 0 & 0 \\ 0 & 1 & 0 & 0 & 0 & 0 & 0 & 0 \\ 0 & 0 & \cos\alpha & -\sin\alpha & 0 & 0 & 0 & 0 \\ 0 & 0 & \sin\alpha & \cos\alpha & 0 & 0 & 0 & 0 \\ 0 & 0 & \sin\alpha & -(1-\cos\alpha) & 1 & 0 & 0 & 0 \\ 0 & 0 & 0 & 0 & 0 & 1 & 0 & 0 \\ A_f\sin\alpha & 0 & 0 & 0 & 0 & 0 & \cos\alpha & -\sin\alpha \\ A_f(1-\cos\alpha) & 0 & 0 & 0 & 0 & 0 & \sin\alpha & \cos\alpha \end{bmatrix} \begin{Bmatrix} P \\ \Psi_x \\ U_y \\ U_z \\ V \\ M_x \\ F_y \\ F_z \end{Bmatrix}_L \tag{11}$$

Additional point matrices [*P*] can be formulated for multiple pipe junctions, dead ends, valves, pumps, surge devices and the like [1, 2, 5]. Point matrices [*P*] for structural members such as springs, rigid supports, and external forces are described by Pestel and Leckie [11] and Lesmez [12].

Global Transfer Matrix for Piping System. A global transfer matrix which relates the state vector at one end of the piping system to that at the other end is obtained by a systematic multiplication of the interior point and field matrices along a defined path:

$$\{S\}_i = [T][P][T] \ldots . \{S\}_N \tag{12}$$

Branching and parallel segments of the piping system are handled in a manner described by Chaudhry [1] or Wylie and Streeter [2]. Setting the determinant of equation (12) to zero and solving the eigenvalue problem will produce natural frequencies and corresponding mode shapes.

Application

Results from two experimental studies are employed to verify the analytical method, as well as, show the various piping configurations that can be analyzed. The first experiment was reported by Davidson and Smith [13], and the second by Lesmez [12].

Example 1: Single Pipe Bend. Consider the pipe bend shown in Fig. 3; pertinent data for the system are given in Table 2. Excitation is provided by fluid oscillation at location A. The pipe section has been extensively analyzed and compared with experimental data. The previous modeling efforts included direct analytical solution of simultaneous differential equations [13], and component synthesis using finite element discretization (Nastran) for the structural elements [14]. The present modeling makes use of the transfer matrix technique embodied in equation (12). Seven pipe sections are used to model the piping, see Fig. 3. The three sections CD, DE, and DF, which define the pipe bend, are considered to be mitered short straight sections. Flexural stiffness of these sections were reduced by an ovalization factor [15].

Predicted mobility amplitudes at three locations are shown in Fig. 4: (*a*) liquid mobility at location A; (*b*) liquid mobility at location F; and (*c*) pipe mobility at location H. Here mobility is defined as the ratio velocity to force. Experimental data [13] are shown along with the predictions. The predictions based on the transfer matrix method follow the experimental trends, and although not shown herein, they match well with the earlier predictions [13, 14]. Table 3 shows a comparison between the natural frequencies predicted using the transfer matrix method and a Nastran finite element prediction of the liquid-filled piping. In the latter prediction, fluid-structure interaction was not included.

Example 2: Piping System With U-Bend

Apparatus. The components of the experimental apparatus include pressurized tanks, piping, an external shaker and data acquisition equipment [16]. Table 2 describes the properties of the piping and liquid used in the experiments. The piping

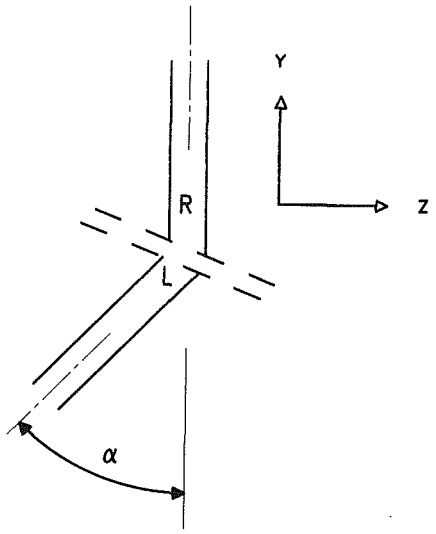

Fig. 2 Pipe bend discontinuity

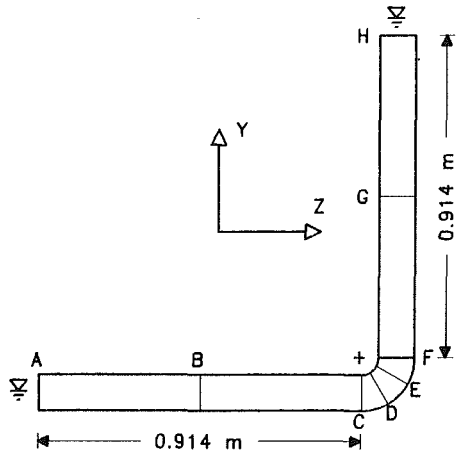

Fig. 3 Single bend piping system (example 1)

consisted of three main sections as shown in Fig. 5. The first section is between the closed-end and the U-type bend; a rigid support is located between these two sections. The second section is a U-type bend with legs 1.82 meters long; it is free to move in an in-plane fashion. The last section is between the U-bend and the open end. Another rigid support is located between the U-bend and the last section. No pipe motion is allowed at either end. The external shaker is a crank mechanism consisting of a variable-speed motor, flywheel, and a driving arm. The driving arm is connected to the pipe by a stiff spring. The data acquisition equipment consisted of PCB-manufactured pressure transducers (Model 111A26) and accelerometers (Model 302A) coupled to a Digital PDP-11/73 computer.

Table 2 Properties of experimental piping

	Single bend (example 1)	U-bend (example 2)
Material	70% Cu, 30% Ni	Copper
Density (kg/m^3)	9000	8900
Modulus of elasticity (GPa)	157	117
Poisson's ratio	0.34	0.35
Outside diameter (mm)	114	28.6
Inside diameter (mm)	102	26.0
Radius of bends (mm)	102	---
Boundary conditions at pipe ends	fixed-free	fixed-fixed
Liquid	Oil	Water
Density (kg/m^3)	872	997
Bulk modulus (GPa)	1.95	2.20
Liquid boundary conditions at pipe ends	closed-open	closed-open

Table 3 Natural frequencies in Hz for single pipe bend (example 1)

Transfer matrix	Nastran [13] (pipe only)
22	22
48	48
193 F	
299	305
393	391
516 F	
788	758
859 F	
970	929
1141	1139
1236 F	
1522	1539
1615 F	
1843	1761
1916 F	
2093	2056

F - designates fluid mode of excitation

Structural displacements were obtained by using PCB integrator/amplifiers. The transducers measure dynamic responses; the estimated accuracies are ±2 mm over a range of 40 mm for the displacements. The natural frequencies are 400 and 45 kHz for the pressure and accelerometer transducers, respectively. Additional details are provided in Reference [12].

Procedure. Two piping configurations were used to study the liquid and structural responses. Configuration *A* is 80.14 meters long whereas configuration *B* is 55.69 meters in length. The length difference is due to the shorter distance between the closed end and the U-bend for configuration *B*. Figure 5 is a diagram of the piping configurations. The length of each pipe reach is given in Table 4.

Two types of experiments were performed. The first consisted of changing the speed of the motor, and therefore the frequency of excitation, from 3 Hz to 32 Hz. A total of 66 frequency readings were taken for that frequency range. Displacements at locations D1 and D2, and pressures at locations P1 and P2, Fig. 5, were recorded for each frequency. The sampling rate for all frequency readings was 1000 Hz, and the total sampling time for each frequency was 4096 milliseconds. A time interval of 30 seconds between samplings was allowed so the system could return to steady-state conditions. The second type of experiment involved recording the system responses at natural frequencies. Signals from the pressure transducer P1 and the accelerometer D1 were input to an oscilloscope. The frequency was adjusted until either a liquid or structural response reached a peak. Then responses at the four locations were sampled. Subsequent to sampling, a fast

(a) Amplitude of mobility of liquid at A

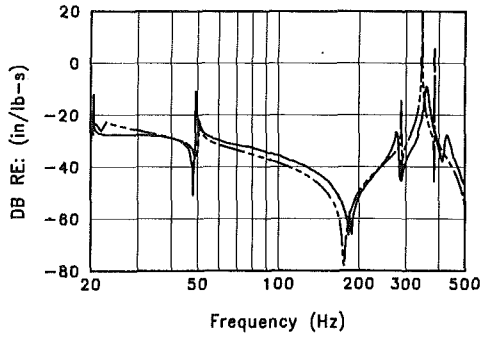

Fig. 4(*a*)

(b) Amplitude of mobility of liquid at F

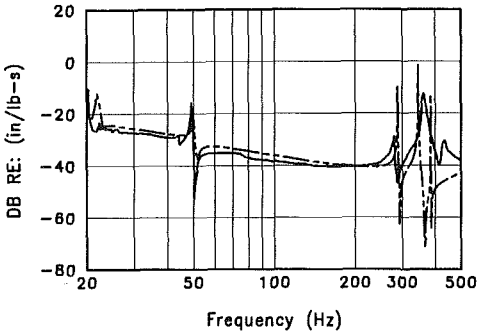

Fig. 4(*b*)

(c) Amplitude of mobility of pipe at H, Y direction

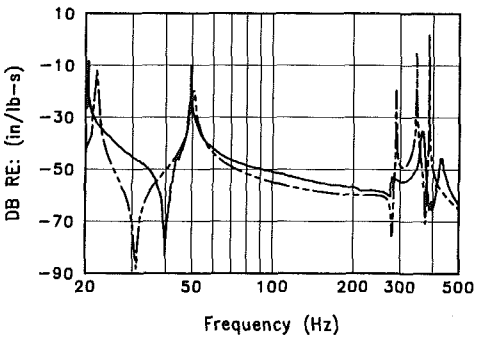

Fig. 4(*c*)

Fig. 4 Mobility diagrams for single bend system (——— experimental; — - - — prediction)

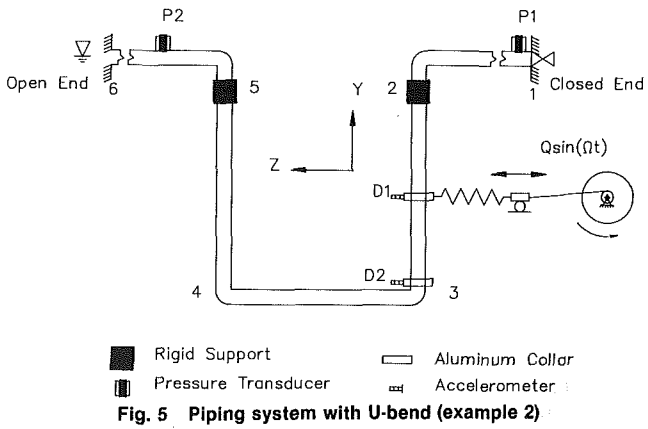

Fig. 5 Piping system with U-bend (example 2)

Table 4 Piping configuration for U-bend (example 2)

Section	Reach	Config. A length (m)	Config. B length (m)
1	1-P1	0.14	0.14
	P1-2	24.88	0.44
2	2-D1	0.91	0.91
	D1-D2	0.83	0.83
	D2-3	0.09	0.09
	3-4	1.83	1.83
	4-5	1.83	1.83
3	5-P2	0.61	0.61
	P2-6	49.02	49.01
	Total	80.14	55.69

P = pressure transducer, D = accelerometer

Table 5 Experimental versus computed results for configuration A (example 2)

			Displacement (mm)			Pressure (kPa)		
Freq. (Hz)	Type	Location	Location D1	Location D2	Ratio D2/D1	Location P1	Location P2	Ratio P2/P1
3.9	E	F1	1.7	3.5	2.1	102	80	0.78
4.0	C				2.8			0.81
4.4	E	S1	12.9	38.5	3.0	99	119	1.20
4.4	C				2.8			1.18
12.0	E	F3	0.4	0.1	0.3	41	10	0.24
12.0	C				2.3			0.24
18.1	E	S2	9.3	2.0	0.2	0	7	--
17.5	C				0.5			18.53
19.8	E	F5	0.3	0.2	0.7	36	34	0.94
19.7	C				0.8			0.97
27.8	E	F9	1.7	0.3	0.2	290	118	0.41
27.4	C				0.2			0.46
28.6	E	S3	6.4	1.6	0.3	154	145	0.94
28.6	C				0.2			1.53

E = experimental, C = computed, F = fluid, S = structural frequency

Table 6 Experimental versus computed results for configuration B (example 2)

			Displacement (mm)			Pressure (kPa)		
Freq. (Hz)	Type	Location	Location D1	Location D2	Ratio D2/D1	Location P1	Location P2	Ratio P2/P1
4.4	E	S1	11.8	30.2	2.1	49	8	0.16
4.4	C				2.3			0.21
5.6	E	F1	0.3	1.8	6.0	11	8	0.73
5.6	C				2.3			0.99
17.1	E	F2	1.2	0.1	0.1	18	16	0.89
16.8	C				0.0			0.94
18.1	E	S2	3.9	0.7	0.2	0	0	--
16.9	C				0.0			0.87
28.3	E	F3	3.1	0.6	0.2	521	310	0.60
27.9	C				0.5			0.57
28.8	E	S3	5.2	1.3	0.3	239	225	0.94
28.4	C				0.5			0.88
29.8	C	S4						

E = experimental, C = computed, F = fluid, S = structural frequency

Fourier transform analysis was performed to find the natural frequencies and amplitude of the responses for each of the four signals. This process was completed for each of the 66 forcing frequencies.

Results. The experimental and computed results for the two pipe configurations are given in Tables 5 and 6. Figure 6 shows the computed pressure mode shapes at the structural natural frequencies, and Fig. 7 shows the computed pressure mode shapes at the fluid natural frequencies. Experimental fluid

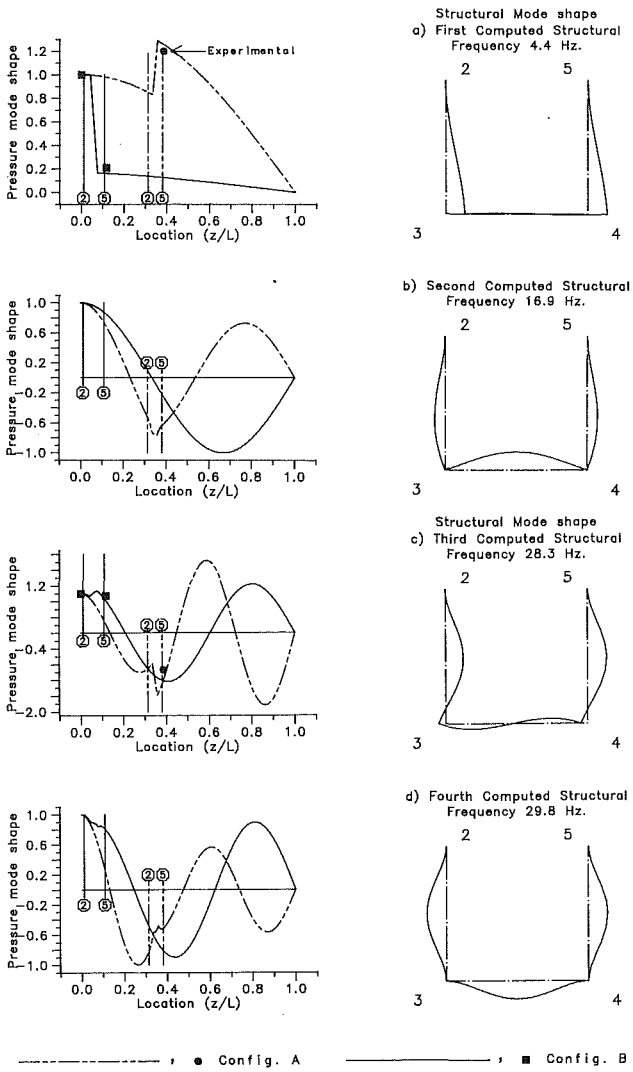

Fig. 6 Liquid pressure mode shapes at structural frequencies

pressure responses are also plotted in Figs. 6 and 7. The numbers 2 and 5 in these two figures correspond to the ends of the U-bend.

The largest experimental pressure responses at the closed end occurred at the ninth (27.8 Hz) fluid harmonic for configuration *A*, and at the third (28.3 Hz) fluid harmonic for configuration *B*. These large fluid pressure responses are associated with the third structural frequency (28.7 Hz). There is a slight motion of the elbows (locations 3 and 4 in Fig. 1) at this frequency, as shown in Fig. 6(*c*). This elbow motion interacts with the fluid through the junction coupling mechanism, amplifying the fluid response. These results can be compared with the findings of Jaeger [16], who reported several incidents of hydraulic resonance, and pointed out the significance of vibrations from higher fluid harmonics.

Liquid and structural natural frequencies are in good agreement. The largest discrepancy occurs at the second structural frequency. This frequency is associated with the second mode shape as shown in Fig. 6(*b*). This mode reveals large motion at approximately the mid-points of each leg. The added mass, at D1, Fig. 5, introduced to the system by the weight of the accelerometer, and the attachments of the piping to the shaker were not included in the computed model. The magnitude of the experimental responses cannot be compared with the analytical model since the model includes neither structural damping nor fluid friction.

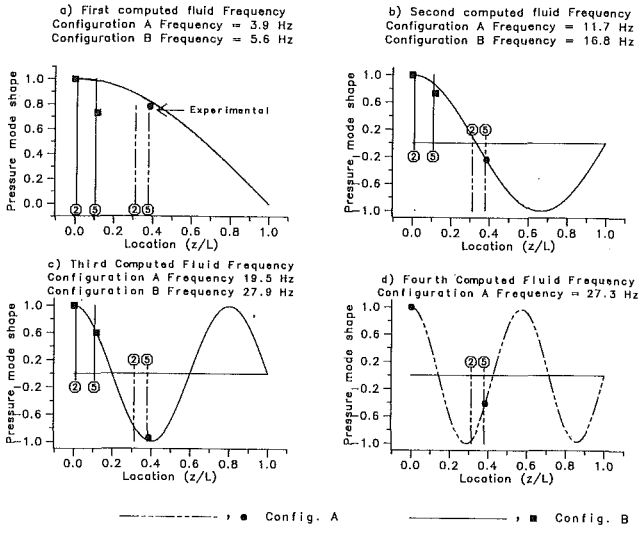

Fig. 7 Liquid pressure mode shapes

The pressure ratios in Tables 5 and 6, and plotted in Figs. 6 and 7, show good agreement between the experimental and analytical results at the fluid natural frequencies. The largest discrepancy for the fluid pressure occurs at the second structural natural frequency; here the magnitude of the experimental fluid pressure is small, which may introduce a measurement error. The displacement ratios between the experimental and computed results are better at the structural than at the fluid natural frequencies. The pressure ratios match better than the displacement ratios for both configurations.

Summary

The transfer matrix method for analysis of fluid structure interaction in piping systems provides an alternative to reported numerical and analytical methods. In addition, the appropriate coupling mechanisms are properly accounted for; this includes distributed Poisson coupling which cannot be modeled by the conventional methods. All of the long wave motion in the piping and the liquid is represented. Modes of the piping cross-section have not been included, inasmuch as they tend to occur beyond the range of frequencies for those of interest in most piping systems.

The results from the two experimental systems presented serve to verify the method as well as show the type of system configuration which can be analyzed. The extension to more complex piping geometries is straightforward: beyond what is presented herein, it is necessary only to define additional point matrices for various types of discontinuities and couple them with the field transfer matrices for the pipe sections to form a global transfer matrix.

Acknowledgment

This material is based upon work supported by the National Science Foundation under grant No. MEA-8401339.

References

1 Chaudhry, M. H., *Applied Hydraulic Transients*, Van Nostrand Reinhold, 1987.

2 Wylie, E. B., Streeter, V. L., *Fluid Transients*, FEB Press, 1983.

3 Clough, R. W., and Penzien, J., *Dynamics of Structures*, McGraw-Hill, 1975.

4 Hatfield, F. J., Wiggert, D. C., and Otwell, R. S., "Fluid-Structure Interaction in Piping by Component Synthesis," ASME JOURNAL OF FLUIDS ENGINEERING, Vol. 104, No. 4, Sept. 1982, pp. 318–325.

5 Wilkinson, D. H., "Acoustic and Mechanical Vibrations in Liquid Filled Pipework Systems," *Proceedings of the Vibration in Nuclear Plant Conference*, British Nuclear Engineering Society, May 1978.

6 Skalak, R., "An Extension of the Theory of Water Hammer," *Trans.* ASME, Vol. 78, No. 1, 1956, pp. 105–116.

7 Williams, D. J., "Waterhammer in Non-Rigid Pipes: Precursor Waves and Mechanical Damping," *Journal of Mechanical Engineering Science*, Institute of Mechanical Engineers, Vol. 19, No. 6, 1977, pp. 237–242.

8 Walker, J. S., and Phillips, J. W., "Pulse Propagation in Fluid Tubes," ASME *Journal of Applied Mechanics*, March 1977, pp. 31–35.

9 Wiggert, D. C., Otwell, R. S., and Hatfield, F. J., "The Effect of Elbow Restraint on Pressure Transients," ASME JOURNAL OF FLUIDS ENGINEERING, Vol. 107, No. 3, Sept. 1985, pp. 402–406.

10 Wiggert, D. C., Hatfield, F. J., and Stuckenbruck, S., "Analysis of Liquid and Structural Transients in Piping by the Method of Characteristics," ASME JOURNAL OF FLUIDS ENGINEERING, Vol. 109, No. 2, June 1987, pp. 161–165.

11 Pestel, E. C., and Leckie, F. A., *Matrix Methods in Elasto Mechanics*, McGraw-Hill, 1963.

12 Lesmez, M. W., "Modal Analysis of Vibrations in Liquid-Filled Piping Systems," Ph.D. dissertation, Michigan State University, 1989.

13 Davidson, L. C., and Smith, J. E., "Liquid-Structure Coupling in Curved Pipes," *Shock and Vibration Bulletin*, No. 40, Part 4, Dec. 1969, pp. 197–207.

14 Hatfield, F. J., Davidson, L. C., and Wiggert, D. C., "Experimental Validation of the Component Synthesis Method for Predicting Vibration of Liquid-Filled Piping," *Shock and Vibration Bulletin*, No. 53, Part 2, May 1983, pp. 1–10.

15 Vigness, I., "Elastic Properties of Curved Tubes," *Trans.* ASME, Vol. 65, 1943, pp. 105–117.

16 Jaeger, C., "The Theory of Resonance in Hydropower Systems. Discussion of Incidents and Accidents Occurring in Pressure Systems," ASME *Journal of Basic Engineering*, Vol. 85, Dec., 1963, p. 631.

APPENDIX

Fundamental Equations of Fluid and Structural Elements

Liquid pressure and displacement; axial pipe stress and displacement:

$$f_z \quad -A_p\nu\frac{r}{e}p - EA_p\frac{\partial u_z}{\partial z} = 0 \qquad (a)$$

$$\frac{\partial f_z}{\partial z} = \rho_p A_p\frac{\partial^2 u_z}{\partial t^2} = 0 \qquad (b)$$

$$p \quad +K^*\frac{\partial v}{\partial z} - 2\nu K^*\frac{\partial u_z}{\partial z} = 0 \qquad (c) \quad (13)$$

$$\frac{\partial p}{\partial z} + \rho_f\frac{\partial^2 v}{\partial t^2} = 0 \qquad (d)$$

$$K^* = \frac{K}{1+\dfrac{2Kr(1-\nu^2)}{Ee}} \qquad (e)$$

Flexure in the x-z plane:

$$m_y \quad -EI_p\frac{\partial \psi_y}{\partial z} = 0 \qquad (a)$$

$$f_x \quad -GA_p\left(\frac{\partial u_x}{\partial z} - \psi_y\right) = 0 \qquad (b) \qquad (14)$$

$$\frac{\partial f_x}{\partial z} \quad -(\rho_p A_p + \rho_f A_f)\frac{\partial^2 u_x}{\partial t^2} = 0 \qquad (c)$$

$$\frac{\partial m_y}{\partial z} + f_x - (\rho_p I_p + \rho_f I_f)\frac{\partial^2 \psi_y}{\partial t^2} = 0 \qquad (d)$$

Flexure in the y-z plane:

$$
\begin{aligned}
m_y &- EI_p \frac{\partial \psi_x}{\partial z} = 0 && (a)\\
f_y &- GA_p\left(\frac{\partial u_y}{\partial z} + \psi_x\right) = 0 && (b)\\
\frac{\partial f_y}{\partial z} &- (\rho_p A_p + \rho_f A_f)\frac{\partial^2 u_y}{\partial t^2} = 0 && (c)\\
\frac{\partial m_x}{\partial z} &- f_y - (\rho_p I_p + \rho_f I_f)\frac{\partial^2 \psi_x}{\partial t^2} = 0 && (d)
\end{aligned}
\tag{15}
$$

Torsion about the z-axis:

$$
\begin{aligned}
m_z &- GJ_p \frac{\partial \psi_z}{\partial z} = 0 && (a)\\
\frac{\partial m_z}{\partial z} &- \rho_p J_p \frac{\partial^2 \psi_z}{\partial t^2} = 0 && (b)
\end{aligned}
\tag{16}
$$

Flow Regulation Characteristics of Thin-Walled Compliant Tubes: Part I—Theoretical Analysis

Ifiyenia Kececioglu
Assistant Professor,
Department of Mechanical Engineering,
The University of Illinois at Chicago,
Chicago, Ill. 60680

The objective of this investigation is the study of the flow limitation behavior of thin-walled compliant tubes for the design of a flow regulator employing a collapsible tube as its active element. In this paper, the theoretical basis is set up for the high-Reynolds-number wave-speed flow regulation and the low-Reynolds-number frictional flow regulation behaviors of thin-walled compliant tubes. In Part II of this paper [1], experimental results and design criteria are provided in support of the analytically derived characteristic flow regulation curve for the wave-speed flow regulator.

1 Introduction

The flow of fluids in thin-walled highly compliant tubes is very strongly coupled to the structural mechanics of the tube, especially when the tube is partially collapsed because of an internal pressure less than that acting externally. This strong coupling is the central feature underlying many diverse phenomena observed in flows through collapsible tubes. They include a wide variety of steady and unsteady flows of both incompressible and compressible fluids. They span the whole range from friction-dominated low Reynolds number flows to inertia-dominated high Reynolds number flows which may be either stable or unstable. Collapsible tube flows exhibit many phenomena analogous to those found in gas-dynamics and free-surface gravity flows such as wave propagation, flow limitation, transition from subcritical to supercritical flow, frictional choking, and shock-like transitions. A wide variety of physiological, diagnositic, and therapeutic applications as examples of flow in collapsible tubes have been identified and described by Shapiro [2, 3]. Collapsible tube flow behavior may also be exploited for engineering applications such as fluidic switching, logic operations, amplification [4, 5], and flow regulation. In this paper we wish to investigate the flow limitation characteristics of uniform collapsible tubes with a view to designing a fluid flow regulator and specifying the characteristic regulation curve of flow rate as a function of imposed pressure differences.

Thin-walled, highly compliant tubes collapse very easily under small negative transmural pressures (transmural pressure ≡ internal pressure minus external pressure) of the order of a few centimeters of water. The static pressure-area relationship for uniformly deformed tubes is highly nonlinear and, for negative transmural pressures, small changes in transmural pressure result in large changes in cross-sectional area (see Fig. 1). Consequently, the speed of propagation of small-amplitude area waves based on the inviscid one-dimensional fluid flow equations is very small in the collapsed state and rises abruptly to much larger values for positive transmural pressures (see Fig. 2). As a result, the mean speed of fluid flow through collapsible tubes, may reach and even exceed the speed of propagation of small-amplitude area waves. As in gas-dynamic flows and in free-surface open-channel flows, no disturbances can travel upstream beyond the critical point at which the mean flow speed and the wave speed are equal. Therefore, conditions downstream of this point can have no influence on the flow rate. Further, the flow rate cannot exceed its maximum value which is equal to the product of the cross-sectional area and the local wave speed at the critical point, and thus flow limitation occurs. In collapsible-tube flows, the dimensionless number that is analogous to the Mach number in gas-dynamics and the Froude number in free-surface open channel flows is the speed index, S [$S \equiv$ (mean flow speed)/(speed of propagation of small-amplitude area waves) $= u/c$] (see Table 1). Griffiths [6 to 10] was the first to identify the speed index S as the controlling parameter of steady, one-dimensional flows. Griffiths discovered that, as in gas-dynamic flows, friction has the effect of decreasing area and pressure in the direction of flow when $S<1$ and that it has the opposite effect for $S>1$. Oates [11] extended the work of Griffiths by showing how the changes in flow variables depend on the simultaneous effects of wall friction, wall properties, resting area, and elevation in the gravity field. Oates [12] also considered shock-like transitions and the propagation of finite-amplitude waves. He identified the property of the tube law $(3+\alpha(d^2\hat{P}/d\alpha^2)/(d\hat{P}/d\alpha))$ that governs the steepening or broadening of compression waves, where, $\hat{P} \equiv (p-p_e)/K_B$, is the ratio of the transmural pressure to the bending stiffness of the tube wall in the plane of the cross-sectional area; $\alpha \equiv A/A_o$, is the dimensionless area ratio evaluated with respect to A_o, i.e., the cross-sectional area at zero transmural pressure. This parameter was also identified by Shapiro [3] as M, the determinant of nonlinear steepening or broadening of propagating finite-amplitude waves. The nonlinear steepening

Contributed by the Fluids Engineering Division for publication in the JOURNAL OF FLUIDS ENGINEERING. Manuscript received by the Fluids Engineering Division August 17, 1989.

of propagating finite-amplitude waves leads to the formation of shock waves. The formation of shock waves in collapsible tubes has been experimentally observed by Griffiths [7] and theoretically partially explained on the basis of the propagation and steepening of area waves by Oates [12] and Shapiro [3]. The first quantitative measurements made to characterize either the trans-shock jump conditions or the detailed structure of such waves was first reported by Kececioglu et al. [13], Kececioglu [14], McClurken [15], Kececioglu et al. [16], and McClurken et al. [17]. Kececioglu [14] provided the first theoretical formulations that successfully modelled the experimental observations. Accordingly, the following conclusions were drawn about the prominent features of shock waves in collapsible tubes. They are:

- The wave speed that is relevant to the problem is the speed of small-amplitude inviscid waves, c, where $c \equiv \sqrt{(A/\rho)[d(p-p_e)/dA]}$. The controlling parameter of the one-dimensional flow problem is the speed index S ($S \equiv u/c$).
- The inlet flow is supercritical ($S > 1$).
- A large change in cross-sectional area is achieved in a relatively short distance (exit to inlet area ratios of about 5 were observed over a distance of three tube diameters).
- Large longitudinal wall curvatures are prevalent.
- Large losses in stagnation pressure across the shock have been measured. This is probably due to flow separation and conversion of mean flow energy into turbulent eddy energy.
- Standing precursor area and pressure waves of substantial amplitudes are observed to precede the shock.
- Once a shock is established in the tube, the upstream conditions, including the flow rate, become independent of changes in downstream conditions. (This is consistent with the flow limitation behavior observed in gas-dynamic shocks and hydraulic jumps in free-surface channel flows.)

The objective of this paper is to set up the theoretical basis for the characterization of the flow regulation behavior of thin-walled compliant tubes due to either high-Reynolds-number wave-speed flow limitation or low-Reynolds-number frictional flow limitation.

2 Formulation of the Governing Equations

The highly nonlinear pressure-area relationship of a collapsible tube leads to strong coupling between the mechanics of the tube wall and the mechanics of the fluid flow through it. In particular, when the fluid inertia in a uniformly collapsed compliant tube is important, wave-speed-induced flow limitation can occur. As a result, if a region of supercritical flow is present, then conditions upstream of it, including the flow rate, are independent of the downstream flow conditions. If, in addition, a shock wave forms downstream of the supercritical region, although the position of the shock will depend on the downstream pressure, upstream conditions will remain independent of it. In a collapsible tube, flow limitation can also be observed when the fluid flow is dominated by viscous forces. Then, the highly nonlinear flow-conductivity-transmural-pressure relationship of a collapsible tube again results in the flow rate being relatively unaffected by the downstream pressure when the tube is partially collapsed at its downstream end [18].

The purpose of this study is to provide the fundamental tools needed for the design of a flow regulator whose function is to maintain the flow rate constant, independent of downstream pressure variations, when it is connected to a fluid supply at fixed pressure (see Fig. 3). Expressions will be developed for predicting the flow rate as a function of downstream pressure, namely the regulation characteristic curve.

2.1 The Constitutive Relation Governing the Compliant Tube Deformation. The coupling between the deformation of the tube wall and the mechanics of the fluid flow takes place through a constitutive relationship which is a property of the tube alone and is an expression that relates the transmural pressure across the tube wall to the cross-sectional area of the tube. For a uniformly collapsed tube with constant, nonretarded wall properties, the constitutive law provides a unique relationship between the two variables. In this sense, it is analogous to the equation of state for gases in gas-dynamics, and to the relationship between fluid pressure and the depth below the surface in open-channel flows.

Nomenclature

A = cross-sectional area of the compliant tube
A_0 = resting area or area of the compliant tube at zero transmural pressure
A_R = known cross-sectional area of rigid reference section in the experimental apparatus
a = area-probe cross-sectional area
c = speed of propagation of small-amplitude inviscid area waves
D_0 = diameter corresponding to resting area A_0
D_h = hydraulic diameter for tube; $D_h \equiv 4A/P$
E = Young's modulus
f = friction factor ($\tau_w \equiv 1/2\rho u^2 f$)
K_E = extensional stiffness of tube wall
K_B = bending stiffness of tube wall
K_L = loss coefficient related to K_e by equation (36)
K_c = contraction loss coefficient
K_e = expansion loss coefficient
L_R = length between two electrodes in reference section of experiment
L_P = length between two electrodes mounted on the pressure-area catheter probe
M = parameter that determines the nonlinear steepening or broadening of propagating compliant-tube area waves of finite amplitude
P = wetted perimeter of compliant tube
$\hat{P}$ = normalized transmural pressure ($\hat{P} \equiv (p-p_e)/K_B$)
Po_i = stagnation pressure at inlet to flow regulator
$\hat{P}_B$ = normalized buckling transmural pressure
$\hat{P}_L$ = normalized transmural pressure at line contact initiation
$\hat{P}_P$ = normalized transmural pressure at point contact initiation
p = pressure inside the compliant tube
p_c = pressure inside tube at constriction
p_e = external pressure
$\hat{p}_e$ = effective external pressure
$(p-p_e)_x$ = effective contribution to $(p-p_e)$ from the wall stresses due to longitudinal deformations of the tube wall

The manner in which a thin-walled compliant tube resists deformation in the distended state under positive transmural pressures is very different from that in the collapsed state under negative transmural pressures. When distended, the cross-sectional area of the tube is circular, and its size is determined by a balance between the *membrane hoop stresses* and the in-plane *extensional stiffness* of the tube wall. When collapsed, the shape of the cross-section is usually oval or twin-lobed, depending upon the degree of collapse. Its shape and size is then determined primarily by a balance between the *bending moment* exerted on each wall element by the negative transmural pressure and the *bending stiffness* of the tube wall. Since the bending stiffness is much smaller than the extensional stiffness of the tube wall, the tube suffers very large changes in cross-sectional area under relatively small negative transmural pressures as indicated in Fig. 1. As the degree of collapse increases, the opposite sides of the tube wall first come into point contact and subsequently make line contact. Treloar [19] showed experimentally that under positive transmural pressure for both large and small deformations the hoop tension per unit length T_θ can be related to the elastic properties of the wall (Poisson's ratio ν and Young's Modulus E) and the tube dimensions (thickness t, current radius R, and radius at zero transmural pressure R_o) by the expression

$$T_\theta = \frac{Et}{2(1+\nu)}\left[\left(\frac{R}{R_o}\right) - \left(\frac{R_o}{R}\right)^3\right] . \tag{1}$$

Furthermore, the balance between the hoop tension and the positive transmural pressure $(p-p_e)$ yields

$$T_\theta = (p-p_e)R . \tag{2}$$

Combining equations (1) and (2) we obtain an expression for the pressure-area relationship for a uniformly distended, thin, elastic tube in terms of the extensional stiffness of the tube wall $K_E \equiv E(t/R_o)^3/[12(1-\nu^2)]$, given by

$$(p-p_e) = K_E\left(1 - \frac{1}{\alpha^2}\right) . \tag{3}$$

The speed of propagation of small area waves for $\alpha > 1$ is therefore equal to $c = (1/\alpha)\sqrt{2K_E/\rho}$.

As the transmural pressure is progressively reduced and becomes negative, a critical value is reached at which the tube begins to buckle. The buckling pressure for an initially circular tube for the oval mode has been calculated by Tadbakhsh and Odeh [20] to be equal to

$$|\hat{P}_B| \equiv \frac{|(p-p_e)|}{K_B} = 3 \tag{4}$$

where K_B is the bending stiffness of the tube wall given by $K_B \equiv E(t/R_o)^3/[12(1-\nu^2)]$.

The post-buckling deformation of compliant tubes has been considered by many authors [20–23]. All of these analyses employ the constraint of inextensionality of the tube wall. This is a valid assumption as the in-plane strains are small in the collapsed state and the deformation of the cross-section is primarily due to rotations. The analysis of Flaherty et al. [21] is the most complete and incorporates the effect of normal forces created when the opposing walls come in contact. Point contact first begins at $|\hat{P}| = |\hat{P}_P|$ and continues until $|\hat{P}| = |\hat{P}_L|$ when the curvature at the point of contact becomes zero and line contact begins. For all negative transmural pressures larger than $|\hat{P}_L|$ the governing equations and the boundary conditions remain the same while the extent of the line contact, s_L, and $|\hat{P}_L|$ vary. Consequently, the solutions of the problem for any $|\hat{P}| > |\hat{P}_L|$ can be found from that for $|\hat{P}| = |\hat{P}_L|$ by a similarity transformation [21] or equivalently

$$\frac{\hat{P}}{\hat{P}_L} = \left(\frac{\alpha}{\alpha_L}\right)^{-3/2} . \tag{5}$$

From the calculations of Flaherty et al. [21], we have: $\hat{P}_P = -5.247$ at $\alpha_P \simeq 0.27$ and $\hat{P}_L = -10.34$ at $\alpha_L \simeq 0.21$. As a result the tube law in the similarlity region becomes:

$$\hat{P} \simeq -\alpha^{-3/2} . \tag{6}$$

The above functional relationship can also be obtained through *dimensional analysis* arguments and from the fact that there is no characteristic length for the problem in the similarity range. The radius of curvature R_c at any typical location is a function of only the bending stiffness $Et^3/12(1-\nu^2)$ and the transmural pressure $(p-p_e)$. Further,

Nomenclature (cont.)

$(p_o-p_e)^{**}$ = value of outlet transmural pressure at which the tube buckles and the flow starts to oscillate
$(p_o-p_e)^{*}$ = value of outlet transmural pressure at which the shock is located at the exit to the constriction
p_i = inlet pressure to flow regulator
p_o = outlet pressure to flow regulator
Q = flow rate
R = current radius of tube (positive transmural pressure)
Re_{D_h} = Reynolds number based on the hydraulic diameter for the tube
r = specific resistivity of the ionic solution
S = speed index (mean flow velocity/speed of propagation of small-amplitude inviscid area waves)
T_o = initial longitudinal wall pretension; $T_o \simeq E\epsilon_{xx}t$
T_θ = hoop tension per unit length (positive transmural pressure)
t = thickness of collapsible-tube wall
$\hat{u}$ = fluid flow velocity
u = mean flow velocity
V_P = voltage measured across two electrodes in area probe
V_R = voltage measured across two electrodes in reference section
x = distance along tube
$(x_1'-x_1)^{**}$ = farthest stable shock position when $(p_o-p_e) = (p_o-p_e)^{**}$
α = area ratio; $\alpha \equiv A/A_o$
α_B = area ratio at initiation of buckling
α_L = area ratio at initiation of line contact
α_P = area ratio at initiation of point contact
α_c = area ratio at constriction
α_i = area ratio at inlet to flow regulator
α_o = area ratio at outlet to flow regulator
ϵ_{xx} = longitudinal strain
ν = Poisson's ratio
ρ = fluid density
σ = hydraulic conductance of tube; $\sigma \equiv -Q/(dp/dx)$
σ_L = hydraulic conductance at inception of line contact
τ_w = wall shear stress

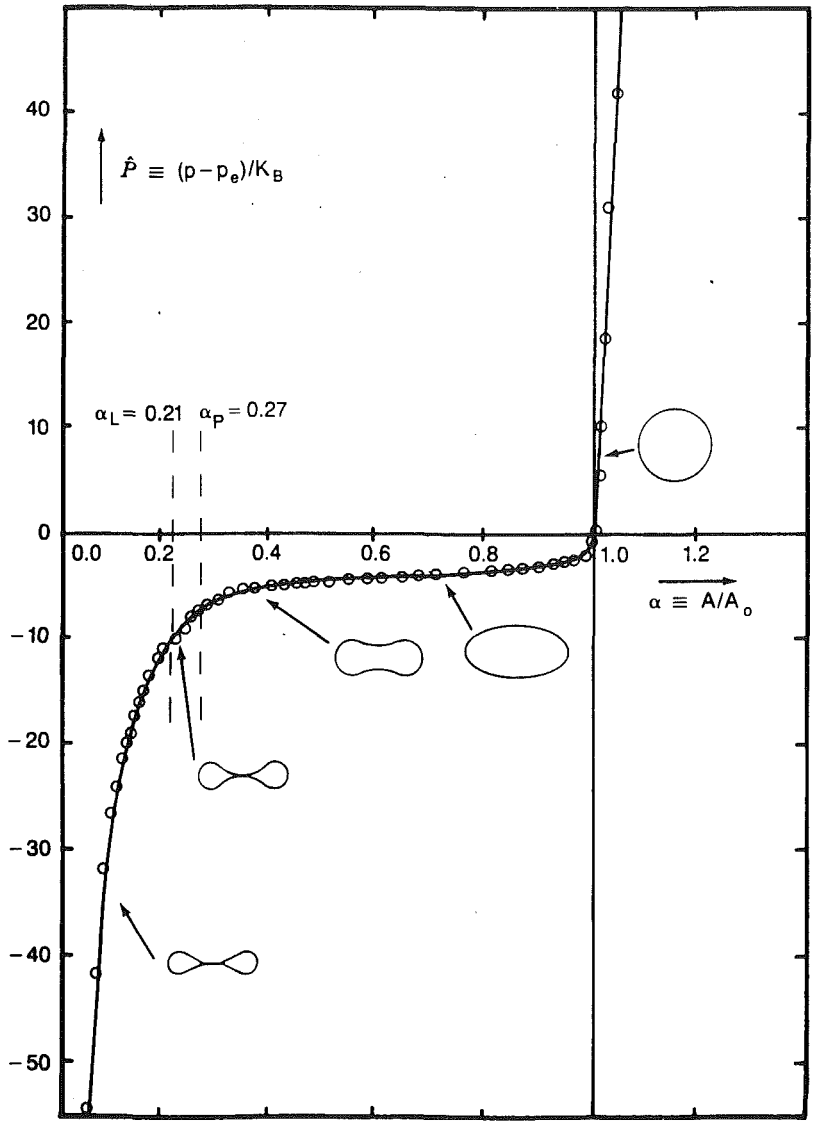

Fig. 1 Experimentally determined tube law for a uniformly collapsed thin-walled rubber latex tube. (K_B obtained from the logarithmic plot in the similarity region = 406 ± 10 dynes cm^2 at 95 percent confidence level.) (Uncertainty in $(p - p_e)/K_B = \pm 1.0$ and in $\alpha = \pm 0.005$ at 95 percent confidence level.)

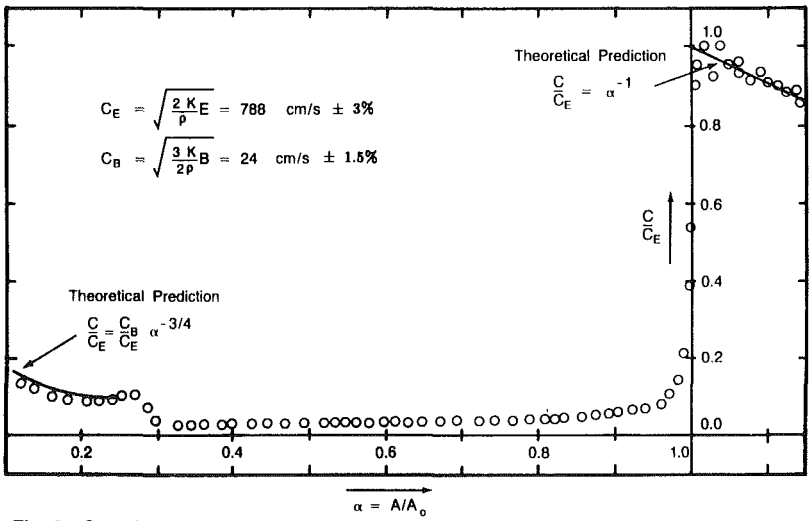

Fig. 2 Speed of propagation of small amplitude waves obtained by differntiation of the smoothed tube law data of Fig. 1. (Uncertainty in $c/c_E = \pm 0.01$ and in $\alpha = \pm 0.005$ at 95 percent confidence level.) (The extensional stiffness of the tube, K_E, is equal to 3.23×10^5 dynes/cm^2 ±5% at 95 percent confidence level; the bending stiffness K_B is equal to 406 ± 10 dynes/cm^2 at 95 percent confidence level.)

Table 1 Analogous physical quantities for collapsible tube, gas dynamic, and open channel flows

Analogous Physical Quantity	Collapsible tube flow	Gas dynamic flow	Open channel flow
Flow speed	u	u	u
Fluid pressure	p	p	p
Mass storage variable	A	ρ	h
Equation of state	$A=A(p-p_e)$	$\rho=\rho(p)$	$h=\dfrac{p-p_a}{\rho g}$
Wave speed	$c^2=\dfrac{A}{\rho}\dfrac{d(p-p_e)}{dA}$	$c^2=\dfrac{\rho}{\rho}\dfrac{dp}{d\rho}=\left(\dfrac{dp}{d\rho}\right)_s$	$c^2=\dfrac{h}{\rho}\dfrac{dp}{d\rho}=gh$
Speed index	$S=u/c$ Speed index	$M=u/c$ Mach number	$F=u/c$ Froude number

by recognizing that the cross-sectional area must vary as R_c^2 we obtain the functional relationship of equation (6) within an arbitrary multiplicative constant which is then taken to be about equal to 1. No simple closed-form expressions exist for the range $\alpha_L \le \alpha \le 1$ and the solution must be obtained numerically as it was done by Flaherty et al. [21]. Another method would be to curve-fit the experimentally obtained pressure-area relationship. Since the character of the solution changes for $\alpha \ge \alpha_B$, $\alpha_P \le \alpha \le \alpha_B$, and $\alpha \le \alpha_P$, where α_B corresponds to the nondimensional cross-sectional area when the tube begins to buckle, it may be necessary to use three separate functional relationships.

The *tube law* discussed above is strictly valid only if the following assumptions are satisfied. The elastic properties of the wall must be isotropic, and the elastic properties, wall thickness, resting area, and the applied transmural pressure must be constant along the tube wall at any given cross-section and also along its length. Under these conditions the tube will collapse uniformly and without twist, when subjected to a negative transmural pressure. When the above-mentioned quantities do vary along its length, however, the uniform collapse tube law will be approximately valid if their gradients in the longitudinal direction are small. For example, in the case of a uniform tube along which an area wave is propagating, this tube law is valid only if the ratio of the wave amplitude to the wavelength is small. For a tube of uniform properties that suffers significant longitudinal gradients, the tube law will have to be modified to include the effect due to longitudinal in-plane tension and bending forces. The pressure-area relationship is not then a unique function of the area alone but will also reflect its variations in the longitudinal direction through its longitudinal derivatives [14, 16, 17]. Then

$$p-p_e=K_B\hat{P}(\alpha)+(p-p_e)_x \tag{7a}$$

where $(p-p_e)_x$ is the contribution due to longitudinal deformation. For the present purpose it is convenient to define an effective external pressure $\hat{p}_e$ as

$$\hat{p}_e \equiv p_e+(p-p_e)_x \tag{7b}$$

so that the tube law becomes

$$p-\hat{p}_e=K_B\hat{P}(\alpha)\ . \tag{7c}$$

The pressure-area relationship shown in Fig. 1 was obtained experimentally for a uniformly collapsed latex rubber tube (I.D. $2R_o=2.54$ cm, wall thickness $t=0.083$ cm, length $L=70$ cm, Young's modulus $E\simeq 1.6\times 10^7$ dynes/cm^2) by means of an electrical impedance method of area measurement described in references [14] and [16]. In the apparatus shown in Fig. 4, the latex tube was mounted horizontally between two rigid tubes and placed under a longitudinal strain of 6 percent. The inside of the tube was filled with salt-water and the outside chamber with a glycerin-water solution. The densities of the two solutions were matched to better than 1 percent to eliminate buoyancy effects. The inside and outside chambers were connected to glass manometers mounted on a vertical scale. The transmural pressure was read directly by means of a cathetometer. The external chamber was connected to a large movable reservoir full of glycerine-water solution. Thus, the external pressure could be varied, if required, by altering the height of the reservoir. The internal pressure was varied by withdrawing small amounts of salt-water using a syringe. The area in the relatively uniformly-collapsed region in the center of the tube was measured by means of the electrical impedance method described in detail in [14] and [16]. Accordingly, an A.C. voltage is applied across a column of salt-water located inside a compliant tube and also a rigid tube section which is arranged in series with the collapsible tube as shown in Fig. 4. The rigid tube section serves as a reference section of known cross-sectional area A_R. In the reference section, the voltage V_R across two electrodes, spaced a fixed distance L_R apart, is measured. An area probe consisting of two electrodes mounted on a small-diameter catheter at a known distance L_P apart is placed parallel to the tube axis in the salt solution inside the tube. If the area of the tube-cross-section at the position of the area probe is A, the catheter cross-sectional area is a, and the voltage measured across the area probe is V_P, then

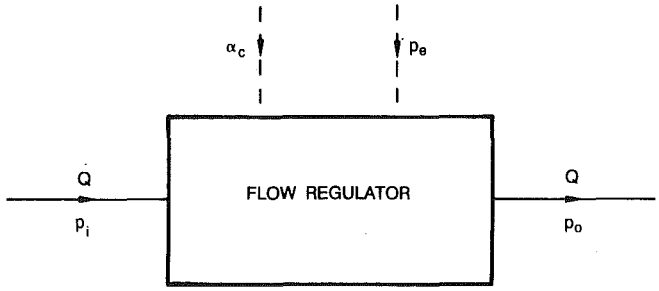

CONTROL VARIABLES: External Pressure p_e ; Constriction Size α_c
FLOW VARIABLES: Flow Rate Q ; Inlet Pressure p_i ; Outlet Pressure p_o
FLOW REGULATOR FUNCTION: Maintain Q Constant for Fixed p_i and Variable p_o

Fig. 3 The collapsible-tube flow regulator

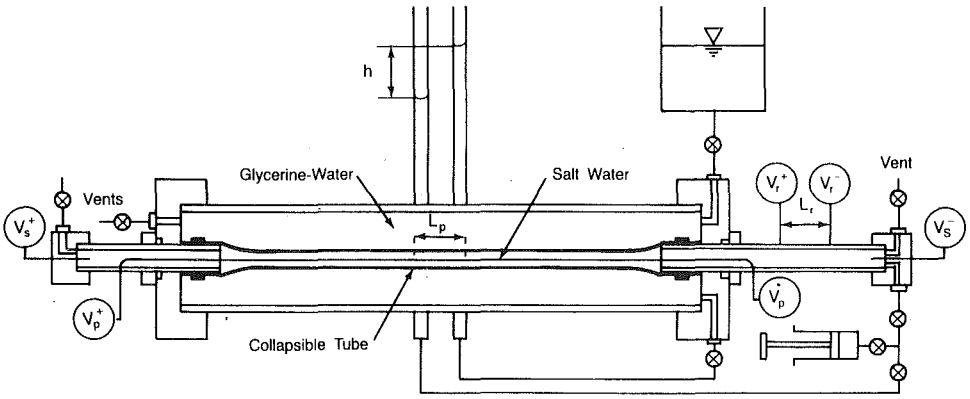

Fig. 4 The apparatus for the determination of the uniform collapse tube law

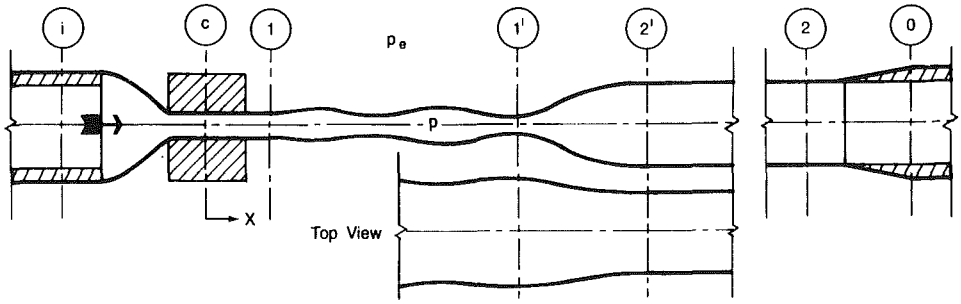

Fig. 5(*a*) Top and side views of precursor waves and shock transition in a collapsible tube

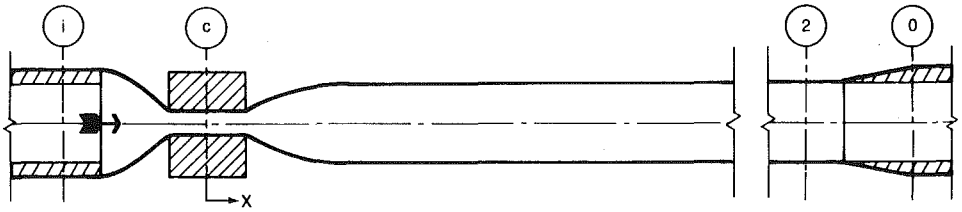

Fig. 5(*b*) Shock located at the exit of the constriction at positive downstream transmural pressure

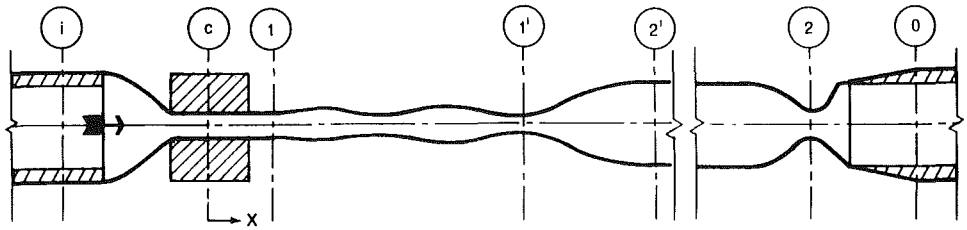

Fig. 5(*c*) Pinching of the downstream end of the collapsible tube just before and during the occurrence of oscillations

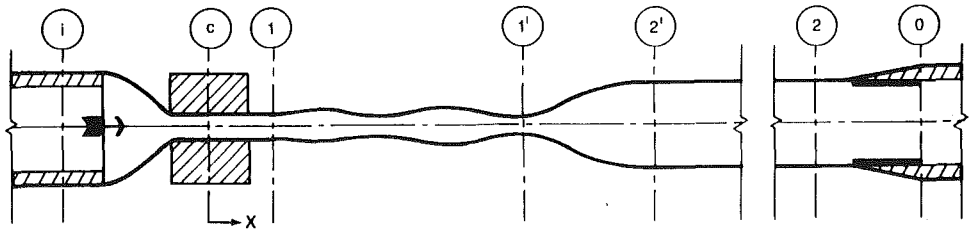

Fig. 5(*d*) Folding in of the downstream end of the collaspible tube at large negative downstream transmural pressures

$V_P = rIL_P/(A-a)$ and $V_R = rI(L_R/A_R)$ where r is the specific resistivity of the ionic solution and I is the current that passes through both the reference and probe positions. Thus the expression for the area A at any cross-section can be determined from

$$A = a + \left(\frac{L_P}{L_R}A_R\right)\left(\frac{V_R}{V_P}\right)$$

where, the quantity $[(L_P/L_R)A_R]$ was determined as an area-measurement constant by pulling the probe into the reference section.

2.2 Friction Factors for Flow Through Compliant Tubes. Since the cross-sectional shape and wetted perimeter of a compliant tube vary significantly with the degree of collapse, it is necessary to modify the standard formulations or to develop new expressions for viscous fluid drag.

2.2.1 Laminar Flow. For a locally Poisseuille flow through an enclosure the following equations have to be satisfied. They are:

$$\textit{Momentum: } \frac{dp}{dx}=\mu\left(\frac{\partial^2\hat{u}}{\partial y^2}+\frac{\partial^2\hat{u}}{\partial z^2}\right) \quad \text{in } A \tag{8}$$

$$\textit{Boundary Condition: } \hat{u}=0 \textit{ on } P \tag{9}$$

$$\textit{Flow Rate: } Q=\int\int_A \hat{u}(x,y,z)dydz=Au \tag{10}$$

$$\textit{Wall friction: } \frac{\tau_w P}{A}=-\frac{dp}{dx} \tag{11}$$

where P is the length of the wetted perimeter, A is the area of the flow region, and $\hat{u}$ and u are the local and average velocities of the flow, respectively.

Flaherty et al. [21] have solved this problem numerically for the two-lobed mode of collapse. For the similarity region of collapse ($\alpha<0.21$) they have obtained a similarity relationship for the hydraulic conductance σ of the tube given by:

$$\frac{\hat{\sigma}}{\hat{\sigma}_L}=\left(\frac{\hat{P}}{\hat{P}_L}\right)^{-4/3} \tag{12}$$

where $\sigma\equiv(R_o{}^4/\mu)\hat{\sigma}$, $\sigma\equiv Q/(-dp/dx)$, and the subscript L refers to the conditions at the inception of line contact of the opposing walls. Using the similarity relation between $\hat{P}$ and α we then obtain

$$\frac{\hat{\sigma}}{\hat{\sigma}_L}=\left(\frac{\alpha}{\alpha_L}\right)^2 \tag{13}$$

where $\hat{\sigma}_L=0.008$ and $\alpha_L=0.21$. Thus for $\alpha\le 0.21$,

$$\hat{\sigma}=0.1814\alpha^2. \tag{14}$$

Combining equations (10), (11), and (14) and modifying the multiplicative constant from 2.165 to 2.785, as recommended by Kamm [24], we obtain for $\alpha\le 0.36$:

$$\frac{\tau_w P}{A}=\left(\frac{8\pi\mu u}{A_0}\right)\frac{2.785}{\alpha}. \tag{15}$$

The modification of the multiplicative constant to 2.785 was made to extend the validity of the above relationship up to $\alpha\simeq 0.36$.

For the region $0.36\le\alpha\le 1$, the cross-section of the tube is approximately elliptical and the Poiseuille flow relationship for flow through elliptical tubes [25] can be used to develop an approximate expression for the wall friction.

For an elliptical tube of major and minor semiaxes a and b, the cross-sectional area is given by: $A=\pi ab$, and the perimeter by: $P\simeq\pi[2(a^2+b^2)]^{1/2}$. For laminar, Poiseuille flow through an elliptical tube the flow rate is given in terms of the dimensions of the major and minor semiaxes by $Q=(\pi/4\mu)[a^3b^3/(a^2+b^2)]\ (-dp/dx)$. This expression can then be manipulated to give:

$$Q\simeq\frac{1}{2\mu}\frac{A^3}{P^2}\left(\frac{-dp}{dx}\right). \tag{16}$$

As the wetted perimeter is constant in length during deformation in this area range ($0.36\le\alpha\le 1.0$), it can be calculated from the expression $P=\sqrt{4\pi A_o}$. Hence, for $0.36\le\alpha\le 1.0$, $\hat{\sigma}=\pi/8\ \alpha^3$ and then,

$$\frac{\tau_w P}{A}=\left(\frac{8\pi\mu u}{A_0}\right)\frac{1}{\alpha^2}. \tag{17}$$

For area ratio $\alpha\ge 1$, the cross-sectional area is circular and by following the same procedure as we did for elliptical cross-sections, setting $a=b=\sqrt{A_0\alpha/\pi}$ and combining with equation (11) we obtain $\hat{\sigma}=\pi/8\ \alpha^2$ and, therefore:

$$\frac{\tau_w P}{A}=\left(\frac{8\pi\mu u}{A_0}\right)\frac{1}{\alpha}. \tag{18}$$

The influence of mild area gradients on the laminar Poiseuille flow relationship for an elliptical tube has been considered by Wild et al. [26] by means of a perturbation analysis. Their solution, recast in dimensional variables, is

$$\frac{-dp}{dx}=\frac{4\mu}{\pi}\left(\frac{a^2+b^2}{a^3b^3}\right)Q-\frac{4}{A}\frac{\partial A}{\partial x}\frac{1}{2}\rho\left(\frac{Q}{A}\right)^2 \tag{19}$$

where, the cross-sectional area is given by $A=\pi a(x)b(x)$. There are three observations that can be made from the above expression. First, the first term is the Poiseuille-flow relationship for fully developed flow. Second, it shows that the first-order correction to the basic solution is inertial in nature and is related to the acceleration or deceleration of the fluid. Third, it shows that this correction is directly proportional to the area gradient. The inertial term can be shown to be small, if the modified Reynolds number $\mathrm{Re}_M\equiv(1/4P)\ (\partial A/\partial x)\mathrm{Re}_{D_h}\ll 1$, where $\mathrm{Re}_{D_h}\equiv(Q/A)D_h/\nu$, and $D_h\equiv 4A/P$.

2.2.2 Turbulent Flow. As in the previous section, the turbulent flow is considered to be fully developed. If the Reynolds number on the hydraulic diameter is sufficiently high for transition from laminar to turbulent flow to have occurred, then the viscous effects are confined to a very narrow region adjacent to the wall, and they are independent of the exact shape of the tube cross-section (Schlichting [27]). As a result, it is possible to use the correlation for the friction factor given by Schlichting for turbulent flow in smooth pipes, provided the Reynolds number is based on the appropriate hydraulic diameter. Thus,

$$\tau_w=\left(\frac{0.0791}{\mathrm{Re}_{D_h}{}^{0.25}}\right)\frac{1}{2}\rho u^2. \tag{20}$$

For tubes with the whole wall perimeter exposed to the flow, the wetted perimeter, hydraulic diameter, and Reynolds number are given by

$$P=\sqrt{4\pi A_0}, \tag{21a}$$

$$D_h\equiv\frac{4A}{P}=\sqrt{\frac{4A_0}{\pi}}\alpha, \tag{21b}$$

$$\mathrm{Re}_{D_h}\equiv\frac{(Q/A)D_h}{\nu}=\frac{Q}{\nu}\sqrt{\frac{4}{\pi A_0}}. \tag{21c}$$

Thus

$$\frac{\tau_w P}{A}=\frac{0.0791}{\mathrm{Re}_{D_h}{}^{0.25}}\sqrt{\frac{4\pi}{A_0}}\frac{1}{\alpha}\frac{1}{2}\rho u^2. \tag{22}$$

For tubes with cross-sections in the dumbbell shape with two fluid channels and with only part of the perimeter exposed to flow, each channel can approximately be assumed to be cir-

cular in the computation of the wetted perimeter. Thus,

$$P=\sqrt{8\pi A_0\alpha}\ , \tag{23a}$$

$$D_h\equiv\frac{4A}{P}=\sqrt{\frac{2A_0\alpha}{\pi}}\ , \tag{23b}$$

$$\mathrm{Re}_{D_h}=\frac{Q}{\nu}\sqrt{\frac{2}{\pi A_0\alpha}}\ . \tag{23c}$$

Therefore, for dumbell-shaped cross-sections,

$$\frac{\tau_w P}{A}=\frac{0.0791}{\mathrm{Re}_{D_h}^{0.25}}\sqrt{\frac{8\pi}{A_0\alpha}}\ \frac{1}{2}\rho u^2. \tag{24}$$

These results can be conveniently summarized in the following single alternative form

$$\frac{\tau_w P}{A}=\frac{4f}{D_o}\ \frac{1}{2}\rho u^2\ , \tag{25}$$

where D_o is the diameter corresponding to the resting area A_0 and f is a friction factor tabulated in Table 2 for the various flow regimes.

2.3 The Principle of Operation of a Wave-Speed Flow Regulator. The flow regulator configuration considered here is shown in Fig. 5(*a*). The inlet pressure p_i and the outlet pressure p_o are measured at stations (*i*) and (*o*), respectively. The constriction (*c*) creates a supercritical flow ($S>1$) immediately downstream of it at station (1). The shock transition occurs between stations (1)′ and (2)′, where (1)′ corresponds to the minimum point in the pressure and area distributions and (2)′ corresponds to the maximum in the pressure downstream of the shock. The constriction exerts a nonuniform external pressure on the outside of the tube so that the tube law is valid only outside the constriction.

The equation of continuity is

$$Q=A_0\alpha u\ . \tag{26}$$

Neglecting frictional losses over the short distance between (*i*) and (*c*) and neglecting losses at the entrance to the constriction gives

$$Po_i=p_c+\frac{1}{2}\rho u_c^2\ , \tag{27}$$

where, Po_i is the stagnation pressure at the inlet. Combining equations (26) and (27) we obtain

$$Q=A_0\alpha_c\sqrt{\frac{2}{\rho}[(Po_i-\hat{p}_e)-(p_c-\hat{p}_e)]} \tag{28}$$

where $\hat{p}_e$ is the effective external pressure on the tube within the constriction. Since the tube law for the tube within the constriction is unknown, it can be approximately represented by

$$(p_c-\hat{p}_e)\simeq F(\alpha_c)\ . \tag{29}$$

We note that $Q\to 0$ as $(p_c-\hat{p}_e)\to(Po_i-\hat{p}_e)$, and also when $(p_c-\hat{p}_e)\to-\infty$(i.e., $\alpha_c\to 0$). Thus, the flow rate Q possesses a maximum with respect to α_c. We compute this by setting

$$\frac{dQ}{d(p_c-p_e)}=\frac{A_o\alpha_c}{\rho u_c}(S^2-1)=0\ . \tag{30}$$

This yields the maximum flow rate at $S=1$ as $Q_{\max}=A_0\alpha_c c$, i.e., this maximum occurs when the mean flow speed is equal to the wave speed computed from the effective tube law. If the effective tube law is not very different from that of the tube itself, then it follows that whenever the flow is significantly supercritical at the exit to the constriction [i.e., Station (1)] there is some location inside the constriction at which the flow is critical. Thus, the flow is limited at that point. However, since the effective tube law is unknown, the flow rate can be evaluated by considering the flow at the constriction exit.

Now, if the losses at the entrance ot the constriction are taken into account, equation (27) becomes

$$Po_i=p_1+\frac{1}{2}\rho u_1^2+K_c\frac{1}{2}\rho u_c^2. \tag{31}$$

The tube law for station (1) is given by

$$(p_1-p_e)=K_B\hat{P}(\alpha_1). \tag{32}$$

Hence, combining equations (26) and (32) with (31), we obtain

$$\frac{Q}{A_c\sqrt{\frac{2}{\rho}(Po_i-p_e)}}=\left[\frac{1-\frac{K_B\hat{P}(\alpha_1)}{Po_i-p_e}}{\left(\frac{\alpha_c}{\alpha_1}\right)^2+K_c}\right]^{1/2}\ . \tag{33}$$

In this expression, the cross-sectional area A_c at the constriction has been introduced as a known parameter depending only on the undeformed dimensions of the tube and the adjustment of the constriction.

If the flow at Station (1) is supercritical (i.e., $S_1>1$), then the flow rate given by equation (33) is unaffected by changes in the downstream pressure p_o. Also, if the flow at station (1) is supercritical, a shock wave usually forms downstream of it. The position of the shock wave depends on the pressure difference (p_o-p_e). When this is made increasingly positive, the shock moves toward the constriction and at a certain value $(p_o-p_e)^*$, the shock vanishes into the constriction (see Fig. 5(*b*)). Then, the flow rate begins to fall. This is due to the fact the region of supercritical flow no longer exists and the flow inside the constriction becomes subcritical. As a result, downstream pressure variations can now travel upstream and decrease the flow rate. Consequently, the flow regulation curve has the form given in Fig. 6. It has a plateau region when a supercritical flow is present and a fall-off curve when the flow is subcritical everywhere. This situation is analogous to supercritical flow in a convergent-divergent nozzle when the back pressure is gradually increased from below its "design" value (Shapiro [28]). The flow rate corresponding to the plateau region is given by equation (33). This expression shows how the plateau increases with increasing tube stiffness.

In order to specify the range of downstream pressures over which the flow rate is effectively constant, it is necessary to determine the value $(p_o-p_e)^*$ characterizing the knee of the regulation characteristic. This can be obtained by applying the "modified Bernoulli" equation to the flow when the shock is at the constriction (see Fig. 5(*b*)). Allowing for contraction and expansion losses at the constriction and for frictional losses downstream of it, we obtain

$$Po_i=p_o+\frac{1}{2}\rho u_o^2+(K_e+K_c)\frac{1}{2}\rho u_c^2+\int_0^L\frac{\tau_w P}{A}dx\ . \tag{34}$$

Since conditions downstream are approximately uniform, $(\tau_w P/A)$ can be considered to be constant. It is given by equation (25) with the friction factor chosen from Table 2. Thus using the continuity equation we obtain

$$\left(\frac{p_o-p_e}{Po_i-p_e}\right)^*=1-\left[\frac{Q}{A_c\sqrt{\frac{2}{\rho}(Po_i-p_e)}}\right]^{*2}\times\left[\left(\frac{\alpha_c}{\alpha_o}\right)^2+(K_e+K_c)+\frac{4fL}{D_o}\left(\frac{\alpha_c}{\alpha_2}\right)^2\right]\ . \tag{35}$$

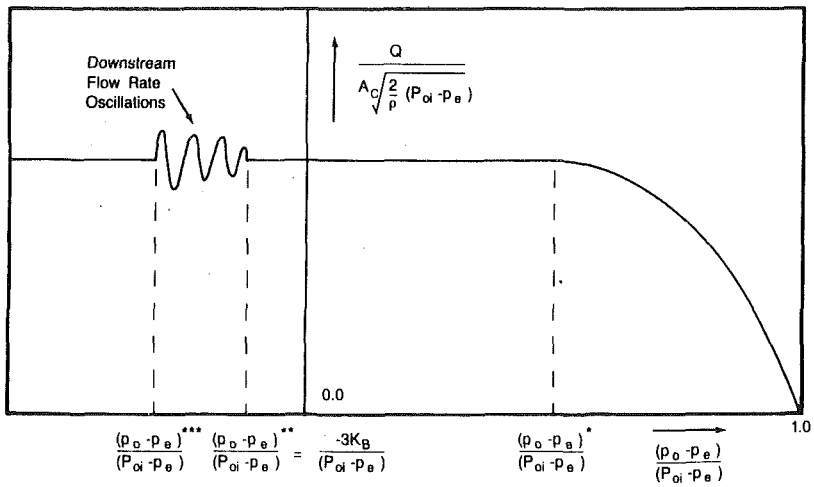

Fig. 6 Flow regulator characteristic for a high-Reynolds-number wave-speed collapsible-tube flow regulator. (Normalized flow rate versus normalized downstream pressure.)

In the above expression the (*) signifies that the values are those at the knee of the regulation characteristic and α_2 and α_o are the downstream area ratio and the rigid exit pipe area ratio, respectively. The value of the flow rate in equation (34) is equal to that of the plateau region and is thus given by equation (33).

The expansion loss coefficient K_e can be expressed as

$$K_e = K_L\left(1 - \frac{\alpha_c}{\alpha_2}\right)^2. \tag{36}$$

For a sudden expansion, K_L is only a weak function of the Reynolds number at the constriction. At very high Reynolds numbers, K_L tends to unity. It should be noted, however, that for the diffuser-like geometry of the tube expansion region, K_L would be a function not only of the Reynolds number but also of the shape of the cross-sections and, in particular, of the area gradient in the flow direction. Loss coefficients for conical diffusers as a function of area gradients have been experimentally obtained by Henry [29]. His results indicate that, indeed, K_L is strongly dependent on the area gradient. Another complication is that if the diverging region is followed by a long length of pipe, there is recovery of pressure beyond it as a result of velocity distribution changes due to turbulent mixing [30]. Therefore, any values obtained for K_L from published literature for different geometries must be regarded as very approximate.

In the present investigation, the loss coefficient K_L was experimentally determined from measurement of pressure within the tube with the shock located at the constriction.

When the downstream transmural pressure $(p_o - p_e)$ is decreased from positive values toward zero, the shock moves downstream and remains stable at a new location. When $(p_o - p_e)$ is further decreased to $(p_o - p_e)$ ** (a negative value), the tube begins to buckle inwards near the constriction to the downstream rigid pipe and forms a pinch as shown in Fig. 5(*c*). When this occurs, the position of the shock becomes unstable and it begins to oscillate along the tube. During this oscillatory motion, the shock stops short of the constriction, so that there is always a region of supercritical flow downstream of the constriction. Accordingly, the flow rate at the inlet remains unaffected, but both downstream flow rate and pressure oscillate with a characteristic frequency. The oscillations consist of periods of relatively high outflow, when the region downstream from the shock is approximately uniform, separated by momentary slowing as the downstream end is pinched in and then re-opened.

When the downstream pressure is still further reduced and is equal to $(p_o - p_e)$***, the tube folds on itself and moves into the downstream rigid pipe as shown in Fig. 5(*d*). Once this happens the flow again becomes stable with a shock standing in the test section. However, contrary to the case when the

Table 2 Friction factors for flow through a collapsible tube

Flow regime	Area ratio and shape	Friction factor f $\mathrm{Re}_{D_o} \equiv \frac{Q}{\nu}\sqrt{\frac{4}{\pi A_o}}$
Turbulent	$\alpha \le 0.36$	$f = \frac{0.0791}{\mathrm{Re}_{D_h}^{0.25}}\sqrt{\frac{2}{\alpha}}$ $\mathrm{Re}_{D_h} = \frac{\mathrm{Re}_{D_o}}{\sqrt{2\alpha}}$
	$0.36 \le \alpha \le 1.0$	$f = \frac{0.0791}{\mathrm{Re}_{D_h}^{0.25}}\frac{1}{\alpha}$ $\mathrm{Re}_{D_h} = \mathrm{Re}_{D_o}$
Laminar	$\alpha \le 0.36$	$f = \frac{16}{\mathrm{Re}_{D_h}} \times 1.969$ $\mathrm{Re}_{D_h} = \frac{\mathrm{Re}_{D_o}}{\sqrt{2\alpha}}$
	$0.36 \le \alpha \le 1.0$ elliptical cross-section	$f = \frac{16}{\mathrm{Re}_{D_h}}\frac{1}{\alpha}$ $\mathrm{Re}_{D_h} = \mathrm{Re}_{D_o}$
	$\alpha \ge 1.0$ circular cross-section	$f = \frac{16}{\mathrm{Re}_{D_h}}$ $\mathrm{Re}_{D_h} = \mathrm{Re}_{D_o}$

tube is not sucked into the pipe, initial reduction in downstream pressure moves the shock upstream to a new position and an increase in downstream pressure moves the shock downstream. On increasing the downstream pressure further, the shock reverses itself, moves upstream, and suddenly the downstream end of the tube moves out of the rigid end-pipe without any oscillations.

Similar oscillatory behavior in the outflow of collapsible tubes has been observed by Griffiths [10] and has been explained by him on the basis of wave propagation. For the present purpose of designing a flow regulator, however, it is only important to determine the value of $(p_o - p_e)^{**}$ below which the flow rate at the exit would begin to oscillate. This value can be approximately determined from the fact that the downstream end must first buckle before oscillations can begin. The buckling pressure for a collapsible tube is given by equation (4) and is equal to $(-3K_B)$. Thus,

$$\left(\frac{p_o - p_e}{Po_i - p_e}\right)^{**} \simeq \frac{-3K_B}{Po_i - p_e} . \tag{37}$$

The buckling pressure given by equation (37) may also increase or decrease depending on whether the wall tension at the exit station (2) is positive or negative. Further, oscillations begin at a transmural pressure $(p_o - p_e)$ somewhat lower than that at which the tube first begins to buckle. However, experimental results given in Part II of this paper [1] indicate that this is a good approximation.

2.4 The Principle of Operation of a Low Reynolds Number Flow Regulator. When the inertia forces are much smaller than the viscous forces and the Reynolds number based on the hydraulic diameter is much smaller than unity, a collapsible tube can still exhibit insensitivity to downstream pressure variations provided the tube is partially collapsed at its downstream end. This is due to the marked reduction in flow conductivity of the tube at negative transmural pressures.

For small longitudinal gradients, the flow is locally a Poiseuille flow and satisfies equations (8) through (11). For constant external pressure the flow rate is given in terms of the flow conductivity σ by

$$Q = -\sigma\frac{dp}{dx} = -\sigma(p - p_e)\frac{d(p - p_e)}{dx} \tag{38}$$

where σ is obtained as a function of $(p - p_e)$ using the expressions developed in Section 2.2.1. A plot of σ versus $(p - p_e)$ for a uniformly collapsed tube has been given by Flaherty et al. [21]. This is given in Fig. 7, replotted and extended to positive transmural pressures.

Consider now a flow regulator consisting of a collapsible tube of length L mounted between two rigid pipes. If the flow rate is Q and the inlet, exit, and external pressures are p_i, p_o, and p_e, respectively, integration of equation (38) between the inlet and the exit yields, for constant Q,

$$Q = \frac{R_o^4}{\mu L}\int_{p_o - p_e}^{p_i - p_e} \hat{\sigma}(p - p_e)d(p - p_e) . \tag{39}$$

From Fig. 7 it is seen that σ decreases sharply below the buckling pressure $p - p_e \simeq -3K_B$ and that beyond $p - p_e \simeq -5K_B$ it is approximately 1/40 as large as it is when the tube is under

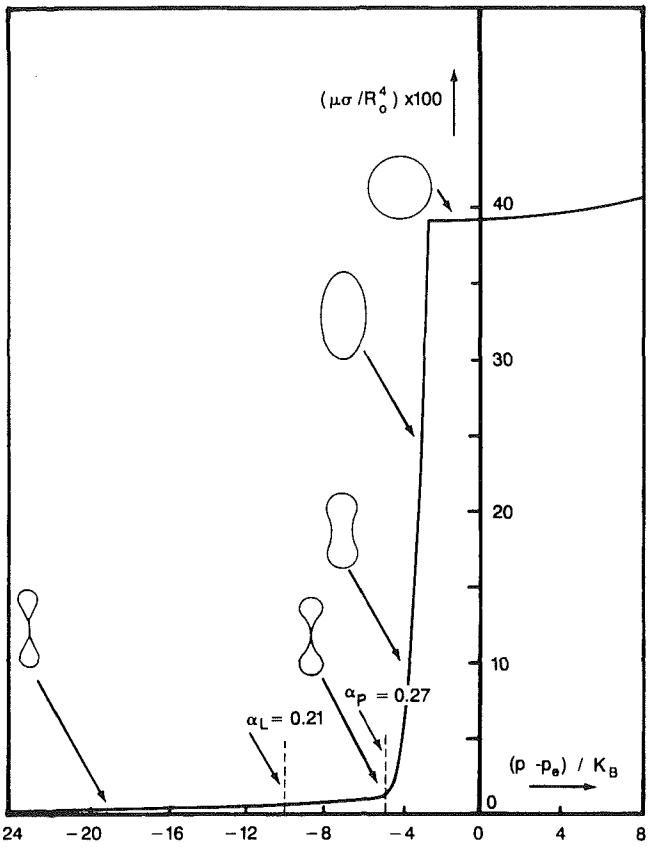

Fig. 7 Nondimensional flow conductivity versus nondimensional transmural pressure for a uniformly collapsed tube in the viscous flow regime

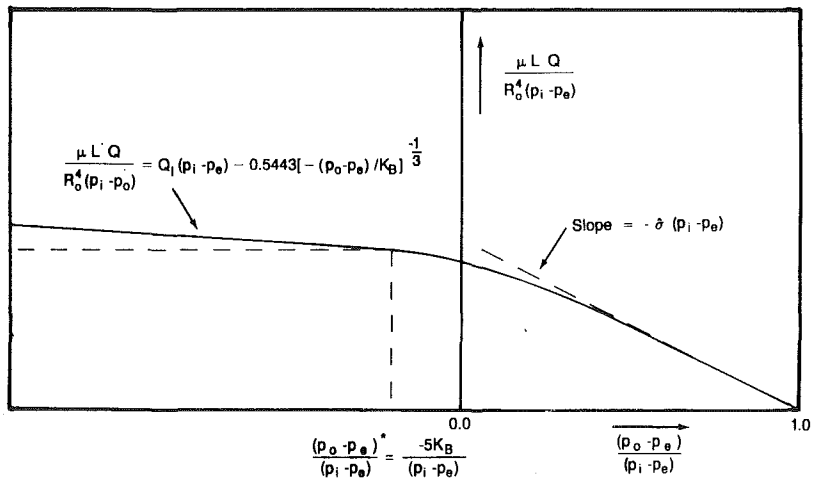

Fig. 8 Flow regulation characteristic for a low-Reynolds-number frictional collapsible-tube flow regulator. (Normalized flow rate versus normalized downstream pressure.)

zero transmural pressure. In the similarity region of the tube law (i.e., $\alpha \leq 0.21$)

$$\hat{\sigma} = 0.1814 \left(\frac{p_e - p}{K_B} \right)^{-4/3} . \tag{40}$$

As a result, below approximately $-5K_B$ (i.e., $\alpha \leq 0.27$), the downstream pressure difference $(p_o - p_e)$ has very little influence on the flow rate given by the integral in equation (39). From equation (39), for $(p_o - p_e) < -5K_B$,

$$\frac{\mu LQ}{K_B R_o^4} = \int_{-5}^{\frac{(p_i - p_e)}{K_B}} \hat{\sigma}(\hat{p}) d\hat{p} + \int_{\frac{(p_o - p_e)}{K_B}}^{-5} \hat{\sigma}(\hat{p}) d\hat{p} . \tag{41}$$

Combining equations (40) and (41) we obtain the expression

$$\frac{\mu LQ}{K_B R_o^4} = Q_1 (p_i - p_e) - 0.5443 \left(\frac{p_e - p_o}{K_B} \right)^{-1/3} \tag{42}$$

where Q_1 is a function of the material parameters and $(p_i - p_e)$ and is independent of $(p_o - p_e)$. From equation (42), for a tube with the exit end in the similarity collapse range, the flow rate is seen to be a weak function of $(p_o - p_e)$.

When $(p_i - p_o)$ is small and $(p_o - p_e) > 0$, then equation (39) can be approximated by

$$\frac{\mu LQ}{K_B R_o^4} \simeq \hat{\sigma}(p_i - p_e) \left(\frac{p_i - p_o}{K_B} \right) . \tag{43}$$

Thus, in this region, the flow rate is directly proportional to the driving pressure difference $(p_i - p_o)$. The value of $\hat{\sigma}(p_i - p_e)$ is obtained from equation (3) and the fact that, for $\alpha \geq 1$, $\hat{\sigma} = \pi/8\ \alpha^2$. Then,

$$\hat{\sigma} = \frac{\pi}{8} \left(1 - \frac{p - p_e}{K_E} \right)^{-1} \tag{44}$$

where K_E is the extensional stiffness of the tube wall defined in Section 2.1.

The regulation characteristic of the collapsible tube is conveniently represented by the plot of $\mu LQ/[R_o^4 (p_i - p_e)]$ versus $(p_o - p_e)/(p_i - p_e)$. It has the shape shown in Fig. 8. The knee of the curve corresponds to the knee of the conductivity-transmural pressure relationship, beyond which the conductivity is small. The initial slope of the characteristic when $(p_i - p_o)$ is small and the tube is inflated is given by equation (43). The small negative slope for negative transmural pressures $(p_o - p_e)$ is given by equation (42).

3 Conclusions

In this paper the theoretical foundation of the flow limitation characteristics of uniform compliant tubes was set up. Two different mechanisms of compliant-tube flow limitation were identified. They correspond to flow limitation when the flow is either friction dominated (frictional flow limitation for low-Reynolds-number flows) or inertia dominated (wave-speed flow limitation for high-Reynolds-number flows). The flow regulation characteristic curves for the inertia dominated and friction dominated flow regimes are given in Figs. 6 and 8, respectively. The experimental verification of the findings of the analysis presented here and the design of a flow regulator when the flow is inertia dominated will be addressed in Part II [1] of this paper.

References

1 Kececioglu, I., "Flow Regulation Characteristics of Thin-Walled Compliant Tubes, Part II: Experimental Verification and Design of the Wave-Speed Flow Regulator," ASME JOURNAL OF FLUIDS ENGINEERING, published in this issue pp. 330-337.

2 Shapiro, A. H., "Physiologic and Medical Aspects of Flow in Collapsible Tubes," *Proc. 6th Canadian Congr. of Appl. Mech.*, Vancouver, 1977.

3 Shapiro, A. H., "Steady Flow in Collapsible Tubes," ASME *Journal of Biomechanical Engineering*, Vol. 99, (1977), pp. 126-147.

4 Conrad, W. A., "Pressure-Flow Relationships in Collapsible Tubes," *IEEE Trans. Bio-Med. Engrg.*, BME-16(4), 1969, pp. 284-295.

5 Kirshner, J. M., *Fluid Amplifiers*, 1966, McGraw-Hill, New York.

6 Griffiths, D. J., "Urethral Elasticity and Micturition Hydrodynamics in Females," *Med. & Biol. Engrg.*, Vol. 7, 1969, pp. 201-215.

7 Griffiths, D. J., "Hydrodynamics of Male Micturition: I & II. Theory of Steady Flow Through Elastic-Walled Tube," *Med. & Biol. Engrg.*, Vol. 9, 1971, pp. 581-596.

8 Griffiths, D. J., "Steady Flow Through Veins and Collapsible Tubes," *Med. & Biol. Engrg.*, Vol. 9, 1971, pp. 597-602.

9 Griffiths, D. J., "The Mechanics of the Urethra and of Micturition," *Brit. J. Urol.*, Vol. 45, 1973, pp. 497-507.

10 Griffiths, D. J., "Oscillations in the Outflow from a Collapsible Tube," *Med. & Biol. Engrg.*, Vol. 15, 1977, pp. 357-362.

11 Oates, G. C., "Fluid Flow in Soft-Walled Tubes; Part I: Steady Flow," *Med. & Biol. Engrg.*, Vol. 13, 1975, pp. 773-778.

12 Oates, G. C., "Fluids Flow in Soft-Walled Tubes; Part II: Behavior of Finite Waves," *Med. & Biol. Engrg.*, Vol. 13, 1975, pp. 778-784.

13 Kececioglu, I. Kamm, R. D., and Shapiro, A. H., "Structure of Shock Waves in Collapsible-Tube Flow," *Proc. 31st Ann. Conf. Engrng. Medicine & Biology*, Atlanta, Georgia, 1978, p. 92.

14 Kececioglu, I., "Experimental Determination of the Structure of Shock Waves in Fluid Flow Through Collapsible Tubes With Application to the Design of a Flow Regulator," Thesis for the Degree of Engineer, Dept. of Mechanical Engineering, Massachusetts Institute of Technology, 1979.

15 McClurken, M. E., "Supercritical Flow in Collapsible Tubes," Ph.D. thesis, Dept. of Mechanical Engineering, Massachusetts Institute of Technology, 1980.

16 Kececioglu, I., McClurken, M. E., Kamm, R. D., and Shapiro, A. H., "Steady Supercritical Flow in Collapsible Tubes. Part 1. Experimental Observations," *Journal of Fluid Mechanics*, Vol. 109, 1981, pp. 367-389.

17 McClurken, M. E., Kececioglu, I., Kamm, R. D., and Shapiro, A. H., "Steady Supercritical Flow in Collapsible Tubes. Part 2. Theoretical Studies," *Journal of Fluid Mechanics*, Vol. 109, 1981, pp. 391-415.

18 Rubinow, S. I., and Keller, J. B., "Flow of a Viscous Fluid Through an Elastic Tube With Applications to Blood Flow," *J. Theor. Biol.*, Vol. 35, 1972, pp. 299-313.

19 Treloar, L. R. G., *The Physics of Rubber Elasticity*, Clarendon Press, 1958.

20 Tadbakhsh, I., and Odeh, F., "Equilibrium States of Elastic Rings," *J. Math. Anal. & Appl.*, Vol. 18, 1967, pp. 59-74.

21 Flaherty, J. E., Keller, J. B., and Rubinow, S. I., "Post-buckling behavior of elastic tubes and rings with opposite sides in contact," *SIAM J. Appl. Math.*, Vol. 24, No. 4, 1972, pp. 446-455.

22 Kresh, E., and Noordergraaf, A., "Cross-sectional Shape of Collapsible Tubes," *Biophys. J.*, Vol. 12, 1972, pp. 274-294.

23 Heywood, J. H., "Post-buckling Analysis of a Circular Elastic Ring or a Long Cylindrical Shell," *Proc. Symp. on Theory of Thin Elastic Shells*, W. T. Koiter, ed., North Holland Publ. Co., 1960, pp. 123-133.

24 Kamm, R. D., "A Study of External Pneumatic Compression for the Prevention of Deep Vein Thrombosis," Ph.D. thesis, Dept. of Mechanical Engineering, Massachusetts Institute of Technology, 1977.

25 White, F. M., *Viscous Fluid Flow*, McGraw-Hill, New York, 1974, p. 123.

26 Wild, R., Pedley, T. J., and Riley, D. S., "Viscous Flow in Collapsible Tubes of Slowly Varying Elliptical Cross-Section," *J. Fluid Mech.*, Vol. 81, 1977, pp. 273-294.

27 Schlichting, H., *Boundary Layer Theory*, McGraw-Hill, New York, 1968, pp. 561-575.

28 Shapiro, A. H., *The Dynamics and Thermodynamics of Compressible Fluid Flow*, Vol. II, The Ronald Press Co., New York, 1953.

29 Henry, J. R., National Advisory Comm. Aeronautics, ARR No. 14F26, June 1944.

30 Patterson, G. N., "Modern Diffuser Design," *Aircraft Engrng.*, Vol. 10, 1938, pp. 267-273.

Flow Regulation Characteristics of Thin-Walled Compliant Tubes: Part II—Experimental Verification and Design of the Wave-Speed Flow Regulator

Ifiyenia Kececioglu
Assistant Professor,
Department of Mechanical Engineering,
The University of Illinois at Chicago,
Chicago, Ill. 60680

The theoretical foundation of the two different mechanisms of compliant-tube flow limitation when the flow is either friction dominated (frictional flow limitation for low-Reynolds-number flow) or inertia dominated (wave-speed flow limitation for high-Reynolds-number flow) was formulated in Part I [1] of this paper. In this part of the paper, the high-Reynolds-number wave-speed flow limitation behavior of compliant tubes is verified experimentally and applied to the design of a flow regulator employing a collapsible tube as its active element. Criteria for the design of an inertia-dominated compliant-tube flow regulator are established and checked against findings of experiments.

1 Experimental Determination of the Flow Regulation Characteristic Curve and Comparison With Theory[1]

Experiments were conducted to determine the regulation characteristic curve of a high Reynolds number, wave-speed type flow regulator. The experimental parameters varied and the corresponding ranges of variation are given in Table 1. During the experiments, attention was focused on the determination of the overall behavior of the flow regulator as a unit and not on the details of the flow within it.

A schematic diagram of the experimental apparatus used is shown in Fig. 1. The measurement technique used is the same as the one described in Part I [1] of this paper (Section 2.1). In addition, the pressures p_i and p_0 at the inlet and outlet of the apparatus were also measured by means of manometers. A diagrammatic representation of the locations at which the measurements made are critical to the analysis presented here is shown in Fig. 2. For each flow rate, the position of the shock along the tube was altered in steps by adjustment of the downstream pressure; measurements were made until the shock was at its farthest stable position from the constriction, toward the downstream end. As predicted by the analysis presented in Part I [1], the experimental data verified that the flow rate was independent of downstream pressure variations, provided the upstream conditions ($p_i - p_e$, α_c) were fixed; α_c is the cross-sectional area at the constriction nondimensionalized with respect to the resting area of the tube, A_0, at zero transmural pressure, $(p - p_e)$, and p_e is the pressure applied externally on the tube. This result is best presented by a plot of normalized flow rate

$$\frac{Q}{A_c\sqrt{\frac{2}{\rho}(Po_i - p_e)}}$$

versus the normalized outlet pressure $\frac{(p_0 - p_e)}{(Po_i - p_e)}$ as shown in Fig. 3 (Po_i is the stagnation pressure at the inlet). Hence, the data obtained under different inlet and outlet conditions can be presented on a single graph; this is the characteristic curve

Table 1 Ranges of parameter variation for flow-regulator characteristic-curve experiments (uncertainty estimates at 95 percent confidence level)

Quantity	Symbol	Range
Reynolds number based on resting diameter	$\mathrm{Re}_{D_0} \equiv \frac{Q}{\nu}\sqrt{\frac{4}{\pi A_0}}$	12,000–20,000 ± 0.5%
Inlet Reynolds number based on hydraulic diameter	$\mathrm{Re}_{D_h} = \frac{\mathrm{Re}_{D_0}}{\sqrt{2\alpha_1}}$	18,000–33,000 ± 1.5%
Inlet speed index	$S_1 = \frac{u_1}{c_1}$	2.7–11.0 ± 0.1
Constriction area ratio	$\alpha_c = \frac{A_c}{A_0}$	0.15–0.38 ± 0.005
Flow rate	Q	13.5–23.0 l/min ± 0.5%
Longitudinal prestrain	ϵ_{xx}	0.06 (fixed) ± 0.5%

[1]Nomenclature is listed in Part I of this two-part paper.

Contributed by the Fluids Engineering Division for publication in the JOURNAL OF FLUIDS ENGINEERING. Manuscript received by the Fluids Engineering Division August 17, 1989.

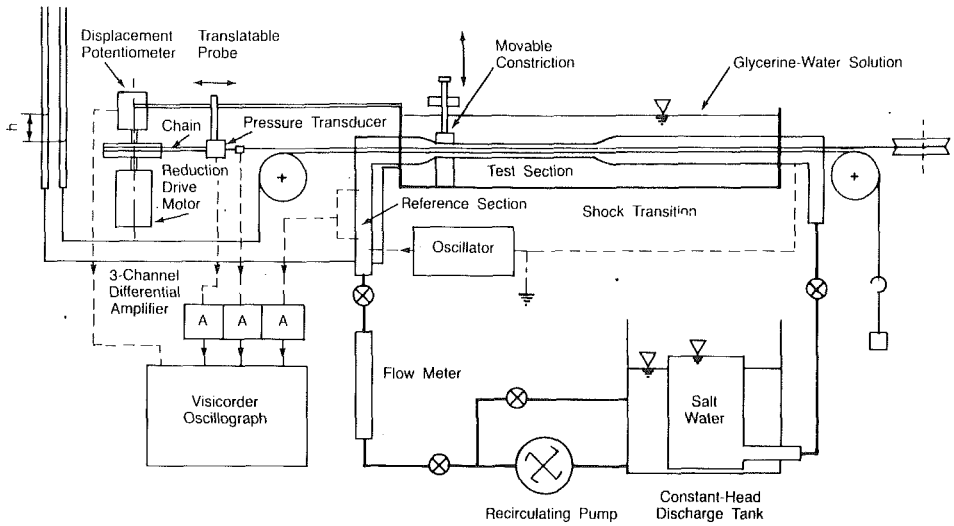

Fig. 1 Apparatus for the measurement of area and pressure distributions within a standing shock wave in a collapsible tube

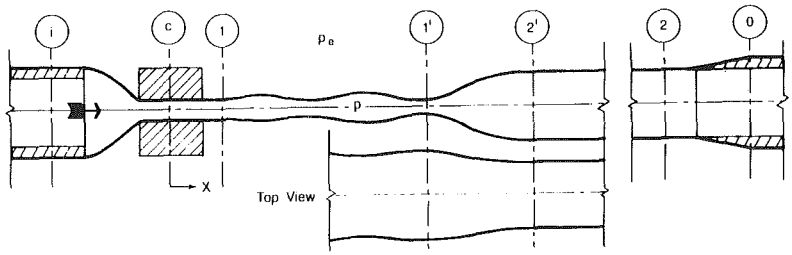

Fig. 2 Diagrammatic representation of locations at which measurements were made for the characterization of the wave-speed flow regulator

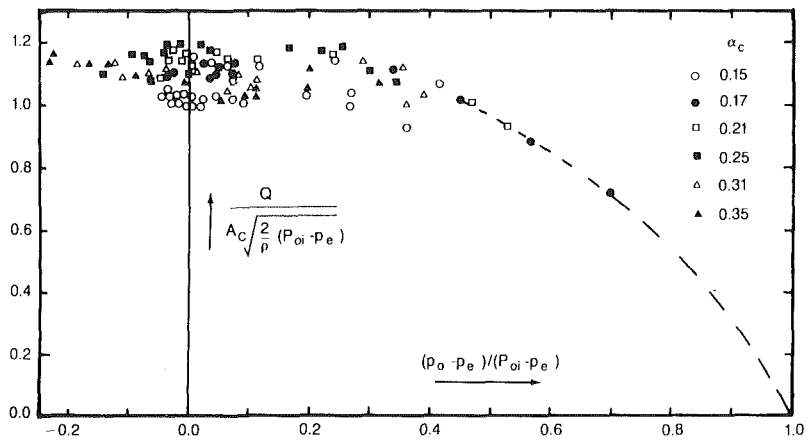

Fig. 3 Flow regulator characteristic for the wave-speed flow regulator: normalized flow rate vs. normalized downstream pressure; variable parameter: constriction are ratio α_c. (Experimental results). (Uncertainty in $\frac{p_0-p_e}{Po_i-p_e}=\pm 0.01$ and in $\frac{Q}{A_c\sqrt{\frac{2}{\rho}(Po_i-p_e)}}=\pm 0.01$ at 95 percent confidence level.)

for the wave-speed flow regulator. Comparison between Figs. 3 and 4 shows good agreement between the experimentally measured and the theoretically derived characteristic flow regulation curves. The expression for the normalized flow rate when a shock exists downstream of the constriction was derived earlier (see equation (33) in Part I [1]). In that expression, the cross-sectional area A_c at the constriction was introduced as a design parameter rather than the area A_1 immediately downstream of it. The plot of α_1 against α_c shows that the data can fit on a straight line. The straight line representing the least squares fit to the experimental data is given by

$$\alpha_1 = 1.019\alpha_c + 0.049 \tag{1}$$

The correlation coefficient of the least squares fit is 0.94. It is thus seen that α_1 is only slightly larger than α_c for α_c values approximately between 0.2 and 0.4. Hence, for design purposes, α_1 may be taken to be approximately equal to α_c. Also,

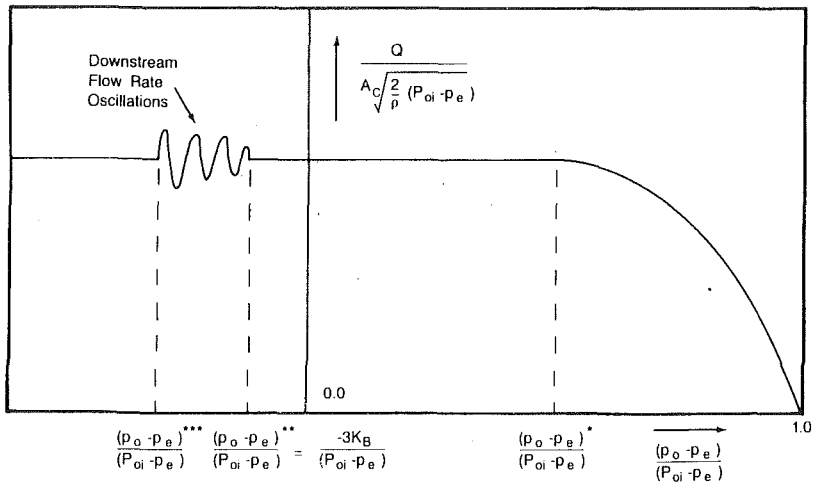

Fig. 4 Theoretically derived characteristic curve for the wave-speed compliant-tube flow regulator. (Normalized flow rate versus normalized downstream pressure.)

for design purposes, equation (33) in Part I [1] of this paper can be more conveniently expressed by

$$\frac{Q}{A_0\sqrt{\frac{2K_B}{\rho}}}=\left[\frac{\frac{p_i-p_e}{K_B}-\hat{P}(\alpha_1)}{\frac{1}{\alpha_1^2}+\frac{K_c}{\alpha_c^2}-\frac{1}{\alpha_i^2}}\right]^{1/2} \tag{2}$$

where, $\hat{P}\equiv\frac{(p-p_e)}{K_B}$, is the ratio of the transmural pressure to the bending stiffness of the tube wall in the plane of the cross-sectional area ($K_B\equiv\frac{E}{12(1-\nu^2)}\left(\frac{t}{R_0}\right)^3$, where, E is the Young's modulus, ν is the Poisson's ratio, t is the tube thickness, and R_0 is the tube radius at zero transmural pressure). As discussed in Part I [1], the variation of $\hat{P}$ as a function of the nondimensional crosssectional area α is the constitutive relationship uniquely characterizing the tube-wall behavior and may be referred to as the *tube law*. For the tube used in the experiments reported here, the experimentally obtained functional relationship is depicted in Fig. 5.

The areas of the rigid inlet and outlet tubing of the experimental apparatus were equal to the resting area of the latex tube so that $\alpha_i\simeq\alpha_0=1$. This geometry is convenient and is recommended for design calculations. Further, the loss coefficient K_c at the constriction entrance is also small and may be neglected. Combining equation (2) with equation (1) yields a relationship between $Q/A_0\sqrt{2K_B/\rho}$ as a function of $(p_i-p_e)/K_B$ with α_c as an independent parameter. That is

$$\frac{Q}{A_0\sqrt{2K_B/\rho}}=\bar{f}\left(\alpha_c,\frac{p_i-p_e}{K_B}\right). \tag{3}$$

The theoretical prediction of equation (3) and the corresponding experimental data are plotted in Fig. 6 and they show good agreement.

The above relationship is valid only as long as a stable shock exists downstream of the constriction. Two necessary conditions for shock formation are that the Reynolds number of the flow is large and that the flow downstream of the constriction is supercritical. In addition, the transmural pressure difference (p_0-p_e) must not be so high as to force the shock inside the constriction, nor should it be so low that the tube buckles at its exit end before the shock starts oscillating along the tube.

It is therefore necessary to establish the upper and lower limits $(p_0-p_e)^*$ and $(p_0-p_e)^{**}$ (see Fig. 4) between which the downstream pressure difference can be allowed to vary while still maintaining a constant exit flowrate. As discussed before, the lower limit can be approximated by equation (37) of Part I [1]. The validity of this expression is verified by the plot of Fig. 7. Therefore, for design calculations we can say that

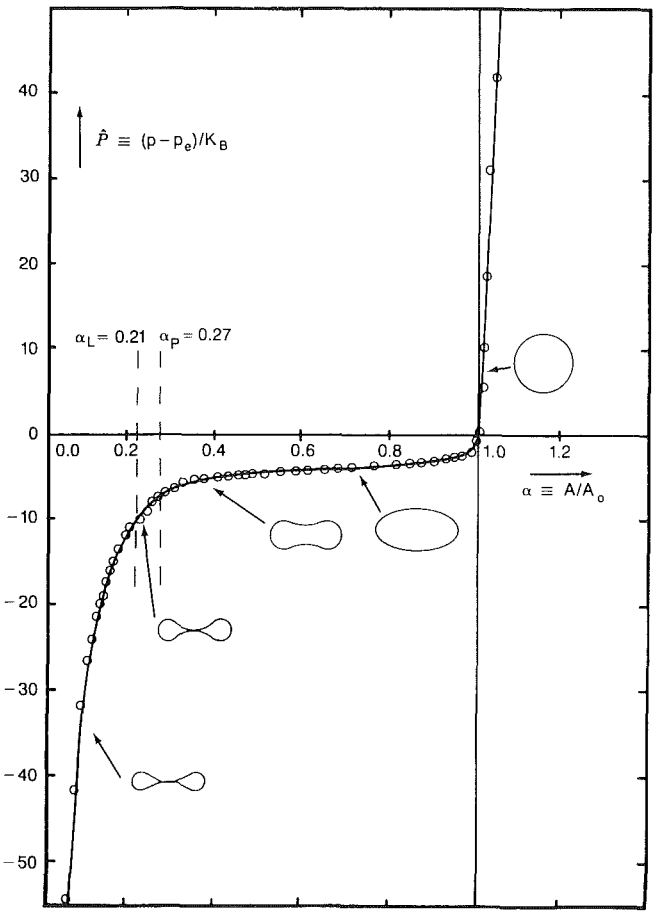

Fig. 5 Experimentally determined tube law for a uniformly collapsed thin-walled rubber latex tube. (K_B obtained from the logarithmic plot in the similarity region = 406 ± 10 dynes/cm² at 95 percent confidence level.) (Uncertainty in $\frac{p-p_e}{K_B}$ = ± 1.0 and in α = ± 0.005 at 95 percent confidence level.)

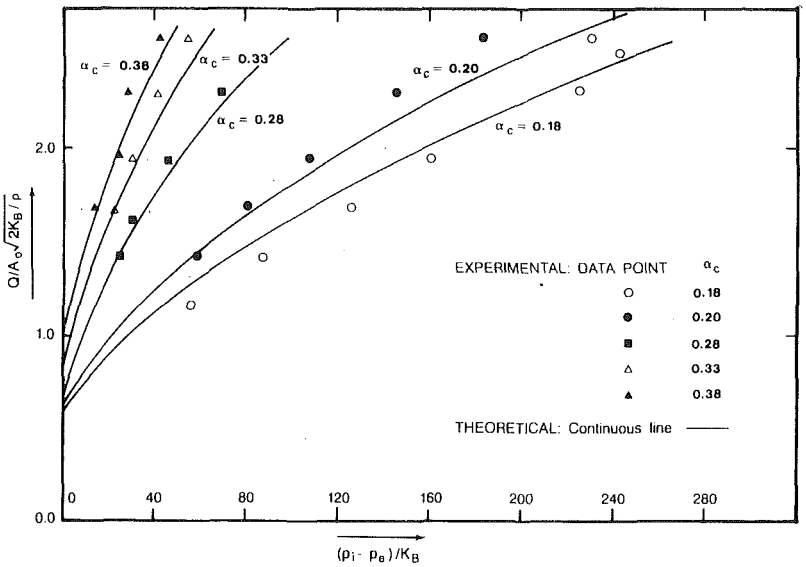

Fig. 6 Normalized flow rate versus normalized inlet transmural pressure. (Uncertainty in $\frac{Q}{A_0\sqrt{\frac{2K_B}{\rho}}} = \pm 0.05$ and in $\frac{p_i - p_e}{K_B} = \pm 1.0$ at 95 percent confidence level.)

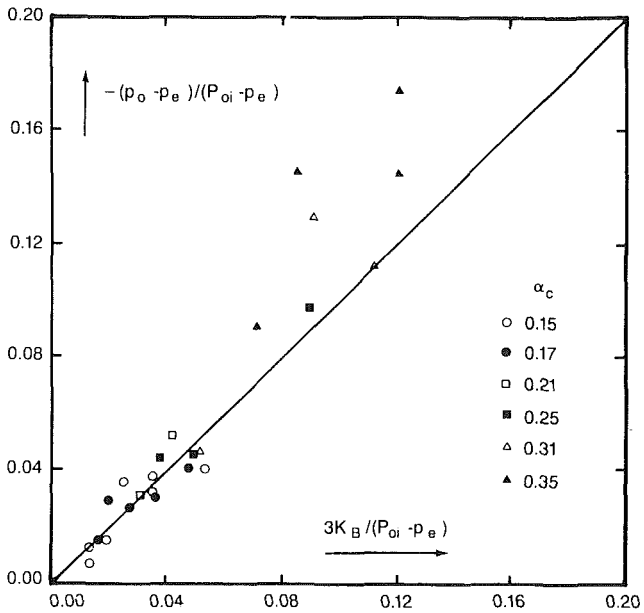

Fig. 7 Normalized downstream pressure at farthest downstream stable position versus normalized buckling pressure. Variable parameter: Constriction area ratio α_c. (Experimental results.) (Uncertainty in $\frac{p_o - p_e}{Po_i - p_e} = \pm 0.002$ and in $\frac{3K_B}{Po_i - p_e} = \pm 0.002$ at 95 percent confidence level.)

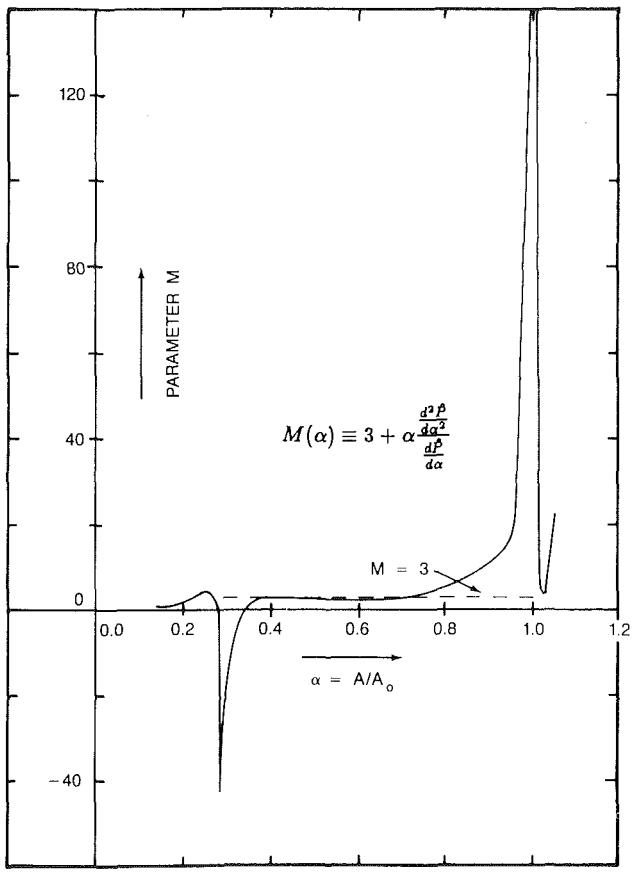

Fig. 8 Parameter M versus area ratio obtained by differentiation of smoothed data of Fig. 5. (Uncertainty in $M = \pm 1$ and in $\alpha = \pm 0.005$ at 95 percent confidence level.)

$$\left(\frac{p_0 - p_e}{K_B}\right)^{**} \simeq -3. \tag{4}$$

The upper limit can be approximately found from equations (35) and (33) of Part I [1]. As a result,

$$\left(\frac{p_0 - p_e}{K_B}\right)^{*} = \left(\frac{p_i - p_e}{K_B}\right) - \left(\frac{Q}{A_0\sqrt{2K_B/\rho}}\right)^2 \left(\frac{1}{\alpha_0^2} - \frac{1}{\alpha_i^2} + \frac{K_c + K_e}{\alpha_c^2} + \frac{4f_0 L}{D_0}\frac{1}{\alpha_2^3}\right) \tag{5}$$

where the friction factor f_0 is given by

$$f_0 = \frac{0.0791}{\mathrm{Re}_{D_o}^{0.25}}, \tag{6}$$

where, D_0 is the tube diameter corresponding to the resting area A_0. The flowrate in equation (5) is taken to be the value on the plateau region of the regulation characteristic given by equation (2). Thus $\left(\frac{p_0-p_e}{K_B}\right)^*$ corresponds to the knee of the regulation characteristic as indicated in Fig. 4.

The loss coefficient K_e can be expressed in the form

$$K_e = K_L\left(1-\frac{\alpha_c}{\alpha_2}\right)^2. \tag{7}$$

If the nondimensional stagnation pressure loss across the shock is plotted against $(1-\alpha_1'/\alpha_2')^2$, where α_1' and α_2' are the nondimensional cross-sectional areas at the inlet and exit to the shock, respectively, for the experimentally observed shock distributions (see Fig. 2), the slope of the least squares straight line fit to this data may be taken to represent K_L. Thus, with $K_L = 0.586$ and $\alpha_0 = \alpha_i = 1$, $\alpha_2 \simeq 1$, $\left(\frac{p_0-p_e}{K_B}\right)^*$ can be computed from equation (5) for given α_c and $\left(\frac{p_i-p_e}{K_B}\right)$.

Lastly, it is necessary to predict both the stagnation pressure loss upstream of the shock and the position of the shock. These values will be needed for the determination of the required length of collapsible tube in the regulator. This undertaking is complicated by the fact that the area increases in an oscillatory fashion between the constriction and the shock [2 to 5]. As a result, it is necessary to make some simplifying assumptions. It is first assumed that the stagnation pressure loss is primarily due to the change in mean area and that the effect of the oscillatory component of area growth on the frictional pressure drop integrated over the entire tube length upstream of the shock is negligible. Secondly, it is assumed that the parameter M determining the steepening or broadening of compression waves is approximately constant. This is approximately valid over most of the range of areas of interest $(0.35 < \alpha < 0.8)$ (see Fig. 8). Thus, the governing equations are:

$$\frac{(1-S^2)}{\alpha}\frac{d\alpha}{dx} = -\frac{(1-S^2)}{u}\frac{du}{dx} = -L(x, S^2) \tag{8}$$

$$\frac{(1-S^2)}{S^2}\frac{dS^2}{dx} = H(x, S^2) = ML(x, S^2) \tag{9}$$

$$\frac{(1-S^2)}{\rho u^2}\frac{dp}{dx} = -\left(\frac{1}{2}\frac{4f}{D_0}+\frac{1}{\rho c^2}\frac{d\hat{p_e}}{dx}\right) \tag{10}$$

with

$$L(x, S^2) \equiv \left(\frac{1}{2}S^2\frac{4f}{D_0}+\frac{1}{\rho c^2}\frac{d\hat{p_e}}{dx}\right) \tag{11}$$

$$M \equiv 3+\alpha\frac{\frac{d^2\hat{P}}{d\alpha^2}}{\frac{d\hat{P}}{d\alpha}} = M(\alpha) \simeq constant \tag{12}$$

where $f = f_0/\alpha$ and f_0 is defined by equation (6), and $\frac{d\hat{p_e}}{dx}$ is the change in the effective external pressure $\hat{p}_e$ as a function of axial position x due to wall-tension and bending (Part I [1]). Moreover, $c \equiv \sqrt{(A/\rho)[d(p-p_e)/dA]}$, is the speed of propagation of small-amplitude inviscid area waves, and the speed index $S\left(S \equiv \frac{u}{c}\right)$ is the fluid velocity nondimensionalized with respect to the local speed of propagation of small-amplitude inviscid area waves.

For the tube used in the reported experiments c was obtained as a function of α by differentiation of the smoothed tube-law data of Fig. 5 and is shown in Fig. 9. In Fig. 9,

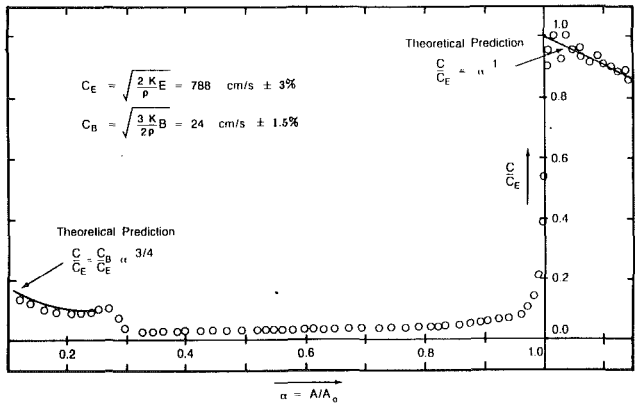

Fig. 9 Speed of propagation of small amplitude waves obtained by differentiation of the smoothed tube law data of Fig. 5. (Uncertainty in $\frac{c}{c_E} = \pm 0.01$ and in $\alpha = \pm 0.005$ at 95 percent confidence level.) (The extensional stiffness of the tube, K_E, is equal to 3.23×10^5 dynes/cm² ± 5 percent at 95 percent confidence level; the bending stiffness K_B is equal to 406 ± 10 dynes/cm² at 95 percent confidence level.)

$K_E \equiv \frac{E}{2(1+\nu)}\left(\frac{t}{R_0}\right)$ is the extensional stiffness of the tube wall and was calculated to be 3.23×10^5 dynes/cm² ± 5 percent (at 95 percent confidence level).

At this point, it is interesting to derive the form of the tube law for which a finite amplitude wave would propagate unchanged. Setting $M = 0$ gives

$$\frac{d^2\hat{P}}{d\alpha^2}+\frac{3}{\alpha}\frac{d\hat{P}}{d\alpha} = 0. \tag{13}$$

Solving for $\hat{P}$ and imposing the condition for unity area ratio at zero transmural pressure, i.e., $\hat{P}(1) = 0$, gives

$$\hat{P}(\alpha) = C\left(1-\frac{1}{\alpha^2}\right) \tag{14}$$

where C is an arbitrary constant. When C is replaced by the extensional stiffness of the tube wall K_E, the result of equation (14) is seen to be identical to the tube law derived by Treloar [6] from kinetic theory for a thin rubber tube under positive transmural pressure.

For specified inlet conditions and neglecting $\frac{d\hat{p_e}}{dx}$ due to wall tension and bending, integrating (8), (9), and (10) yields

$$\frac{S}{S_1} = \left(\frac{\alpha}{\alpha_1}\right)^{-\frac{M}{2}} \tag{15}$$

$$\frac{2f_0}{\alpha_1}\frac{x-x_1}{D_0} = \left(\frac{\alpha}{\alpha_1}-1-\frac{\left(\frac{\alpha}{\alpha_1}\right)^{M+1}-1}{S_1^2(M+1)}\right) \tag{16}$$

$$\frac{p-p_1}{\frac{1}{2}\rho u_1^2} = \frac{2}{S_1^2}\frac{\left(\frac{\alpha}{\alpha_1}\right)^{M-2}-1}{(M-2)} \tag{17}$$

$$\frac{\Delta p_f}{\frac{1}{2}\rho u_1^2} = 1-\left(\frac{\alpha_1}{\alpha}\right)^2-\left(\frac{p-p_1}{\frac{1}{2}\rho u_1^2}\right) \tag{18}$$

where, Δp_f is the total stagnation pressure loss due to fluid friction.

From the above it can be seen that for the computed values of M given in Fig. 8 and for $S_1^2 \gg 1$, the mean pressure increase given by (17) is very small. This is consistent with the small

mean upstream pressure increase measured in the shock experiments. Further, under the same conditions, equation (16) predicts that the *mean* area distribution will be relatively independent of the inlet speed index, and will be a weak function of the flow rate through the friction factor f_0. Thus, equation (16) reduces to the simple result

$$\alpha = \alpha_1 + 2f_0\frac{(x-x_1)}{D_0} \tag{19}$$

The experimentally acquired area distributions show that the mean area growth is relatively linear as predicted by equation (19). The average slope of the mean area curve in these measured distributions and the slope ($2f_0$) predicted by the above equation differ at most by about 15 percent. Further, it is possible to compute the shock position by substituting (x_1', α_1') in equation (16).

It is now possible to develop an approximate expression for the length of the tube required for the flow regulator. The shock is at its farthest stable position from the constriction, when the outlet end of the tube is about to buckle inwards. The tube length then must exceed this distance by several diameters. Thus, the tube length is arbitrarily taken to be equal to

$$L = (x_1' - x_1)^{**} + 6D_0 \tag{20}$$

The farthest stable position $(x_1' - x_1)^{**}$ of the shock is found by writing the modified Bernoulli relation between the inlet and the outlet. Thus,

$$p_i + \frac{1}{2}\rho u_i^2 = p_0^{**} + \frac{1}{2}\rho u_0^2 + \Delta p_c + \Delta p_{f1} + \Delta p_s + \Delta p_{f2} \tag{21}$$

where Δp_c, Δp_{f1}, Δp_s, Δp_{f2}, are the stagnation head losses across the constriction, across the tube section upstream of the shock, across the shock, and across the tube section downstream of the shock respectively. Each of these losses can be expressed approximately by the following relations.

$$\Delta p_c = K_c\frac{1}{2}\rho u_c^2 \tag{22}$$

$$\Delta p_{f1} = \left(1 - \left(\frac{\alpha_1}{\alpha_1'}\right)^2 - \frac{2}{S_1^2}\left(\frac{\alpha_1'}{\alpha_1}\right)^{M-2}\right)\frac{1}{2}\rho u_1^2 \tag{23}$$

$$\Delta p_s = K_L\left(1 - \frac{\alpha_1'}{\alpha_2'}\right)^2\frac{1}{2}\rho u_1'^2 \tag{24}$$

$$\Delta p_{f2} = \frac{4f_0}{D_0}\left(\frac{L - (x_1' - x_1)^{**}}{\alpha_2'}\right)\frac{1}{2}\rho u_2^2 . \tag{25}$$

Equation (23) has been obtained from equations (17) and (18). As before, it will be assumed that $\alpha_i = \alpha_0 = 1$, $\alpha_2' \simeq 1$, $K_c \simeq 0$. Further, it can be estimated that the last term of (23) is negligible and that $\Delta p_{f2} \ll \Delta p_{f1}$. Hence, equation (21) can be written as

$$\left(\frac{p_i - p_e}{K_B}\right) \simeq \left(\frac{p_0 - p_e}{K_B}\right)^{**} + \left(\frac{Q}{A_0\sqrt{2K_B/\rho}}\right)^2\left(\frac{1}{\alpha_1^2} - \frac{1}{\alpha_1'^2} + K_L\left(\frac{1}{\alpha_1'} - 1\right)^2\right). \tag{26}$$

Combining equation (26) with equations (4), and (2) gives

$$\left(\frac{p_i - p_e}{K_B}\right) \simeq -3 + \left(\frac{p_i - p_e}{K_B} - \hat{P}(\alpha_1)\right)\left(1 - \left(\frac{\alpha_1}{\alpha_1'}\right)^2 + K_L\alpha_1^2\left(\frac{1}{\alpha_1'} - 1\right)^2\right). \tag{27}$$

For given $\left(\alpha_c, \frac{p_i - p_e}{K_B}\right)$, α_1' can be found by using equations (1) and (27). Having found α_1', the distance $(x_1' - x_1)^{**}$ can be found from the approximate relation

$$(x_1' - x_1)^{**} = \frac{D_0}{2f_0}(\alpha_1' - \alpha_1) \tag{28}$$

and the tube length can be computed from the relation given by equation (20).

In summary, the experimental data for the characterization of the flow regulator have been used for the development of expressions to be used in the selection of design parameters. In particular, for large Reynolds number and large inlet speed index, the required length of collapsible tube for the minimum possible downstream pressure and specified inlet conditions is given by equations (1), (27), (28), and (20). Further, equations (5) and (7) lead to the determination of the maximum possible downstream pressure for continuous flow regulation.

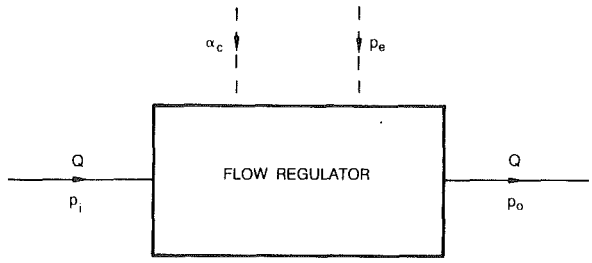

CONTROL VARIABLES: External Pressure p_e ; Constriction Size α_c
FLOW VARIABLES: Flow Rate Q ; Inlet Pressure p_i ; Outlet Pressure p_o
FLOW REGULATOR FUNCTION: Maintain Q Constant for Fixed p_i and Variable p_o

Fig. 10 The collapsible-tube flow regulator

2 Development of Design Criteria

In this section, a procedure for the design of a collapsible tube flow regulator will be developed on the basis of the relations derived earlier (Section 1). The design procedure will be illustrated by means of a design example.

The function of the proposed flow regulator is indicated in Fig. 10. The objective is to maintain the flow rate at the outlet fixed within a narrow specified range independent of downstream pressure which can vary by a predetermined finite amount. The upstream pressure is held fixed at a specified value. The basic configuration of the flow regulator is shown in Fig. 11. Two external control variables are allowed, namely, the constriction area ratio α_c and the external pressure p_e. The area ratio α_c may be varied by means of a mechanical constriction. The external pressure p_e may be kept fixed either by connection to the atmosphere or may be made adjustable by connection to a regulated, external air supply.

The variables that need to be considered in the design of the flow regulator fall into two separate categories, namely, specified variables, and design variables. The latter group can be divided into primary design variables and secondary design variables depending on the degree of their importance in the design. This categorization of variables is given in Table 2. Neglecting for the moment the secondary design variables, the flow rate Q can be expressed as a function of all the remaining specified and design variables. Thus,

$$Q = f(A_0, L, K_B, \mu, \rho, A_c, p_i - p_e, T_0). \tag{29}$$

In the above expression, on the basis of prior knowledge, only the inlet and outlet transmural pressure differences have been included. By dimensional analysis, this can be alternatively compressed as a relation between nondimensional groups as given below, i.e.,

$$\frac{Q}{A_0\sqrt{2K_B/\rho}} = f\left(\mathrm{Re}_{D_0}, \frac{L}{D_0}, \alpha_c, \frac{(p_i - p_e)}{K_B}, \frac{(p_0 - p_e)}{K_B}, \frac{T_0}{D_0K_B}\right). \tag{30}$$

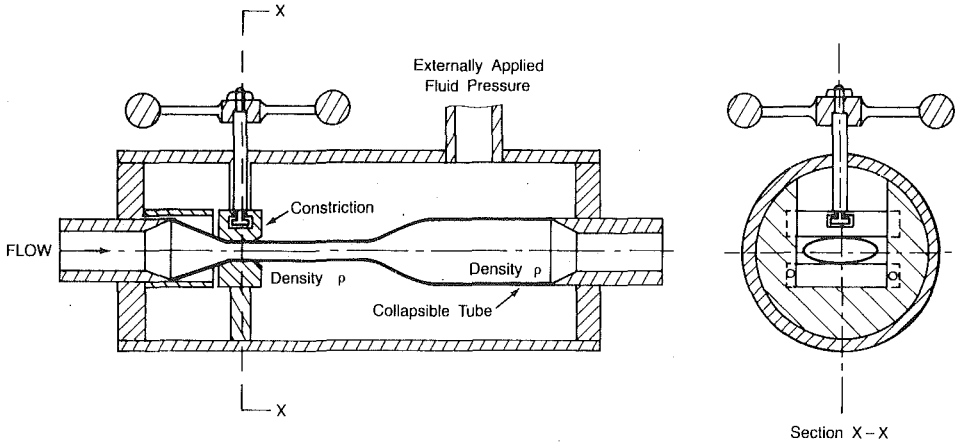

Fig. 11 Proposed flow regulator configuration

Table 2 List of flow regulator variables

Specified variables

Flow rate Q ($Q_{max} > Q > Q_{min}$)
Inlet pressure p_i ($p_{imax} > p_i > p_{imin}$)
Outlet pressure p_0 ($p_{0max} > p_0 > p_{0min}$)
Fluid viscosity μ
Fluid density ρ

Design Variables

Primary design variables:

Resting area $A_0 = \frac{1}{4}\pi D_0^2$
Tube bending stiffness K_B — Tube parameters
Tube length L

External pressure p_e
Constriction area ratio $\alpha_c = A_c/A_0$ — *Control variables*

Wall pretension T_0

Secondary Design Variables:

Rigid inlet area A_i
Rigid outlet area A_e
Loss coefficients K_c, K_e

The above functional relationship reduces to a simpler form when the specified variables and the design variables fall within the design range of the flow regulator. It then assumes the form of equation (3) provided the following conditions, which specify its range of validity are satisfied. They are:

1. The flow is inertia dominated (i.e., $Re_{D0} \gg 1$).
2. The flow immediately downstream of the constriction is supercritical (i.e., $S_1^2 \gg 1$).
3. The range of variation of the pressure difference at the outlet is such that

$$\frac{(p_{0max} - p_e)}{K_B} < \frac{(p_0 - p_e)^*}{K_B} \tag{31}$$

and

$$\frac{(p_{0min} - p_e)}{K_B} > \frac{(p_0 - p_e)^{**}}{K_B} \simeq -3. \tag{32}$$

At the first limit given above, the shock vanishes into the constriction and the flow is no longer regulated. Beyond the second limit, the shock begins to oscillate along the tube and the outlet flow also oscillates in time.

4. The length of the collapsible tube must be greater than the maximum distance from the constriction at which a stable shock can be formed, i.e., $L > (x_1' - x_1)^{**}$.

The procedure for the design of the flow regulator for a given set of specified variables (Q, p_i, p_{0max}, $p_{0\,min}$, ρ, μ) is described below.

Selection of A_0, K_B, p_e:

The resting area A_0 (or equivalently the corresponding tube diameter D_0), the bending stiffness K_B, and the external pressure p_e are selected to satisfy the four conditions described above.

In making this selection, the designer should also be guided by other practical considerations in the choice of materials and dimensions. For example, the structural strength, resistance to corrosion and wear, fabrication constraints, and cost are some of the factors that may have to be considered. If the critical Reynolds number for turbulence is not exceeded, then the appropriate laminar-flow friction factors for noncircular ducts should be employed. To evaluate S_1, the area ratio α_1 can be approximated by the constriction area ratio α_c, and its useful practical range of variation should be taken as $0.15 < \alpha_c < 0.45$. The wave speed for a given α_c in computing S_1 can be obtained from the nondimensional plot in Fig. 9. It is also suggested that $(p_{0\,min} - p_e)$ be selected to be a positive quantity and that S_1 be chosen to be greater than about 3.

Selection of α_c:

Once (A_0, K_B, p_c) have been chosen, the values of the normalized flow rate $(Q/A_0\sqrt{2K_B/\rho})$ and the normalized pressure difference $(p_i - p_e)/K_B$ are computed. The corresponding value of the constriction area ratio α_c is then calculated from equation (3) or is obtained from the plot of Fig. 6.

If the same flow regulator is required to function over a range of flow rates ($Q_{min} < Q < Q_{max}$) and a range of inlet pressures ($p_{min} < p < p_{max}$), the corresponding values of the constriction area ratio α_c can be located in the plot of Fig. 6 with α_c varying between the practical lower and upper limits of about 0.15 and 0.45, respectively.

Selection of L:

The length of the collapsible tube is found from relation (20) which expresses the fact that the tube length must be several diameters greater than the distance $(x_1' - x_1)^{**}$ of the shock from the constriction when it is in its farthest stable position. The value of the area ratio α_1' at the entry to the shock in this position is first calculated from (1) and (27). Then relation (28) is used to compute the distance $(x_1' - x_1)^{**}$.

Check on $p_{0\,max}$:

Finally one must make sure that the maximum downstream pressure is not so high as to force the shock inside the constriction because this would cause the flow rate to fall below its specified value for fixed inlet pressure. Thus, one should

make sure that equation (31) is satisfied once $(p_0-p_e)^*/K_B$ is computed from equations (5) and (6). If this last step is satisfied, then the basic design is complete. If it is not, then the design values of (A_0, K_B, p_e, L) have to be suitably altered until all the conditions are satisfied. For this purpose, it is useful to know how sensitive the design is to changes in the values of variables.

The sensitivity of the regulated flowrate to changes in design variables can be found from equation (2) with $\alpha_i = 1$ and $K_c = 0$. The fractional change in flow rate Q due to fractional changes in the design variables is obtained by differentiating equation (2). Then,

$$\frac{dQ}{Q} = Q_{A_0}\frac{dA_0}{A_0} + Q_{KB}\frac{dK_B}{K_B} + Q_{(p_i-p_e)}\frac{d(p_i-p_e)}{(p_i-p_e)} + Q_{\alpha_c}\frac{d\alpha_c}{\alpha_c} \tag{33}$$

where

$$Q_{A_0} = 1 \tag{34a}$$

$$Q_{K_B} = -\frac{1}{2(\beta-1)} \tag{34b}$$

$$Q_{(p_i-p_e)} = \frac{\beta}{2(\beta-1)} \tag{34c}$$

$$Q_{\alpha_c} = \left(\frac{1}{1-\alpha_c^2} - \frac{1}{2(\beta-1)}\frac{\alpha_c}{\hat{P}(\alpha_c)}\frac{d\hat{P}}{d\alpha}\bigg|_{\alpha_c}\right) \tag{34d}$$

and

$$\beta \equiv \frac{p_i-p_e}{K_B\hat{P}(\alpha_c)}\,. \tag{34e}$$

The sensitivity coefficients will now be calculated for a typical flow regulator design in which a relatively large flow rate of water is to be delivered from a constant low pressure source to a vessel in which the pressure varies by as much as 100 percent of its average value. Let us say that we want to maintain a fixed flow rate Q of 17.5 l/min between a vessel at a fixed source pressure $p_i = 35$ cm H_2O and another vessel whose pressure may vary between $p_{0\,\min} = 5$ cm H_2O and $p_{0\,\max} = 15$ cm H_2O. The liquid viscosity and density are $\mu = 0.01$g/cm − s and $\rho = 1.0$g/cm^3 respectively. We select a collapsible tube made of latex tube of approximately 1 mm wall thickness and an internal diameter of 2.54 cm. This is satisfactory from the point of view of strength and durability. For such a tube $K_B = 400$ dynes/cm^2. Using these values with $p_e = 5$ cm H_20 we obtain $\mathrm{Re}_{D0} = 14{,}620 \gg 1$, $S_1^2 \approx 13.4 > 1$ (taking $\alpha_1 \approx 0.2$), and $\left(\frac{p_{0\min}-p_e}{K_B}\right) \approx 0$. Next, we assume that $\alpha_c \approx \alpha_1$, and take $K_c \approx 0$.

Then, $Q/A_0\sqrt{2K_B/\rho} = 2.035$, and $(p_i-p_e)/K_B = 73.58$. Then from equation (3) α_c is calculated to be about equal to 0.217; since this value is close to the initially assumed value of 0.2 our calculations, so far, are valid. Subsequently, the length selection step yields $\alpha_1' = 0.722$, $(x_1'-x_1)^{**} = 89.2$ cm, and therefore $L = 104.4$ cm. Finally, we wish to ensure that the shock will not be driven to the constriction at the highest vessel pressure. We calculate the value of $(p_0-p_e)^*/K_B$ to be 37.1, and, therefore, $p_0^* = 20.1$ cm H_2O, whereas $p_{0\max} = 15$ cm H_2O. Hence, the proposed design meets all the requirements.

The sensitivity analysis yields

$$\frac{dQ}{Q} = \frac{dA_0}{A_0} + 0.061\frac{dK_B}{K_B} + 0.439\frac{d(p_i-p_e)}{(p_i-p_e)} + 0.958\frac{d\alpha_c}{\alpha_c}\,. \tag{35}$$

As a result of equation (35), in the neighborhood of the design-parameter-values employed, an increase in each of the variables (A_0, K_B, p_i-p_e, α_c) leads to an increase in flow rate. If A_0 and K_B are considered to be fixed for this design, then the flow rate is more sensitive to changes in constriction area ratio than to changes in inlet pressure difference.

3 Conclusions

This paper focused on the experimental verification of the analytically derived (Part I [1]) characteristic flow regulation curve for the compliant-tube wave-speed flow regulator. As shown in Fig. 3, the conducted experiments satisfactorily demonstrated that the flow rate was indeed independent of downstream pressure variations, as predicted by the analysis, provided the upstream conditions of inlet pressure and constriction area were maintained fixed. The experimental data for the characterization of the flow regulator were subsequently applied to the development of expression to be used in the selection of flow-regulator design parameters (Section 1). The flow-regulator design procedure was illustrated by means of an example (Section 2) and the sensitivity of the regulated flow rate to changes in design variables was estimated for a typical flow regulator design (equations (33) through (35)). In the neighborhood of the selected parameter values, the regulated flow rate is primarily sensitive to changes in the resting cross-sectional area of the tube A_0, and to changes in the constriction area ratio α_c; it is less sensitive to changes in the inlet pressure difference (p_i-p_e) and considerably less sensitive to changes in the tube bending stiffness K_B.

References

1 Kececioglu, I., "Flow Regulation Characteristics of Thin-Walled Compliant Tubes. Part I: Theoretical Analysis," ASME Journal of Fluids Engineering, published in this issue. pp. 319–329.

2 Kececioglu, I., Kamm, R. D., and A. H. Shapiro, "Structure of Shock Waves in Collapsible-Tube Flow," *Proc. 31st Ann. Conf. Engrng. Medicine & Biology*, Atlanta, Georgia, 1978, p. 92.

3 Kececioglu, I., "Experimental Determination of the Structure of Shock Waves in Fluid Flow through Collapsible Tubes With Application to the Design of a Flow Regulator," Thesis for the Degree of Engineer, Dept. of Mechanical Engineering, Massachusetts Institute of Technology, 1979.

4 Kececioglu, I., McClurken, M. E., Kamm, R. D., and A. H. Shapiro, "Steady Supercritical Flow in Collapsible Tubes. Part I. Experimental Observations," *Journal of Fluid Mechanics*, Vol. 109, 1981, pp. 367–389.

5 McClurken, M. E., Kececioglu, I., Kamm, R. D., and A. H. Shapiro, "Steady Supercritical Flow in Collapsible Tubes. Part 2. Theoretical Studies," *Journal of Fluid Mechanics*, Vol. 109, 1981, pp. 391–415.

6 Treloar, L. R. G., *The Physics of Rubber Elasticity*, Clarendon Press, 1958.

L. Briançon-Marjollet
Bassin D'Essais des Carènes,
G.T.H.,
27100 - Le Val de Reuil, France

J. M. Michel
Institut de Mécanique de Grenoble,
Domaine Universitaire,
38041 - Grenoble Cedex, France

The Hydrodynamic Tunnel of I.M.G.: Former and Recent Equipments

The I.M.G. Hydrodynamic Tunnel is described in its initial state and with successive equipments that improved its performances. Particular attention is given to the recent nuclei control system.

Introduction

The Hydrodynamic Tunnel of the Institut de Mécanique de Grenoble was designed and built by the Sogreah Company (later Neyrtec, now Alsthom-A.C.B.-C.E.R.G.) during the years 1965–1967, on the order of the Grenoble University, with the financial support of the French "Direction des recherches et Moyens d'Essais (abbreviation, D.R.M.E., now D.R.E.T., i.e. "Direction des Recherches, Etudes et Techniques). At that time, in France as in other countries, the development of hydraulic machinery and the Navy interest in fast vessels stimulated the need for fundamental research in the field of high speed hydrodynamics. It was decided that a research team would be gradually assembled around an experimental research facility, taking in account on one side the initial works on rapid water jets by Dodu [1] at the Grenoble University and, on the other side, the old experience in various fields of cavitation research inside the Sogreah Company (for instance, Danel and Duport [2]).

The tunnel had to meet the following requirements:

1 To be versatile, either by the flow configuration: free surface channel or solid wall channel with circular or rectangular cross section, or by the flow regime: cavitating or non-cavitating flow and flows with ventilation.

2 To produce a good-quality flow, with regard to the head steadiness at the channel entry, the air content of water, the mean velocity profile and the turbulence rate.

3 To make significantly reduced the influence of the external boundaries.

4 To permit the observation of a large flow field. Besides, the size of the tunnel was to be moderate, in order to facilitate the fitting up of subsequent equipments.

These conditions led the designer to propose a tunnel of which overall dimensions were about 20 m in length, 9 m in height, for which the maximum flow discharge and the maximum water velocity were 0.65 m^3/s and 13 m/s respectively, with a minimum cavitation number turning around 0.02 and a total volume of water of about 40 m^3. The available information was largely used, particularly the one which was discussed at the first Symposium on Cavitation Research Facilities and Techniques [3], to which we are very indebted.

Contributed by the Fluids Engineering Division of THE AMERICAN SOCIETY OF MECHANICAL ENGINEERS. Manuscript received by the Fluids Engineering Division November 8, 1988.

In its initial state, the I.M.G. had only one test section equipped with a free surface channel [4]. Later, in 1974–1975, a second branch was added in parallel to the first one at the tunnel upper level, in order to vary the possible flow configurations and to improve the efficiency of the experimental work. It was also provided with a free surface channel.

Hereafter, a brief survey of the experimental research history at the Grenoble University in the field of ventilated and cavitating flows will be given first, because it helps to understand the present tunnel design. Second, the main parts of the tunnel will be described. A particular development will be devoted to the recent equipment intended to control the nuclei concentration of the tunnel water.

1 The Main Steps of the Experimental Research

The I.M.G. Tunnel was initially used to study the physical behavior of supercavitating or ventilated flows, with a special attention paid to the cavity geometry and to the conditions of air entrainment in the cavity wake [5]. During the years 1970–1977, Rowe [6, 7] conducted experiments on base-vented hydrofoils using the first then the second test section. His interest was in the hydrodynamic forces and the behavior of the wings at various operating conditions. He designed a hydrodynamic balance on each test section. The second balance, which is supplied with an automatic device for data acquisition and treatment, was designed with the assistance of the French O.N.E.R.A. and is still used today. In 1974, the construction of the second branch of the tunnel was utilized as an opportunity to place an intermediate free surface tank downstream of the two test sections (Fig. 2), to improve the separation of the air injected at the basis of the foils. The ventilated flows around 3-D base-vented hydrofoils were then experimentally studied by Verron [8], using the first and the second free surface channels. The interest of Laali, 1978–1980, was in the relation between the airflow discharge and the pressure inside the ventilated cavities. To this end, the so-called "half-cavity configuration," in which an air cavity is formed between an initially horizontal water jet and a solid bottom, was adapted to the first tunnel section [9].

From about 1980, several studies centering around developed cavitation were conducted at I.M.G. They used several body

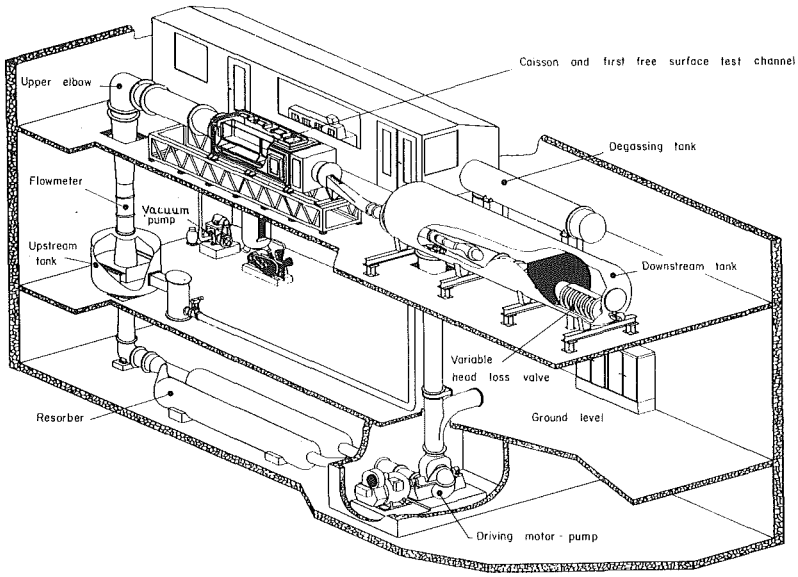

Fig. 1 General layout of the research facility in its first state

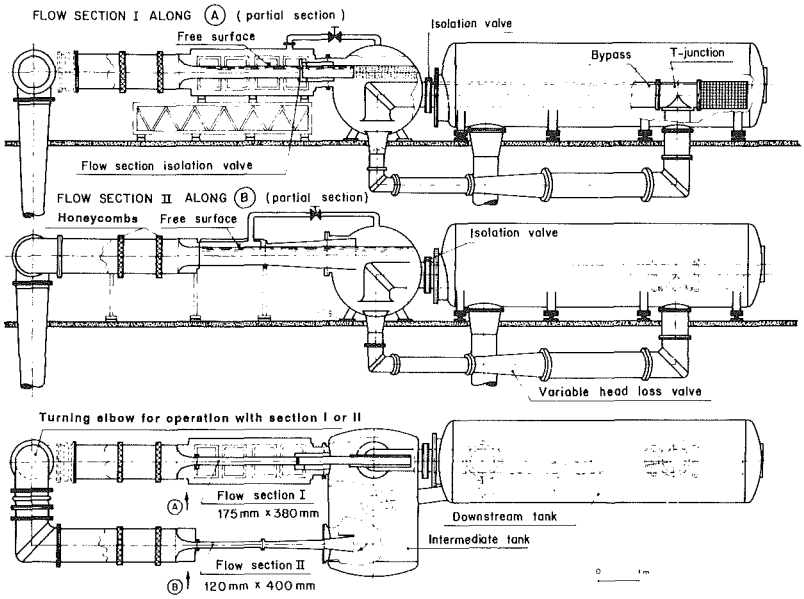

Fig. 2 The upper part of the tunnel with the intermediate tank and the second flow section

shapes in 2-D flows, such as wedges, cylinders elliptical foils, NACA foils [10]. Work concentrated on attached cavitation and its relation with the boundary layer behavior. The same concern led Franc, in 1983–1985, to observe the detachment of an attached cavity on a Naca foil oscillating in incidence, by the means of numerous high speed films [11, 12]. The foil oscillation is produced by a mechanical system with a possible frequency up to 25 Hz and an amplitude up to ± 5 deg. The instantaneous recording and the treatment of various measurements such as attack angle and forces is made through a computer. The control of the foil incidence from the computer is also possible. Recently (1985–1986), new equipment completed the capacities of the Hydrodynamic Tunnel in producing either attached cavities or cavitation with transient bubbles. It includes a nuclei injection device and a nuclei counting device, both of them forming a complete control system. That equipment was built by the A.C.B.-C.E.R.G. Company and then tested and used by the first present author. It will be described hereafter and its performances will be analyzed with some details.

2 Description of the Hydrodynamic Tunnel

2.1 The General Layout of the Facility. In the initial state of the tunnel (Fig. 1) the main loop comprised the driving pump and the resorber at the lower level, then the upstream tank and the flowmeter in the vertical ascending branch, the upper elbow, the converging nozzle, the free surface channel and the downstream tank at the upper level, and then the descending duct. The first tank was intended to establish constant value of the head at the test channel entry while the second was assigned to separate the air bubbles from the main water flow downstream of the test section, as far as it is possible. The centrifugal pump gives a 0.65 m^3/s flow discharge at 1120 rpm under a head equal to 20m. The power of the motor is 165 kW. Its variable speed is adjustable between 200 and 1200 rpm.

The function of the resorber is to dissolve the minute air bubbles which may be not separated from water after their passage in the main downstream tank. Also it ensures heat exchanges with the water of the cistern in which it is immersed.

It is made of two horizontal parallel ducts (0.900m in diameter, 6.500m in length).

As shown in Fig. 1 the upstream tank (2m in diameter) permits the creation of a free surface and an internal overflow which is bypassed directly to the downstream tank, in view to filter the possible variations of the flow discharge. Actually, the motor-pump runs at a very constant value of its rotation speed, and the internal device of the upstream tank is not used. Usually, this tank is filled with water, apart an air cushion at its upper part. The bypass is used to lower the water velocity in the test section below 3 m/s.

The flowmeter is a helical blade-wheel which is placed in the vertical ascending duct (0.500 m in diameter). It is followed by a conical diverging duct up to the upper elbow (0.800 m in diameter). The flowmeter gives 60 voltage impulses per revolution. The uncertainties of the discharge measurements are + 0.8 percent. The elbow is made with sixteen blades which have a low cavitation index. In the horizontal duct which follows the elbow, two honeycombs with 8 mm cells reduce the turbulence level $T_u = \sqrt{\overline{u'^2}}/U_\infty$, as measured in the test section, to 0.12–0.16 percent.

The converging nozzle has a rectangular cross-section which evolves according to a law given by the model of 2-D free jets issuing from a large container. It emerges into the free surface channel with rectangular section of 0.175 m in width and 0.280 m in height. Thus the area ratio between the upstream and downstream part of the converging nozzle is close to 10. In its initial state, the test channel was built with glass plates (2.500 m in length) and was enclosed in a caisson which sustained the pressure difference. This device gave a good quality flow but was not easy to operate. It will be replaced shortly by a solid wall channel with plexiglas walls.

In its initial state, the test section was connected to the downstream tank through a curved duct and a variable head loss valve. The latter device, which was then immersed into the downstream tank, gives there a pressure lower than the test section pressure. Thus it is possible to work with high σ_v values and simultaneously achieve a high level of water deaeration rate. The degassing tank (Fig. 1) was intended to increase the deaeration rate. In fact, the prominent role in deaeration is played by the downstream tank, due to its large cross-section (2 m in diameter) and the long residence-time of water under the free surface. Thus the degassing tank is no longer used. The total oxygen content of the initially saturated tunnel water, as measured by a Beckman apparatus, is reduced by 4 or 5 after an hour of run under low ambient pressure.

2.2 Modification of the Tunnel at Its Upper Level. The so-described tunnel achieved the promised performances but cavitation in the curved duct downstream of the section could be a source of problems in some operating conditions. Besides, the intensive injection of air, which was needed for the study of ventilated flows, was partly impeded by the too large value of the minimum head loss in the variable head loss valve. Thus, as previously mentioned, the construction of the second test section was started together with the setting-up of the intermediate tank downstream of both the test sections (Fig. 2).

The intermediate tank was designed, after a preliminary experimental study on a model, to separate about 90 percent of the air injected. It can be connected directly to the downstream tank. Another possibility is to use the variable head loss valve, which is now placed out of the tank. Thus, large amounts of air (up to 5.5×10^{-3} kg/s) can be injected in the water flow without any recirculation: for the lower pressures, the height of the air-water mixture at the channel outlet can reach 1.25 times the water height at the entry.

The second branch of the tunnel is served by the first upper elbow which can be rotated by 90 deg, as shown on Fig. 2. The cross-section area of the second test section (0.120 m in width, 0.400 m in height) is close to the first one, but its shape reduces the boundary influence and it facilitates the setting-up of the hydrodynamic wall balance. The length of the test section is 1.600 m, the thickness of the plexiglas walls is 0.070 m.

The present structure of the I.M.G. Hydrodynamic Tunnel results in two main consequences. On one side, it is favorable to the study of unsteady cavitating flows around oscillating bodies because it tends to make the test section uncoupled from the other parts of the loop: the upstream flow at the channel entry is unaffected by the foil oscillation. On the other side, the two free surface tanks for the air decanting tend to destroy the air nuclei down to a critical pressure of -3×10^4 Pa at least. Thus the tunnel is suited to the study of the attached cavity-boundary layer interaction and that helps to distinguish the effect of the air nuclei from the viscous effect. However, from the viewpoint of applications, that character can become a disadvantage, considering particularly the similarity laws relative to the nuclei influence [3]: although they are still not fully established in detail, their main tendencies indicate that a large nuclei concentration is required in the case of small model flows. That last point led to the additional equipment of the nuclei control system, in order to vary the flow patterns and to enlarge the application field of the experimental work.

3 The Nuclei Control System

The choice of the control system results from the nuclei effects which are expected in the study of flows around slender bodies such NACA foils in the I.M.G. Hydrodynamic Tunnel. A first investigation gave the following order of magnitude for the nuclei population: the characteristic size of the microbubbles should be mainly centered in the 4 – 15 μm range, i.e., in critical pressure of the order $-2{,}5 \times 10^4$ Pa to -4×10^3 Pa and the total nuclei density had to be between about 0.1 and 10 per cubic centimeter. Those data were obtained from the Lecoffre's previous experience in measuring nuclei population by the venturi counter [14, 15]. Then, taking in account the discharge of the tunnel at a channel velocity of 10 m/s, i.e., about 0.5 m^3/s, the seeding system has to furnish about 5×10^6 nuclei per second, at least if we want a uniform distribution of the nuclei population through the flow cross section. In the same way, the measuring device must be able to count this kind of population. Having an understanding of the performances of the first venturi counter, this one seemed not well suited to our situation, because it is saturated by small enough nuclei concentrations and thus is to be considered rather as a cavitation susceptibility meter. It happened that a new venturi counter, whose geometry is deeply different from the first one, was proposed by Lecoffre and the A.C.B.-C.E.R.G. Company. When accompanied by a dilution method, this device offers a large enough measurement range for the total nuclei density. In particular, it will be shown that the performance of the measuring device is dependent on the design of the tunnel on which it is implanted.

Another point must be emphasized here: by the analysis of high-speed films, we get the number of bubbles which explode in the vicinity of a NACA foil in the tunnel test section. At the zero incidence, that foil gives a flat pressure distribution over upper side in such a way the air nuclei undergo a negative pressure step. Now, from the counting of the air nuclei upstream of the test section, it is possible to estimate the number of bubbles which probably should explode in the foil region, taking in account their critical pressure and the pressure chart inside the flow field. The estimate gives a number which is between 0.5 and 2.5 times the number of bubbles which actually explode for two different configurations of the flow. Of course, such an estimate can be only rough. However it shows that, whatever the uncertainties of the counting device may be, the number of the active nuclei it gives is not far from reality.

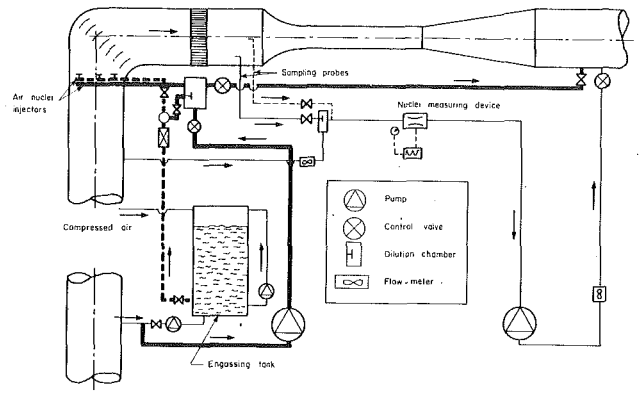

Fig. 3 Sketch of the air nuclei control system

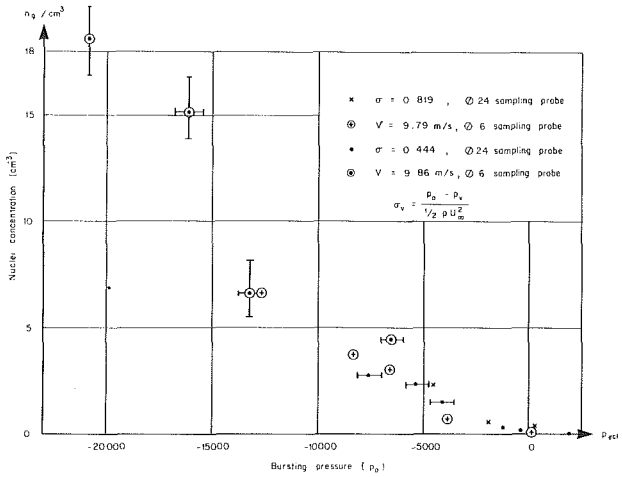

Fig. 4 Nuclei counting in the case of full nuclei seeding

Remark here that a similar procedure was followed by Kodama et al [16] using other injection and counting techniques. The results are of the same order of magnitude.

3.1 The Nuclei Injection Device. The possible nuclei injection devices are numerous and their capacities were discussed largely by Oldenziel [17]. The system in use at I.M.G. is based on the expansion method in which water saturated with air at high pressure ($P_{gen} \simeq 2$ to 5×10^5 Pa) is injected into the tunnel through small orifices. There the liquid path is such that small supercavities are formed which release a high number of tiny bubbles. As a first approximation, the bubbles number in each injector is a function of the injector cavitation number, which is defined as

$$(\sigma_v)_{inj} = (p_{am} - p_v)/(p_{gen} - p_{am})$$

In this expression, p_{am} is the absolute pressure which is established at the injector exit, i.e., the pressure upstream the tunnel converging nozzle.

Figure 3 shows the main parts of the injection device, namely the generator or engassing tank and the injection circuits. The injection is made between the two upper elbows of the tunnel second branch at about 4 m upstream of the test section. Two injection methods are possible. A first method is to make direct injection through 9 injectors distributed over the cross-section of the 0.800m duct. Each injector gives about 6×10^5 nuclei/second at its maximum. In order to decrease the nuclei concentration, it is also possible to make an indirect injection through a dilution chamber in which saturated water expands and is mixed with water which previously is drawn off the tunnel loop. A part of the mixing is then injected into the tunnel through pipes in which many holes are drilled, the other part returns to the downstream tank.

Our present experience with this injection device leads us to formulate some remarks. Firstly, because of the high value of the convergence ratio at the channel entry, the injection is made in a region where the water velocity is small. Thus, for the smaller test velocities, the air nuclei can reside about ten seconds in the large diameter duct. This time is sufficient to make possible a partial decantation of the bubble population under the buoyant gravity effect, and in addition to allow the air escape from bubbles by diffusion. Indeed, those effects can be observed qualitatively, if not measured. Secondly, it was found that the dispersion of the nuclei through the channel cross-section is not achieved with the present location of the injectors: the concentration profile, measured upstream of the converging nozzle, shows spatial variations of about ± 20 percent. By some aspect, that dispersion insufficiency is advantageous because it permits to produce simultaneously very different phenomena on each part of the hydrofoil span. An example will be given below. Finally, the mean nuclei content seems to be slightly too small with respect to some expected effects. Thus the injectors implantation will be shortly modified in order to concentrate the nuclei injection near the middle horizontal plane of the duct.

3.2 The Nuclei Measuring Device. The measuring device is sketched on Fig. 3. It comprises two sampling probes located upstream of the converging nozzle, the nuclei counter and the pipe which conducts the sampled water through a variable speed pump and a flowmeter to the downstream tank.

The sampling probes traverse the 0,800 m duct over one of eight possible radii. The first probe has an internal diameter of 24 mm. Its sampled water passes directly to the nuclei counter. The second probe (diameter 6 mm) is supplied with a dilution chamber in which sampled water is mixed with tunnel water.

The nuclei counter is made by a hydraulic component with a venturi throat followed by a rapidly diverging duct in which an ogive is placed. The narrower annular cross-section has about 1 mm in thickness and 60 mm in circumference. That arrangement avoids interaction between exploding bubbles and permits a larger amount of water to be treated. The counting is made by a piezoelectrical ceramic which detects the noise emitted when the bubbles implode.

In such a device, the measured quantities are the absolute pressure p_1 upstream the venturi throat, the flow discharge q and the total number N of noise peaks recorded during a time t_c. The mean pressure p_2 at the narrower section S_2 is deduced from the Bernoulli equation:

$$p_2 = p_1 - \rho \frac{Q^2}{2}\left(\frac{1}{S_2^2} - \frac{1}{S_1^2}\right), \frac{S_1}{S_2} \simeq 10 \qquad (1)$$

It is assumed that the bursting pressure p_{ec1} of the nuclei which actually explode is larger or equal to the pressure p_2. Here we distinguish the bursting pressure from the critical pressure in view of possible dynamic effects.

Two points are particularly sensitive in that method. The threshold from which noise peaks are counted is somewhat difficult to define acutely. Also, because of the smooth shape of the ogive, the actual value of the cross-section area S_2 is not well defined. Thus a calibration is necessary: it is made by injecting a large amount of air nuclei and assuming that the bursting pressure of the weakest among them is close to the vapor pressure p_v.

When working with the nuclei counting device under various tunnel conditions, we noticed two limitations. The first one is due to the capacity of the noise signal treatment. A saturation appears at about 1800 peaks per seconds. The second restriction is brought by the appearance of an attached cavity around the nose of the ogive. That happens for the value $\sigma_l \simeq 0.7$ of the venturi cavitation number which is defined as:

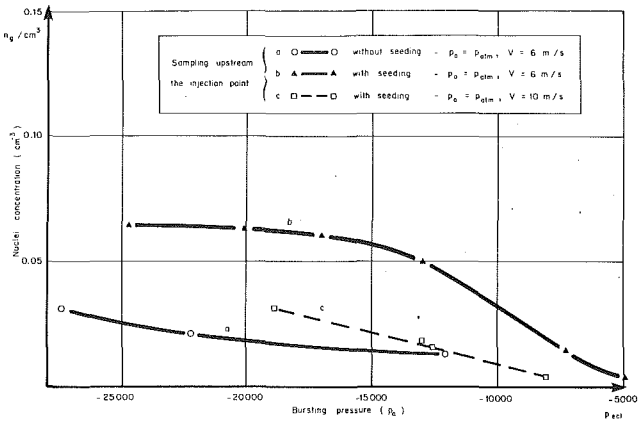

Fig. 5 Tests of nuclei recirculation

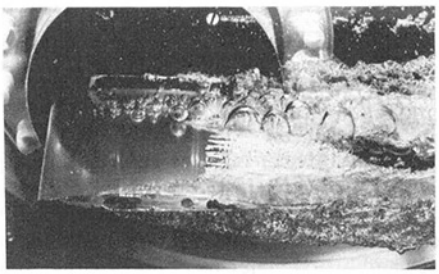

$\alpha = 0°$, $\sigma_v = 0.065$, $R_e = \frac{\rho U_\infty c}{\mu} = 941500$, c : foil chord, c = 0.10 m.

Fig. 6 An example of nuclei effect

$$\sigma_{\text{vent}} = (p_1 - p_v)/\frac{1}{2}\rho\left(\frac{Q}{S_2}\right)^2 \tag{2}$$

where p_1 is close to the value p_{am} of the pressure upstream the tunnel converging nozzle. If we combine equations (1) and (2) and we take the condition $\sigma_{\text{vent}} > \sigma_l$, we find an approximate limit value for the bursting pressure p_{ecl} of the nuclei:

$$p_v - p_{\text{ecl}} \gtrsim \frac{1-\sigma_l}{\sigma_l}(p_{am} - p_v) \tag{3}$$

Thus the measuring range is strongly connected to the operating conditions in the tunnel. It is extended by the largest values of the ambient pressure and the channel velocity.

On the whole, if we keep in mind the limitations which are inherent in this kind of measuring method, we can consider that the present venturi device gives information which deserves confidence, particularly when we compare the results of the measurements to the counting of the exploding bubbles on the foil, as was mentioned previously.

3.3 Experimental Results With Nuclei Injection. Figure 4 shows a typical example of the nuclei measurements under different values of the ambient pressure p_0 inside the tunnel test section and with a velocity value of 10 m/s. Then the nuclei seeding system is fully operated. Both the sampling probes are used. The uncertainties are larger in the case of a large nuclei concentration. That is due, for its most part, to uncertainty in the flow discharge which is obtained as the difference of two large quantities. Indeed, the configuration of Fig. 3 is adopted in view to avoid any cavitational bubbling between the small sampling probe and the venturi counter.

In Fig. 4, each point results from the averaging of the counted nuclei over a 100 s measuring duration. Thus, with a maximum flowrate of one liter per second in the venturi counter, the sampled water volume can reach 0.1 m^3, which is significant with regard to the water volume in the hydrofoil vicinity.

On Fig. 5, are presented tests of nuclei recirculation. The nuclei concentration upstream of the injection point, when the nuclei seeding is operated, is small: its value is less than 0.1 nuclei per cubic centimeter (Fig. 5, cases b and c). Practically we obtain the same concentration if seeding is not made (Fig. 5, case a).

Finally, the photograph of Fig. 6 shows two juxtaposed typical aspects of cavitation on a NACA 16209 foil. On one part of the span, an attached cavity is visible at the rear part of the foil. On the other part, transient bubbles explode from the vicinity of the minimum pressure point and sweep the cavity away. The 2-D pressure distributions on each part are very different. It is noticeable that they seem to match within a small transverse thickness.

References

1 Dodu, J., "Contribution à l'étude de la dispersion des jets liquides à grande vitesse," Publications Scientifiques et Techniques du Ministère de l'Air, numéro 407, 1964.

2 Danel, P., and Duport, J., "The Selection of Length and Head Scales for Cavitation Tests," ASME *Journal of Basic Engineering*, Vol. 82, 1960, pp. 784–790.

3 Holl, J. W., and Wood, G. Y., Ed., "Cavitation Research Facilities and Techniques," ASME Fluids Eng. Div. Conference, Philadelphia, May 1964.

4 Dodu, J., Duport, J., and Michel, J. M., "Le Tunnel Hydrodynamique de l'Université de Grenoble," La Houille Blanche, Vol. 7, 1968, pp. 697–702.

5 Michel, J. M., "Profils minces supercavitants à arrière tronqué: étude physique du sillage en écoulement plan," *La Houille Blanche*, 1974, No. 6, pp. 429–445.

6 Rowe, A., "Profils minces supercavitants à arrière tronqué: Influence de la ventilation sur les caractéristiques de profils portants évoluant au voisinage d'une surface libre," *La Houille Blanche*, No. 3, 1974, pp. 215–230.

7 Rowe, A., "Evaluation of a Three-Speed Hydrofoil With Wetted Upper Side," *J. of Ship Research*, Vol. 23, pp. 215–230.

8 Verron, J., and Michel, J. M., "Based-Vented Hydrofoils of Finite Span Under a Free Surface: An Experimental Investigation," *J. of Ship Research*, Vol. 28, No. 2, June 1984, pp. 90–106.

9 Laali, A. R., and Michel, J. M., "Air Entrainment in Ventilated Cavities: Case of the Fully Developed Half-Cavity," ASME JOURNAL OF FLUIDS ENGINEERING, Vol. 106, Sept. 1984, pp. 327–335.

10 Franc, J. P., and Michel, J. M., "Attached Cavitation and the Boundary Layer: Experimental Investigation and Numerical Treatment," *J. of Fluid Mech.*, Vol. 154, May 1985, pp. 63–90.

11 Franc, J. P., and Michel, J. M., "Experimental Investigation of Unsteady Effects in Cavity Detachment on an Oscillating Hydrofoil," *Proc. of the Int. Symp. on Propeller and Cavitation*, Wuxi, China, Apr. 1986, pp. 286–294.

12 Franc, J. P., and Michel, J. M., "Unsteady Attached Cavitation on an Oscillating Hydrofoil," *J. Fluid Mech.*, Vol. 193, Aug. 1988, pp. 171–189.

13 Holl, J. W., and Wislicenus, G. F., "Scale Effects on Cavitation," ASME *J. of Basic Eng.*, 1961, pp. 385–395.

14 Le Goff, J., Lecoffre, Y., "Nuclei and Cavitation," *Proc. of the 14th Symp. on Naval Hydrodynamics*, Ann Arbor 1982, National Academy Press, pp. 215–242.

15 Oldenziel, D. M., "A New Instrument in Cavitation Research: The Cavitation Susceptibility Meter," ASME, JOURNAL OF FLUIDS ENGINEERING, Vol. 102, pp. 433–438.

16 Kodoma, Y., Tamiya, S., Take, N., and Kato, H., "The Effects of Nuclei on the Inception of Bubble and Sheet Cavitation on Axisymmetric Bodies," ASME *Intern. Symp. on Cavitation Inception*, New York, Dec. 2–7, 1979, Proc., pp. 75–86.

17 Oldenziel, D. M., "Bubble Cavitation in Relation to Liquid Quality," Thesis Delft Hydraulics Laboratory, Pub. No. 211, May 1979.

Hubert Chanson
Engineering Consultant,
F75116 Paris, France

Study of Air Demand on Spillway Aerator

1 Introduction

1.1 Presentation. The irregularities on the spillway surfaces will in a high speed flow cause small areas of flow separation. In these regions the pressure will be lowered and if the velocities are high enough the pressure may fall to below the local vapor pressure of the water. Vapor bubbles will form and when they are carried away downstream into high pressure region the bubbles collapse and possible cavitation damage may occur. Experimental investigations (Volkart and Rutschmann (1984)) show that the damage can start at clear water velocities of between 12 to 15 m/s. Up to velocities of 20 m/s the surfaces may be protected by streamlining the boundaries, improving the surface finishes or using resistant materials.

When air is present in the water the resulting mixture is compressible and this damps the high pressure caused by the bubble collapses (Peterka (1953)). Peterka, Russell and Sheehan (1974) performed experiments on concrete specimens and showed that air concentrations of 1–2 percent reduce substantially the cavitation erosion and above 5–7 percent no erosion was observed. When there is not enough surface aeration (i.e., downstream of a gate) or if the tolerances of surface finish required to avoid cavitation are too severe (i.e., V > 30 m/s), air can be artificially introduced by aeration devices (called aerators) located on the spillway floor and sometimes on the side walls.

1.2 Aeration Devices. The design of a small deflection in a spillway structure (i.e., ramp, offset) tends to deflect the high velocity flow away from the spillway surface (Fig. 1). In the cavity formed below the nappe, a local subpressure beneath the nappe (ΔP) is produced by which air is sucked into the flow (Q_{air}^{inlet}).

The properties of the different types of aeration devices were detailed by Vischer et al. (1982). A combination of a ramp, an offset, and a groove provides the best design: the ramp dominates operation at small discharges while the groove provides space for the air supply and the offset enlarges the trajectory of the jet at higher discharges. Volkart and Chervet (1983) have studied on model the behavior of a large range of aerators.

1.3 Mechanisms of Air Entrainment. Chanson (1989) showed that the air entrainment above an aerator (Fig. 2) is characterized by: 1 air entrainment through the upper and lower free surfaces of the water jet called nappe entrainment, 2 plunging jet entrainment at the intersection of the water jet and the rollers, and 3 air recirculation in the cavity below the jet. The study of the different mechanisms of air entrainment is complex because of the interactions between the different air entrainment processes.

The first step is the study of the air demand relationship. The air demand may be defined as the relationship between the air discharge provided by the air supply system, the subpressure in the cavity and its distribution along the nappe, and the flow characteristics. The operating point of a bottom aerator is then obtained by combining the pressure drop curves of the air supply system with the air demand characteristic curves as detailed by Low (1986). This calculation fixes the cavity under pressure, and hence the jet trajectory and the cavity geometry.

Previous authors (Pinto et al. (1982), Tan (1984)) presented the air demand relationship as: $q_{air}^{inlet} = K * L_{jet}$ but this does not take in account the air recirculation and the plunging jet entrainment and it becomes usual (Chanson (1989) and Low (1986)), to study the air demand as: $Q_{air}^{inlet}/Q_w = f(P_N, \text{Fr})$.

1.4 Experiments. The author (Chanson (1988)) performed experiments on a 1:15 scale model of the Clyde dam spillway with a slope $\alpha = 52.33°$. The model provided Froude numbers in the range 3 to 25 with initial average flow velocities from 3 m/s to 14 m/s. By adjusting the gate at the entry of the flume the initial flow depth was from 20 mm to 120 mm. The first aerator configuration included a ramp of 5.7° (t_r = 30 mm, L_{ramp} = 300 mm) and an offset of 30 mm height. This geometry was the same as that used by Low (1986). The second configuration had no ramp and an offset of 30 mm height as

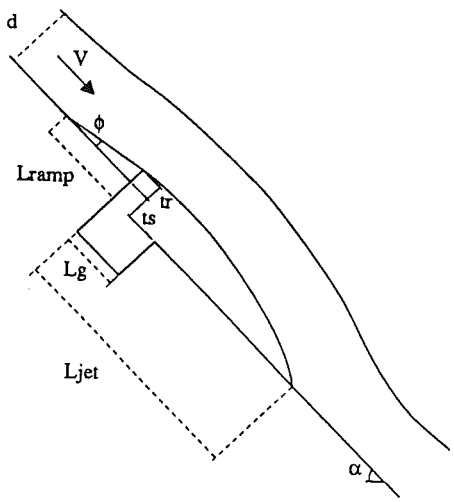

Fig. 1 Geometry of an aerator device

Contributed by the Fluids Engineering Division for publication in the JOURNAL OF FLUIDS ENGINEERING. Manuscript received by the Fluids Engineering Division March 7, 1989.

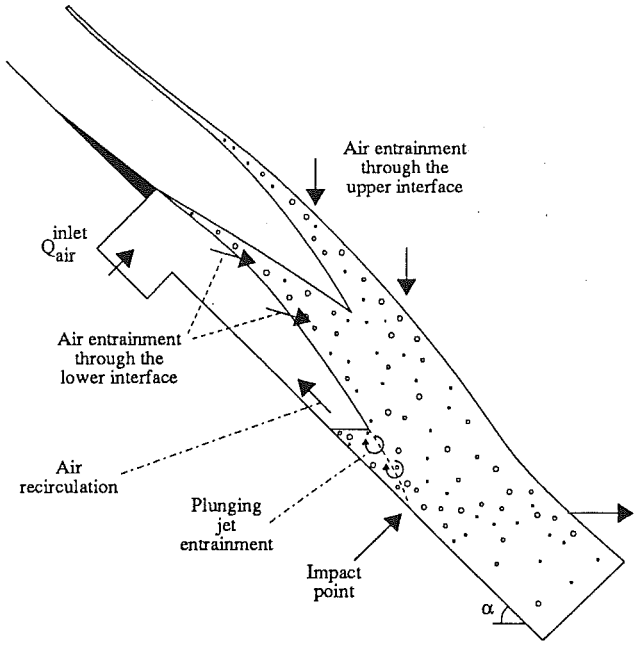

Fig. 2 Air entrainment above an aerator

that used by Tan (1984). The author performed air demand experiments with both aerator configurations. In some cases two fans were connected to the air supply inlets to boost the pressure beneath the nappe to the atmospheric pressure.

First various parameters are detailed, then the experimental results are presented and finally a study of the particular case $Q_{air}^{inlet} = 0$ is developed.

2 Dimensionless Parameters

2.1 Parameters. The relevant parameters needed for any dimensional analysis come from the following groups:

A Fluid Properties. These consist of: the pressure above the flow P_0 (Pa), the density of water ρ_w (kg/m^3), the density of air ρ_{air} (kg/m^3), the dynamic viscosity of water μ (N.s/m^2), the surface tension of the water (N/m), the vapor pressure at the experiment temperature P_v (Pa) and the acceleration of gravity g (m/s^2).

B Spillway and Aerator Geometry. They are: the spillway slope α, the channel width W (m), the roughness of the spillway surface k_s (m), the offset height t_s (m), the groove length L_g (m), the duct area below the spillway surface A_d (m^2), the angle between the ramp and the spillway ϕ and the ramp length L_{ramp} (m).

C Geometry of the Air Inlets.

D Flow Properties. These consist of: the velocity distribution, the air concentration distribution at the end of the approach flow, the distribution of the axial component of turbulent velocity, and the distribution of the lateral component of turbulent velocity. Normally the distributions of these parameters are replaced by their mean value: the water depth of the flow in the approach zone d (m), the flow velocity V (m/s), the root mean square of axial component of turbulent velocity u' (m/s), and the root mean square of lateral component of turbulent velocity v' (m/s).

E Undernappe Cavity Properties. These consist of: the water jet length L_{jet} (m), the difference between atmospheric pressure and air pressure beneath the nappe ΔP (Pa), and the air discharge through the ducts Q_{air}^{inlet} (m^3/s).

F Downstream Flow Properties. These consist of: the air concentration distribution, the flow depth and the velocity distribution downstream of the aerator.

The study on spillway model uses the atmospheric pressure as pressure above the flow and when the vapor pressure P_v is small compare to the atmospheric pressure and the pressure in the cavity ($P_0 - \Delta P$), the parameters P_0 and P_v may be neglected. Laali (1980) performed experiments with variations of the pressure above the flow and his results will be discussed later.

Ervine and Falvey (1987) showed that the lateral component of turbulence intensity v'/V is proportional to the axial turbulence intensity u'/V and for an axisymmetric jet their results fitted: $v'/V = 0.38 * u'/V$. For a two-dimensional plane jet it is reasonable to assume that there will be a similar relationship and this enables us to replace u' and v' by the independent parameter u'.

Nomenclature

A_d = duct area below the surface spillway (m^2)
C = air concentration defined as the volume of air per unit volume
C_{QV} = volume air flow coefficient (13)
d = characteristic depth (m) defined as: $d = \int_0^{Y_{90}} (1 - C) * dy$
Eu = Euler number defined as: $\text{Eu} = V/\sqrt{\Delta P/\rho_{air}}$
Fr = Froude number defined as: $\text{Fr} = V/\sqrt{g*d}$
g = gravity constant (m/s^2) - local value: $g = 9.8050$ m/s^2 (Christchurch, New Zealand)
L = distance along the spillway from the end of the deflector (m)
L_{jet} = distance of the impact point of the jet from the end of the deflector (m)
P_{atm} = atmospheric pressure (Pa)
P_o = pressure above the jet (Pa)
P_N = pressure gradient number defined as: $P_N = \Delta P/(\rho_w * g * d)$
Q_{air} = air discharge (m^3/s)
Q_{air}^{inlet} = air discharge provided by the air supply system (m^3/s)
Q_w = water discharge (m^3/s)
q_{air}^{inlet} = air discharge provided by the air supply system per meter width (m^3/s/m)
Re = Reynolds number defined as: $\text{Re} = \rho_w * V * d/\mu$
Sygma = relative subpressure
t_r = ramp height (m)
t_s = offset height (m)
Tu = turbulence intensity defined as: $\text{Tu} = u'/V$
U_w = average water velocity (m/s) defined as: $U_w = q_w/d$
u' = root mean square of axial component of turbulent velocity (m/s)
V = velocity (m/s)
W = channel width (m)
We = Weber number
y = depth measured perpendicular to the spillway surface (m)
α = spillway slope
β^{inlet} = dimensionless air discharge provided by the air supply system
ΔP = difference between the pressure above the flow and the air pressure beneath the nappe (Pa): $\Delta P = Po - Pcavity$
ϕ = angle between the ramp and the spillway
μ = dynamic viscosity of water (N.s/m^2)
ρ_{air} = density of air (kg/m^3)
ρ_w = density of water (kg/m^3)

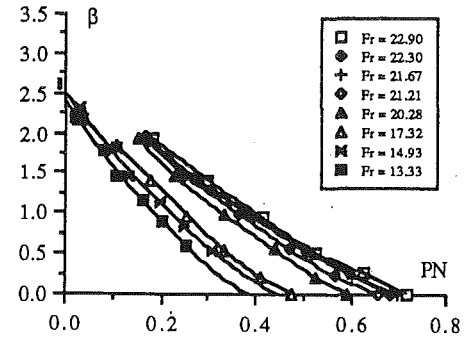

Fig. 3(*a*) Ramp 5.7° – d/t_s = 0.95

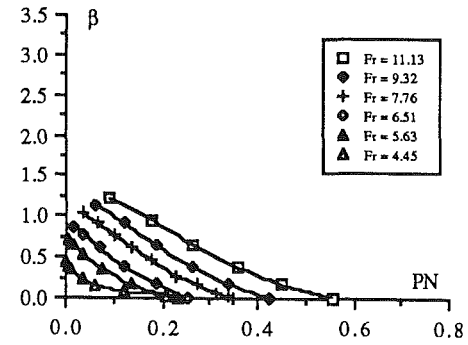

Fig. 3(*b*) Ramp 5.7° – d/t_s = 2.17

Fig. 3 Characteristic curves—aerator with a 30 mm offset height and a ramp

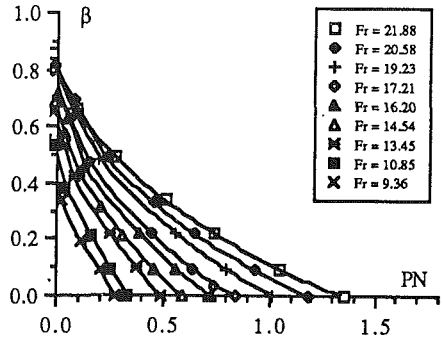

Fig. 4(*a*) No ramp – d/t_s = 0.95

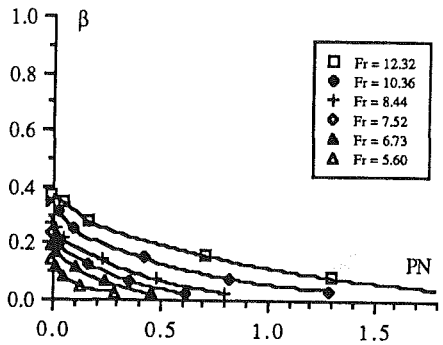

Fig. 4(*b*) No ramp – d/t_s = 2.17

Fig. 4 Characteristic curves—aerator with a 30 mm offset height

The parameters required to design an aerator are: 1 the air discharge Q_{air}^{inlet}, 2 the air concentration near the floor downstream of the aerator C_b, 3 the difference between the atmospheric pressure and the pressure in the cavity beneath the nappe ΔP and 4 the water jet length L_{jet}. Each of these design parameters is a function of the initial independent parameters:

$$L_{jet},\ Q_{air}^{inlet},\ \Delta P,\ C_b = f(\rho_w,\ \rho_{air},\ \mu,\ \sigma,\ g,\ \alpha,\ W,\ k_s,)$$
$$t_s,\ L_g,\ A_d,\ \phi,\ L_{ramp},\ V,\ d,\ u') \qquad (1)$$

2.2 Dimensionless Numbers. The variables above give the following dimensionless numbers: the nondimensional air discharge $\beta^{inlet} = Q_{air}^{inlet}/Q_w$, the air concentration at the bed C_b, the jet length L_{jet}/d, the dimensionless geometric variables k_s/d, t_s/d, L_g/d, $A_d/(d*W)$, L_{ramp}/d, the Froude, Reynolds, Weber and Euler numbers, the density ratio ρ_{air}/ρ_w and the turbulence intensity: Tu = u'/V.

Any combination of these numbers is also dimensionless and may be used to replace one of the combinations. It will be shown later that it is convenient to replace the Euler number by a pressure gradient number P_N defined as

$$P_N = \frac{\Delta P}{\rho_w * g * d}$$

This number is obtained from the others by the relation:

$$P_N = \left(\frac{\mathrm{Fr}}{\mathrm{Eu}}\right)^2 * \frac{\rho_{air}}{\rho_w}$$

For the study of cavity at the rear of a hydrofoil other workers (Laali and Michel (1984)) have used, in place of the air discharge β^{inlet} and the pressure gradient P_N, 1 the volume air flow coefficient C_{QW} and 2 the relative subpressure Sygma defined as

$$C_{QV} = \frac{Q_{air}^{inlet}}{V * W * (t_S + t_r)} \quad \mathrm{Sygma} = \frac{\Delta P + \rho_w * g * d}{\frac{1}{2} * \rho_w * V^2}$$

The coefficient C_{QV} is equal to the ratio of the mean air velocity in the cavity over the flow velocity in the jet and for vapor cavity ($P_{cavity} = P_v$) the number Sygma equals the cavitation number σ_v. Both coefficients may be deduced from the others:

$$C_{QV} = \beta^{inlet} * \frac{d}{t_s + t_r} \quad \mathrm{Sygma} = 2 * \left(\frac{P_N + 1}{\mathrm{Fr}^2}\right)$$

Studies are performed on geometrically similar models and it is convenient to use a slice model. Side effects may appear due to the boundary layers on the side walls. However if these boundary effects are assumed small, the problem becomes a two-dimensional study. The nappe subpressure is usually controlled by valves on the air inlet systems and this enables the underpressure to be treated as an independent parameter. The density ratio is almost constant. From these considerations the relationship (1) is rewritten in terms of dimensionless parameters:

$$\frac{L_{jet}}{d},\ \beta^{inlet},\ C_b$$
$$= f\left(\mathrm{Re},\ \mathrm{We},\ \mathrm{Fr},\ \alpha,\ \frac{k_s}{d},\ \frac{t_s}{d},\ \frac{L_g}{d},\ \frac{A_d}{W*d},\ \phi,\ \frac{L_{ramp}}{d},\ \mathrm{Tu},\ P_N\right) \qquad (2)$$

2.3 Discussion. For a given aerator configuration (α, k_s, t_s, L_g, A_d, ϕ, L_{ramp} fixed) and a given flow depth d, the relationship (2) becomes:

$$L_{jet}/d,\ \beta^{inlet},\ C_b = f(\mathrm{Re},\ \mathrm{We},\ \mathrm{Fr},\ \mathrm{Tu},\ P_N) \qquad (3)$$

According to Laali (1984), Kobus (1984), and Pinto (1984) the Reynolds and Weber numbers do not influence the processes in any significant way if: 1 the Reynolds number is greater than 10^5 and 2 – the Weber number $W_1 = \dfrac{V}{\sqrt{\sigma/(\rho_w * L_{jet})}}$ is greater than 400.

The ratio W_1 is defined by Pinto (1984) using the jet length

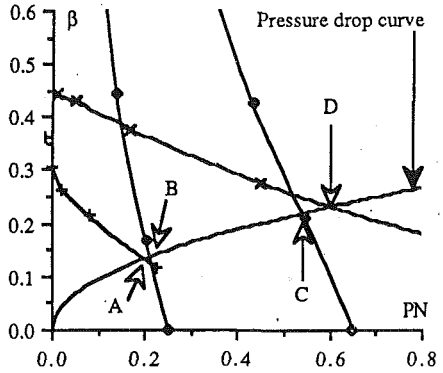

Fig. 5 Influence of the ramp – d/t_s = 1.65
Ramp 5.7°: ◇ Fr = 13.49 ◆ Fr = 7.56
No ramp: × Fr = 13.76 + Fr = 7.47

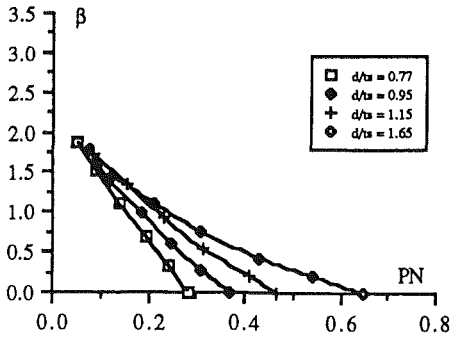

Fig. 6(*a*) Ramp 5.7° – Fr = 14.5

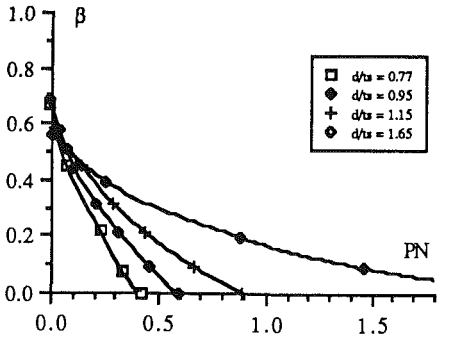

Fig. 6(*b*) Ramp 5.7° – Fr = 14.7

Fig. 6 Influence of the depth of water on the characteristic curves

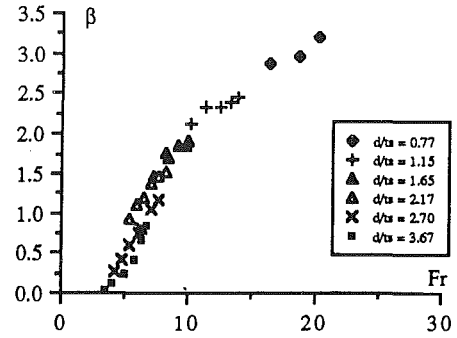

Fig. 7(*a*) Ramp 5.7° – P_N = 0.0

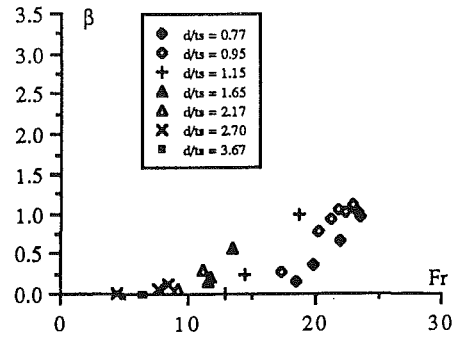

Fig. 7(*b*) Ramp 5.7° – P_N = 0.4

Fig. 7 Curves $\beta^{inlet} = f(Fr)$—aerator with a 30 mm offset height and a ramp

as characteristic length. Pinto et al. (1982) performed experiments on a series of hydraulic model whose scale varied from 1:8 through to 1:50 and were able to show that the model reproduced the prototype air demand for all water discharges for scales larger than 1:15. For scales 1:30 and 1:50 the correct air demand was only reproduced for the larger discharges. The dimensionless equation (3) then becomes:

$$L_{jet}/d,\ \beta^{inlet},\ C_b = f(\mathrm{Fr},\ \mathrm{Tu},\ P_N)$$

There is little information available on the effects of turbulence. Often the studies neglect the influence of the turbulence intensity (Vischer et al. (1987), Low (1986), and Laali and Michel (1984)) and it then becomes:

$$L_{jet}/d,\ \beta^{inlet},\ C_b = f(\mathrm{Fr},\ P_N) \qquad (4)$$

As discussed earlier the air entrainment above an aerator may occur by different processes. Each of these processes yields a different nondimensional equation and the interactions between these processes must be considered. More the upstream conditions include the air concentration, velocity, turbulence and pressure distributions rather than the average values. Therefore it is believed that the type of relation defined in equation (4) is incomplete and neither does it characterize any single physical process.

The data obtained on the Clyde dam spillway model are analyzed using equation (4) and the equation inadequacy is discussed later.

3 Characteristic Curves

3.1 Results. For different flow depths we measured the characteristic curves $\rho^{inlet} = f(P_N)$ for several Froude numbers (Figs. 3 and 4). It must be noticed that the scales of the graphs are not the same for the two aerator configurations. The relationship between the three dimensionless numbers shows that a decrease of air discharge brings an increase of the nappe subpressure and for the same nappe subpressure the air discharge increases with the Froude number.

Figure 5 shows the air demand curves for two Froude numbers with both aerator geometries and they are compared with a typical pressure drop curve of the air supply system. At low Froude numbers the operating point of the aerator with ramp (point B) shows that this configuration provides a larger air discharge than the aerator configuration without ramp (point A). At high Froude numbers the aerator without ramp (point D) supplies more air than with ramp (point C). This phenomenon occurs because the presence of the ramp increases the slope of the curve $\beta^{inlet} = f(P_N)$ for identical upstream flow conditions.

Figure 6 presents β^{inlet} as function of the initial depth of water d/t_s for constant Froude numbers. The results show that an increase of the flow depth decreases the average slope of $\beta^{inlet} = f(P_N)$, increases the pressure gradient for $\beta^{inlet} = 0$ and decreases the air discharge β^{inlet} when P_N reaches zero. It must be emphasized that we cannot separate the effects of two parameters d/t_s and d/L_{ramp}. For a geometry with ramp, for the same flow depth, increasing the ramp length increases the

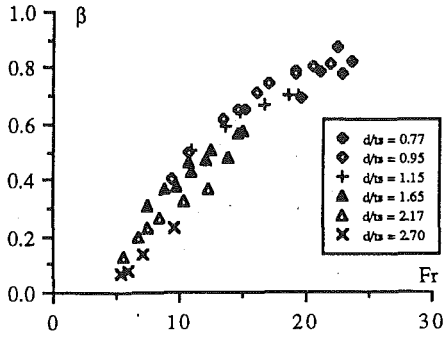

Fig. 8(*a*) No ramp – $P_N = 0$

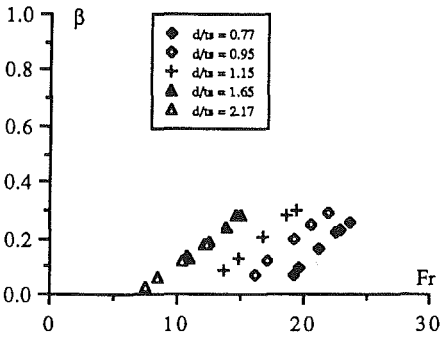

Fig. 8(*b*) No ramp – $P_N = 0.6$

Fig. 8 Curves $\beta^{inlet} = f(Fr)$—aerator with a 30 mm offset height—no ramp

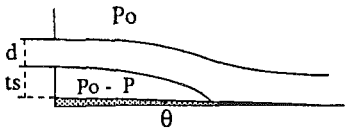

Fig. 9 Half-cavity geometry—Laali (1980)

depth of flow for which the streamlines are parallel to the ramp. Above this depth the streamlines are less affected by the slope.

Another way to present the characteristic curves is by plotting β^{inlet} as a function of the Froude number for constant pressure gradient (Figs. 7 and 8).

3.2 Discussion. Laali performed experiments on a horizontal half-cavity (Fig. 9) within the framework of study of cavity in the rear of hydrofoils. His data were originally plotted as: $C_{QV} = f(\text{Sygma})$ and are presented as $\beta^{inlet} = f(P_N)$ in analogy of the study on spillway model.

The air demand plotted as $\beta^{inlet} = f(P_N)$ has two linear sections connected by a transition zone (Fig. 10). These regions correspond to different air entrainment processes. For low air discharges and low Froude numbers most of the air is evacuated at the rear of the cavity by plunging jet entrainment. For middle values of the air inflow (transition zone) Michel (1984) indicates that plunging jet entrainment becomes insufficient and a pulsation phenomenon may appear which is characterized by evacuation of pockets of air trapped by a re-entrant jet at the rear of the cavity. Similar pulsation phenomena were observed on spillway model Chanson (1988) and on prototype (Frizell (1985)). A hysteresis process occurs at the transition between high and low air discharges: the relationship $\beta^{inlet} = f(P_N)$ has a different shape for increasing and decreasing air supply discharges. All experiments presented (1988; 1980) were performed with a decreasing flow rate to avoid this phenomenon.

For high air discharges most of the air is entrained by nappe entrainment. For large jet lengths and hence for high Froude

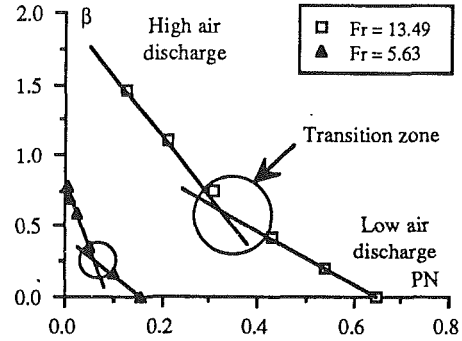

Fig. 10(*a*) Author's data Chanson (1988) ramp 5.7° – $d/t_s = 1.65$

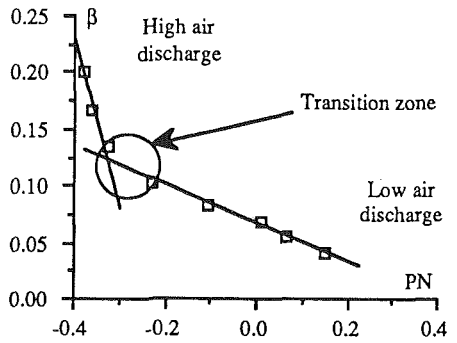

Fig. 10(*b*) Laali (1980) $P_0 = 1.03\ 10^4$ Pa – $d/t_s = 2.05$

Fig. 10 Characteristic curves $\mu^{inlet} = f(P_N)$

Laali's data (1980) $\Delta(P_0) = \pm$ 73 Pa $\Delta(\beta^{inlet})/\beta^{inlet} = \pm$ 2 percent
$\Delta(P_N) = \pm$ 2 percent $\Delta(Fr)/Fr = \pm$ 0.34 percent

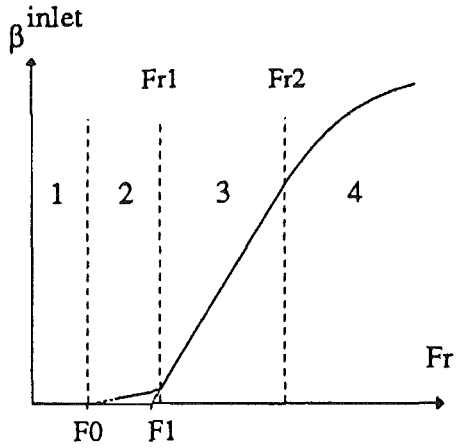

Fig. 11 Scheme of the relation $\beta^{inlet} = f(Fr)$

numbers Laali (1980) suggests that the air-water mixture along the lower interface of the jet tends to block the formation of the re-entrant jet and at the limit the pulsation regime may disappear. This is in agreement with the data obtained on spillway model (Fig. 10(*a*)) that show two different shapes of curve $\beta^{inlet} = f(P_N)$ with the transition zone.

For a given depth of water and aerator geometry, the relationship $\beta^{inlet} = f(\text{Fr})$ for a constant pressure gradient indicates four characteristic regions (Fig. 11). For low Froude numbers (region 1) there is no air entrainment. Observations of the experiments indicate that no air is entrained through the free-surfaces of the jet, and according to Ervine and Ahmed (1982), air entrainment by plunging jet entrainment does not occur below a critical velocity $V_c = 0.8$ m/s. Hence a characteristic Froude number F_0 can be defined such there is no entrainment for: $\text{Fr} < F_0 = V_c/\sqrt{g * d}$.

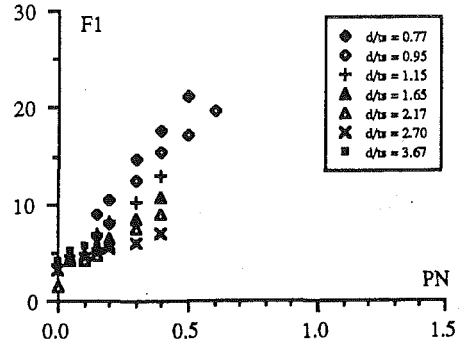

Fig. 12(*a*) Aerator with ramp 5.7°

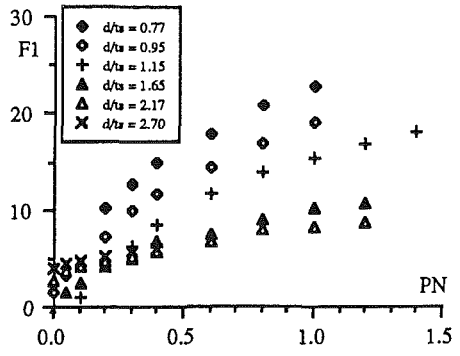

Fig. 12(*b*) Aerator without ramp

Fig. 12 Variations of the characteristic Froude number F_1 $\Delta(F_1) = \pm$ 5 percent

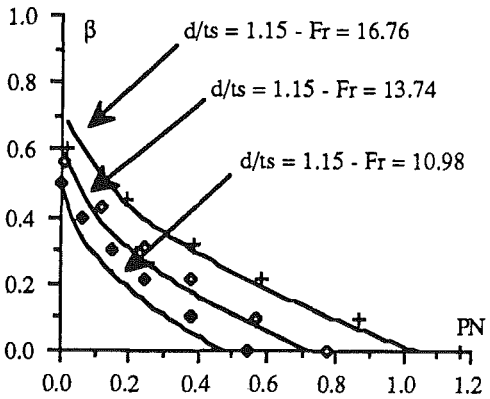

Fig. 13 Comparison between the data and the equation (7) aerator without ramp

In the region 2, most of the air is entrained by plunging jet entrainment and photographs show that no nappe entrainment occurs. Air bubbles are entrapped when the water jet intersects the rollers and dragged away by the flow.

For a high velocity jet nappe entrainment occurs and the air is entrained by high intensity turbulent eddies close to the free-surface. This process occurs in the region 3 and the air is entrained by addition of plunging jet entrainment and nappe entrainment. The latter becomes major for higher Froude numbers. The start of nappe entrainment is well marked and may be characterized by a characteristic Froude number Fr^1. For a given flow depth and pressure gradient P_N, the relationship $\beta^{inlet} = f(Fr)$ is almost linear in the region 3 and is estimated as:

$$\beta^{inlet} = K_1 * (Fr - F_1) \tag{5}$$

At higher Froude numbers (region 4) the air entrainment is limited by the limit air transport capacity of the flow. Kobus

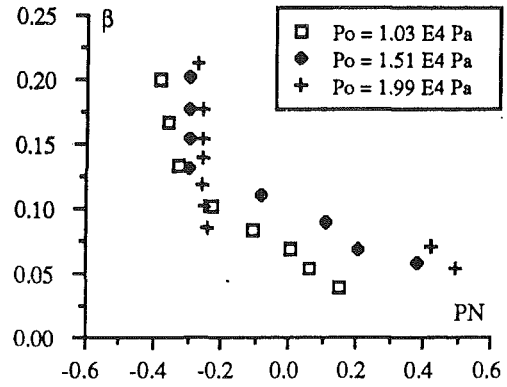

Fig. 14 Influence of the pressure P_0 on air demand—Laali (1980)

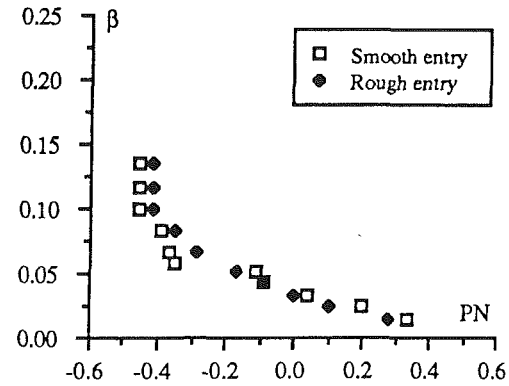

Fig. 15 Influence of the roughness on air demand—Laali (1980)

(1984) and Brauer (1971) indicate that this limit is given by the maximum air bubble concentration in the flow. The relationship $\beta^{inlet} = f(Fr)$ is no longer linear. A statistical study Chanson (1988) suggests:

$$\beta^{inlet} = K_2 * \sqrt{Fr - F_2} \tag{6}$$

The change of mechanism of air entrainment observed between the regions 2 and 3 is clearly marked in both aerator geometries for different flow depths, cavity subpressures and flow velocities. To a first approximation the characteristic Froude number F_1 (equation (5)) is assumed to represent the start of nappe entrainment. Variations of F_1 as a function of the depths of water and Froude numbers are shown in Fig. 12 for both geometries. A statistical study of the coefficients K_1 and F_1 Chanson (1988) indicates that in the region 3 (Fig. 11) the air demand characteristic curves $\beta^{inlet} = f(Fr, P_N)$ are estimated by:

$$\beta^{inlet} = K_1 * (Fr - f_1 - E_1 * \sqrt{P_N}) \tag{7}$$

where $E_1 = 23.51 * (d/t_s)^{-3/2}$

$f_1 = -8.17 + 5.77 * (d/t_s) - 0.605 * (d/t_s)^2$

$K_1 = 0.2$ (Ramp 5.7° $K_1 = 0.06$ (No ramp)

It must be noticed that the coefficients E_1 and f_1 are independent of the ramp and the characteristic Froude number F_1 is only function of P_N and d/t_s. The equation (7) provides a good fit of the experimental data from the Clyde dam spillway model (Fig. 13) but may not be generally applicable to aerators of differing geometry or different spillway slopes.

3.3 Influence of Other Parameters. Laali (1980) was able to vary parameters as the absolute pressure above the flow P_o and the roughness of the injector. His results are presented on Figs. 14 and 15 and the different flow conditions are reported on Table 1. In the range of considered pressure (10^4 Pa, 2 10^4

Table 1 Laali's experimental configuration

	d m	ts m	θ	Fr	Po
Fig. 10(b)	0.1003	0.049	1.87°	8.065	$1.03\ 10^4$
Fig. 14	0.1003	0.049	1.87°	8.065	variable
Fig. 15	0.1389	0.030	3.10°	6.442	$1.41\ 10^4$

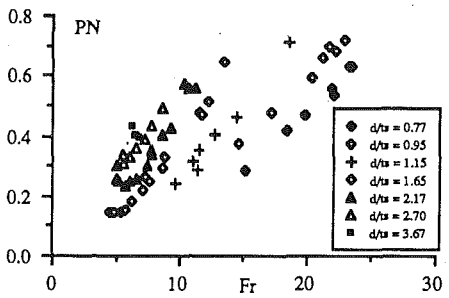

Fig. 16(a) Ramp 5.7°

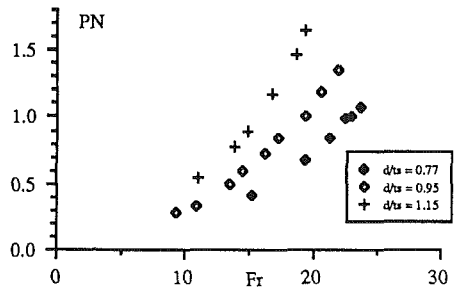

Fig. 16(b) No ramp

Fig. 16 Plot of P_N as a function of the Froude number for $Q_{air}^{inlet} = 0$

Pa) the Fig. 14 indicates that, for a given pressure gradient and Froude number, the air discharge decreases when the ambient pressure above the jet P_o decreases. This suggests that the performances of aerator located at high altitude may be affected by the lower atmospheric pressure.

Laali (1980) then introduced artificial roughness (paper sand k_s = 0.4 mm) on the lower surface of the nozzle of the orifice in order to modify the free-surface irregularities of the jet and the experimental results are plotted in Fig. 15. The presence of roughness on the nozzle of the injector increases the thickness of the initial boundary layer and therefore reduces the height of the uniform turbulent flow. The results are then expected to be similar to the effects of a reduction of the jet thickness and this is observed on Fig. 15. Laali (1980) indicated that the effect of the roughness is less important for large Froude numbers as the boundary layer thickness is reduced as the Reynolds number increases.

Ervine and Falvey (1987) investigate the effect of turbulence on free jets discharging horizontally and suggest that some important processes in turbulent jets in the atmosphere are dependent on Weber and Reynolds numbers and the turbulence intensity Tu. Then great difficulties appear in modelling free jets and studies must be related to the equation (2).

4 Study of the Case $Q_{air} = 0$

4.1 Introduction. The flow above an aerator when $Q_{air}^{inlet} = 0$ is function of the spillway slope, the aerator geometry and the flow characteristics. At low Froude numbers or for low channel slopes the aerator is submerged when the air discharge is zero. For high channel slopes and high ramp slopes the cavity below the jet is not usually submerged when the air supply system is sealed. The transition between the two regimes corresponds to the conditions of submergence of the aerator. When the aerator is not submerged and for $Q_{air}^{inlet} = 0$, the cavity below the nappe is subject to air recirculation Chanson (1989).

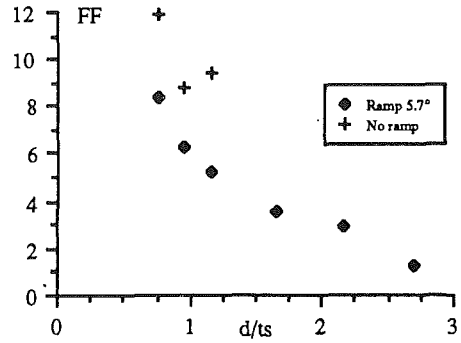

Fig. 17 FF versus the flow depth $\Delta(FF)/FF = \pm$ 10 percent

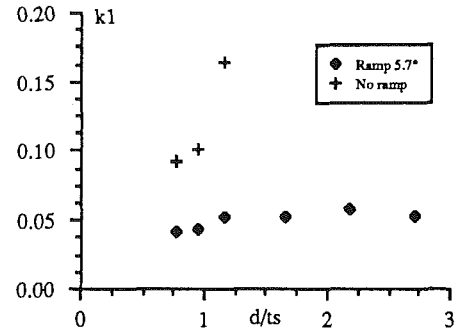

Fig. 18 k_1 versus the flow depth $\Delta(k_4)/k_1 = \pm$ 10 percent

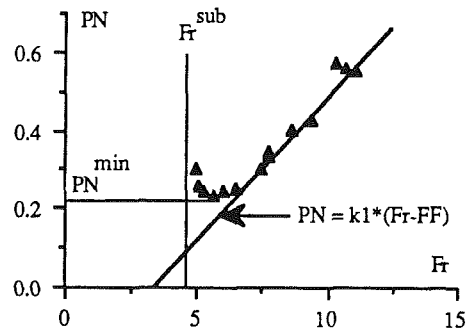

Fig. 19 Curve $P_N = f(Fr)$ for $Q_{air}^{inlet} = 0$—Ramp 5.7°—$d/t_s = 2.17$

4.2 Relationship $P_N = f(Fr)$. When the cavity is not submerged the cavity geometry (for $Q_{air}^{inlet} = 0$) is characterized by the nappe subpressure and the Froude number. Figure 16 present the author's data for various flow depths. The relationship $P_N = f(Fr)$ characterizes the behavior and the shape of the cavity when the air discharge supplied by the air inlets is zero.

The data show a good correlation. For high Froude numbers, the relationship $P_N = f(Fr)$ is almost linear and is estimated by:

$$P_N = k_1 * (Fr - FF) \quad (8)$$

The variations of the coefficients FF and k_1 are plotted on Figs. 17 and 18 versus the dimensionless depth of water for the Clyde dam spillway model.

4.3 Submergence of the Aerator. Under high subpressures the aerator becomes submerged and stops playing its protective role. For small Froude numbers and small air discharges an obstruction (partial or complete) of the air supply increases the pressure gradient above a limit and the aerator could be

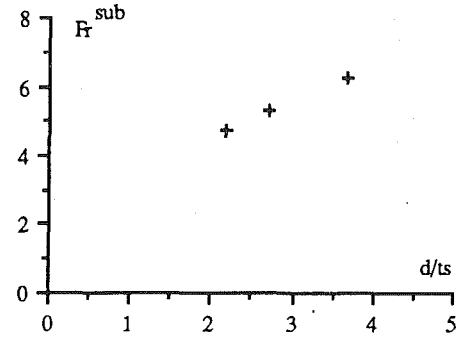

Fig. 20 Fr^{sub} as a function of the flow depth $\Delta(Fr^{sub})/Fr^{sub} = \pm 5$ percent

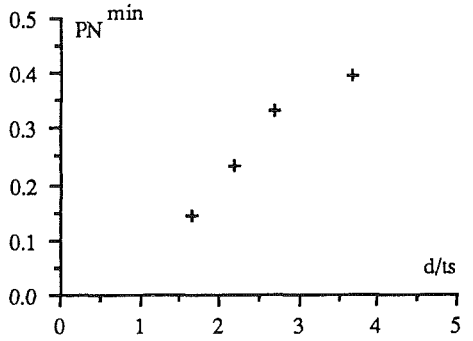

Fig. 21 P_N^{min} as a function of the flow depth $\Delta(P_N^{sub})/P_N^{sub} = \pm 2$ percent

submerged. When the cavity pressure drops the submergence is preceded by the appearance of a large amount of spray falling from the underside the nappe. The rear part of the jet is affected by rollers and the curvature of the jet is pronounced.

The study of the data $P_N = f(\mathrm{Fr})$ for $Q_{air}^{inlet} = 0$ highlights two characteristic parameters (Fig. 19): the submergence Froude number Fr^{sub} such that no submergence occurs for $Fr > Fr^{sub}$ and the minimum pressure gradient P_N^{min}. These parameters are function of the flow depth and the aerator geometry. For the aerator configuration with a 5.7° ramp the parameters Fr^{sub} and P_N^{min} are plotted in Figs. 20 and 21. For the aerator configuration without ramp the only information is: $Fr^{sub} > 15$ for $d/t_s = 1.65$ and $Fr^{sub} < 11$ for $d/t_s = 1.15$.

5 Conclusion

The study of the air demand is complex and the dimensional analysis shows that a similitude between model and prototype is almost impossible to respect. However the air demand provides a relationship between the air discharge, the subpressure and the flow characteristics, and for given flow conditions and aerator geometry the combination of the air demand characteristic curves and the pressure loss curve of the air supply system determinates the subpressure in the cavity beneath the jet and hence the jet trajectory. This enables the determination of the boundary conditions for a complete study of air entrainment above the aerator and the flow conditions downstream of the nappe. The air demand study provides additional informations. Indeed it highlights a characteristic Froude number above which nappe entrainment occurs. For smaller Froude numbers air entrainment occurs by plunging jet entrainment.

When the air inlets are sealed ($Q_{air}^{inlet} = 0$) the aerator is submerged for low Froude numbers. For high velocities the cavity beneath the nappe is clearly marked and the subpressure in the cavity and the cavity geometry is a function of the Froude number for given flow conditions and aerator geometry. The conditions for the disappearance of the cavity, called submergence, were obtained as a function of the initial flow depth for the aerator with ramp.

Acknowledgments

The author wishes to thank the Civil Engineering Department, University of Canterbury (New Zealand), the University Grant Committee (New Zealand) and the ministry of Works and Development (New Zealand) for their financial support. The author also thanks Professor I. R. Wood who supervised this project and Dr. J. M. Michel for his help.

References

Volkart, P., and Rutschmann, P., 1984, Air Entrainment Devices, Mitteilungen der Versuchsanstalt fur Wasserbau, Hydrologie und Glaziologie, No. 72, Zürich, Switzerland.

Peterka, A. J., 1953, "The Effect of Entrained Air on Cavitation Pitting," Joint Meeting Paper, IAHR/ASCE, Minneapolis, USA, Aug.

Russell, S. O., and Sheehan, G. J., 1974, "Effect of Entrained Air on Cavitation Damage," *Canadian Journal of Civil Engineering*, Vol. 1.

Vischer, D., Volkart, P., and Sigenthaler, A., 1987, "Hydraulic Modelling of Air Slots on Open Chute Spillways," Int. Conf. on Hyd. Modelling, BHRA Fluid Eng., Coventry, England, Sept.

Volkart, P., and Chervet, A., 1983, "Air Slots for Flow Aeration," Mitteilungen der Versuchsanstalt fur Wasserbau, Hydrologie und Glaziologie, No. 66, Zürich, Switzerland.

Chanson, H., 1989, "Study of Air Entrainment and Aeration Devices," *Jl. of Hyd. Res.*, Vol. 27, No. 3, pp. 301-319.

Low, H. S., 1986, "Model Studies of Clyde Dam Spillway Aerators," Master Report, Ref. 86-6, University of Canterbury, New Zealand.

Pinto, N. L. de S., Neidert, S. H., and Ota, J. J., 1982, "Aeration at High Velocity Flows," Water Power & Dam Construction, Feb.-Mar.

Tan, T. P., 1984, "Model Studies of Aerators on Spillway," Master Report, Ref. 84-6, University of Canterbury, New Zealand.

Chanson, H., 1988, "Study of Air Entrainment and Aeration Devices on Spillway Model," Research Report 8-88, University of Canterbury, New Zealand, Oct.

Laali, A. R., 1980, "Ecoulement Ventilés. Etude de l'entraînement d'air. Cas d'une cavité formée entre un jet plan et une paroi solide," Ph.D. thesis, University of Grenoble 1-INPG, France.

Ervine, D. A., and Falvey, H. T., 1987, "Behaviour of Turbulent Water Jets in the Atmosphere and in Plunge Pools," *Proc. Instn. Civ. Engrs.*, Part 2, 1984, 83, Mar., pp. 295-314.

Laali, A. R., and Michel, J. M., 1984, "Air Entrainment in Ventilated Cavities: Case of the Fully Developed Half-Cavity," ASME JOURNAL OF FLUIDS ENGINEERING, Vol. 106, Sept. pp. 327-335.

Kobus, H., 1984, "Local Air Entrainment and Detrainment," *Symp. on Scale Effects in Modelling Hydraulic Structures*, IARH.

Michel, J. M., 1984, "Some Features on Water Flows with Ventilated Cavities," ASME JOURNAL OF FLUIDS ENGINEERING, Vol. 106, Sept. pp. 319-326.

Pinto, N. L. de S., 1984, "Model Evaluation of Aerators in Shooting Flow," *Symp. on Scale Effects in Modelling Hydraulic Structures*, IARH.

Frizell, K. W., 1985, Glenn Canyon Dam Spillway Tests. Model-Prototype Comparison Hydraulics and Hydrology in the Small Computer Age, ASCE, New York.

Ervine, D. A., and Ahmed, A. A., 1982, "A Scaling Relatinship for a Two-Dimensional Dropshaft Hyd. Modelling of Civil Eng. Structures," BHRA Fluid Eng., Coventry, England.

Brauer, H., 1971, Grundlagen der Einphasenund Mehrphasenstromungen Verlag Sauerlander, Aarau and Frankfurt am Main.

Solid Phase Contribution in the Two-Phase Turbulence Kinetic Energy Equation

T. W. Abou-Arab
Department of Mechanical Engineering,
Jordan University of Science and Technology,
Irbid, Jordan

M. C. Roco*
Department of Mechanical Engineering,
University of Kentucky,
Lexington, KY 40506

This paper presents a multiphase turbulence closure employing one transport equation, namely, the turbulence kinetic energy equation. The proposed form of this equation is different from the earlier formulations in some aspects. The power spectrum of the carrier fluid is divided into two regions, which interact in different ways and at different rates with the suspended particles as a function of the particle-eddy size ratio and density ratio. The length scale is described algebraically. A double-time averaging approach for the momentum and kinetic energy equations is adopted. The resulting turbulence correlations are modeled under less restrictive assumptions comparative to the previous work. The closures for the momentum and kinetic energy equations are given. Comparisons of the predictions with experimental results on liquid-solid jet and gas-solid pipe flow show satisfactory agreement.

1 Introduction

Multiphase flows are widely applied in engineering processes from chemical, mechanical, petroleum, mining and other industries. Various theoretical and experimental techniques for the investigation of those flows are available. Some of them are a straightforward extension from the single phase flow models by introducing some ad hoc modifications. Other investigations originate from the gas-solid flow (Soo, 1983) or fluidized bed models (Wang et al., 1988).

Increasing concern for the prediction of turbulent multiphase flows have been noticed during the last twenty years (Danon et al., 1974; Al-Tawell and Landau, 1977; Genchev and Karpuzov, 1980; Melville and Bray, 1979; Crowe and Sharma, 1978; Michaelides and Farmer, 1983; and Shuen et al., 1983). Two equation turbulence models have been proposed for dilute particulate flows by Elghobashi et al. (1982, 1983, 1984), Crowder et al. (1984). Algebraic and one equation turbulence models have been suggested also for dense liquid-solid flows (Roco et al., 1983, 1985, 1986) in which the particle-particle interactions play an important role besides the fluid-fluid and fluid-solid interactions. Most of these studies as well as other earlier investigations have some limitations. In the above mentioned studies the response of solids to the turbulent fluctuations of the carrier fluid is obtained under restrictions similar to those referred by Hinze (1975, p. 460), which limit their use. In addition to that, empirical functions are usually introduced in these models.

The purpose of the present paper is

(i) To propose a specific double-time averaging approach for multiphase turbulent flows. From the liquid-solid interactions only the drag interaction for fine particles in the Stokes range and in dilute suspensions is considered in this paper. Even if the approach is developed for incompressible flow, its application for other multiphase flows is foreseen.

(ii) To improve the one-equation turbulence model reported by Roco and Mahadevan (1986) by including the modulation of turbulence produced by particles as a function of turbulence size and density. A limiting case is analyzed here: the solid particles play only a passive role on turbulence, with negligible vortex shedding and cross-trajectory effects.

(iii) To test the proposed model with other modes and experimental data for various two-phase flows, without adopting any adjusting empirical coefficients.

2 Double-Time Averaging Approach

The continuum transport equations for multiphase flows can be obtained by assuming a continuum medium with averaged field quantities by using either time, local volume, local mass or spectral averaging (see Buyevich, 1971; Soo, 1967; Delhaye and Vernier, 1968; Hetsroni, 1982). The averaging for multiphase flow systems may be performed in various ways. Mass weighted averaging technique was applied by Elgobashi and Abou-Arab (1983) for turbulent incompressible and compressible flows. To express the spatial nonuniformities and interactions between the flow components Roco and Shook (1985) have developed a specific volume-time averaging technique for turbulent multicomponent systems, in which the size of the averaging volume Δv is related to the turbulence scale. Since the Eulerian description of the flow is more convenient than the Lagrangian description and there are more comprehensive mathematical schemes for such formulation, they transformed the volume-time averaging into a specific double-time averaging. For any flow property f and any component K in the mixture, at a position $\mathbf{r}$ and time t, we have

*Presently at NSF, Washington, D.C.

Contributed by the Fluids Engineering Division and presented at the Third International Symposium on Liquid-Solid Flows, Winter Annual Meetings, Chicago, Nov. 1988, of THE AMERICAN SOCIETY OF MECHANICAL ENGINEERS. Manuscript received by the Fluids Engineering Division December 6, 1988.

$$\bar{f}_K = \frac{1}{\Delta T}\int_{t-\Delta T/2}^{t+\Delta T/2} \langle f_K \rangle dt \tag{1}$$

where:

ΔT is the time averaging interval corresponding to the turbulence production range ($\Delta T \to \infty$)

$$\langle f_K \rangle = \frac{1}{\rho_K \Delta t}\int_{t-\Delta t/2}^{t+\Delta t/2} f \rho_K K R d\tau \tag{2a}$$

is the intrinsic average of f over Δt and flow component K

$$\Delta t = \int_0^\infty R(\tau - t) \cdot d\tau,$$

is the Eulerian time scale for the most energetic eddies corresponding to the Taylor's time scale. Note that $\Delta t \ll \Delta T$, but much larger than the particle residence time at $\mathbf{r}$

$$K(\mathbf{r},\tau) = \begin{cases} 1 & \text{if the component } K \text{ resides} \\ & \text{at point } \mathbf{r} \text{ and time } \tau \\ 0 & \text{otherwise} \end{cases} \tag{2b}$$

is the phase distribution function, and

$$R(\tau - t) = \frac{\overline{u''(t)u''(t-\tau)}}{\overline{u''^2}} \tag{2c}$$

is the auto-correlation coefficient of the velocity fluctuations of the most energetic eddies (in the turbulence transfer range).

The time averaging over Δt corresponds to the spatial averaging over local volume Δv. The dimension of Δv is given by the turbulence mixing length, and of Δt by the ratio of the length scale of Δv to the local mean velocity. By integrating over a flow component K, its interfaces with other flow components become boundary of integration, and the interaction terms are derived in a straightforward manner in the differential formulation. We assume that the fluctuations in the production and transfer range are not correlated because they originate and operate in different zones of the turbulence spectrum. According to (1) and (2*a*), any instantaneous property differs from the double-time averaged value by a turbulence fluctuation f' with two components f'_K and f''_K:

$$f_K = \bar{f}_K + f' = \bar{f}_K = f'_K + f''_K \tag{3}$$

where:

$$f''_K = f_K - \langle f_K \rangle \tag{4}$$

is the temporal fluctuations in Δt, (this is equivalent to the spatial nonuniformities in the local averaging volume Δv), and

$$f'_K = \langle f_K \rangle - \bar{f}_K \tag{5}$$

is the temporal fluctuation of $\langle f_k \rangle$ within ΔT.

Since the averaging time interval Δt is the Eulerian time scale for the most energetic eddies, the temporal fluctuation f''_K corresponds to the turbulence transfer range. The temporal nonuniformities f'_K reflect the turbulence fluctuations in the production range.

By averaging with formula (1) the point instantaneous conservation equations, one obtains the double-time averaged equations. This formulation is equivalent to the mass-time averaging or volume-time averaging for incompressible mixture flow. The momentum and kinetic energy equations are given in Appendix A.

In this paper we model the phase interaction by using spectral analysis and suggest a closure of a double-time averaged equations for linear momentum and kinetic energy. The averaged equations are initially written with all their terms, and then simplified formulations for various flow conditions are suggested.

3 Energy Spectrum and Solids-Eddy Interaction

It is well accepted that turbulence is characterized by fluctuating motions defined by an energy spectrum (Tennekes and Lumely, 1972). Single time scale models, which usually are applied for the prediction of turbulent flows, seem simplistic because different turbulent interactions are associated with different parts of the energy spectrum (Hanjalic' et al., 1979). A typical energy spectrum can be divided into three regions. The first region is the production region of large eddies and low wave numbers. The third region is the dissipation region with small eddies and high wave numbers, in which the kinetic energy produced at the lower wave numbers is dissipated. The intermediate range of wave numbers represents the transfer range. If the velocity fluctuations in the production and transfer range are not correlated and the kinetic energy in the dissipation range is neglected, then the total kinetic energy k of turbulence may be divided into production range (k_P) and transfer range (k_T):

$$k \simeq k_P + k_T \tag{6}$$

where:

$$k_P = \frac{1}{2}\overline{u_i'^2}, \tag{7a}$$

$$k_T = \frac{1}{2}\overline{u_i''^2} \tag{7b}$$

Nomenclature

a = amplitude ratio
$\mathbf{b}$ = body force
$C_{\phi 1} - C_{\phi 5}$, C_μ = constants
d = injector diameter
d_S = particle diameter
D = turbulent diffusion coefficient for solid phase
$E(\kappa)$ = energy spectrum
f = flow property
$(\mathbf{I}_K)_{M-K}$ = interaction vector of $(M-K)$ flow components on the Kth component
$\mathbf{J}_\phi$ = flux vector for a variable ϕ
k = kinetic energy of turbulence
l = length scale
N_S = Stokes number
$K(\mathbf{r}, \tau)$ = phase distribution function, equation (2*b*)
p = pressure
r = radius
$\mathbf{r}$ = position vector
$R(\tau - t)$ = Eulerian cross correlation
Re_T = Reynolds number based on the most energetic eddy size
s = density ratio
t = time
u, v = Eulerian and Lagrangian velocities, respectively
V = volume
x_i, x_j, x_n = Cartesian coordinates
y = distance from the wall
z = distance along the axis
α = concentration by volume
ΔT, Δt = averaging time intervals corresponding to the turbulence production and transfer range, respectively
Δv = averaging volume
ϵ = dissipation rate of turbulence kinetic energy
Γ_{SL}, Γ_{RL} = defined in equations (51) and (52)

u_i', u_i'' are the fluctuating velocities in the production and transfer range, respectively.

This partitioning of the energy spectrum was shown to be important for swirling flows (Chen, 1986), and heterogeneous mixture flows such as two-phase jet (Al-Taweel and Landau, 1977).

By using spectral analysis in conjunction with double-time averaging some additional turbulent correlations will result in the mixture flow equations comparative to homogeneous flows. These correlations can be classified into five categories:

(i) Eddy-eddy interaction
(ii) Eddy-mean flow interaction
(iii) Eddy-particle interaction
(iv) Particle-mean flow interaction
(v) Particle-particle interaction (for dense suspension flow).

These correlations have to be modeled. Since the suspended particles may be of different sizes and different materials, their response to the carrier fluid fluctuations will vary as a function of the mean and fluctuating properties of the flow. The present work will consider a two-way interaction mechanism between solid particles and fluid vorticies in dilute suspensions. This interaction mechanism depends on the ratio between the particle size d_S and the turbulent vortex (eddy) size l_e.

To determine the particle-eddy interaction the energy spectrum for multiphase flow system is divided into three typical zones (Fig. 1):

1. "Large vortex zone" (#1), where the turbulence energy is extracted from the mean flow by low frequency eddies. Here, the eddy length scale l_{e1} is larger than the particle size d_S:
$$l_{e1} > d_S > \eta \tag{8a}$$
where η is the Kolmogorov's length scale
2. "Medium vortex zone" (#2), where the solid particles are about the same size with the vortex size, i.e.,
$$l_{e2} \approx d_S > \eta \tag{8b}$$
3. "Small vortex zone" (#3), which would correspond to the Kolmogorov's length scale, i.e.,
$$d_S > l_{e3} \approx \eta \tag{8c}$$

In zone #1 the solid particles generally follow the motion within a vortex, and have a dissipative effect. The particle response to the turbulent fluctuations (turbulence modulation) is fully determined (see Hinze, 1975). In the small vortex zone #3 the solid particles can not significantly affect the turbulence

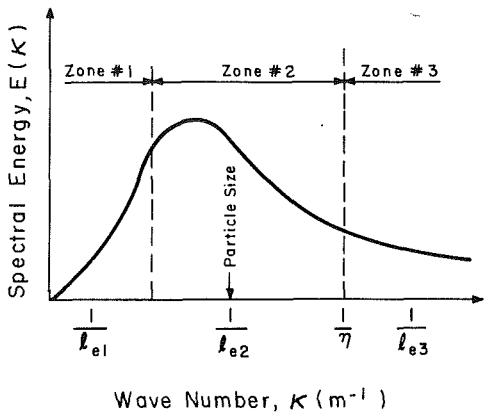

Fig. 1 Schematic showing the relative particle size to different eddy sizes in the energy spectrum

microstructure if the particles are small and vortex shedding is negligible. Achenbach (1974) found experimentally that the inferior limit for vortex shedding can be defined at particle Reynolds number equal to 400. This is much larger than the unity particle Reynolds number considered in our assumptions. For the intermediate zone #2 a linear variation of the particle response is considered. This partitioning allows for the particles-nonuniform size eddies interaction to be efficiently modeled.

The present formulation originates from the idea of subgrid scale modeling and the characteristic of the energy spectrum. Accordingly, any flow quantity, u, v, α, k, . . . , etc. may be separated into three parts (equation (3)), where f_K' and f_K'' define the fluctuations in the production and transfer ranges of the energy spectrum, respectively. By starting from the particle equation of motion in its general form, the relation between the particle motion and different fluid eddies can be determined, and from here the fluctuation components f_K' and f_K'' (see Section 6).

4 Composed Averaged Equations

4.1 Mean Flow Governing Equations. The double-time averaged momentum equation (Appendix A, equation (A2), with $f_K = f_K' + f_K''$, yields:

$$\rho_K \frac{\partial}{\partial t}(\bar{\alpha}_K \bar{u}_{Ki} + \overline{\alpha_K' u_K'} + \overline{\alpha_K'' u_K''} + \overline{\alpha' u_{Ki}''} + \overline{\alpha'' u_{Ki}'})$$

Time Rate Change of Mean Flow Convection

Nomenclature (cont.)

η = Kolmogorov length scale
κ = wave number
μ = dynamic viscosity
ρ = density
σ, σ_{LS} = turbulent Prandtl and Schmidt-Prandtl number, respectively
τ = shear stress, or current time

Subscripts

ax = axial
i,j,n = denote Cartesian coordinates (= 1, 2,3)
e = eddy
$\langle f_K \rangle$ = intrinsic average of f over Δt and the flow component K
k = turbulence kinetic energy
K = flow component K
KP = phase K in production range
KT = phase K in transfer range
l = laminar
L = liquid or incompressible fluid
LS = liquid-solid
m = modulus
P = production range
rms = root mean square
S = solid phase
t = turbulent
T = transfer range
ϵ = dissipation rate of turbulence kinetic energy
Σ = average over area

Superscripts

$\bar{f}$ = double-time average of f
f' = turbulence fluctuation of f
f' = fluctuation of f at low wave number (in the turbulence production range)
f'' = fluctuation of f at intermediate wave number (in the transfer range)
P = production
T = transfer

$$+\rho_K\frac{\partial}{\partial x_j}(\bar{\alpha}_K\bar{u}_{Ki}\bar{u}_{Kj})$$

Mean Flow Convection

$$+\rho_K\frac{\partial}{\partial x_j}(\bar{\alpha}_K\overline{u'_{Ki}u'_{Kj}}+\bar{\alpha}_K\overline{u''_{Ki}u''_{Kj}})$$

Inertial Effect →

$$+\rho_K\frac{\partial}{\partial x_j}[(\overline{\alpha'_Ku'_{Ki}u'_{Kj}}+\overline{\alpha''_Ku''_{Ki}u''_{Kj}})+\bar{u}_{Kj}(\overline{\alpha'_Ku'_{Ki}}+\overline{\alpha''_Ku''_{Ki}})$$

Collisional-Inertial Effects →

$$+\bar{u}_{Ki}(\overline{\alpha'_Ku'_{Kj}}+\overline{\alpha''_Ku''_{Kj}})+\bar{\alpha}_K(\overline{u'_{Ki}u''_{Kj}}+\overline{u''_{Ki}u'_{Kj}})$$
$$+\bar{u}_{Ki}\overline{\alpha'_Ku''_{Kj}}+\bar{u}_{Kj}\overline{\alpha'_Ku''_{Ki}}+\overline{\alpha'_Ku''_{Ki}u''_{Kj}}+\overline{\alpha'_Ku''_{Ki}u''_{Kj}}$$
$$+\overline{\alpha''_Ku'_{Ki}}\,\bar{u}_{Ki}+\overline{\alpha''_Ku'_{Ki}}\,\bar{u}_{Kj}+\overline{\alpha''_Ku'_{Kj}u'_{Ki}}+\overline{\alpha''_Ku''_{Ki}u'_{Kj}}]$$
$$=\rho_K\bar{\alpha}_Kb_{Ki}$$

Body Force

$$-\frac{\partial}{\partial x_i}(\bar{\alpha}_K\bar{p}_K+\overline{\alpha'_Kp'_K}+\overline{\alpha''_Kp''_K}+\overline{\alpha'_Kp''_K}+\overline{\alpha''_Kp'_K})$$

Pressure Effect →

$$+\left(\bar{p}_K\frac{\partial\bar{\alpha}_K}{\partial x_i}+\overline{p'_K\frac{\partial\alpha'_K}{\partial x_i}}+\overline{p''_K\frac{\partial\alpha''_K}{\partial x_i}}+p''_K\overline{\frac{\partial\alpha'_K}{\partial x_i}}+\ldots\right)$$
$$+\frac{\partial}{\partial x_j}(\bar{\alpha}_K\bar{\tau}_{Kji}+\overline{\alpha'_K\tau'_{K\Sigma ji}}+\overline{\alpha''_K\tau''_{K\Sigma ji}}$$

Frictional Effect →

$$+\overline{\alpha''_K\tau'_K\Sigma_{ji}}+\overline{\alpha'_K\tau''_K\Sigma_{ji}})+(\overline{I_{Ki}})_{M-K} \tag{9}$$

Phase Interaction

where K is a flow component, b_{Ki} is the body acceleration in the ith direction, and $(I_{Ki})_{M-K}$ is the projection in the ith direction of the interaction vector $(\mathbf{I}_K)_{M-K}$. Equation (9) contains correlations which are related to the production and transfer wave number ranges of the turbulence spectrum.

4.2 The Kinetic Energy Equation. The exact form of the double-time averaged turbulent kinetic energy equation, with $f'_K=f'_K+f''_K$, is given in Appendix A (equation (A5)). This equation contains more than one hundred correlations which are related to the eddies in the production and transfer ranges as well as some mixed correlations. Only some of these are predominant in a given flow situation as a function of relative particle-vortex size and density ratio.

4.3 Some Modeling Principles and Assumptions. Some simplifying modeling assumptions are adopted based on the physical interpretation and the nature of each term. First, previous experimental and theoretical findings can help in modeling "collectively" similar terms with minimum number of empirical constants. Second, carrying out an order of magnitude analysis for different correlations which appear in the governing equations some terms may be neglected. Third, the micromechanics which control the ability of the flow variables to correlate with each other and the factors affecting the magnitude of these correlations are considered. One can assume for the sake of simplicity that:

(1) The correlations between the fluctuations in the production range and transfer range (mixed correlations $\overline{f'f''}$) can be neglected as they originate differently and they are related to different ranges of the power spectrum. Similar assumptions are accepted in the classical single fluid turbulence theory.

(2) The concentration fluctuations occur mainly at low frequencies i.e.,

$$\alpha=\bar{\alpha}+\alpha'+\alpha'' \tag{10}$$

with

$$\alpha'\gg\alpha'' \tag{11}$$

This is a simplifying assumption which is acceptable for such complicated problems. If the particles are of small diameter their concentration is relatively uniform distributed in the Taylor length scale. High concentration fluctuations are mostly associated with large size and high density particulates. These large particles are mainly fluctuating at low frequencies due to their high inertia, hence they in turn correlate weakly at high frequencies.

(3) The correlations of higher order than three, for instance $\overline{\alpha'u'\frac{\partial p'}{\partial x_i}}$ and $\overline{u'_j\frac{\partial p'}{\partial x_j}}$, are neglected. These are at least an order magnitude smaller than those of the third order (see Hanjalic' and Launder, 1972).

(4) Pressure diffusion contribution to the total turbulent diffusion in the kinetic energy equation will be neglected because of its relatively small magnitude (Hanjelic' and Launder, 1972).

(5) The Boussinesq gradient type approximation is adopted for modeling of different fluxes and triple correlations after adopting assumptions similar with Elghobashi and Abou-Arab (1983) and Roco and Mahadevan (1986).

(6) The following constitutive relations are employed for the shear stress of carrier fluid:

$$-\rho\overline{u'_iu'_j}=\mu_{LP}\left(\frac{\partial\bar{u}_i}{\partial x_j}+\frac{\partial\bar{u}_j}{\partial x_i}\right)-\frac{1}{3}\rho k_{LP}\delta_{ij}+\frac{2}{3}\mu_{LP}\delta_{ij}\frac{\partial\bar{u}_n}{\partial x_n} \tag{12}$$

$$-\rho\overline{u''_iu''_j}=\mu_{LT}\left(\frac{\partial\bar{u}_i}{\partial x_j}+\frac{\partial\bar{u}_j}{\partial x_i}\right)-\frac{1}{3}\rho k_{LT}\delta_{ij}+\frac{2}{3}\mu_{LT}\delta_{ij}\frac{\partial\bar{u}_n}{\partial x_n} \tag{13}$$

and

$$\rho\overline{u'_iu'_j}=\rho\overline{u'_iu'_j}+\rho\overline{u''_iu''_j}, \tag{14}$$

where

$$\mu_{LP} = C_{\mu P}\rho_L k_{LP}^{1/2}1_P, \tag{15}$$
$$\mu_{LT} = C_{\mu T}\rho_L k_{LT}^{1/2}1_T, \text{ and} \tag{16}$$
$$\mu_{Lt} = \mu_{LP}+\mu_{LT}=C_\mu\rho_L k_L^{1/2}1_L \tag{17}$$

Similar relations can be written for the viscosity of the dispersed phase μ_{St} (Roco and Balakrishnan (1985)). However, in the present work we choose to define the eddy viscosity of solids as follows:

$$\nu_{St}=\nu_{Lt}/\sigma \tag{18}$$

where

$$\sigma=\sigma_{LS}/\sigma_S \tag{19}$$

and

$$\sigma_{LS} = \nu_{Lt}/D_S \tag{20}$$
$$\sigma_S = \nu_{St}/D_S \tag{21}$$

Appropriate expressions for the fluid-solid Schmidt number σ_{LS} are cited in many articles such as Peskin (1971), Picart et al. (1986), and Hetsroni (1982). The Schmidt number for solid phase is assumed to take values about its average $\sigma_S=1.5$ (Peskin, 1971; Abou-Ellail and Abou-Arab, 1985).

(7) In the present approach for dilute particulate flows the turbulence kinetic energy equation is written only for the carrier fluid. The solid phase turbulence kinetic energy and turbulence correlations are evaluated from it.

(8) Terms which are of similar nature i.e., convection, diffusion, dissipation, etc. can be modeled collectively. The length, velocity- and time-scale which are appropriate for the description of their rate of change are identified from the physical interpretation of these terms.

(9) The response of solid particles to the eddying motion is obtained from the equation of motion of solid particles, as a function of local dimensionless parameter d_S/l_e and ρ_S/ρ_L.

5 Closure for the Mean Flow Equations

With the first assumption ($\overline{f'f''}=0$, $\overline{f'g''}=0$, $\overline{f'f''g'}=0$, etc.) given in the previous section, the steady state mean flow momentum equation (9) for a flow component K remains with 16 correlations, half of them in the production "large eddy" range of the spectrum. The turbulent stresses caused by the large and most energetic eddies, $-\rho_L\overline{u_i'u_j'}$ and $-\rho_L\overline{u_i''u_j''}$, are modeled using equations (12) and (13). The collisional effect correlations are modeled after Launder (1978). In the production range it reads

$$\overline{\alpha_K'u_{Ki}'u_{Kj}'}=-C_{\phi 5}^{P}\frac{k_{KP}}{\epsilon_{KP}}\left(\overline{u_{Ki}'u_{Kl}'}\frac{\partial}{\partial x_l}\overline{u_{Kj}'\alpha_K'}+\overline{u_{Kj}'u_{Kl}'}\frac{\partial}{\partial x_l}\overline{u_{Ki}'\alpha_K'}\right) \tag{22}$$

where $C_{\phi 5}^{P}$ is a constant of a value of about 0.1. The triple correlation in the transfer range $\overline{\alpha_K''u_{Ki}''u_{Kj}''}$ has a similar expression, with a constant $C_{\phi 5}^{T}$. These fluxes can also be collectively modeled:

$$\overline{\alpha_K'u_{Ki}'u_{Kj}'}+\overline{\alpha_K''u_{Ki}''u_{Kj}''}=-C_{\phi 5}\frac{k_K}{\epsilon_K}\left(\overline{u_{Ki}'u_{Kl}'}\cdot\frac{\partial}{\partial x_l}\overline{u_{Kj}'\alpha_K'}+\overline{u_{Kj}'u_{Kl}'}\cdot\frac{\partial}{\partial x_l}\overline{u_{Ki}'\alpha_K'}\right) \tag{23}$$

The diffusion fluxes $\overline{\alpha_K'u_{Ki}'}$ and $\overline{\alpha_K''u_{Ki}''}$ are modeled using Boussinesq approximation:

$$-\overline{\alpha_K'u_{Ki}'}=\frac{\nu_{LP}}{\sigma_{LK}^{P}}\frac{\partial\bar{\alpha}_K}{\partial x_i} \tag{24}$$

$$-\overline{\alpha_K''u_{Ki}''}=\frac{\nu_{LT}}{\sigma_{LK}^{T}}\frac{\partial\bar{\alpha}_K}{\partial x_i} \tag{25}$$

where the coefficients σ_{LK} are defined by equation (20) with $S=K$.

According to the model assumptions concerning the concentration fluctuation at high frequencies α'' the fluxes in equations (24) and (25) can be modeled collectively as:

$$-\overline{\alpha_K'u_{Ki}'}=\frac{\nu_{Lt}}{\sigma_{LK}}\frac{\partial\bar{\alpha}_K}{\partial x_i} \tag{26}$$

The fourth group of terms with the concentration-shear stress turbulent correlations contains the laminar viscosity as a multiplier, and will be neglected due to its smaller order of magnitude.

The pressure effect contribution to the mean flow equation consists of two groups. Each contains three terms. The first of these terms is the mean pressure-mean concentration product. The second and the third terms are the pressure-concentration correlations which can be modeled after Elghobashi and Abou-Arab (1983) by

$$\overline{\alpha_K'p_K'}+\overline{\alpha_K''p_K''}=\psi_1+\psi_2 \tag{27}$$

where

$$\psi_1=-C_{\phi 3}\rho_K k_K^{1/2}/\epsilon_K\cdot\overline{u_{Km}'\alpha_K'}$$

and

$$\psi_2=C_{\phi 4}\rho_K k_K^{1/2}/\epsilon_K\cdot\overline{u_{Km}'\alpha_K'}$$

where ϵ_K is the dissipation rate, and m denotes modulus of a vector. The constants $C_{\phi 3}$ and $C_{\phi 4}$ are about unity.

The second correlation in the second group of terms can be also modeled following Launder (1978). The final form is

$$\overline{p_K'\frac{\partial\alpha_K'}{\partial x_i}}+\overline{p_K''\frac{\partial\alpha_K''}{\partial x_i}}=-\rho_K\left(\frac{\epsilon}{k}\right)_K\left[C_{\phi 1}\cdot\overline{u_{Ki}'\alpha_K'}+C_{\phi 2}\left(\frac{\overline{u_{Ki}'u_{Kl}'}}{k_K}-\frac{2}{3}\delta_i 1\right)\cdot\overline{u_{Kl}'\alpha_K'}\right]+\rho_K\left(0.8\overline{u_{Kl}'\alpha_K'}\cdot\frac{\partial\bar{u}_{Ki}}{\partial x_i}-0.2\overline{u_{Kl}'\alpha_K'}\cdot\frac{\partial\bar{u}_{Kl}}{\partial x_i}\right) \tag{28}$$

The constants $C_{\phi 1}$ and $C_{\phi 2}$ are 4.3 and -3.2, respectively. The modeling of these correlations suffers from the embodied assumptions concerning the velocity and length scale description.

The interaction term $\overline{(I_{Ki})}_{M-K}$ for $K=L$ (liquid) and $M-K=S$ (solid) is modeled for dilute suspensions, with relatively fine particles, which play a passive role on turbulence

$$\overline{(I_{Li})_S}=-(18\mu_L/d_S^2)\left[(\bar{u}_{Li}-\bar{u}_{Si})\bar{\alpha}_S+\left(\frac{\nu_{LP}}{\sigma_{LS}^{P}}+\frac{\nu_{LT}}{\sigma_{LS}^{T}}\right)\frac{\partial\bar{\alpha}_L}{\partial x_i}+\left(\frac{\nu_{LP}}{\sigma\sigma_{LS}^{P}}+\frac{\nu_{LT}}{\sigma\sigma_{LS}^{T}}\right)\frac{\partial\bar{\alpha}_S}{\partial x_i}\right] \tag{29}$$

where the first term is the drag interaction for particles in the Stokes range. The second and third terms are the turbulent fluxes due to the relative motion between particles and fluid. The gradient transport model with the exchange coefficients ν_{LP} and ν_{LT} corresponding to the production and transfer ranges was adopted for these fluxes ($\overline{\alpha_L'u_{Li}'}$, $\overline{\alpha_L''u_{Li}''}$, $\overline{\alpha_S'u_{Si}'}$ and $\overline{\alpha_S''u_{Si}''}$). If only a velocity scale is chosen for the whole energy spectrum $(k_L)^{0.5}$, there will be only one momentum exchange coefficient ν_{Lt} in (29) instead of ν_{LP} and ν_{LT}.

6 Closure For the Kinetic Energy Equation

In the present work, the turbulence kinetic energy for the liquid phase "k_L" (turbulence velocity scale) is obtained from an exact transport equation (equation (A5) in Appendix A), and the length scale "l" is described algebraically.

The first group of terms in the k-equation (Group #1) is the *convection* of the total specific kinetic energy, where

$$\frac{\partial k_L}{\partial x_j}=\frac{\partial k_{LP}}{\partial x_j}+\frac{\partial k_{LT}}{\partial x_j} \tag{30}$$

The *diffusion transport* of k_L is composed of two main parts. The first part (Group #2) is the velocity diffusion and it contains the 3rd order velocity correlations, while the second part (Group #3) is the pressure diffusion with the pressure-velocity correlations. The modeling of the velocity diffusion part in the production range is:

$$\rho_L\bar{\alpha}_L\,\overline{u_{Lj}'u_{Li}'u_{Li}'}=-\rho_L\bar{\alpha}_L\frac{\nu_{LP}}{\sigma_k^{P}}\frac{\partial k_{LP}}{\partial x_j} \tag{31}$$

where σ_k^{P} is the turbulent Prandtl-Schmidt number for the kinetic energy in the production range. A similar expression can be written for the transfer range ($\rho_L\bar{\alpha}_L\,\overline{u_{Lj}''u_{Li}''u_{Li}''}$) with σ_k^{T}. To reduce the number of empirical constants and the number of governing equations the above two correlations are modeled collectively

$$\rho_L\bar{\alpha}_L\overline{u_{Lj}'u_{Li}'u_{Li}'}=-\rho_L\bar{\alpha}_L\frac{\nu_{LT}}{\sigma_K}\frac{\partial k_L}{\partial x_j} \tag{32}$$

where σ_k is the order of unity.

The *pressure diffusion* term is neglected compared with the velocity diffusion (Hanjalic' and Launder, 1972).

Mixed and higher order correlations (Groups #3 and #5) can be neglected according to the modeling assumptions stated and discussed in Section 4.3 of the present paper.

The *production terms* are divided into two groups. The first group (Group #6) is common for single and multiphase incompressible flows,

$\rho_L\bar{\alpha}_L\,\overline{u_{Li}'u_{Lj}'}\frac{\partial\bar{u}_{Li}}{\partial x_j}+\rho_L\bar{\alpha}_L\,\overline{u_{Li}''u_{Lj}''}\frac{\partial\bar{u}_{Li}}{\partial x_j}$, and can be modeled collectively as follows:

$$\rho_L\bar{\alpha}_L\,\overline{u_{Li}'u_{Lj}'}\frac{\partial\bar{u}_{Li}}{\partial x_j}=\bar{\alpha}_L\mu_{Lt}\left(\frac{\partial\bar{u}_{Li}}{\partial x_j}\right)^2 \tag{33}$$

The physics of turbulence and the consideration of the spectral energy transfer assume that the production is only due to the interaction between the mean flow and the large eddy. Since the $\overline{u_{Li}''u_{Lj}''}$ correlation is for medium size eddies which

have almost no direct interaction with the mean flow, it results that the contribution of these eddies to the turbulence production is small. This also means that $\overline{u''_{Li}u''_{Lj}}$ correlation is weak if $i \neq j$. Only the turbulent normal stress components ($\overline{u_i''^2}, i=1, 2, 3$) are significant. According to Hanjalic et al. (1979) multiple scale model the turbulent viscosity is

$$\mu_{Lt}/\rho_L = C_\mu k_L (k_{LP}/\epsilon_{LP}) \tag{34}$$

where $k_L = k_{LP} + k_{LT}$ and $C_\mu = 0.09$. This equation can be rewritten as

$$\mu_{Lt}/\rho_L = C_\mu \left(\frac{k_{LP}^2}{\epsilon_{LP}} + \frac{k_{LT}k_{LP}}{\epsilon_{LP}}\right)$$
$$= C_{\mu P} k_{LP}^{0.5} l_{LP} + C_{\mu T} k_{LT}^{0.5} l_{LT} = (\mu_{LP} + \mu_{LP})/\rho_L \tag{35}$$

where $C_{\mu P}$ and $C_{\mu T}$ are two additional constants and l_P and l_T are also two additional length scales for the large and medium size eddies. The length scales can be related (from equations (34) and (35))

$$l_{LT} = C_1 l_{LP} (k_{LT}/k_{LP}) \tag{36}$$

Since the ratio k_{LT}/k_{LP} is the order of unity and $l_{LP} > l_{LT}$, the constant C_1 should be smaller than unity. Thus if the multiple time scale model is not recommended (due to its large number of additional constants) an alternative approach is to consider a multiple velocity scale model. In this model only two differential equations for k_{LP} and k_{LT} have to be solved. The length scales can be obtained by using equation (36) and any expression for the length scale of the large eddies l_{LP}, for example that used by Spalding (1977) (the linear law $l_{LP} \approx 0.4 y + 0.0001$) or Roco and Balakrishnan (1985) (equation 35 in that reference) for cylindrical pipes.

The models for the *additional production* terms (Group #7) are

$$-\overline{\alpha'_L u'_{Li}} \frac{\partial \bar{p}_L}{\partial x_i} = \frac{\nu_{LP}}{\sigma_{LS}^P} \frac{\partial \bar{\alpha}_L}{\partial x_i} \frac{\partial \bar{p}_L}{\partial x_i} \tag{37a}$$

$$-\overline{\alpha''_L u''_L} \frac{\partial \bar{p}_L}{\partial x_i} = \frac{\nu_{LT}}{\sigma_{LS}^T} \frac{\partial \bar{\alpha}_L}{\partial x_i} \frac{\partial \bar{p}_L}{\partial x_i} \tag{37b}$$

and both collectively as

$$-(\overline{\alpha'_L u'_{Li}} + \overline{\alpha''_L u''_{Li}}) \frac{\partial \bar{p}_L}{\partial x_i} = \frac{\nu_{Lt}}{\sigma_{LS}} \frac{\partial \bar{\alpha}_L}{\partial x_i} \frac{\partial \bar{p}_L}{\partial x_i} \tag{37c}$$

The terms like $\overline{\alpha'_L u'_{Li}} \frac{\partial \bar{u}_{Li}}{\partial x_i}$ and $\overline{\alpha''_L u''_{Li}} \frac{\partial \bar{u}_{Li}}{\partial x_i}$ are modeled in a similar manner

$$-(\overline{\alpha'_L u'_{Lj}} + \overline{\alpha''_L u''_{Lj}}) \frac{\partial \bar{u}_{Li}}{\partial x_i} = \frac{\nu_{Lt}}{\sigma_{LS}} \frac{\partial \bar{u}_{Li}}{\partial x_i} \frac{\partial \bar{\alpha}_L}{\partial x_j} \tag{38}$$

The *extra production* terms (Group #7) can be written in the following form

$$\frac{\nu_{Lt}}{\sigma_{LS}} \frac{\partial \bar{\alpha}_L}{\partial x_i} \left(\frac{\partial \bar{p}_L}{\partial x_i} + \bar{u}_{Lj} \frac{\partial \bar{u}_{Li}}{\partial x_j}\right) + \frac{\nu_{Lt}}{\sigma_{LS}} \frac{\partial \bar{\alpha}_L}{\partial x_j} \left(\bar{u}_{Li} \frac{\partial \bar{u}_{Li}}{\partial x_j}\right) \tag{39}$$

The terms $\rho_L \bar{\alpha}_L \nu_L \overline{\frac{\partial u'_{Li}}{\partial x_j} \frac{\partial u'_{Li}}{\partial x_j}}$ and $\rho_L \bar{\alpha}_L \nu_L \overline{\frac{\partial u''_{Li}}{\partial x_j} \frac{\partial u''_{Li}}{\partial x_j}}$ in Group #8 represents the *dissipation rate* from large eddies ϵ_{LP} and transfer eddies ϵ_{LT}, respectively. Since viscous dissipation is confined to small scale eddies and to simplify the mathematical form of the multiple time scale turbulence models, Hanjalic' et al. (1979) have assumed that there is an equilibrium spectrum energy transfer between the dissipation and transfer region, i.e., $\epsilon_{\text{total}} = \epsilon_L$, where ϵ_L is the dissipation rate in the single scale scheme. Thus

$$\rho_L \bar{\alpha}_L \nu_L \overline{\frac{\partial u'_{Li}}{\partial x_j} \frac{\partial u'_{Li}}{\partial x_j}} = -\rho_L \bar{\alpha}_L \epsilon_{LP} = \bar{\alpha}_L \mu_{LT} \left(\frac{\partial \bar{u}_{Li}}{\partial x_j}\right)^2 \tag{40}$$

where

$$\epsilon_{LP} = C_{DP} k_{LP}^{3/2}/l_{LP}$$

A similar formulation to (40) is written for the corresponding transfer range term ϵ_{LT}. In equation (40) a spectral cascading between the production and transfer eddies is considered (Hanjalic' et al. (1979)). This equation gives an additional relation between the spectrum scales.

The correlations between the fluctuating velocity component and the fluctuating friction forces (*interaction terms* in Groups #8 and #10) are due to fluid-fluid and fluid-solid drag force in dilute flows. The friction interaction terms due to molecular collisions (fluid-fluid interaction, Group #8) are given by equations of type (40). The form of the correlation between the fluctuating drag force and the velocity fluctuations depends on the expression adopted for the drag force. The viscous drag correlation (VDC) in Group #10 for Stokes flow over particles in dilute suspensions is

$$\text{VDC} = -\frac{18\mu_L}{d_S^2}(\bar{u}_{Li} - \bar{u}_{Si}) \cdot \Delta_1 - \frac{18\mu_L}{d_S^2}(\bar{\alpha}_S \cdot \Delta_2 + \Delta_3) \tag{41a}$$

where

$$\Delta_1 = \overline{\alpha'_S u'_i} + \overline{\alpha''_S u''_i} \tag{41b}$$

$$\Delta_2 = \overline{u'_{Li}(u'_{Li} - u'_{Si})} + \overline{u''_{Li}(u''_{Li} - u''_{Si})} \tag{41c}$$

$$\Delta_3 = \overline{\alpha'_S u'_{Li}(u'_{Li} - u'_{Si})} + \overline{\alpha''_S u''_{Li}(u''_{Li} - u''_{Si})} \tag{41d}$$

The first correlation group Δ_1 (41*b*) can be approximated using the gradient type assumption. The second correlation in this expression (41*c*) is that due to the relative slip fluctuating motion $\overline{u'_{Li}(u'_{Si} - u'_{Li})}$ and $\overline{u''_{Li}(u''_{Li} - u''_{Si})}$. These correlations can be modeled using a similar approach to that of Elghobashi and Abou-Arab (1983) but with some modifications which allow for different particle-eddy interaction according to their relative size. These modifications are based on the spectral analysis carried out by Hinze (1975) and Xie (1987) for the response of the particles to the turbulent fluctuations of the carrier fluid. For *very large eddies* $\kappa \ll \kappa_S$ of the carrier fluid, the solution of the Basset-Boussinesq-Oseen equation with some simplifying assumptions is

$$u'_S = (v'_S)_\kappa = (v'_L)a \cdot \exp[-i(\kappa \bar{u}_L t + \beta)] \tag{42}$$

where: κ is the fluid wave number; κ_S is the Basset-Boussinesq-Ossen wave number defined as $1/d_S$; $(v'_S)_\kappa$ and $(v'_L)_\kappa$ are the solid and liquid Lagrangian velocity components with the wave number κ; a is the amplitude ratio of oscillation

$$a = [(1+q_1)^2 + q_2^2]^{0.5} \tag{43a}$$

and β is the phase angle of oscillation

$$\beta = \tan^{-1} q_1/(1+q_2) \tag{43b}$$

The expressions for q_1 and q_2 are

$$q_1 = \frac{\left(1 + \frac{9N_S}{\sqrt{2}(s+0.5)}\right)\left(\frac{1-s}{s+0.5}\right)}{\frac{81}{(s+0.5)^2}\left(2N_S^2 + \frac{N_S}{\sqrt{2}}\right)^2 + \left(1 + \frac{9N_S}{\sqrt{2}(s+0.5)}\right)^2} \tag{44a}$$

$$q_2 = \frac{\frac{9(1-s)}{(s+0.5)^2}\left(2N_S^2 + \frac{N_S}{2}\right)}{\frac{81}{(s+0.5)^2}\left(2N_S^2 + \frac{N_S}{\sqrt{2}}\right)^2 + \left(1 + \frac{9N_S}{\sqrt{2}(s+0.5)}\right)^2} \tag{44b}$$

with the following dimensionless parameters:

$$s = \rho_S/\rho_L$$

$$N_S = \left(\frac{\nu_L}{u_L \kappa d_S^2}\right)^{0.5} = \frac{\kappa}{\kappa_T}\left(\frac{\kappa Re_T}{\kappa_T}\right)^{0.5}$$

where κ_T is the wavenumber of the most energetic eddies, Re_T is Reynolds number based on l_T, and N_S is Stokes number.

For *small eddies* with wave numbers $\kappa \gg \kappa_S$, the particle response can be described by a Langevin equation (Xie, 1987), and be approximated by

$$u_S' = (v_S')_\kappa = (v_L')_\kappa \left(\frac{\kappa_S}{\kappa}\right)^3 \frac{\rho_L}{\rho_S} \tag{45}$$

For the *intermediate eddy size* $\kappa \approx \kappa_S$ one can use (42) with

$$a_{\text{int}} = 1/s, \text{ and} \tag{46a}$$

$$\beta_{\text{int}} = \tan^{-1}(s) \tag{46b}$$

which matches asymptotically the solutions of large and small eddies $\kappa = \kappa_S$.

If the fluctuating slip velocity w_i' is defined as

$$w_i' = u_{Si}' - u_{Li}' \tag{47}$$

then the ratio of the mean square $\overline{w_i'^2}$ and $\overline{u_{Li}'^2}$ becomes

$$\overline{w'^2_i}/\overline{u_{Li}'^2} = (\overline{u_{Si}'^2} - 2\overline{u_{Li}'u_{Si}'} + \overline{u_{Li}'^2})/\overline{u_{Li}'^2} \tag{48}$$

with

$$\overline{u_{Li}'u_{Si}'} = \frac{1}{2}\overline{u_{Li}'^2}(1 + \overline{u_{Si}'^2}/\overline{u_{Li}'^2} - \overline{w_i'^2}/\overline{u_{Li}'^2})$$

$$= \frac{1}{2}\overline{u_{Li}'^2}\,(1 + \Gamma_{SL} - \Gamma_{RL}) \tag{49}$$

The values of Γ_{SL} and Γ_{RL} can be obtained using the solution of equations (42), (45), and (46):

$$\Gamma_{SL} = \overline{u_{Si}'^2}/\overline{u_{Li}'^2} = \left[\int_0^{\kappa_S} a^2 E_L(\kappa)d\kappa + \right.$$

$$\left. + \int_{\kappa_S}^{\infty} \left(\frac{\kappa_S}{\kappa}\right)^6 s^{-2} E_L(\kappa)d\kappa\right] / \int_0^{\infty} E_L(\kappa)d\kappa \tag{50}$$

or

$$\Gamma_{SL} = \frac{2h}{\pi(h+1)}\tan^{-1}(\kappa_S/\kappa_T) \tag{51}$$

where

$$h = \frac{A}{\kappa_T u_L'} = \frac{18}{(s+0.5)}(\kappa_S/\kappa_T)^2/\text{Re}_T,$$

$$A = \frac{18\nu_L}{(s+0.5)d_S^2}$$

and

$$\Gamma_{RL} = \overline{w_i'^2}/\overline{u_i'^2} = \left[\int_0^{\kappa_S} (a-1)^2 E_L(\kappa)d\kappa \right.$$

$$\left. + \int_{\kappa_S}^{\infty} \left(\left(\frac{\kappa_S}{\kappa}\right)^3 s^{-1} - 1\right)^2 E_L(\kappa)d\kappa\right] / \int_0^{\infty} E_L(\kappa)d\kappa \tag{52}$$

where $a_1 = (f_1^2 + f_2^2)^{0.5}$, and $E_L(\kappa)$ is the liquid energy spectrum function, for which the following form is adopted

$$E_L(\kappa) = \frac{2}{\pi}\frac{\overline{u_{Li}'^2}}{\kappa_T}\frac{1}{1+(\kappa/\kappa_T)^2} \tag{53}$$

Figure 2 illustrates the effect of eddy to particle size ratio expressed as κ_S/κ_T on the ratio $\Gamma_{SL} = \overline{u_{Si}'^2}/\overline{u_{Li}'^2}$, as a function of the density ratio $S = \rho_S/\rho_L$. It can be noticed that at high values of κ_S/κ_T (i.e, small particle or large eddy) the particles follows quite well the eddying motion.

Substituting the expressions for Γ_{SL} and Γ_{RL} (equations (50) and (52)) into equation (49), the correlation Δ_2 can be obtained. The above analysis applies equally well to the large eddies as to small eddies. The energy spectrum function $E_L(\kappa)$ for a two-phase flow is given by Al-Taweel and Landau (1977). However, since its form is not that important (Xie (1987)), it is sufficient

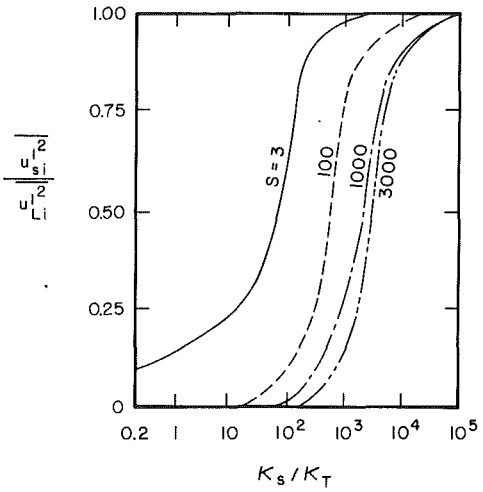

Fig. 2 The effect of eddy-particle size ratio κ_S/κ_T on the particle response to the eddy fluctuations $\overline{u_{Si}^{\prime 2}}/\overline{u_{Li}^{\prime 2}}$

to adopt any simple form as that given by equation (53). It is also clear from the above analysis that the particle response to the carrier fluid fluctuations is function of the density ratio ρ_S/ρ_L, size of interacting eddy relative to particle size κ_S/κ and Reynolds number based on the size of the most energetic eddies of the flow. An analogous expression for Δ_1 can be obtained starting from the Chao's solution (see Chao, 1964). This solution can be considered as a substitution of Xie's solution only for $\kappa \ll \kappa_S$, i.e., for fine particles.

The last term to be modeled in the VCD group, Δ_3, is separated into four correlations:

$$\Delta_3 = -\frac{18\mu_L}{d_S^2}(\overline{\alpha_S' u_{Li}' u_{Li}'} + \overline{\alpha_S'' u_{Li}'' u_{Li}''} - \overline{\alpha_S' u_{Li}' u_{Si}'} - \overline{\alpha_S'' u_{Li}'' u_{Si}''})$$

$$\qquad T1 \qquad\quad T2 \qquad\quad T3 \qquad\quad T4 \tag{54}$$

where the triple correlations $T3$ and $T4$ are modeled in a similar manner to that used for the calculation of $T1$ and $T2$ with equations type (22). Therefore

$$T1 = \overline{\alpha_S' u_{Li}' u_{Li}'} = -C_{\phi 5}^P (k_{LP}/\epsilon_{LP})\left(2\overline{u_{Li}' u_{Ll}'}\frac{\partial \overline{u_{Li}'\alpha_S'}}{\partial x_l}\right)_P,$$

$$T2 = \overline{\alpha_S'' u_{Li}'' u_{Li}''} = -C_{\phi 5}^T (k_{LT}/\epsilon_{LT})\left(2\overline{u_{Li}'' u_{Ll}''}\frac{\partial \overline{u_{Li}''\alpha_S''}}{\partial x_l}\right)_T,$$

$$T3 = -C_{\phi 5}^T (k_{LP}/\epsilon_{LP})\left(\overline{u_{Li}' u_{Sl}'}\frac{\partial \overline{u_{Si}'\alpha_S'}}{\partial x_l} + \overline{u_{Si}' u_{Ll}'}\frac{\partial \overline{u_{Li}'\alpha_S'}}{\partial x_l}\right)_P, \text{ and}$$

$$T_4 = -C_{\phi 5}^T (k_{LT}/\epsilon_{LT})\left(\overline{u_{Li}'' u_{Sl}''}\frac{\partial \overline{u_{Si}''\alpha_S''}}{\partial x_l} + \overline{u_{Si}'' u_{Ll}''}\frac{\partial \overline{u_{Li}''\alpha_l''}}{\partial x_l}\right)_T \tag{55}$$

These correlations can also be collectively modeled using single velocity and length-scale, and total k_L and ϵ_L. The first two terms yield:

$$T1 + T2 = -C_{\phi 5}\frac{2k_L}{\epsilon_L}\overline{u_{Li}' u_{Ll}'}\frac{\partial \overline{u_{Li}'\alpha_S'}}{\partial x_l} \tag{56a}$$

$$T3 + T4 = -C_{\phi 5}\frac{2k_L}{\epsilon_L}\left(\overline{u_{Li}' u_{Sl}'}\frac{\partial \overline{u_{Si}'\alpha_S'}}{\partial x_l} + \overline{u_{Si}' u_{Ll}'}\frac{\partial \overline{u_{Li}'\alpha_S'}}{\partial x_l}\right) \tag{56b}$$

where $C_{\phi 5}$ takes the same value (0.1) as that used for momentum equation in (23).

The terms in Group #9 of equation (A5) are of diffusive and dissipative nature. The diffusion terms as they appeared

in Group #9 are multiplied by the molecular viscosity and therefore will be neglected. Other higher order correlations and mixed correlations in this group are also neglected according to the modeling principles stated previously in Section 4.3.

By substituting all previously modeled terms into the exact form of the turbulence kinetic energy equation (A5), and rearranging these terms, the steady-state turbulence kinetic energy equation ($K=L$) is:

$$\rho_L \bar{\alpha}_L \bar{u}_{Lj} \frac{\partial k_L}{\partial x_j} = \frac{\partial}{\partial x_j}\left(\bar{\alpha}_L \frac{\mu_{Lt}}{\sigma_k}\frac{\partial k_L}{\partial x_j}\right) + \alpha_L \mu_{Lt}\left(\frac{\partial u_{Li}}{\partial x_j}\right)^2$$

Convection Diffusion Production

$$+\frac{\nu_{Lt}}{\sigma_{\alpha S}}\frac{\partial \bar{\alpha}_L}{\partial x_1}\left(\frac{\partial \bar{P}_L}{\partial x_1} + \bar{u}_{Lj}\frac{\partial \bar{u}_{Li}}{\partial x_j}\right) + \frac{\nu_{Lt}}{\sigma_{\alpha S}}\frac{\partial \alpha_L}{\partial x_j}\left(u_{Li}\frac{\partial u_{Li}}{\partial x_j}\right)$$

Extra Production

$$-\rho_L \alpha_L \epsilon_L + \frac{18\mu_L}{d_S^2}\left((u_{Li}-u_{Si})\frac{\nu_{Lt}}{\sigma_{\alpha S}}\frac{\partial \alpha_L}{\partial x_i}\right.$$

Dissipation Extra Dissipation

$$\left. -0.5\alpha_S k_L(1+\Gamma_{SL}-\Gamma_{RL}) - (T1+T2-T3-T4)\right) \quad (57)$$

where Γ_{SL}, Γ_{RL}, $T1$, $T2$, $T3$, and $T4$ were given in equations (50), (52), and (56).

The present model is based on an the exact turbulence kinetic energy equation, and the modeled form of this equation has no adjusting coefficients. The only modeling assumption is that of the Boussinesq gradient type, which generally is accepted. The correlations that requires questionable semi-empirical modeling assumptions and introduction of empirical constant are only for the triple correlations of type $\overline{\alpha'_L u'_{Li} u'_{Lj}}$ and $\overline{\alpha'_L u'_{Si} u'_{Lj}}$, which have an order of magnitude smaller (by ratio $\alpha'/\bar{\alpha}$) compared to other main terms in the k-equation. A new correlation is used in the present closure for the relative motion between phases (equation (29)). This is modeled with less restrictions and taking into consideration the effect of the particle diameter-eddy size ratio on the particle response to the eddying motion. The main limitation of the present one-equation k model closure is the algebraic formulation for the length scale. Since there are many factors affecting this length scale and since it is even difficult in many practical applications to give a unique and accurate description of the length scale, the use of a transport equation for the length scale in the two-equation model of Elghobashi and Abou-Arab (1983) is expected to give better results with fine particles ($d_S < \eta$). However, it should be noticed that the former model and any other similar models contain some empirical constants specific for various flow conditions, and they require the solution for an additional transport equation. It can be expected that the present model combined with an appropriate length scale equation e.g., dissipation rate equation will simulate better most of the important features of multiphase turbulent flows, particularly the fluid particle interaction.

7 Sample of Results

Figures 3 to 6 compare the present predictions with LDV-measurements for single and two-phase turbulent pipe flow of Maeda et al. (1980) and turbulent round water jet laden with uniform-size solid particles of Parthasarathy and Faeth (1987). Both flows are oriented vertically downward. These flows are axisymmetrical. The concentration profiles are given as input data based on experimental results.

In these flow situations the average eddy size l_e was from about one d_s to few hundreds d_S as a function of position. The corresponding representative eddy size in the transfer range was only a fraction of particle diameter in the pipe flow case.

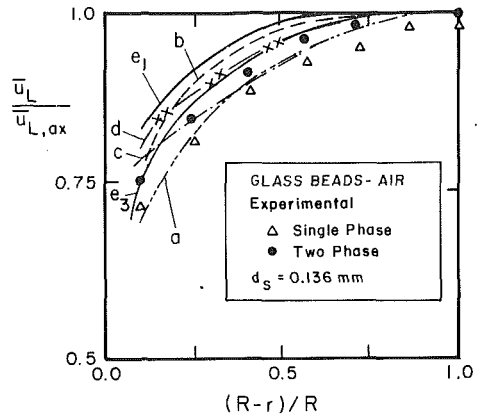

Fig. 3 Computed and measured (Maeda et al., 1980) mean velocity distribution of air in air-glass beads mixture pipe flow ($d_S = 0.136$ mm, $\bar{\alpha}_{s,av} = 1.4\ 10^{-4}$ vol): (*a*) Single phase (present k-model with the length scale after (Roco and Balakrishnan, 1985)), (*b*) $k-\epsilon$ model (Elghobashi and Abou-Arab, 1983), (*c*) k-model (Roco and Mahadevan, 1986), (*d*) k-model after (Elghobashi and Abou-Arab, 1983)), e_1 present k-model with the mixing length after (Roco and Balakrishnan, 1985), e_3. Present k-model with mixing length calculated with a transport equation (Abou-Arab and Roco, 1989).

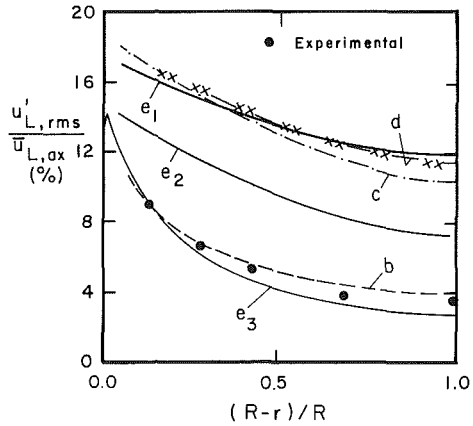

Fig. 4 Computed and measured (Maeda et al., 1980) radial distribution of the turbulence intensity of air in air-glass beads mixture pipe flow (*b*) k-ϵ model (Elghobashi and Abou-Arab, 1983), (*c*) k-model (Roco and Mahadevan, 1986), (*d*) k-model after (Elghobashi and Abou-Arab, 1983), e_1 present k-model with mixing length after (Roco and Balakrishnan, 1985), e_2. Present k-model with mixing length after Spalding (1977), e_3. Present k-model with mixing length calculated with a transport equation (Abou-Arab and Roco, 1989).

These scales are field variables, and they depend upon the flow configuration, location in the flow domain and particle dimensions.

Two-phase flow solutions were obtained by solving the flow governing equations in their modeled form which are described in the previous sections. The empirical constants are the same as those used in single fluid flow modeling: $C_{\phi 1} = 4.3$, $C_{\phi 2} = 3.2$, $C_{\phi 3} = 1$, $C_{\phi 4} = 1$, $C_{\phi 5} = 0.1$, and $C_\mu = 0.09$. They are applied in both test cases presented in this section. The numerical procedure used for these predictions is based on a developed version of the Genmix-Code of Spalding. The CPU Time for the two considered flow cases was about 4 minutes on a VAX 760 Mini-Computer and 2 minutes on IBM 3084.

Case I: Gas Solid Vertical Pipe Flow. Figures 3 and 4 show comparisons between the experimental data of Maeda et al. (1980) and the present predictions using four models of turbulence: $k-\epsilon$ model of Elghobashi and Abou-Arab (1983) (curves *b*); one-equation k-model of Roco and Mahadevan (1986) (curves *c*); k-equation as given in the k-ϵ model of Elghobashi and Abou-Arab (1983) (curves *d*); and the present

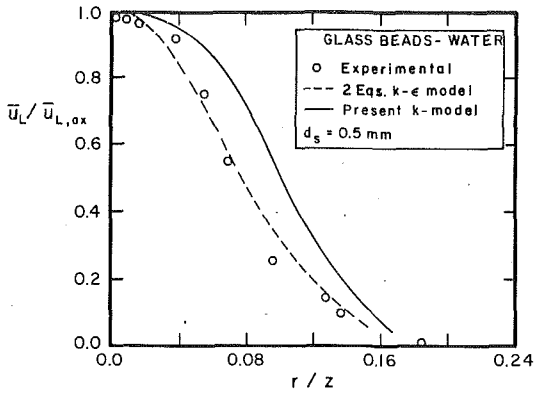

Fig. 5 Computed and experimental (Parthasarathy and Faeth, 1987) *mean liquid velocity distribution in water-glass beads mixture jet flow* at $z/d = 40$ ($d_S = 0.5$ mm, $\bar{\alpha}_{S,av} = 2.4\ 10^{-2}$ vol).

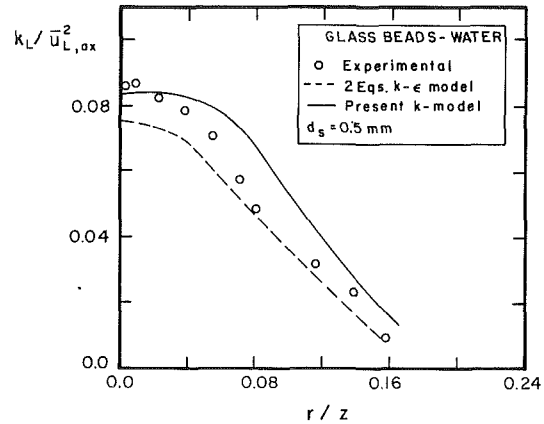

Fig. 6 Computed and experimental (Parthasarathy and Faeth, 1987) radial distribution of the turbulence intensity of water in water-solid jet flow at $z/d = 40$

one-equation k-model (curve a for air flow, curves e for two-phase flow with different mixing length formulations). In the present computation, the concentration profiles are assumed based on experimental data. When direct measurements are not available, the inlet concentration distribution is taken to be the best curve fit after the experimental data of Soo (1967). The near wall treatment is based on a modified form for the law of wall (see Abou-Ellail and Abou-Arab (1984), Lee and Chung (1987)) and the particle slip condition at the pipe wall. Figure 3 displays the mean axial velocity distributions normalized by the axial velocity in the fully developed zone of the pipe flow. The experimental data show an increase of $\bar{u}_L$ when the solid particles are present. All considered models (curves a-e) exhibit the same tendency. The differences between the predictions of the one-equation turbulence models are partially caused by the mixing length formulation, which was not optimized or adjusted. Our model with the mixing length as used by Roco and Balakrishnan (1985) (curve e_1 in Fig. 3) leads to a flatter mean velocity profile because the fluctuations are overpredicted in the core of the flow (see curve e_1 in Fig. 4). If the mixing length is computed with a transport equation (2), our mean and fluctuation velocity predictions are the closest to the experimental data (see curves e_3). Figure 4 compares the calculated relative turbulence intensity $u_{Lrms}/\bar{u}_{L,ax}$ with the measurements. Here $u'_{L,rms} = (\overline{u'^2})^{0.5} = (2/3k_L)^{0.5}$ denotes the root-mean-square of the fluid velocity fluctuation. The differences between the present k-model predictions with three turbulence length scale formulations are evident: the curve e_1 is for the algebraic length scale used by Roco and Balakrishnan (1985), the curve e_2 is for the algebraic length scale used by Spalding (1977) ($\approx 0.4\,y + 0.0001$, where y is the distance from the wall), and the curve e_3 is for the length scale computed from a transport equation.

If similar length scale formulations are used, the present k-model predicts slightly better the mean and fluctuating velocities as compared with the turbulence models of Elghobashi (1983, 1987). The improvement relative to other one-equation turbulence models is more pronounced in the near the wall region where the turbulence intensity and its modulation is more significant. In our model no coefficient was adjusted. The same coefficients were applied as those already used for single fluid flow in reference publications. The differences between our and previous predictions are caused by the modeling of turbulence modulation by particles.

Case II: Turbulent Round Water Jet Laden With Uniform-Size Solid Particles. Comparison between experimental data and numerical predictions of different turbulence closures are given in Figs. 5 and 6. The two-phase flow measurements on velocity, concentration and turbulence correlations used for comparisons are taken from Parthasarathy and Faeth (1987). Different axial locations within the round jet, between eight and forty jet diameters from the injection nozzle are considered. The radial distribution of solid concentration given in Fig. 7 are at eight diameters from the nozzle. The comparison shows that the two-equation two-phase k-ϵ model of Elghobashi and Abou-Arab (1983) describes both flows better than the one-equation double-time averaged turbulence model. However, if a similar turbulence length scale formulation is applied, the predictions are better with the present model even if the closure is without adjusting any empirical coefficients. At the same time, the present closure is in its early stages and more refinements are required in modeling the turbulence modification, by relaxing some assumptions.

The differences between the predictions of the mean and fluctuating flow velocity components ($\Delta u'_{L,rms}$ *and* $\Delta \bar{u}_L$, respectively) as obtained by the present k-formulation and that of Elghobashi (1987) are functions of the particle size relative to its surrounding eddies. Figure 8 illustrates these differences for the vertical pipe flow ("Case 1"), at two different loading ratios, at a radial distance $(R - r)/R$ equal 0.1. The predictions with the k-formulation of Elghobashi and Abou-Arab (1983), denoted $u'_{L,rms}$ and $\bar{u}_L$ in Fig. 8, are used as reference data. It is obvious that the discrepancies between our predictions with the new turbulence modulation terms and that from the previous work are more important if the particle size and load ratio increase.

8 Concluding Remarks

The turbulence closure presented in this paper for dilute suspension flow is based on the fluid turbulence kinetic energy equation. The main features of this model are:

(1) Two velocity scales are adopted in computation for large and medium size eddies, corresponding to the turbulence production and transfer range, respectively. They are introduced into the governing equations by a specific double-time averaging. On this basis the spatial and temporal transfer rates of the thermodynamic quantities and the particle-eddy interaction are better estimated.

(2) To keep the number of transport equations of the turbulence closure and the number of empirical constants as minimum as possible, the length scales l_P and l_T are described using algebraic expressions. Relations between these scales (equations (36) and (40)) are suggested.

(3) Spectral analysis of the interaction mechanism between particles and most energetic eddies provide analytical correlations for closure. The particle response and the modulation of turbulent eddying motion is given as a function of the particle-fluid density and size ratios. The limiting case in which the particles play only a passive role on turbulence was analyzed in this paper.

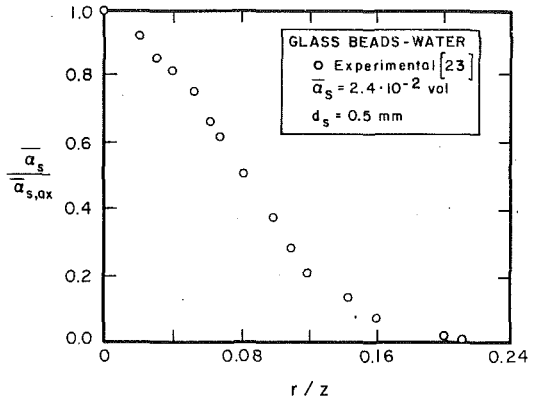

Fig. 7 Radial distribution of solid phase concentration in water-solid jet flow, after [23]

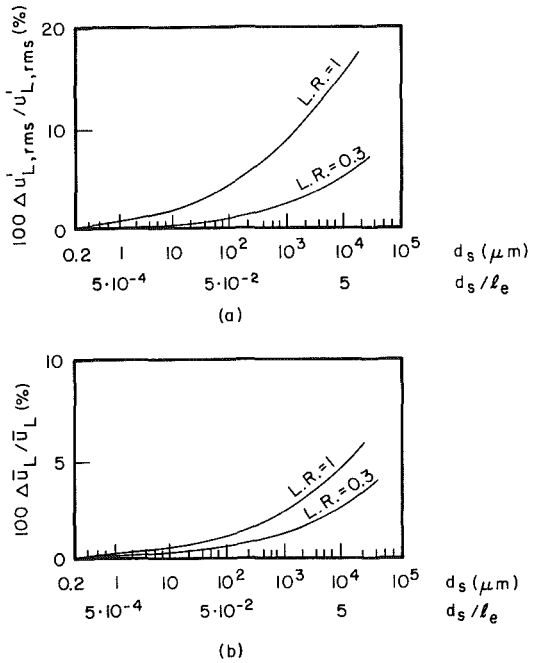

Fig. 8 Differences between the present *k*-formulation and that of Elghobashi and Abou-Arab, 1983 for different mass loading ratios *L.R.*: (*a*) fluctuating and (*b*) mean axial velocity

(4) The model does not introduce additional empirical constants to the closure of the velocity scale equation.

Acknowledgments

This work has been partially supported by NSF CBT grant and Center for Computational Sciences at the University of Kentucky. The first co-author would like to acknowledge also the Jordan University of Science and Technology.

References

Abou-Arab, T. W., 1987, "Turbulence Models for Two-Phase Flows," *Encyclopedia of Fluid Mechanics*, Vol. 3, ed. N. P. Cheremisinoff, Gulf Publ., New Jersey, pp. 863-907.

Abou-Arab, T. W., and Roco, M. C., 1989, "Turbulence Length Scale Equation for Two-phase Flow," *Proceedings of 7th Int. Symp. on Turbulent Shear Flows*, Stanford.

Abou-Ellail, M. M. M., and Abou-Arab, T. W., 1985, "Prediction of Two-Phase Flow and Heat Transfer in Vertical Pipes," *5th Int. Symp. Turbulent Shear Flows*, pp. 8.1-8.9.

Achenbach, E., 1974, "Vortex Shedding from Spheres," *J. Fluid Mech.*, Vol. 62, pp. 209-221.

Al Taweel, A. M., and Landau, J., 1977, "Turbulence Modulation in Two-Phase Jets," *Int. Multiphase Flow*, Vol. 3, pp. 341-351.

Buyevich, Yu, A., 1971, "Statistical Hydrodynamics of Disperse Systems," Part 4, Physical Background and General Equations," *J. Fluid Mech.*, Vol. 40, No. 3, pp. 340-507.

Chao, B. T., 1964, "Turbulent Transport Behavior of Small Particles in Dilute Suspension," *Osterreiches Ing.-Archiv.*, Vol. 18, 1964, pp. 7-21.

Chen, C. P., 1986, "Multiple-Scale Turbulence Model in Confined Swirling Jet Predictions," *AIAA-J.*, Vol. 24, No. 10.

Crowder, R. S., Daily, J. W., and Humphrey, J. A. C. 1984, "Numerical Calculation of Particle Dispersion in a Turbulent Mixing Layer Flow," *J. of Pipelines*, Vol. 4, No. 3, pp. 159-170.

Crowe, C. T., and Sharma, M. P., 1978, "A Novel Physico-computational Model for Quasi One-dimensional Gas Particle Flows," ASME JOURNAL OF FLUIDS ENGINEERING, Vol. 100, pp. 343-349.

Danon, H., Wolfshtein, M., and Hetsroni, G., 1977, "Numerical Calculations of Two-phase Turbulent Round Jets," *Int. Multiphase Flow*, Vol. 3, 1977, pp. 223-234.

Elghobashi, S. E., and Abou-Arab, T. W., 1983, "A Two-Equation Turbulence Closure for Two-Phase Flows," *Phys. Fluids*, Vol. 26, No. 4, pp. 931-938.

Elghobashi, S. E., Abou-Arab, T. W., Rizk, M., and Mostafa, A., 1984, "A Prediction of the Particle Laden Jet with a Two Equation Turbulence Model," *Int. J. Multiphase Flow*, Vol. 10, No. 6, pp. 697-710.

Genchiev Ah.D., and Karpuzov, D. S., 1980, "Effects of Motion of Dust Particles on Turbulence Transport Equations," *J. Fluid Mech.*, Vol. 101, No. 4, pp. 833-842.

Hanjalic', K., and Launder, B. E., 1972, "A Reynolds Stress Model of Turbulence and Its Application to Thin Shear Flows," *J. Fluid Mech.*, Vol. 52, No. 4, pp. 609-638.

Hanjalic', K., Launder, B. E., and Schiestel, R., 1979, "Multiple-time Scale Concepts in Turbulent Transport Modeling," *Proc. of the 3rd Int. Symp. on Turbulent Shear Flow*, pp. 10-31.

Hetsroni, G., 1982, *Handbook of Multiphase Flow*, McGraw-Hill, New York.

Hinze, J. O., 1975, *Turbulence*, McGraw-Hill, New York.

Launder, B. E., 1978, "Heat and Mass Transport," *Turbulence*, ed. P. Bradshaw, Springer-Verlag, Berlin, pp. 231-287.

Maeda, M., Hishida, K., and Furutani, T., 1980, "Optical Measurements of Local Gas and Particle Velocity in an Upward Flowing Dilute Gas-solids Suspension," *Proc. Polyphase and Transport Technology*, San Francisco, pp. 211-216.

Melville, W. K. and Bray, Kn. N. C., 1979, "A Model of the Two-Phase Turbulent Jet," *Int. J. Heat Mass Transfer*, Vol. 22, pp. 647-656.

Michaelides, E. E., and Farmer, L. K., 1984, "A Model for Slurry Flows Based on the Equations of Turbulence," ASME-FED Vol. 13 *Liquid-solid Flows and Erosion Wear in Industrial Equipment*, 1984, ed. M. C. Roco, New York, 1984, pp. 27-32.

Parthasarathy, R. N., and Faeth, G. M., 1987, "Structure of Particle-laden Turbulent Water Jets in Still Water," *Int. J. Multiphase Flow*, Vol. 13, No. 5, 1987, pp. 699-716.

Peskin, R. L., 1971, "Stochastic Application to Turbulent-diffusion," in *Int. Symposium on Stochastic Hydraulics*, ed. C. L. Chiu, Univ. of Pittsburg, PA, pp. 251-267.

Picart, A., Berlemont, A., and Gouesbet, G, 1986, "Modelling and Predicting Turbulent Fields and the Dispersion of Discrete Particles Transported by Turbulent Flows," *Int. J. Multiphase Flow*, Vol. 12, No. 2, pp. 237-261.

Roco, M. C., and Balakrishnan, N., 1985, "Multi-Dimensional Flow Analysis of Solid-liquid Mixtures," *J. of Rheology*, Vol. 29, No. 4, pp. 431-456.

Roco, M. C., and Mahadevan, S., 1986, "Scale-Up Technique of Slurry Pipelines-Part A: Turbulence Modeling," ASME *Journal of Energy Resources Technology*, Vol. 108, pp. 269-277.

Roco, M. C., and Shook, C. A., 1983, "Modeling Slurry Flow: The Effect of Particle Size," *Canadian J. Chem. Eng.*, Vol. 61, No. 4, pp. 494-503.

Roco, M. C., and Shook, C. A., 1985, "Turbulent Flow of Incompressible Mixtures," ASME JOURNAL OF FLUIDS ENGINEERING, Vol. 107, pp. 224-231.

Shuen, J. S., Chen, L. D., and Faeth, G. M., 1983, "Prediction of the Structure of Turbulent Particle Laden in Round Jets," *AIAA J.*, Vol. 21, pp. 1480-1483.

Soo, S. L., 1967, "Multiphase Fluid Dynamics," Revised Edition, S. L. Soo Assoc., 1983, also "Fluid Dynamic of Multiphase Systems," Blaidesll, Waltham, MA.

Spalding, D. B., 1977, "A General Computer Program for Two-Dimensional Parabolic Phenomena," Dept. of Mech. Engng., Report No. HTS/77/9, Imperial College, London.

Vernier Ph., and Delhaye, J. H., 1968, "General Two-Phase Flow Equations Applied to the Thermodynamics of Boiling Water Nuclear Reactors," *Energy Primaire*, Vol. 4, No. 1-2, 1968, p. 5.

Tennekes, H., and Lumley, J. L., 1981, *A First Course in Turbulence*, The MIT Press, Cambridge, 7th ed.

Wang, C. S., Lyczkowski, R. W., and Berry, J. F., 1988, "Multiphase Hydrodynamic Modeling and Analysis of Non-Newtonian Coal-Water Slurry Rheology," ASME-FED Vol. 75 *Third Int. Symp. on Liquid-Solid Flows*, Ed. M. C. Roco, New York.

Xie, Dingguo, 1987, "Turbulent Kinetic Energy of Particle Phase in Solid-fluid Suspension Turbulence," *Int. Symp. Multiphase Flow*, China, pp. 396-401.

APPENDIX A

Double-Time Averaged Conservation Equations

By averaging over each flow component ($K=1, 2, \ldots, N$) the conservation equations of mass and momentum one obtains a new system of equations for the mean velocity, concentration and kinetic energy of turbulence. The point instantaneous conservation equation can be written for any flow component (K) or for the entire mixture in the following general form

$$\frac{\partial}{\partial t}(\rho\psi)+\nabla\cdot(\rho\psi\mathbf{u})+\nabla\cdot\mathbf{J}_\psi-S_\psi=0 \tag{A1}$$

where ρ is density, $\mathbf{u}$ is the velocity vector, ψ is the transported quantity, $\mathbf{J}_\psi$ is the flux vector for ψ, and S_ψ is the source term.

Let assume $\psi=u_{Ki}$. By splitting each flow property into mean and fluctuating components ($\bar{u}_{Ki}+u'_{ki}$) and double-time averaging the equation (A1), it results the following *momentum equations* for a phase (K) of constant density, without mass exchange with other flow components (Roco and Shook, 1985):

$$\rho_K\frac{\partial}{\partial t}(\bar{\alpha}_K\bar{u}_{Ki}+\overline{\alpha'_Ku'_{Ki}})+\bar{\rho}_K\frac{\partial}{\partial x_j}(\bar{\alpha}_K\bar{u}_{Ki}\bar{u}_{Kj})$$

Time Rate — Mean Flow Convection

$$=\rho_K\bar{\alpha}_K\overline{b_{Ki}}-\left\{\frac{\partial}{\partial x_i}(\bar{\alpha}_K\bar{p}_K+\overline{\alpha'_Kp'_K})+\bar{p}_K\frac{\partial\bar{\alpha}_K}{\partial x_i}+\overline{p'_K\frac{\partial\alpha'_K}{\partial x_i}}\right\}$$

Body Force — Pressure Effect

$$+\frac{\partial}{\partial x_j}[\bar{\alpha}_K\bar{\tau}_{K\Sigma_{ji}}+\overline{\alpha'_K\tau'_{K\Sigma_{ji}}}-\rho_K\overline{\alpha'_K(u_{Ki}u_{Kj})'}$$

Friction Effect — Collision Effect

$$-\rho_K\overline{\alpha_K\cdot u'_{Ki}u'_{Kj}}]+(\overline{I_{Ki}})_{M-K}$$

Inertial Effect — Interactions with $(M-K)$ (A2)

where K denotes a phase (or generally a flow component); $\bar{f}_K$ is the double-time average of f over K; $i, j=1, 2, 3$ are the Cartesian coordinates; b_{Ki} is the component of the body force in the ith direction; and $(\overline{I_{Ki}})_{M-K}$ is projection of the interaction vector $(\overline{I_K})_{M-K}$ in the ith direction.

The interaction term as it stands for solid-liquid drag is

$$(I_{Si})_L=-(I_{Li})_S=0.75\alpha_S\rho_L\frac{C_{DS}}{d_S}\frac{|u_{Ly}-u_{Sy}|\,(u_{Ly}-u_{Sy})}{(1-\alpha_S)^{1.7}} \tag{A3}$$

This term takes the following form for particle Reynolds numbers less than unity (Re based on particle diameter and slip velocity) flow.

$$(I_{Si})_L=-(I_{Li})_S=\alpha_S(18\mu_L/d_S^2)\,(u_{Li}-u_{Si}) \tag{A4}$$

The transverse effects caused by the presence of other solid particles, particle slip-spin (type Saffman force) and wall are neglected.

Equation (A2) contains terms due to the unsteady flow, mean flow convection, diffusion, pressure, body force, as well as frictional inertial and collisional effects. The mean form of the turbulence kinetic energy governing equation is obtained by subtracting from the steady state instantaneous momentum equation for a component $K=L$ the corresponding mean flow equation, and then multiplying the resulting difference equation by $(u'_{Ki}+u''_{Ki})$. By double-time averaging one obtains the *kinetic energy equation* for a flow component $K=L$

$$\rho_K\bar{\alpha}_K\bar{u}_{Kj}\left(\overline{\frac{\partial u'^2_{Ki}/2}{\partial x_j}}+\overline{\frac{\partial u''^2_{Ki}/2}{\partial x_j}}\right)+\frac{\partial}{\partial x_j}[\rho_K\bar{\alpha}_K(\overline{u'_{Kj}u'_{Ki}u'_{Ki}}$$

Group # 1 (Convection) — Group #2 (Velocity Diffusion)

$$+\overline{u''_{Kj}u''_{Ki}u''_{Ki}}+\overline{u'_{Kj}u'_{Ki}u''_{Ki}}+\overline{u''_{Kj}u''_{Ki}u'_{Ki}}+\overline{u'_{Kj}u''_{Ki}u'_{Ki}}$$
$$+\overline{u'_{Kj}u''_{Ki}u''_{Ki}}+\overline{u''_{Kj}u'_{Ki}u'_{Ki}}+\overline{u''_{Kj}u'_{Ki}u''_{Ki}})]$$
$$+\left[\frac{\partial}{\partial x_j}(\rho_K\,\overline{\alpha'_Ku'_{Ki}u'_{Ki}u'_{Kj}}+\overline{\alpha''_Ku''_{Ki}u''_{Ki}u''_{Kj}})\right.$$

Group #3 (Higher Order Correlations)

$$\left.+\text{ other 4th order and minor terms})\right]$$
$$=-\bar{\alpha}_K\frac{\partial}{\partial x_i}(\overline{u'_{Ki}P'_K}+\overline{u''_{Ki}P''_K}+\overline{u'_{Ki}P''_K}+\overline{u''_{Ki}P'_K})$$

Group #4 (Pressure Diffusion)

$$+\bar{\alpha}_K\left(\overline{P'_K\frac{\partial u'_{Ki}}{\partial x_i}}+\overline{P''_K\frac{\partial u''_{Ki}}{\partial x_i}}+\overline{P'_K\frac{\partial u''_{Ki}}{\partial x_i}}+\overline{P''_K\frac{\partial u'_{Ki}}{\partial x_i}}\right.$$

Group #5 (Extra Production and Transfer)

$$-\overline{(u''_{Ki}\alpha'_K\frac{\partial p''_K}{\partial x_i}}+\overline{u''_{Ki}\alpha''_K\frac{\partial p'_K}{\partial x_i}}+\overline{u''_{Ki}\alpha''_K\frac{\partial p''_K}{\partial x_i}}$$
$$\left.+\overline{\alpha''_Ku'_{Ki}\frac{\partial p''_K}{\partial x_i}}+\overline{\alpha'_Ku'_{Ki}\frac{\partial p''_K}{\partial x_i}}\right)$$
$$-\left(\rho_K\bar{\alpha}_K\overline{u'_{Ki}u'_{Kj}}\frac{\partial\bar{u}_{Ki}}{\partial x_j}+\rho_K\bar{\alpha}_K\overline{u''_{Ki}u''_{Kj}}\frac{\partial\bar{u}_{Ki}}{\partial x_j}\right)$$

Group #6 (Production)

$$-\left[\bar{u}_{Ki}\,\overline{\alpha'_Ku'_{Kj}}\frac{\partial\bar{u}_{Ki}}{\partial x_j}+\bar{u}_{Kj}\,\overline{\alpha'_Ku'_{Ki}}\frac{\partial\bar{u}_{Ki}}{\partial x_j}\right.$$

Group #7 (Extra Production)

$$+\bar{u}_{Ki}\,\overline{\alpha''_Ku''_{Kj}}\frac{\partial\bar{u}_{Ki}}{\partial x_j}+\bar{u}_{Kj}\,\overline{\alpha''_Ku''_{Ki}}\frac{\partial\bar{u}_{Ki}}{\partial x_j}$$
$$\left.-(\overline{\alpha'_Ku'_{Ki}}+\overline{\alpha''_Ku''_{Ki}})\frac{\partial\bar{p}_K}{\partial x_j}+\text{minor terms}\right]$$
$$+\rho_K\bar{\alpha}_K\nu_K\overline{\frac{\partial u'_{Ki}}{\partial x_j}\frac{\partial u'_{Ki}}{\partial x_j}}+\rho_K\bar{\alpha}_K\nu_K\overline{\frac{\partial u''_{Ki}}{\partial x_j}\frac{\partial u''_{Ki}}{\partial x_j}}$$

Group #8 (Dissipation)

$$+\left(\rho_K\overline{\alpha'_K\nu_K\frac{\partial u'_{Ki}}{\partial x_j}\frac{\partial u'_{Ki}}{\partial x_j}}+\rho_K\overline{\alpha''_K\nu_K\frac{\partial u''_{Ki}}{\partial x_j}\frac{\partial u''_{Ki}}{\partial x_j}}+\text{mixed correlations}\right.$$

Group #9 (Extra Dissipation and Diffusion)

$$+\overline{u'_{Ki}(I'_{Ki})_{M-K}}+\overline{u''_{Ki}(I''_{Ki})_{M-K}}$$

Group #10 (Extra Dissipation) (A5)

The Plane Poiseuille Flow of a Particle-Fluid Mixture

D. A. Drew
Department of Mathematical Sciences,
Rensselaer Polytechnic Institute,
Troy, NY 12180-3590

The "laminar" shear flow of a particle-fluid mixture is studied using the two-fluid model, which is based on equations of conservation of mass and momentum for each material. The equations are applied to plane parallel flow, where the equations or mixture axial momentum and an equation for the concentration across the channel are derived. An asymptotic solution to the equations is derived which shows that the particles move to the center of the channel, forming a core which does not shear. The core is surrounded by clear fluid layers where all the shear occurs.

Introduction

The shear flow of a particle-fluid mixture occurs in many natural and technological situations. Sediment flowing in water is an important geological process. Pneumatic transport carries reactants in chemical plants. Slurries of coal suspended in water are pumped into combustors in power plants. The behavior of these mixtures is difficult to predict. The equations governing their behavior are not satisfactorily known.

We shall study the predictions of a set of equations for the flow of a particle-fluid mixture in plane parallel flow with stationary walls, where the flow is driven by a pressure gradient. In single phase flow, this is called plane Poiseuille flow, and we therefore use this terminology for it here also. The predictions of the flow depend on the constitutive assumptions specifying the interactions of the particles with the fluid (the interfacial force density) and the interaction of the materials of each phase with itself (the stresses). Note that even though the average motion is "laminar" in the sense that on average, layers of the particle-fluid mixture slide over one another; on a microscopic level, the motion cannot be laminar, since the particles cannot shear. This complicates the flow by introducing effects that are microscopically nonlocal, such as stress being transmitted by the particles.

We are particularly interested in the mechanisms that determine the distribution of the phases in the cross-channel direction. These forces are quite small, but are important because they are crucial in many applications of these equations, including erosion and heat transfer.

The Model

The equations of motion for the flow of a particle-laden fluid mixture with both phasic densities constant are [1]:

$$\frac{\partial \alpha}{\partial t} + \nabla \cdot \alpha \mathbf{v}_p = 0 \tag{1}$$

$$\frac{\partial (1-\alpha)}{\partial t} + \nabla \cdot (1-\alpha)\mathbf{v}_f = 0 \tag{2}$$

$$\alpha \rho_p \left(\frac{\partial \mathbf{v}_p}{\partial t} + \mathbf{v}_p \cdot \nabla \mathbf{v}_p \right) = -\alpha \nabla p_p + (p_{pi} - p_p) \nabla \alpha + \mathbf{M}_p + \nabla \cdot (\alpha \tau_p) - (\nabla \alpha) \cdot \tau_{pi} + \nabla \cdot (\alpha \tau_p^{\mathrm{Re}}) - \alpha \rho_p \mathbf{g} \tag{3}$$

$$(1-\alpha)\rho_f \left(\frac{\partial \mathbf{v}_f}{\partial t} + \mathbf{v}_f \cdot \nabla \mathbf{v}_f \right) = -(1-\alpha)\nabla p_f - (p_{fi} - p_f)\nabla \alpha - \mathbf{M}_p + \nabla \cdot [(1-\alpha)\tau_f] + (\nabla \alpha) \cdot \tau_{fi} + \nabla \cdot [(1-\alpha)\tau_f^{\mathrm{Re}}] - (1-\alpha)\rho_f \mathbf{g} \tag{4}$$

where α is the volume fraction of particles, ρ_p is the particle density, ρ_f is the fluid density, $\mathbf{v}_p$ is the particle velocity, $\mathbf{v}_f$ is the fluid velocity, p_p is the particle pressure, p_{pi} is the pressure at the particle interface, p_f is the fluid pressure, p_{fi} is the fluid pressure at the interface, $\mathbf{M}_p$ is the interfacial force density, $\mathbf{g}$ is the acceleration due to gravity, τ_p is the particle shear stress, τ_{pi} is the particle shear stress at the interface, τ_f is the fluid shear stress, τ_{fi} is the fluid shear stress at the interface, τ_p^{Re} is the particle Reynolds shear stress, and τ_f^{Re} is the fluid Reynolds shear stress.

These equations (1)–(4) govern the evolution of the averaged velocity, pressure, and concentration fields. They must be supplemented by equations specifying the way in which the materials interact, with themselves and with each other, in terms of the averaged fields. This specification replaces the microscopic details lost in the averaging process. It is this process of formulating constitutive equations that is crucial to obtaining a system of equations that are capable of describing an adequate set of phenomena involved in multiphase flow. Unfortunately, it is not universally agreed upon how to go about this formulation. One school of thought is that constitutive equations should be derived from applying the averaging process to solutions of the microscopic equations. It seems clear that very few solutions to the equations of motion exist, and even then in very restricted (or approximate) situations. (For example, the solution for the inviscid flow around two spheres is given in terms of a series of functions that are singular inside the spheres.) It seems unlikely that this procedure can give constitutive equations for general situations that are to be believed "beyond a shadow of doubt."

The second school of thought regarding the formulation of constitutive equations is that one should postulate forms for

Contributed by the Fluids Engineering Division for publication in the JOURNAL OF FLUIDS ENGINEERING. Manuscript received by the Fluids Engineering Division September 28, 1988.

the interactions, solve the equations for a relatively simple situation, do the corresponding experiment, and measure the coefficient(s). There are pitfalls in each stage of this procedure. If the postulated forms are inadequate, or the solution is incorrect (it is often based on assumptions about the forms taken on by the fields), or the experiment is inadequate, then the procedure fails. It is also not always obvious that the procedure has failed. Then the coefficient so "measured," of the postulated "effect" becomes a part of the technology, and the true mechanism and its correct model could remain undiscovered for a long period.

We suggest here an approach that combines the best of these two approaches. Specifically, we shall include in our constitutive equations terms that have been calculated from microscopic considerations (usually single-sphere results). These terms can come from both the irrotational flow of an inviscid fluid around a sphere, and from Stokes flow around a sphere. Both flows yield similar forms for certain terms, but with different coefficients. Of course, the inviscid calculation produces no drag terms, and no averaged viscous stress terms. Thus, our philosophy in this paper is to assume a form for a constitutive equation that is suggested by a microscopic calculation, but to assume that the coefficient is a parameter. We shall study the effect of the values of the parameters in the special case of plane Poiseuille flow. We do not know if the set of constitutive equations taken is adequate to describe all the physics of shear flows, however, we see within the constitutive equations taken that certain parameter values do not describe the phenomena observed in plane Poiseuille flows.

For the interfacial force density, we take

$$\mathbf{M}_d = \alpha S(\mathbf{v}_f - \mathbf{v}_p) + \alpha\rho_f C_{vm}\left(\frac{\partial \mathbf{v}_f}{\partial t} + \mathbf{v}_f \cdot \nabla \mathbf{v}_f - \frac{\partial \mathbf{v}_p}{\partial t} - \mathbf{v}_p \cdot \nabla \mathbf{v}_p\right) + \alpha\rho_f L(\mathbf{v}_p - \mathbf{v}_f) \times (\nabla \times \mathbf{v}_f) + \mathbf{F}_F \quad (5)$$

where S is the drag coefficient, C_{vm} is the virtual mass coefficient, L is the lift coefficient, $\mathbf{F}_F$ is the Faxen force.

The combination of virtual mass and lift is that derived by Drew and Lahey [2]. This force is calculated by considering the force on a single sphere accelerating relative to an inviscid fluid which is undergoing a pure shear plus a rotation. For small rotation rates, this results in $C_{vm} = \frac{1}{2}$ and $L = \frac{1}{2}$. This force is objective only if $L = C_{vm}$. For our present purposes, we shall assume that the virtual mass-lift combination is objective, hence $L = C_{vm}$, but we shall not assign a specific value for L at this point. We also note that the lift force has been calculated for the case of slow viscous flow by Rubinow and Keller [3]. Somewhat surprisingly, the value for L that they obtain is $L = \frac{1}{2}$.

The Faxen force is usually neglected. Since we wish to treat viscous effects and the Faxen force is comparable to the viscous forces in the fluid phase, we retain this term here. We assume (Happel and Brenner [4])

$$\mathbf{F}_F = k\alpha\mu\nabla^2\mathbf{v}_f. \quad (6)$$

where μ is the viscosity of the fluid.

The assumptions made about the pressures are known to have profound consequences for wave propagation in bubbly flows. We wish to do something here which is consistent with the other assumptions made about other terms such as virtual mass and lift. Therefore, we assume

$$p_p = p_{pi} = p_{fi} = p_f - \xi\rho_f|\mathbf{v}_f - \mathbf{v}_p|^2 \quad (7)$$

Stuhmiller [5] has calculated the average interfacial pressure for inviscid flow. His calculation results in the form given in (7) and the value of the parameter ξ that he calculates is $\xi = \frac{1}{4}$. Givler [6] calculates the average pressure for highly viscous flow and obtains the same form with a value of $\xi = -\frac{9}{32}$. He suggests that negative values of ξ give rise to diffusive effects, while positive values have the opposite trend. The basis for this claim is that in the momentum equation for the particle phase, the term $(p_{pi} - p_p)\nabla\alpha$ in the particle momentum equation (3), with the particle pressure and the interfacial average particle pressures as given in equation (7) give a force on the particles in the direction of sgn $(\xi)\nabla\alpha$. If $\xi > 0$, then this force tends to push particles toward higher concentrations of particles, and hence is "anti-diffusive." Other terms can have a similar interpretation, and the ultimate force depends on several parameters.

We next discuss models for the stress terms. If the particles are small and rigid, they are essentially stress transmitters on the microscale. Thus, we assume that the particle stress and the interfacial stresses are the same. That is,

$$\tau_p = \tau_{pi} = \tau_{fi}. \quad (8)$$

The stress which the particles are transmitting corresponds to the extra needed to make the mixture more viscous. To account for this effect, we take

$$\tau_{pi} = \beta(\alpha)\tau_f. \quad (9)$$

For the viscous stress, we take Ishii's [1] form, which is derived from averaging the microscopic viscous stress tensor. We have

$$\tau_f = \mu\left[\nabla\mathbf{v}_f + (\nabla\mathbf{v}_f)^T - \frac{1}{1-\alpha}\nabla\alpha(\mathbf{v}_f - \mathbf{v}_p) + (\mathbf{v}_f - \mathbf{v}_p)\nabla\alpha\right]. \quad (10)$$

Reynolds stresses appear in the equations of motion. The flows that we study are not "turbulent," in the classical meaning of the word; however, there are velocity fluctuations from the mean flow caused by the kinematical effects due to the relative motions of the different phases These velocity fluctuations can transport momentum. Forms for the Reynolds stresses are not considered standard in the two-phase flow literature, even though they are responsible for diffusive effects in the momentum balance. We take a simple form of a model proposed by Drew and Lahey [7] which has coefficients which can be calculated by integrating the tensor product of the velocity fluctuation with itself determined from inviscid flow around a single sphere [8]. Since the calculation involves a single sphere, the results are valid only to $O(\alpha)$ and higher order terms have been neglected. This gives

$$\tau_f^{\mathrm{Re}} = \alpha\rho_f b_{f1}|\mathbf{v}_f - \mathbf{v}_p|^2\mathbf{I} + \alpha\rho_f b_{f2}(\mathbf{v}_f - \mathbf{v}_p)(\mathbf{v}_f - \mathbf{v}_p) \quad (11a)$$

and

$$\tau_f^{\mathrm{Re}} = \rho_p b_{p1}|\mathbf{v}_f - \mathbf{v}_p|^2\mathbf{I} + \rho_p b_{p2}(\mathbf{v}_f - \mathbf{v}_p)(\mathbf{v}_f - \mathbf{v}_p). \quad (11b)$$

The coefficients calculated for inviscid flow are $b_{f1} = -\frac{3}{20}$ and $b_{f2} = -\frac{1}{20}$. No values for b_{p1} and b_{p2} have been calculated. We include equation (11b) because it gives rise to terms that are diffusive in the same sense as discussed after equation (7). This model can be viewed as resulting from assuming that the particles follow closely the motions of the fluid.

Plane Poisueille Flow

We assume a laminar symmetric flow of neutrally buoyant spherical particles suspended in an incompressible Navier-Stokes fluid in a channel of width $2h$. If the particles are neutrally buoyant, the gravitational force merely allows the use of the dynamic pressure to account for the gravitational forces. The no slip condition on the fluid gives $\mathbf{v}_f = 0$ at $y = \pm h$, and the condition of impenetrability of the wall to particles gives $\mathbf{n}\cdot\mathbf{v}_p = 0$ at $y = \pm h$. We also impose conditions that

the total flow is given, and the concentration of particles in the incoming mixture is known.

$$\int_{-h}^{h} \mathbf{i}\cdot\mathbf{v}_f dy = 2hV_0 \tag{12a}$$

$$\int_{-h}^{h} \mathbf{i}\cdot\mathbf{v}_p dy = 2hU_0 \tag{12b}$$

$$\int_{-h}^{h} \alpha(y)\, dy = 2h<\alpha> \tag{12c}$$

We wish to study the plane Poiseuille flow of a particle-fluid mixture. For plane parallel flow, let

$$\mathbf{v}_p = U(y)\mathbf{i} \tag{13a}$$

$$\mathbf{v}_f = V(y)\mathbf{i} \tag{13b}$$

$$\alpha = \alpha(y). \tag{13c}$$

Then the continuity equations are satisfied automatically, and the momentum equations yield

$$0 = -\alpha \frac{\partial p_f}{\partial x} + \alpha S(V-U) + \alpha\mu \frac{d}{dy}\beta \frac{dV}{dy} + \alpha k\mu \frac{d^2V}{dy^2} \tag{14}$$

$$0 = -(1-\alpha)\frac{\partial p_f}{\partial x} + \alpha S(U-V) + \mu \frac{d}{dy}(1-\alpha)\frac{dV}{dy} - \alpha k\mu \frac{d^2V}{dy^2} + \frac{d\alpha}{dy}\beta\mu \frac{dV}{dy} \tag{15}$$

$$0 = -\alpha \frac{\partial p_f}{\partial y} + 2\alpha\xi\rho_f (U-V)\frac{d}{dy}(U-V) + \alpha\rho_f L(U-V)\frac{dV}{dy} = \frac{d}{dy}\alpha\rho_p b_{p1}(U-V)^2 \tag{16}$$

$$0 = -(1-\alpha)\frac{\partial p_f}{\partial y} + \xi\rho_f (V-U)^2 \frac{d\alpha}{dy} + \alpha\rho_f L(V-U)\frac{dV}{dy} = \frac{d}{dy}\alpha\rho_f b_{f1}(U-V)^2. \tag{17}$$

Differentiating (9) or (10) with respect to x, and using (6) gives

$$\frac{\partial^2 p_f}{\partial x \partial y} = 0$$

so

$$p_f = f(x) + P(y).$$

Differentiating (7) or (8) with respect to x gives

$$f'(x) = 0.$$

Therefore

$$p_f = -\frac{\Delta p}{\Delta x}x + P(y), \tag{18}$$

where Δp is the imposed pressure drop on the channel and Δx is its length. If we add (14) and (15), we have

$$-\frac{\Delta p}{\Delta x} = \frac{d}{dy}\left[(1-\alpha)\mu\frac{dV}{dy} + \alpha\beta\mu\frac{dV}{dy}\right]. \tag{19}$$

Equation (19) should reduce to the Einstein [9] formula for effective viscosity in the appropriate limit, specifically, for low concentrations of spheres that are not subject to any forces. Note that the spheres are rigid, so that they do not contribute to the mean shear rate. Thus, the average shear rate is $(1-\alpha)dV/dy$. Then $\beta = 5/2$ gives the Einstein formula for effective viscosity when the right hand side of equation (19) is expanded for small α. A form which agrees with Einstein's for small α and with that of Frankel and Acrivos [10] for large concentrations is given by Graham [11] as

$$\frac{\mu_{\text{eff}}}{\mu} = \left(1+\frac{5}{2}\alpha\right) + \frac{9}{4}\left[1+\left(\frac{\eta}{2a}\right)\right]^{-1}\left[\frac{1}{\eta/a} - \frac{1}{1+\eta/a} - \frac{1}{(1+\eta/a)^2}\right]$$

where a is the sphere radius, η is the sphere separation, which, for a simple cubic packing, is given by

$$\eta/a = 2\frac{1-(\alpha/\alpha_m)^{1/3}}{(\alpha/\alpha_m)^{1/3}},$$

where α_m is the experimentally determined maximum packing of spheres.

The relative motion between the particles and the fluid can be obtained from either of the remaining momentum equations in the x-direction. If we divide equation (13) by αS, we have

$$U - V = \frac{1}{S}\left(\frac{\Delta p}{\Delta x} + \mu\frac{d}{dy}(\beta+k)\frac{dV}{dy}\right). \tag{21}$$

The momentum equations in the y-direction are instrumental in determining the distribution of particles across the channel. These equations involve the transverse pressure gradient dP/dy. The transverse pressure gradient can be eliminated from equation (15) and equation (16) by subtracting $\alpha/(1-\alpha)$ times equation (16) from equation (15). This gives

$$0 = \left(\xi + b_{p1} - b_{f1}\frac{\alpha}{1-\alpha}\right)2\alpha\rho_f(U-V)\frac{d(U-V)}{dy} + \frac{\alpha}{1-\alpha}\rho_f L(U-V)\frac{dV}{dy} + \left[(-\xi+b_{f1})\frac{\alpha}{1-\alpha} + b_{p1}\right]\rho_f(U-V)^2\frac{d\alpha}{dy} \tag{22}$$

We can further eliminate $(U-V)$ by using equation (21). This gives

$$0 = \alpha\left(\xi + b_{p1} - b_{f1}\frac{\alpha}{1-\alpha}\right)\frac{2\mu}{S}\frac{d^2}{dy^2}(\beta+k)\frac{dV}{dy} + \frac{\alpha}{1-\alpha}L\frac{dV}{dy} + \left[(-\xi+b_{f1})\frac{\alpha}{1-\alpha} + b_{p1}\right] \times \frac{1}{S}\left[\frac{\Delta p}{\Delta x} + \mu\frac{d}{dy}(\beta+k)\frac{dV}{dy}\right]\frac{d\alpha}{dy} \tag{23}$$

Equations (19) and (23) govern the fluid velocity profile and the concentration of particles in the channel. For these equations, the appropriate boundary conditions are

$$V(h) = 0 \tag{24a}$$

$$\int_{-h}^{h} V(y)\, dy = 2hV_0 \tag{24b}$$

$$\int_{-h}^{h} \alpha(y)\, dy = 2h<\alpha>. \tag{24c}$$

Let us nondimensionalize the problem by

$$w = V(y)/V(0) \tag{25a}$$

$$\zeta = y/h. \tag{25b}$$

The equations become

$$[1+(\beta-1)\alpha]\frac{dw}{d\zeta} = -R\zeta \tag{26}$$

$$0 = 2\alpha\left(\xi + b_{p1} - b_{f1}\frac{\alpha}{1-\alpha}\right)\frac{d^2}{d\zeta^2}(\beta+k)\frac{dw}{d\zeta} + LD\frac{\alpha}{1-\alpha}\frac{dw}{d\zeta} + \left[(-\xi+b_{f1})\frac{\alpha}{1-\alpha} + b_{p1}\right]\left[R + \frac{d}{d\zeta}(\beta+k)\frac{dw}{d\zeta}\right]\frac{d\alpha}{d\zeta}. \tag{27}$$

where

$$R = \frac{\Delta p h^2}{\mu \Delta x V(0)} \tag{28a}$$

is the channel Reynolds number, and

$$D = \frac{Sh^2}{\mu} \tag{28b}$$

is the dimensionless drag per unit velocity. Note that if we assume Stokes drag around spherical particles of radius a, then $S = 9\mu/2a^2$, and therefore $D = (h/a)^2$.

The boundary conditions are

$$w(0) = 1 \tag{29a}$$

$$\frac{dw}{d\zeta}(0) = 0 \tag{29b}$$

$$w(1) = 0 \tag{29c}$$

$$\int_0^1 \alpha(\zeta) d\zeta = <\alpha>. \tag{29d}$$

Let us seek a solution for D large. This assumes that the channel is many particle diameters wide. The outer solution assumes $\zeta = 0(1)$. With D large, we must have β large, or $dw/d\zeta$ small, or α small. From equation (26), we see that with $R = 0(1)$, if $dw/d\zeta$ is small, β must be large. With $dw/d\zeta = D^{-q}g$, and $\beta = D^q b'$, we have $\alpha = \alpha_m + D^{-q}\alpha'$, and $b' = -(9/8)(\alpha_m/\alpha')$. In order to obtain a balance in equation (27), we must have $q = 1$.

Let us assume for the moment that the region with α small is near the wall, and that the region with $dw/d\zeta$ small is in a region around the center of the channel, which we shall call the core. Then in the core we have $\alpha = \alpha_m$. The resulting approximate particle concentration is given by

$$\alpha = \begin{cases} \alpha_m, & 0 < \zeta < \zeta^* \\ 0, & \zeta^* < \zeta < 1, \end{cases} \tag{30}$$

where ζ^* is the location of the edge of the core. In the clear fluid region, the fluid velocity must satisfy

$$\frac{dw}{d\zeta} = -R\zeta \tag{31}$$

so that

$$w = -\frac{1}{2} R(\zeta^2 - 1) \tag{32}$$

At ζ^*, we have $w(\zeta^*) = -(R/2)[(\zeta^*)^2 - 1] = 1$. Thus, we see that $R = 2/[1-(\zeta^*)^2]$. If $1 - \zeta^* = 0(1)$, we see that $R = 0(1)$. Since $<\alpha> = \alpha_m \zeta^*$, we have

$$R = \frac{2}{\left(\frac{<\alpha>}{\alpha_m}\right)^2 - 1} \tag{33}$$

Note that R is not small when $<\alpha>$ is near α_m.

The Transition Layer

We next show that a layer exists at $\zeta = \zeta^*$ where α makes a transition from α_m to 0, while $dw/d\zeta$ goes from 0 to $-R\zeta^*$. Note that finding the appropriate α forces $dw/d\zeta$ to have the proper behavior.

We let $\zeta = \zeta^* + D^{-p}\zeta'$. The right-hand side of equation (26) becomes $-R\zeta^*$ to first approximation. Using this, we obtain a balance in equation (27) for $p = 1/2$, and $dw/d\zeta'$ can be eliminated to give

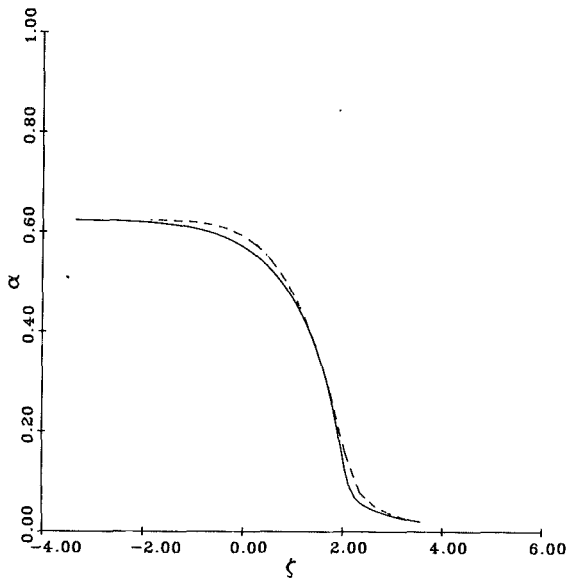

Fig. 1 Transition layer, for two different parameter sets. See the text for parameter values.

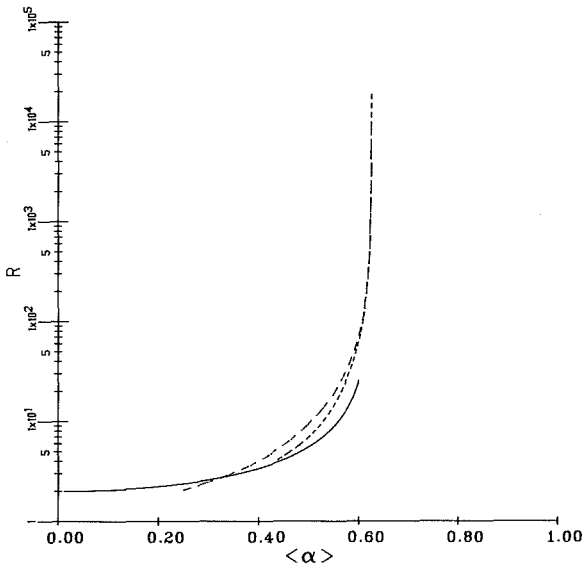

Fig. 2 "Effective Viscosity." The different curves for large $<\alpha>$ are the result of the asymptotic analysis for different values of D. The curve with the shorter dashes represents $D = 50$ and the one with longer dashes represents $D = 200$.

$$\frac{d^2\alpha}{d\zeta'^2} + f_1(\alpha)\left(\frac{d\alpha}{d\zeta'}\right)^2 + f_2(\alpha) = 0 \tag{34}$$

where

$$f_1(\alpha) = \frac{f''(\alpha)}{f'(\alpha)} + \frac{\left[-(\xi + b_{f1})\frac{\alpha}{1-\alpha} + b_{p1}\right]}{\xi + b_{p1} - b_{f1}\frac{\alpha}{1-\alpha}} \frac{1}{2\alpha} \tag{35a}$$

$$f_2(\alpha) = \frac{1}{f'(\alpha)} \frac{1}{\left[\xi + b_{p1} - b_{f1}\frac{\alpha}{1-\alpha}\right]} \frac{1}{1-\alpha} \frac{1}{1+(\beta-1)\alpha} \tag{35b}$$

$$f(\alpha) = \frac{\beta + k}{1 + (\beta - 1)\alpha} \tag{35c}$$

It is not known under what conditions the solutions to equation (34) exhibit the proper behavior. Numerical solutions to

equation (34) with $b_{f1} = -3/20$, $b_{p1} = -3/20$, and $\xi = -9/32$ (dashed curve) and with $b_{f1} = -3/20$, $b_{p1} = -1$, and $\xi = 1/4$ (solid curve) are shown in Fig. 1. Other solutions were attempted with $b_{p1} = 0$, but the derivative $d\alpha/d\zeta$ was positive for α near α_m. Apparently, the usual models (with $b_{p1} = 0$) do not have enough "particle diffusivity" to balance the lift.

Wall in the Transition Layer

When $\zeta^* = 1 - o(1)$, the clear-fluid layer no longer exists, and the wall lies in the transition layer. In this case, R need not be $O(1)$. If we let $\zeta^* = 1$, we see that the same approximation holds in equations (26) and (27), leading to the same equation (34) for α. The difference is that the boundary conditions are not those of matching at $\zeta' = \infty$, but instead we must impose

$$w(0) = 0. \tag{36}$$

In addition, we have

$$<\alpha> = \alpha_m + \int_{-\infty}^{0} \alpha'(\zeta')d\zeta' \tag{37a}$$

and

$$1 = w(-\infty) = -\int_{-\infty}^{0} \frac{dw}{d\zeta'}\, d\zeta' = RD^{-1/2}\int_{-\infty}^{0} \frac{d\zeta'}{1+(\beta-1)\alpha} \tag{37b}$$

The integration can be done numerically using a change of variables so that if the integration of equation (36) has proceeded to some point ζ_0, both $<\alpha>$ and R can be obtained from equations (37*a* and *b*) by letting ζ' be replaced by $\zeta' - \zeta_0$. Note that R depends on D. Figure 2 is a plot of R versus $<\alpha>$ using the analysis alluded to above for $<\alpha>$ near α_m. The conditions for Fig. 2 are $b_{f1} = -3/20$, $b_{p1} = -3/20$, and $\xi = -9/32$.

Effective Viscosity

Figure 2 can be interpreted in terms of the effective viscosity of the particle-fluid flow in Poiseuille flow. One sensible way to define viscosity is to require that for a single-phase fluid of that viscosity, the same pressure drop gives the same centerline velocity. The value of R for a single-phase fluid is 2. Thus, the effective viscosity based on the centerline viscosity is given by

$$\frac{\mu_{\text{eff}}}{\mu} = \frac{R}{2} \tag{38}$$

The centerline velocity is not a useful quantity for defining macroscopic parameters since it is not imposed on the flow through external means. Attempting to interpret effective viscosity in terms of the mass flux is equally unsatisfactory.

Conclusion

The equations of motion described in this paper are capable of describing the distribution of concentration and velocity in the viscous shear flow of a particle-fluid mixture. It also shows the sensitivity of the flow to some of the parameters needed to provide constitutive equations for the mixture. In particular, the Poiseuille flow of a particle-fluid mixture in a channel results in a flow with a strong structure. The structure which occurs consists of a core of particles which are sufficiently "packed" so that they cannot shear, surrounded by a clear-fluid layer where all the shear occurs. The motion is insensitive to the value of the lift coefficient L. Also, the motion seems to be sensitive to parameters that give an effective particle diffusion. As discussed earlier, these include the Reynolds parameters b_{f1} and b_{p1}, and the interfacial pressure coefficient ξ. The parameter b_{f1} is always "anti-diffusive." The parameter b_{p1} is always diffusive. With $\xi > 0$, a sufficiently large value of the particle Reynolds stress coefficient b_{p1} is needed to compensate for the "anti-diffusive" nature of ξ.

The presence of this particular structure has several implications. First, if such a structure occurs in a flow, one must be careful in interpreting measurements of fundamental quantities such as mixture viscosity. The quantity measured may be strongly dependent on the structure. Second, this flow is not useful for measuring any of the quantities which cause the particle separation, even though one (the lift) is large. The reason for this is that the flow becomes so degenerate.

The presence of such a structure in this flow may allow the efficient filtration of such a mixture. Since no particles are near the walls, if fluid can be drawn through the walls without destroying the transition layer, then no particles will stick to the wall to impede the further flow of fluid through them. For this to occur, the transition layer must be stable. If perturbing it causes it to disappear, or to become unsteady or wavy, the desired property of no particles near the wall may not occur.

The physical form of the transition layer is similar to many structures observed in particle-fluid systems, for example, the top of a sediment layer in a river, the "wall" of a bubble in a fluidized bed, and the wall of a spout in a spouted bed dryer. In all of these examples, the stability of the layer is important. Consider, for example, the top of a layer of sediment being overwashed with a fluid. If the fluid flows fast enough, the layer will become unstable and erosion will occur. The analysis performed here suggests only that the structure is "structurally stable," in that if the parameters are such that the layer exists, then changing them a very small amount will not destroy the structure. A dynamic stability analysis is needed to determine whether waves form, etc.

Acknowledgment

This work was supported by the National Science Foundation under Grant Number CPE83-14443 and the Mathematics Division of the U.S. Army Research Office under Contract DAAL29-86-K-0126. The author also wishes to thank Professor G. Belfort and Dr. J. Schonberg for inspiration and many helpful discussions.

References

1 Ishii, M., *Thermo-fluid Dynamic Theory of Two-Phase Flow*, Eyrolles, Paris, 1975.

2 Drew, D. A., and Lahey, R. T., Jr., "The Virtual Mass and Lift Force on a Sphere in Rotating and Straining Inviscid Flow," *International Journal of Multiphase Flow*, Vol. 13, 1987, pp. 113–121; "Some Supplemental Analysis Concerning the Virtual Mass and Lift on a Sphere in Rotating and Straining Inviscid Flow," submitted to *International Journal of Multiphase Flow*.

3 Rubinow, S. I., and Keller, J. B., "The Transverse Force on a Spinning Sphere Moving in a Viscous Fluid," *J. Fluid Mech.*, Vol. 11, 1961, pp. 447–459.

4 Happel, J., and Brenner, H., *Low Reynolds Number Hydrodynamics*, Prentice-Hall, Englewood Cliffs, NJ, 1965.

5 Stuhmiller, J., "The Influence of Interfacial Pressure on the Character of Two-Phase Flow Model Equations," *International Journal of Multiphase Flow*, Vol. 3, 1977, pp. 551–560.

6 Givler, R., "An Interpretation for the Solid Phase Pressure in Slow, Fluid-Particle Flows," *International Journal of Multiphase Flow*, Vol. 13, 1987, pp. 717–722.

7 Drew, D. A., and Lahey, R. T. Jr., "Application of General Constitutive Principles to the Derivation of Multidimensional Two-Phase Flow Equations," *International Journal of Multiphase Flow*, Vol. 5, 1979, pp. 243–264.

8 Nigmatulin, R. I., "Spatial Averaging in the Mechanics of Heterogeneous and Dispersed Systems," *International Journal of Multiphase Flow*, Vol. 5, 1979, pp. 353–385.

9 Einstein, A., "Eine Neue Bestimmung der Molekuldimensionen," *Ann. Phys.*, Vol. 19, 1906, pp. 289–306.

10 Frankel, N. A., and Acrivos, A., "On the Viscosity of a Concentrated Suspension of Solid Spheres," *Chem. Eng. Sci.*, Vol. 22, 1967, pp. 847–853.

11 Graham, A. L., "On the Viscosity of Suspensions of Solid Spheres," *Applied Scientific Research*, Vol. 37, 1981, pp. 275–286.

Journal of Fluids Engineering

Technical Briefs

Intermittency and Length Scale Distributions in a Plane Turbulent Plume

M. S. Chandrasekhara[1] and B. R. Ramaprian[2]

Previous studies have shown that normalized Reynolds shear stress and turbulent heat fluxes in asymptotic plane turbulent plumes are significantly higher than in asymptotic plane turbulent jets. This paper describes an attempt to relate this increase to the length scales in the flow. Hot/cold interface intermittency and integral-length-scale distributions were measured in both these flows. The interface-intermittency distributions were found to be bell-shaped in the plume in contrast to a nearly top-hat shape in a jet, thus providing confirmation of the role of buoyancy in generating larger scales in plumes. These larger scales cause the integral length of turbulence in the plume to increase by nearly 15 percent relative to the nonbuoyant jet.

Nomenclature

b_u = velocity half width
b_t = temperature half width
D = nozzle width at exit
f_c = hot/cold interface crossing frequency
g = acceleration due to gravity
l_u, l_v = integral length scales for u and v velocity fluctuations
R_j = exit Richardson number = $\left(\frac{-\Delta\rho_j}{\rho_j}\right)\frac{gD}{U_j^2}$
R_{uu}, R_{vv} = correlation functions for u and v fluctuations
$\overline{T}$ = local mean temperature excess
T_a = ambient temperature
$\overline{t^2}$ = mean square temperature fluctuations
t_ϕ = time scale
U_j = jet exit velocity
U_m = centerline velocity
$\overline{U}, \overline{V}$ = mean velocities in the x and y directions
$\overline{u^2}, \overline{v^2}$ = mean square velocity fluctuations
x, y = coordinates along and perpendicular to flow axis
ΔT_j = exit temperature excess
$\eta = \frac{y}{b_u}$
ρ_j = density at nozzle exit
Ω = hot/cold interface intermittency

1 Introduction

Early studies by Rouse et al. [1] established the basic growth and decay laws of plane turbulent jets and plumes. In a plume flow, the driving force is buoyancy, i.e., a plume orginates from a source of buoyancy. In a plane plume, the buoyancy and momentum forces are comparable. On the other hand, a jet flow is due to a source of momentum. Figure 1 describes the characteristics of a jet and plume. Kotsovinos [2] characterized the behavior of the velocity and temperature fluctuations as well as the turbulent/nonturbulent interface in a plume flow. More recently, Ramaprian and Chandrasekhara [3, 4, 5] measured both the mean and turbulence properties in asymptotic plane plumes. These studies have shown that, when properly scaled by using the centerline velocity U_m and the half widths b_u or b_t (of the velocity or temperature distributions, respectively), the normalized turbulent stresses and heat fluxes are significantly higher in plumes. In particular, the normalized Reynolds shear stress has been found to be about 50 percent higher in plumes than in jets. This is seen from Fig. 2 taken from [5]. Such large increases imply corresponding increases in the eddy momentum and thermal diffusivities. This increase has been attributed to the production of larger scales in the flow by gravitational instability induced by buoyancy (Kotsovinos [2]). This note reports some quantitative results of comparative measurements of the intermittency and integral length scales in plumes and jets. These results not only confirm that buoyancy increases the length scales in the flow, but also would directly be useful in modelling such flows.

2 Experimental Procedure

2.1 Description. Plane turbulent jets and plumes were produced by injecting hot water vertically upward from a 250 mm span × 5 mm width (D) nozzle into cold water contained in a hydraulic flume. The details of the experimental set up and the individual experimental conditions can be found in [3]. The experiments of relevance to this paper are identified as MSC2, and MSC3. Flow MSC2 is a heated (but, slightly bouyant) vertical plane jet with an exit Richardson number of 0.0008. Flow MSC3 is a positively buoyant, plane plume flow with an exit Richardson number of 0.05, and reaches asymptotic state by $x/D = 30$, where x is the distance downstream from the plume exit. In both the cases, detailed experiments were carried out at streamwise stations corresponding to $x/D = 30$ and 50. Table 1 lists the exit conditions namely, the exit velocity U_j, exit temperature T_j, and ambient temperature T_a for the two flows. The mean and turbulent flow properties of these flows have been fully documented in [4, 5].

[1]Adjunct Research Professor and Assistant Director, Navy-NASA Joint Institute of Aeronautics, Department of Aeronautics and Astronautics, Naval Postgraduate School, Monterey, CA 93943. Fellow ASME.

[2]Professor, Mechanical and Materials Engineering Department, Washington State University, Pullman, WA 99164. Fellow ASME.

Contributed by the Fluids Engineering Division of The American Society of Mechanical Engineers. Manuscript received by the Fluids Engineering Division June 6, 1989.

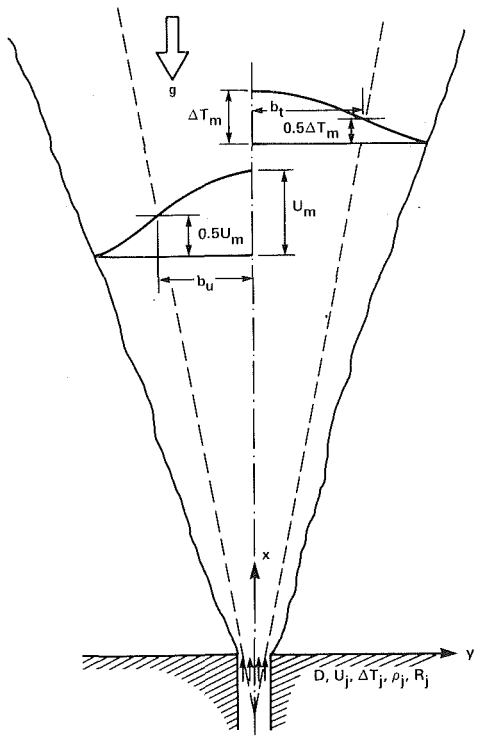

Fig. 1 Schematic and nomenclature of a plane turbulent jet and plume

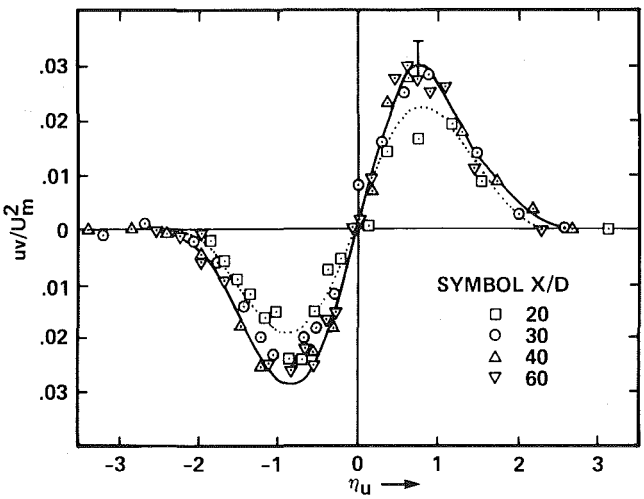

Fig. 2 Reynolds shear stress distribution in plumes. Plume MSC3: x, x/D = 20, o, x/D = 30, Δ, x/D = 40, ▽, x/D = 60; ....., jet MSC2 (from [5]).

Mean velocities ($\overline{U}$, $\overline{V}$) and turbulent stresses ($\overline{u^2}$, $\overline{v^2}$) were measured using two-component, frequency-shifted laser Doppler anemometry. The optics were set up in the forward-scatter mode and frequency trackers were used for signal processing. Temperature ($\overline{T}$) and its fluctuations ($\overline{t^2}$) were measured using cold-wire resistance thermometry. The data were low-pass filtered at 50 Hz, digitized at 100 Hz and acquired with a HP-1000 mini-computer. The sampling frequency of 100 Hz was selected after ascertaining that the spectral bandwidth of turbulence in the plumes was within 0–50 Hz. A total of 61440 samples per channel (of each U, V, and T) were collected. These data were used to compute the hot/cold interface intermittency, turbulent spectra, autocorrelations and length scales.

The integral scales were obtained from the autocorrelation functions R_{uu} and R_{vv} of $\overline{u^2}$ and $\overline{v^2}$, respectively. For this purpose, first the spectra of the turbulent velocity fluctuations $\overline{u^2}$ and $\overline{v^2}$ were estimated using the discrete fast Fourier transform technique. A total of 60 spectra, each computed over 1024 samples were used to obtain the mean spectrum in each case. Next, the autocorrelation functions were obtained by computing the inverse Fourier transform of the mean spectra. The integral time scale t_ϕ ($\phi = u$ or v) of turbulence was then obtained from the definition:

$$t_\phi = \int_0^\infty R_{\phi\phi}(\tau)d\tau. \tag{1}$$

Finally, the integral length scale l_ϕ was obtained using the Taylor approximation: $l_\phi = -\overline{U}t_\phi$.

Table 1 Experimental conditions

Flow designation	$U_j$cm/s	ΔT_j°C	T_a°C	R_j
MSC2	30	3.29	23.0	0.0008
MSC3	10	23.2	24.2	0.05

2.2 Determination of Intermittency. Since the experiments involved heated water being discharged into a cold ambient, one could use the instantaneous local temperature as a tracer for identifying the presence of the jet/plume fluid. In this so-called "heat tagging" technique, detection of the hot fluid anywhere indicates the presence of the jet/plume fluid there. Likewise, detection of the cold fluid implies the penetration of the ambient fluid into that region. This method of determining the hot/cold interface intermittency is very attractive because temperature can easily and reliably be measured. It has been used, in the past, by several researchers (see for e.g., Weir et al. [6]).

The digitized instantaneous velocity and temperature data recorded on disk were used for the estimation of the hot-cold intermittency. Following the usual procedure, a threshold level was selected to distinguish the "hot" fluid from the "cold" fluid. When the temperature level was higher than that of the threshold, the corresponding samples were accepted as "hot" samples. The rest were treated as "cold" samples. The intermittency Ω, was defined as the ratio of the number of hot samples to the total number counted. It is to be noted that Ω is a measure of the intermittency associated with the crossing of the probe volume by the hot/cold interface. It is not necessarily a measure of the turbulent/non-turbulent intermittency. A procedure, well established from earlier studies (LaRue, [7]), was followed in the selection of the threshold level, record length, sample size etc.

In addition to intermittency, the frequency with which the hot/cold interface crosses the probe volume was also determined. The crossing frequency f_c is defined as the number of cross-overs per unit time in a given length of sample. No distinction was made between hot-cold and cold-hot crossings. The crossing frequency at each point was estimated at the same threshold level as that used for the estimation of Ω.

3 Results and Discussion

3.1 Intermittency Studies. The distribution of the hot/cold interfacial intermittency and the crossing frequency for flows MSC2 and MSC3 are shown in Figs. 3(*a*) and 3(*b*). In the jet, the intermittency is uniformly equal to 1 in the central part and drops sharply beyond $\eta = y/b_u \approx 1.0$. The distributions at $x/D = 30$ and 50 are seen to be fairly self-similar and resemble the distributions of turbulent/non-turbulent intermittency measured by Bradbury [8] and Gutmark and Wygnanski [9]. The distributions of the crossing frequency f_c, exhibit some asymmetry, but the maximum crossing frequency occurs at $\Omega \approx 0.5$, as expected. The frequencies encountered here are approximately 0 to 2.5 Hz which correspond to a nondimensional wave number range of $0 \leq 2\pi f_c b_u/\overline{U} \leq 3.0$.

In the plume, the intermittency at the centerline is $\approx 0.92 - 0.95$ at $x/D = 30$, instead of the normally expected value

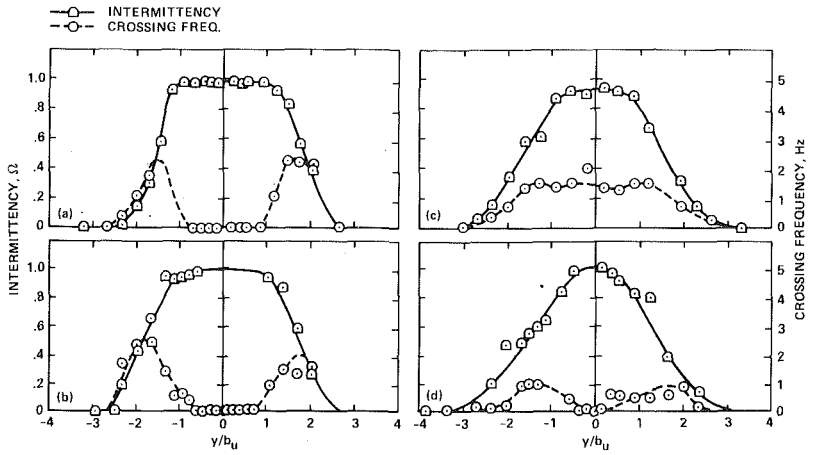

Fig. 3 Intermittency and crossing frequency distributions. (*a,b*) Nonbuoyant jet MSC2; (*c,d*) Plume MSC3. Uncertainties: y/b_u: ±0.06; Ω: ±.05; crossing frequency: ±0.25 Hz.

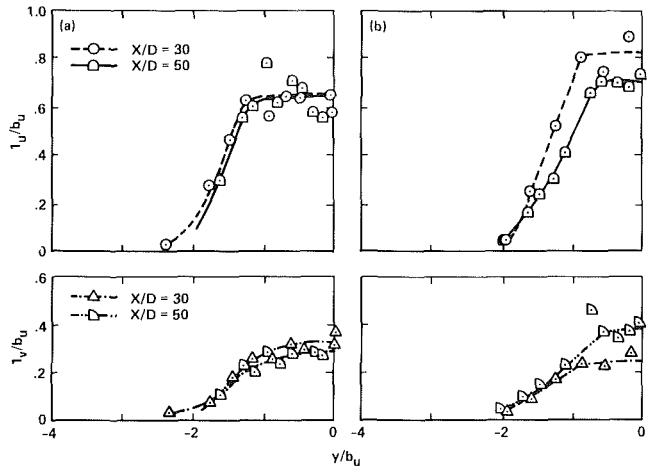

Fig. 4 Distributions of length scales across the flow. (*a*) Nonbuoyant jet MSC2; (*b*) Plume MSC3. Uncertainties: y/b_u: ±0.06; l/b_u: ±0.06.

of 1. This interesting result indicates the presence of cold fluid for about 5 to 8 percent of the time, in the core of the plume. It thus suggests that eddies larger than the width of the plume entrain the outer cold fluid at this station. The intermittency distribution evolves in the streamwise direction, and Ω attains a value of unity at the centerline by $x/D = 50$ (Fig. 3(*b*)). The more significant result, however, is the bell-shaped intermittency distribution in the asymptotic plume in contrast to a flat-topped distribution characteristic of nonbuoyant jets. The maximum crossing frequency in the plume at $x/D = 50$ is about 1 Hz which corresponds to a nondimensional wave number of about 1.3, a value significantly lower than the value of about 3 in the nonbuoyant jet.

The bell-shaped intermittency distribution indicates intermittent mixing in a large part of the interior of the plume, i.e., there is a significant amount of direct transport of ambient fluid by large eddies even in regions of maximum shear stress in the plume (around $\eta = 0.7$). In the case of the jet, the intermittency in this region is almost unity, indicating that large eddies do not penetrate this deep into the jet. The only manner in which the ambient fluid eventually mixes with fluid in the interior of the jet is via smaller scale interaction and transport. The intermittency studies, thus clearly indicate that the large eddies in the plume are larger than in a jet and are responsible for significant transport even near the core of the plume.

3.2 Length Scale Distributions. The presence of the relatively larger eddies in the plumes was also confirmed by the data on the integral length scales of turbulence in plumes and jets. The distributions across one half of the flow are presented in Fig. 4(*a*) and 4(*b*) for the nonbuoyant jet MSC2 and plume MSC3. Flow MSC2 has constant length scales l_u and l_v over the range $\eta = 0$ to 1. The distributions of these scales do not change appreciably from $x/D = 30$ to $x/D = 50$ in the jet, indicating a fairly well developed structure of the flow. In the plume MSC3, however, the length scales (especially l_v) increase as the plume evolves from $x/D = 30$ to 50. It can be seen that, on the average, both the length scales l_u and l_v are eventually increased by buoyancy by about 10 to 15 percent relative to the nonbuoyant jet.

4 Conclusions

The present study confirms that buoyancy augments the large scales of turbulent motions. These motions, which are of the order of the width of the plume, are responsible for causing the mixing between the plume and the ambient to be intermittent even in the region of maximum shear stress. They also cause the integral scales of turbulence in the plume to be about 10–15 percent higher than those in a nonbuoyant jet.

Acknowledgment

The authors gratefully acknowledge the support received from the U.S. National Science Foundation for performing this research.

References

1 Rouse, H., Yih, C. S., and Humphreys, H. W., "Gravitational Convection From a Boundary Source," *Tellus*, Vol. 3, 1952, pp. 201–210.

2 Kotsovinos, N. E., "A Study of the Entrainment and Turbulence in a Plane Buoyant Jet," W. M. Keck Laboratory of Hydraulics and Water Resources Report no. KH-R-32, California Institute of Technology, Pasadena, 1975.

3 Ramaprian, B. R., and Chandrasekhara, M. S., "Study of Vertical Plane Turbulent Jets and Plumes," IIHR Report No. 257, The Institute of Hydraulic Research, University of Iowa, Iowa City, Iowa, 1983.

4 Ramaprian, B. R., and Chandrasekhara, M. S., "LDA Measurements in Plane Turbulent Jets," ASME JOURNAL OF FLUIDS ENGINEERING, Vol. 107, 1985, pp. 264–271.

5 Ramaprian, B. R., and Chandrasekhara, M. S., "Measurements in Vertical Plane Turbulent Plumes," ASME JOURNAL OF FLUIDS ENGINEERING, Vol. 111, 1989, pp. 69–77.

6 Weir, A. D., Wood, D. H., and Bradshaw, P., "Interacting Turbulent Shear Layers in a Plane Jet," *J. Fluid Mech.*, Vol. 107, 1981, pp. 237–263.

7 LaRue, J. C., "Detection of the Turbulent/Nonturbulent Interface Intermittency in Slightly Heated Turbulent Shear Flows," *Phys. Fluids*, Vol. 8, 1974, pp. 1513–1516.

8 Bradbury, L. J. S., "The Structure of a Self-Preserving Plane Turbulent Jet," *J. Fluid Mech.*, Vol. 23, 1965, pp. 31–64.

9 Gutmark, E., and Wygnanski, J., "The Planar Turbulent Jet," *J. Fluid Mech.*, Vol. 73, 1975, pp. 465–495.